STUDY OF STRUCTURAL, ELECTRICAL, MAGNETIC AND OPTICAL PROPERTIES OF DILUTE MAGNETIC SEMICONDUCTOR NANOPARTICLES

A Thesis Submitted to Goa University for the Award of the Degree of

DOCTOR OF PHILOSOPHY

In

PHYSICS

By

Mr. KAPIL YESHWANT SALKAR

School of Physical and Applied Sciences

Goa University

Taleigao Plateau, Goa

2020

STUDY OF STRUCTURAL, ELECTRICAL, MAGNETIC AND OPTICAL PROPERTIES OF DILUTE MAGNETIC SEMICONDUCTOR NANOPARTICLES

A THESIS SUBMITTED TO GOA UNIVERSITY
FOR THE AWARD OF THE DEGREE OF

DOCTOR OF PHILOSOPHY
In
PHYSICS

By

Mr. KAPIL YESHWANT SALKAR

PROF. R.B. TANGSALI
RESEARCH GUIDE

PROF. R. S. GAD
RESEARCH CO-GUIDE

SCHOOL OF PHYSICAL AND APPLIED SCIENCES

GOA UNIVERSITY
TALEIGAO PLATEAU, GOA

2020

DECLARATION

I hereby declare that this thesis entitled **"Study of Structural, Electrical, Magnetic and Optical Properties of Dilute Magnetic Semiconductor Nanoparticles"** leading to the degree of Ph. D in Physics is my original work and that it has not been proposed to any other University or Institution for the award of any Degree, Diploma, Associateship and fellowship or any other similar title to the best of my knowledge.

Place: Taleigao Plateau. Mr. Kapil Yeshwant Salkar

Date: June 2020 (Candidate)

CERTIFICATE

As required under the University ordinance, I certify that thesis entitled **"Study of Structural, Electrical, Magnetic and Optical Properties of Dilute Magnetic Semiconductor Nanoparticles"** submitted by **Mr. Kapil Yeshwant Salkar** leading to the degree of Doctor of Philosophy in Physics is a record of research done by him during the study period under my guidance and that it has not previously formed the basis for the award of any Degree, Diploma, Associateship and fellowship or any other similar titles.

Place: Taleigao Plateau.
Date: June 2020

Prof. R. B. Tangsali
Research Guide
Department of Physics
Goa University

Prof. R. S. Gad
Research Co-Guide
Department of Electronics
Goa University

ACKNOWLEDGEMENT

I wish to express my sincere gratitude to my guiding teacher, ***Prof. Rudraji B. Tangsali****, Department of physics, Goa University, for propounding me an enthralling research topic in the field of nanomaterial and encouraging me to pursue the research work. I shall forever and ever, in my life remain thankful to him for his valuable guidance, immense support, significant evaluation and tireless search for perfection which was a motivation throughout the research period. This continuous motivation and timely suggestions offered by him during my whole research period comprising of time span in experimental work and subsequent data analysis enormously assisted me in finishing the set goals and landing at logical conclusions. His logical way of opinion on scientific problems, understanding, support and guidance have been of immense value for me. I thank my guide for giving me the full freedom to explore the exciting world of Dilute Magnetic Semiconductor materials. I am also thankful to him for being very patient while writing papers for journals and reviewing the thesis extensively.*

I sincerely thank to ***Prof. R. S. Gad****, Department of electronics, Goa University, my research* ***Co-guide****, for his encouragement, valuable suggestions and guidance during research period.*

I extend my thanks to ***Prof. Uma Subramanian,*** *Department of Physics, Goa University,* ***Dr. Jivan parab****, my subject experts, for their thoughtful suggestions and continuous evaluation.*

I am thankful to Scientist in-charge ***Dr. N.V. Chandra Shekar****, Scientist–F* ***Dr. Sujay Chakravarty*** *and Research scholar* ***Mr. Balaram Thakur****, UGC-DAE Consortium of Scientific Research, Kalpakkam Node, Kokilamedu, Tamil Nadu, for proving VSM facility.*

I am thankful to ***Dr. N. K. Prassad*** *and* ***Mr. Asnit gangwar****, Department of Metallurgical Engineering, IIT Banaras Hindu University, Varanasi, for providing TEM facility.*

I also thank

1. All the teaching faculty and non-teaching staff of the Department of Physics, Goa University for extending co-operation and facilities throughout my research work.

2. Goa University for giving Research studentship for my research work.

3. ***Prof. V.M.S Verenkar*** *and Research scholar* ***Ms. Prajyoti Gauss dessai*** *for extending immense help in Vibrating Sample Magnetometer facility.*

4. ***Dr Sunil Kumar Singh****, Director of National Institute of Oceanography, Donapaula, Goa and* ***Mr. Girish Prabhu*** *for availing X-ray diffraction (XRD) facility.*

5. ***Dr. M. Ravichandran****, Director of National Centre for Antarctic and Ocean Research, Vasco da Gama, Goa and* ***Ms. Sahina Gazi*** *for availing Scanning Electron Microscopy (SEM) facility.*

I am grateful to my senior researchers Dr. Manoj Kothwale, Dr. Pranav P. Naik, for their constant support and precious suggestions during my period of research work.

I thank all my research colleagues Dr. Elaine Dias, Dr. Manjunath Nayak, Dr. Bhargav Alavani, Mr. Manoj D. Salgaonkar, Chetana Gaonkar, Rukma Nevgi, Samiksha Malik, Vaishali Gaonkar Dessai, M. Jeyakanthan, Steffi, Santhoshkumar Bandaru, Myren Azavedo, Nafea Bhlos, Praveenkumar Pinapati and Jostin Puthenveetil for all the happy moments we had during my research period.

Above all I thank God for keeping me relaxed and positive and showering blessings on me. Last but not the least, I wish to thank my parents for their constant support and for being patient with me during the period of my research. THANK YOU!

Mr. Kapil Yeshwant Salkar

Dedicated To My Parents

Mrs. Aruna Yeshwant Salkar

Mr. Yeshwant Vencoba Salkar

&

My professor

Prof. Rudraji. B. Tangsali

LIST OF ABBREVIATIONS

AC	Alternating Current
BE	Binding Energy
DC	Direct Current
BMP	Bound Magnetic Polaron
DC	Direct Current
DMO	Dilute Magnetic Oxide
DMS	Dilute Magnetic Semiconductor
DRS	Diffused Reflectance Spectroscopy
EMF	Electromotive Force
FC	Field Cooled
FTIR	Fourier Transforms Infrared
NTA	Nitrilotriacetic Acid
PAA	Polyacrylic Acid
RE	Rare Earth
RT	Room Temperature
RKKY	Ruderman-Kittle-Kasuya-Yoshida
SEM	Scanning Electron Microscopy
TEM	Transmission Electron Microscopy
TM	Transition Metal
UV	Ultra Violet
VSM	Vibrating Sample Magnetometer
XRD	X-Ray Diffraction
ZFC	Zero Field Cooled

TABLE OF CONTENTS

LIST OF FIGURES

LIST OF TABLES

CHAPTER 1
Introduction

1.1 General Introduction

Nanomaterials and Nanotechnology is an area of science having enormous and significant research in the field of condense matter physics. 'Nano' sized structures in which at least one dimension (length, width or thickness) is in the nanometre range of size from 1 to100 nm are termed as Nanoparticles, materials composed of nanoparticles are called as nanomaterials. Nanotechnology "Nanotech" is the science that deals with matter at the nanoscale (i.e., 10^{-9} m = 1 nm) and is also the study of manipulating matter at the atomic and molecular scale [1]. Nanomaterials are of immense interest due to their unique structural, optical, magnetic, electrical, and other emerging properties at Nanoscale and have potential impacts in electronics, medicine, and other application areas. The two foremost reasons why materials at the nanoscale exhibit exceptional properties are increase in relative surface area of the material compared to bulk material and introduction of quantum effects in the material due to low particle size [1,2]. Nanomaterials as such have large surface area to volume ratio, which enhances the chemical reactivity as it is surface area dependent. Similarly at nanoscale, quantum effects turn out to be much more intense in influencing the materials properties and characteristics leading to novel optical, electrical and magnetic behaviour in these materials.

Nanomaterials can be classified on the basis of dimensions wherein the size effect plays an important role to evidently distinguish the material properties. The nanomaterials can be categorized as:-

a) Zero dimensional structure e.g. Nanoparticles, Nanograins etc.

b) One dimensional structure e.g. Nanorods, Nano wires etc.

c) Two dimensional structures e.g. ultra thin films, quantum wells etc. Shown in Figure 1.1 [1,3].

Nanomaterials have given rise to eminent outstanding application based research in various disciplines of science due to quality optical, electrical and magnetic properties as listed below:

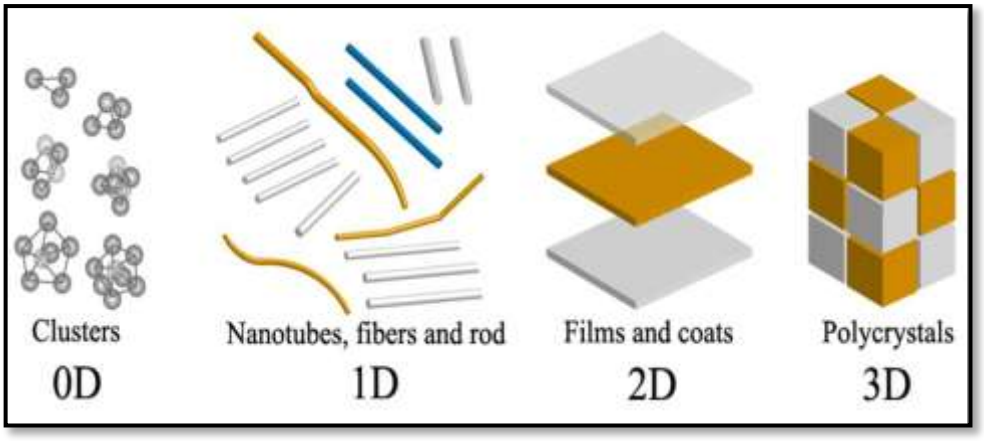

Figure 1.1: Different types of nanomaterials [4].

- Opto-electronic devices, devices which convert electricity to light and vice versa with broad bandwidth and high efficiency, find application in solar cells, light emitting diodes (LEDs), organic LEDs (OLEDs), liquid crystal displays (LCDs), and charge-coupled device (CCD). Opto-electronic devices combined with optical fibres have been widely utilized in the production of thin film transistor (TFT), mobile phone backlighting, DVD players, and digital cameras.
- Lasers, generated from nanoscale quantum dots for the fabrication of Quantum computers in which the wavelength of the laser is depend on the diameter of the quantum dot. These computers can carry out a number of computations (parallel computations) at the same time with high speed. This set of computers would be helpful to solve unambiguous digital computation problems.
- In the field of medical sciences, nanotechnology uncovers the application in diagnosis, therapeutics and tissue engineering etc. because nanomaterials have dimensions analogous to those of biological molecules. By putting together different biomolecules to the nanomaterials they can be utilized in medical applications for specific functions. For example Gold (Au) nanoparticles connected to the shorter segments of DNA, which can be used to sense the genetic sequence of a sample. Bandages surrounded with silver nanoparticles are achieving popularity for providing faster wound healing with anti-microbial protection.
- Carrying out research in catalysis is one of the most beneficial areas for a nanotechnologist. Nanoparticles having a very large surface to volume ratio and is inversely proportional to the size of a particle. A number of chemical reactions

occur on the surface of the catalyst are due to large surface area of nanoparticle, catalyst are more active on the surface as a result chemical catalysis gain more remarkable benefits at nanoscale. Therefore Nanoscale catalysts unlock the way for several processes to make more efficient and improvement in many chemical reactions.

- Single small sized magnetic nanoparticle has single domain and in magnetic nanomaterials the grains communicate with domains. Nanoparticles have unique atomic structures with distinct electronic states that give rise to special magnetic properties in nanomaterial like Super-paramagnetism, Ferromagnetism etc. Magnetic nanocomposites ferrofluids have been utilized for high density information storage and magnetic refrigeration.

"Nanotech" has come into view as most important research in fields such as biomedical sciences and engineering (Bioimaging and Biosensing devices, Drug delivery systems, Drug screening technologies, Tissue engineering), Habitat (Water purifier, humidity and climate control), Advanced electronic device systems (Transistors, Ultra-high definition displays) and food industry (food appearance, food texture, food taste, food shelf-life) [5]. Current researches in 'nanotech' are in progress to fulfil the needs of the human being by controlling the synthesis, size of nanoparticles, controlling multiple functionalities, assembly of nanostructured material, developing and employing innovative theories to design novel devices in the field of quantum nano science which is the future of nanotechnology. Although magnetism by itself, a very old concept has been in investigation for several hundred years, magnetism in nanoparticle semiconductors have attracted the attention of several researchers as introduction of any new idea unfolds the new mysteries by opening new avenues for never ending research. Thus magnetic semiconductors at all the times have proposed new challenges with mesmerizing research for the last several years.

1.2 Spintronics

Spintronics is yet another field of solid state physics which explores the capability of exploiting electron's spins in addition to its charge in transport phenomenon requires compatible devices with new hybrid functionalities and improved performance [6,7]. The devices known as spintronic devices, are fast processing devices having the potential to fulfil the requirements in a wide range

of applications with essential features [7,8]. The basic operation in the device is based on the spin alignment either ‘up’ or ‘down’ which can be controlled by an applied magnetic and electric field. The term ‘spin’ stands for either the intrinsic spin of a single electron or the average spin of a group of electrons, manifested by the magnetization of a material [9]. By using magnetic field, spin – state can be controlled since spin is a manifestation of a magnetic dipole moment. In addition to the external magnetic field, external electric fields can also be used to control the spin-state, by making the spin-state to flip as per the requirement. Addition of the spin degree of freedom to the charge based electronic material enhances the capability, performance, storage capacity, compatibility and lowers the consumption in conventional electronic devices [10].

In electronics, charge carriers electrons and holes are utilized to achieve appropriate functional applications, as they are physically transported to carry signals and process information. But in case of spintronics, the main aim is to combine electron spin and charge to achieve novel material for the same applications. Spintronics provides numerous benefits over traditional charge carriers based electronics. Adding spin degree of freedom to electrons, imparts both magnetic and semiconductor properties in a single device which is expected to be non-volatile, multipurpose, high-speed, capable of doing simultaneous data processing and storage by consuming less energy [6,10]. Use of electron spin in communication can provide several advantages like high speed communication, elimination of eddy current losses, elimination of heat in materials due to electron transport etc. thereby resulting in massive reduction in power dissipation and enhancement of device efficiency. Thus spintronic devices are extensively required as future solution to economize the current microelectronic devices. To fulfil the production of spintronic devices, it is essential to develop semiconductor materials with ferromagnetic ordering at working temperatures well-suited with existing semiconductor materials. Two most important conditions are considered to select the most potential materials for semiconductors spintronics. First, the ferromagnetism in the material should be at suitable temperatures namely Room Temperature (RT) or elevated temperature. Second, it would be a major benefit for the material in the building-up of potential devices which utilizes both spin and charge of electrons [11].

The spintronics materials are mainly classified as:

- Transition metal oxides
- DMS compounds
- Organic compounds
- Heusler alloys
- Perovskite compounds

Spintronics materials based on semiconductor compounds could produce superior quality of devices which could unite storage, detection, logical, and communication capabilities together on a single matrix to fabricate a multifunctional device and can replace numerous conventional components. Moreover the semiconductors optical properties are extremely important to convert magnetic information into optical signal which can be used in magnetic-optoelectronic devices. These kinds of ideas creates the diluted magnetic semiconductors (DMS) specially an unique and fascinating material which have created much eagerness to prepare new DMS material that can merge effortlessly with nonmagnetic semiconductors for spin injection [8]. Some DMS materials have been studied quite intensively due to their multifunctional application based properties, especially in magneto-optic, (blue/UV) light-emitting diodes, solar cell windows, conductive electrodes etc. [12-14]. However there is a large scope for preparing and investigating several other DMS materials. The perception of spintronics for improving electronic technology, information storage and devices engineering would provide the researcher with a significant solution for improving performance, reliability and functionality of the spintronics devices.

1.3 Dilute Magnetic Semiconductors

Dilute magnetic semiconductors (DMS) are materials having both semiconducting and magnetic properties. This type of materials are normally prepared by doping a small amount of magnetic impurity into a semiconducting host thereby introducing magnetic character in a semiconductor material [15,16]. Chemically this can be also expressed as semiconductors produced by replacing a fraction of the cation sites by the magnetic metal ions as shown in Figure 1.3. DMS materials can have wide range of magnetic properties, from paramagnetism to ferromagnetism which depends on the dopant material. DMS materials are expected to play a crucial role in materials science and future spintronic devices

because of charge and spin degrees of freedom combining together into single matrix that can explore the novel properties of the material [17].

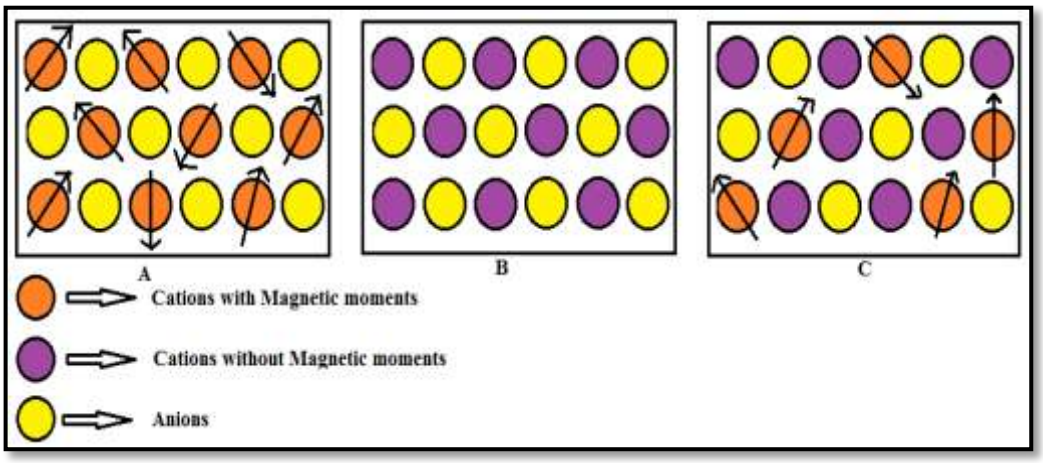

Figure 1.3: A) Magnetic semiconductor B) Non Magnetic semiconductor C) Dilute Magnetic Semiconductor.

The most common DMS materials are II-VI (CdTe, ZnSe, CdSe, Cds,etc.), IV-VI (e.g. PbTe, SnTe) and III-V (e.g. GaAs, InSb) semiconductors doped with transition metal ions (Ti, V, Cr, Mn, Fe, Co, Ni, Cu) and rare earth metal ions like (Eu, Gd, Er, Sm) as magnetic dopant ions in the material [18]. Transition metal ions having partially filled '*d* ' levels and rare earth metal ions having partially filled '*f* ' levels are responsible for magnetic behaviour in the DMS materials. DMS materials with suitable ferromagnetic semiconductor properties would be promising materials that would meet the requirement of perfect materials for spintronics [19].

These materials eventually form an appealing topic for research due to the following reason:

a. These materials could be used to fabricate single chips capable of using in a multifunctional instrument that could perform combined functions of storage, detection, logic and communication, replacing a sizable group of components.

b. These materials possess useful optical properties that are of great interest and could help in converting magnetic information into an optical signal.

c. DMS material can be used as spin polarised magnetic semiconductor material that efficiently allows spin-polarized carriers to be introduced, transported, and manipulated in semiconductor structures in realistic spintronic applications.

Thus it can be seen that DMS materials have the capability to provide new and innovative areas of application not perceived earlier. From the published reports on such materials, one can visualize that these materials could be prepared from various oxide materials that are known to possess semiconducting properties.

Oxides semiconductors like ZnO, TiO_2, In_2O_3, SnO_2, CuO etc. exhibit a wide band gap and possess unique properties due to existence of native defects, being transparent in the visible region [20]. Therefore doping these oxides with transition metals and rare earth metal ions such as Co, Mn, Fe, Ni, V, Eu, Gd, Er, Nd etc. and investigating their fascinating properties in view of emerging spintronics applications has originated as a new research area of enormous interest among present day researchers [20,21]. Moreover, these oxide materials show wide variety of magnetic behaviour from diamagnetism, paramagnetism to ferromagnetism related to the type and concentration of the dopant material. All these unique properties arise from the strong exchange interactions between the charges, orbital, lattice, and spin degrees of freedom in these materials.

1.3.1 Some Advantages of Oxide DMS Materials

❖ Wide energy band gap makes it suitable for applications with short wavelength light.

❖ Shows superior magnetic and electrical properties.

❖ Ability to grow material even at lower temperatures.

❖ Ecological safety, durability and low cost with high efficiency.

1.4 Materials For Research Work

1.4.1 Zinc Oxide (ZnO) Structure And Properties

Zinc oxide is an inorganic compound having formula ZnO, appears as a white powder and nearly insoluble in water. Its crystal structure available as wurtzite (B4), zinc blende (B3), and rock salt (B1) shown in Figure 1.4.1. The hexagonal wurtzite structure is the most stable and exists as n-type semiconductor commonly at ambient pressure and temperature. ZnO exists as a hexagonal lattice structure, belongs to P63*mc* space group with lattice parameters a = 0.3296 and c = 0.52065 nm [23,24]. In ZnO structure each anion is surrounded by four caions at the corner of the tetrahedron [22]. In an ideal hcp lattice the c/a ratio is equal to $\sqrt{8/3}$ [25].

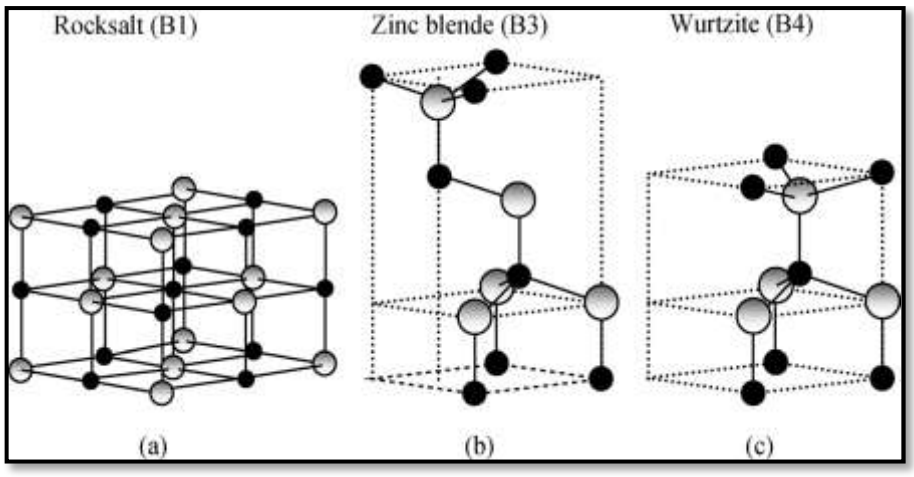

Figure 1.4.1: Stick-and-ball representation of ZnO crystal structures: (a) Cubic rock salt (B1), (b) cubic zinc blende (B3), and (c) hexagonal wurtzite (B4). Shaded gray and black spheres denote Zn and O atoms respectively [22].

In solid state science, ZnO is often called as II-VI semiconductor because zinc and oxygen belong to the 2^{nd} and 6^{th} groups of the periodic table [26]. ZnO has fascinated the researcher's attention because of its latent spintronic applications, as it holds high excitonic binding energy (60 meV) and a quite large direct band gap of approximately 3.37 eV at room temperature. The band gap corresponding to near ultra-violet region is valuably utilized in manufacturing of light emitting diodes and laser diodes [27]. ZnO has several advantages related with the large band gap that include higher breakdown voltages, good capacity to sustain large electric fields and generation of low electronic noise. ZnO is recognized as a fruitful and promising photonic- material in the blue-UV region [28].

Zinc Oxide nanoparticles enjoy good properties such as high refractive index, high thermal conductivity, antibacterial and UV-protection properties. ZnO can be utilized in some products to enhance materials properties which include plastics, ceramics, glass, cement, rubber, lubricant, paint, ointments, adhesives, pigments, food, batteries etc. [29].

1.4.2 Indium Oxide (In_2O_3) Structure And Properties

Indium oxide is a momentous and renowned n-type transparent conducting oxide (TCO) semiconductor having direct gap of 3.5 eV [30]. In stoichiometric condition In_2O_3 is an insulator but develop into a high conductive semiconductor

in its non-stoichiometric condition. In_2O_3 has cubic bixbyite structure also known as c-type rare-earth oxide structure with lattice parameter (a=b=c) of 10.117 A° [31]. Over some decades, several investigations have been done on synthesis of indium oxide in nanoparticle or thin film form and characterize its structural, optical, electrical and magnetic properties. It is important to produce this type of material for a wide range of applications such as solar cells, bio-sensors and transparent electrode material applications in optoelectronic devices [32].

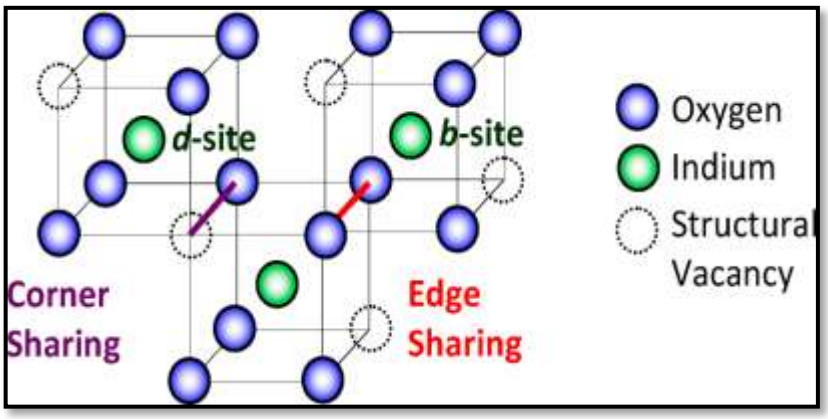

Figure 1.4.2: Cubic bixbyite crystal structure of In_2O_3 [34].

In_2O_3 exists in three different variations classified by space group as I213, R3c and Ia3. Among these three space groups In_2O_3 with Ia3 space group is the most widely investigated material both experimentally as well as from the theoretical point of view. In_2O_3 having cubic bixbyite structure contains 80-atoms in its unit cell with body centred (bcc) unit cell results in complex structure. It includes two types of indium atoms and one type of oxygen atom at Wyckoff positions 8b, 24d and 48e respectively [33]. The ‘b’ and ‘d’ sites are preferred as cation sites, ‘b’ site cations have six equidistant oxygen anion connected side to side, that are found more or less at the corners of a cube with two vacant anion positions along the body diagonal in the structure as shown in Figure 1.4.2. The position of the ‘d’ site cations is synchronized with six oxygen anions at three different distances, positioned near the corners of a cube having two empty ions with one face diagonal. The two types of indium atoms are enclosed by oxygen in octahedral and trigonal coordination respectively [33,34].

In_2O_3 can be prepared as nano spheres, nano wires, nano rods [35-38] and have a significant interest because of good sensing properties [39]. A promising

way to enhance the sensitivity is by reducing the particle size in the nanometer range and In_2O_3 also shows good optical, electrical and magnetic properties. Reduction in crystallite size maximizes the surface area which is important for the gas adsorption and reaction. In addition, with decreasing crystallite sizes high number of grain boundaries and potential barriers increase the resistance of the sensing layer. However, it is difficult to prepare In_2O_3 nanoparticles from any method of sample preparation, due to the high degree of agglomeration and unequal particle morphology. In current investigations auto-combustion process has been employed to prepare nano In_2O_3 powder having minimal agglomeration.

1.4.3 Copper Oxide (CuO) Structure And Properties

Copper oxide or CuO is also called black copper or cupric oxide. It is available in the most stable form of oxidised copper and belongs to the monoclinic crystal structure with space group C2/c as shown in Figure 1.4.3. The Cu vacancy in CuO makes it a p-type semiconductor and has narrow band gap [40]. Each atom in CuO has four nearest neighbours and in (110) plane has Cu atom linked with four nearly co-planar oxygen atoms at the corner in the monoclinic structure. The lattice constants a = 4.6837, b= 3.4226, c=5.1288 and the interfacial angles are $\alpha = \gamma = 90^o$and $\beta = 99.54^o$ [41]. A pure cupric oxide is a black solid having density of 6.52 g/cm^3 also has a high melting point of 1201 ^{o}C and is insoluble in water. CuO have large solar absorbance and a partial transparency in the visible range [42].

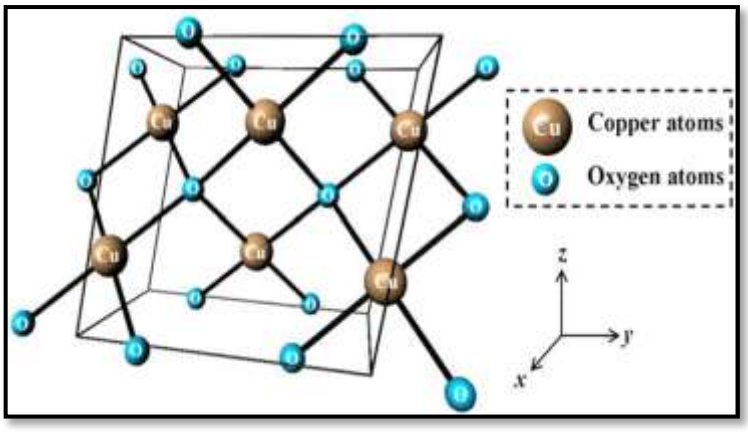

Figure 1.4.3: Monoclinic crystal Structure of CuO [43].

CuO are been investigated for its use in photo electrochemical (PEC) cells and in dye sensitized solar cells also used in manufacturing fibres, ceramics materials and for welding fluxes [44]. It can be used as a colour in ceramics utensil to produce blue, red, and green and sometimes grey, pink, or black glazes. Copper (II) oxide has a wide application that can be used to produce dry cell batteries and can also be used in wet cell batteries as cathode. CuO have attracted much scientific interest due to its interesting size-dependent on chemical and physical properties and also in the spintronic applications. These advantages make CuO as an appropriate compound for novel studies and to set up its applicability as a material of solar cell because of its photoconductivity and photoelectric cell properties.

1.5 Basics of Magnetism

Magnetic behavior normally depends on the ordering of the spin in the lattice, categorized as diamagnetic, paramagnetic, ferromagnetic, antiferromagnetic and ferrimagnetic.

1.5.1 Diamagnetism

Diamagnetic materials normally can be described by its magnetic susceptibility (χ) which has small and negative value of magnetic susceptibility (χ). This type of magnetism arises due to distorted electron orbital rotating motion about the nuclei which is produced by an application of external field. Diamagnetic material obeys "Lenz law", the induced current generates a magnetic flux which opposes change producing external magnetic field. The negative susceptibility of the magnetic material signifies that the magnetization has taken place in the reverse direction of the applied magnetic field. Magnetic dipole arrangements for a diamagnetic material in the presence or absence of applied magnetic field are shown in Figure 1.5.1. The diamagnetic atoms or ions have zero resultant magnetic moment due to completely filled orbital shells. Some examples of diamagnetic materials are copper, silver, gold, zinc, alumina and mercury etc. [45].

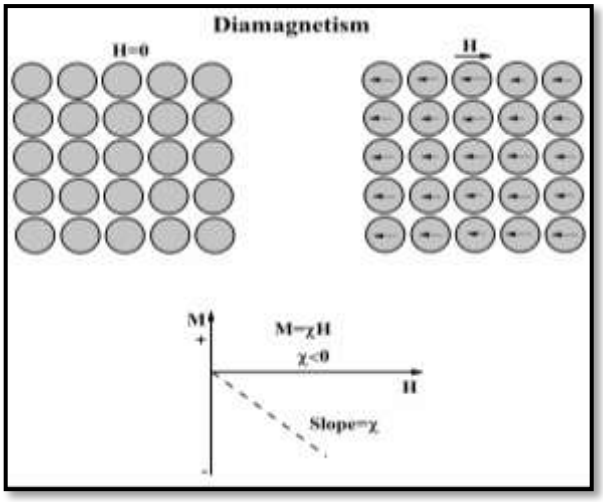

Figure 1.5.1: Spin alignment representation in a Diamagnetic material without external field and with external field.

1.5.2 Paramagnetism

Paramagnetic material includes atoms or ions whose spins are arbitrarily oriented in their surrounding as shown in Figure 1.5.2. In presence of an external magnetic field the spins gets oriented in the direction of the applied magnetic field resulting a weak magnetization as shown in Figure 1.5.2. The magnetic susceptibility (χ) of paramagnetic materials is positive and has small susceptibility. The spin gets different orientations and the susceptibility obeys the Curie law at some finite temperature. Some examples of paramagnetic materials are potassium, manganese, rare-earth elements, alkaline earth materials etc. [46].

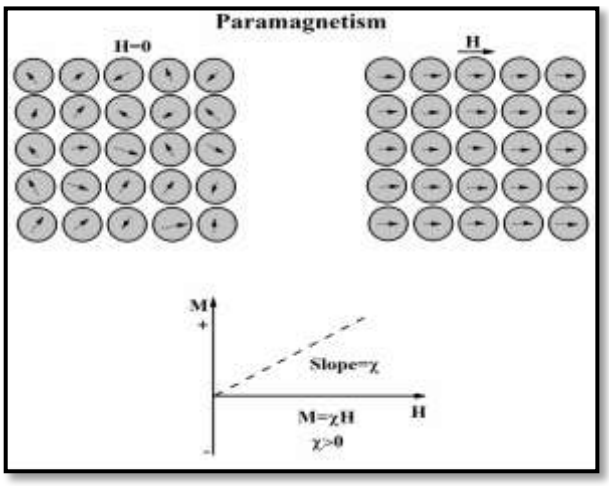

Figure 1.5.2: Spin alignment representation in Paramagnetic material without external field and with external field.

1.5.3 Ferromagnetism

In ferromagnetic material the atomic magnetic moments are lined up parallel to each other as displayed in Figure 1.5.3 (a). The parallel assemble of spins in one direction is attributed to the positive and strong interaction between them. Ferromagnetic susceptibility (χ) is in the range of 10^3 - 10^6 H/m. Ferromagnetic material does not generally exist in magnetized state but presents in a demagnetized state. The interior block of ferromagnetic material is separated into various magnetic domains. Moreover each of the domains is spontaneously magnetized and the magnetizations directions of the domains are random. In presence of external magnetic field, the magnetization of the material enhances until it attains its saturation value (Ms) as shown in Figure 1.5.3 (b). Examples of ferromagnetic materials generally include iron, cobalt, nickel and several alloys [47]. These types of materials have Curie temperature Tc which is the temperature at which there is a transition from ferromagnetic to paramagnetic state as shown in Figure 1.5.3 (b).

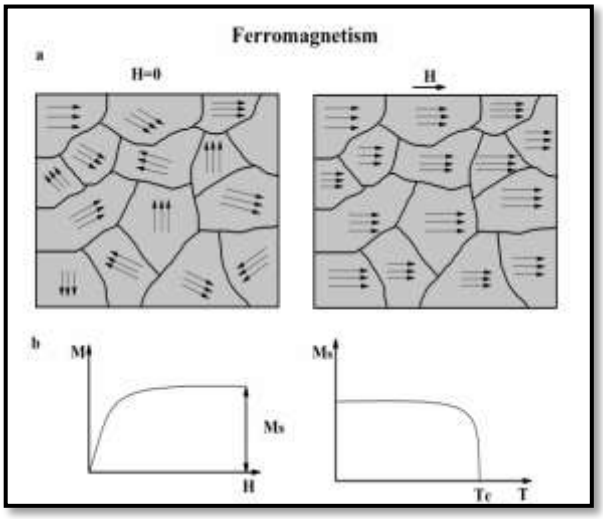

Figure 1.5.3: (a) Spin alignment representation in a ferromagnetic material without external field and with external field (b) Magnetization curve for ferromagnetic material and Variation of spontaneous magnetization Ms with respect to temperature.

1.5.4 Antiferromagnetism

Antiferromagnetic materials have weak magnetization, positive and small magnetic susceptibility (χ). In these types of materials the magnetic atomic

moments are distributed among two sub lattices. The moments have equal magnitude but arranged in antipararalled way to each other. The total magnetic moment of antiferromagnetic material is zero as shown in Figure 1.5.4. The antiferromagnetic materials are temperature dependable and characterized by a kink in the magnetic susceptibility curve. This kink point is termed as Neel temperature displayed in Figure 1.5.4. Below Neel temperature the spin magnetic moments are antiparallel whereas above this point spins are randomly oriented and the material becomes paramagnetic. Some general examples of antiferromagnetic materials having antiferromagnetic ordering are MnO, FeO, CoO and NiO [48].

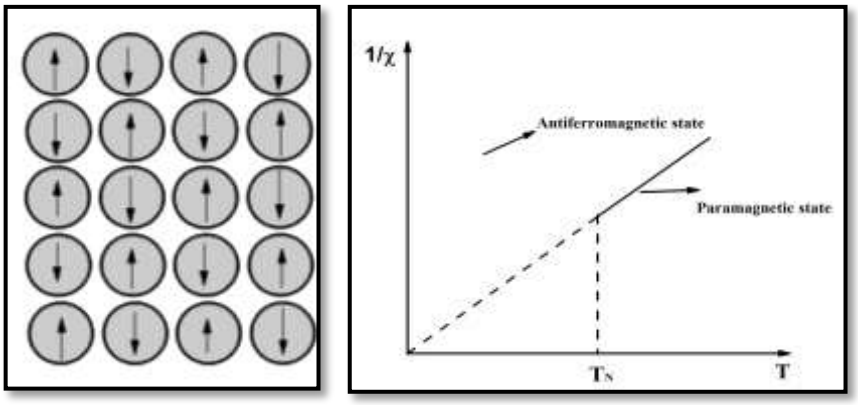

Figure 1.5.4: Spin alignment representation in an Antiferromagnetic material and Variation of 1/χ with respect to T in antiferromagnetic material.

1.5.5 Ferrimagnetism

In case of ferrimagnetic materials, the magnetic ion takes up two dissimilar kinds of lattice positions. The total magnetic moments of the two positions are oriented in reverse directions and are unequal in magnitude as displayed in Figure 1.5.5. This could occur from the fact that either the ions has different magnetic moments in building the ferrimagnetic materials or the number of atoms with unusual single spin direction is formed which are in the opposite spin direction. Such magnetization is generated without applying any external magnetic field. This magnetization it is termed as spontaneous magnetization (Ms) [49]. By enhancing the material temperature, the spins are distressed by thermal agitation, which is accompanied by a decline in spontaneous magnetization and disappears at Neel temperature as shown in Figure 1.5.5.

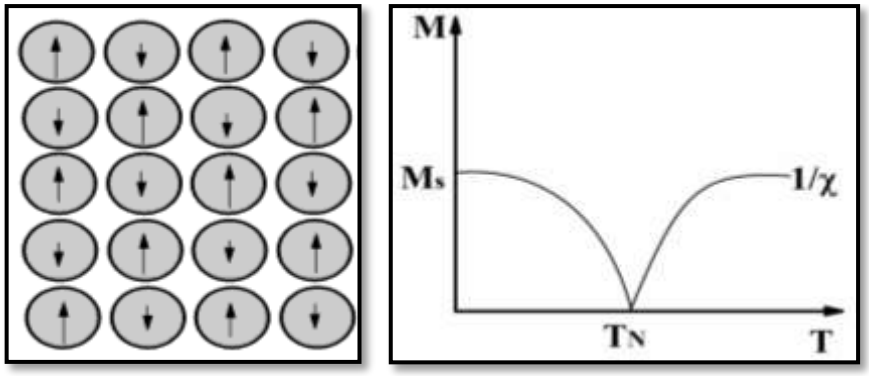

Figure 1.5.5: Spin alignment representation in a Ferrimagnetic material and Variation of M and 1/χ versus T curves in Ferrimagnetic materials.

1.6 Mechanism of Ferromagnetism In DMS Materials

When non magnetic semiconductors are doped with magnetic ions the exchange mechanisms takes place between the host semiconductor and the magnetic ion. The exchange mechanisms can ultimately conclude the magnetic behaviour of the material. The exchange mechanisms can be divided into two main categories that is direct and indirect mechanism. The indirect interaction mechanism contains four type's interactions namely double exchange, super exchange, RKKY and BMP exchange interactions. These exchange interactions are illustrated in the subsequent subsection.

1.6.1 Direct Exchange Interactions

Direct exchange interaction takes place between the neighbouring magnetic atoms which are having overlapping wave function and occur due to columbic interaction between the electrons. If the spins are parallel and are directed toward the same direction then the exchange interaction energy is positive; on the other hand, if the spins are anti-parallel then the exchange interaction energy is negative. According to Bethe and Slater premise, when the inter-atomic distance is small the electrons utilized their most of the time in between nearby atoms, consequently antiparallel alignment and negative exchange offers antiferromagnetic contribution as shown in Figure 1.6.1 [50]. If the atoms are far-away from one another than the electrons utilize it's time to reduce the electron-electron repulsion. Parallel alignment or positive exchange interaction provides ferromagnetic contribution as depicted in Figure 1.6.1. Usually orbits of doped

atoms do not have proper overlapping and cannot build up FM by direct exchange interaction. Therefore, indirect mechanisms are useful in constructing magnetic semiconductors [51].

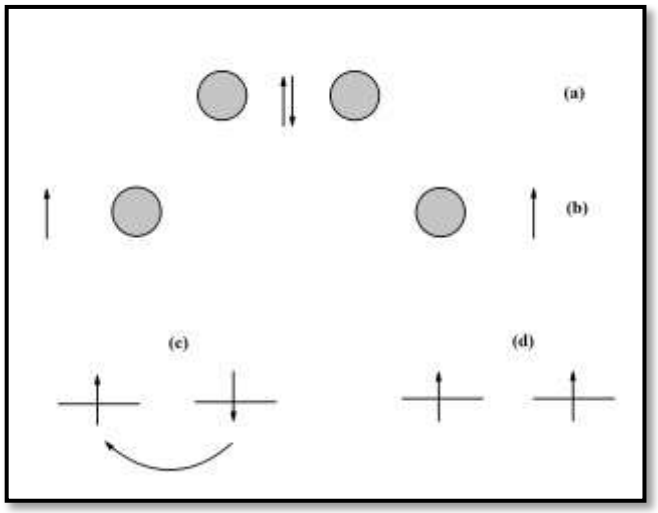

Figure 1.6.1: (a) Antiparallel spin alignment for small interatomic distances, (b) Parallel spin alignment for large interatomic distances. Simple picture for direct exchange interaction: (c) Preferential antiparallel spins alignment, because it permits the electrons to jump to the neighbouring site. (d) For parallel spins hopping is restrained by the Pauli principle.

1.6.2 Indirect Exchange Interaction

To elucidate the ferromagnetism in DMS materials numerous indirect mechanisms were anticipated. The indirect mechanism includes RKKY interaction, Super exchange, double exchange, Bound Magnetic Polarons etc.

1.6.2.1 RKKY Interaction

Ruderman, Kittel, Kasuya and Yosida (by Ruderman and Kittel, 1954; Kasuya, 1956; Yosida, 1957) Proposed a theory for ferromagnetism and is named as RKKY by following their names [52]. This hypothesis was initially originated to illustrate the FM in metals, it becomes very important simply when a high concentration of free carriers is present in the material. The fundamental proposal of RKKY interaction is the pairing of magnetic moments during coulomb exchanges through band electrons explained by the s-d Kondo Hamiltonian, ensuing from the second-order perturbation. The exchange energy of the pairing

depends on the exchange integral of the s-d interaction and on the density of states of the free carriers at the Fermi level. The original RKKY study reviled that the RKKY exchange coefficient *j* fluctuates from positive to negative via changing ion separation from the localized moments and creates damped oscillatory character. Therefore, the magnetic coupling can be ferromagnetic or anti-ferromagnetic depending on the separation between ions pair [53].

1.6.2.2 Super Exchange

Super-exchange interaction occurs in those materials which are having coupling of nearest-neighbour by sharing cation as shown in Figure 1.6.2.2. This type of mechanism appears after the virtual hopping of carriers between the fully occupied p orbitals of anions and the d orbitals of the magnetic cations. To occupy the same p-level with the electrons from both nearby atoms and should be having opposite spins to trail the Pauli exclusion principle [54,55]. As a result, anti-ferromagnetic coupling of nearest-neighbor cations is produced by sharing an anion. This mechanism is perfectly fited for ionic solids such as transition metal oxides [56]. In case of transition metal ions the orbital's bonding are produced by 3d electrons in atoms and the 2p valance electrons of the diamagnetic oxygen. The sp-d hybridization generates the super-exchange interaction in II-VI DMS because of spin-spin interaction [57].

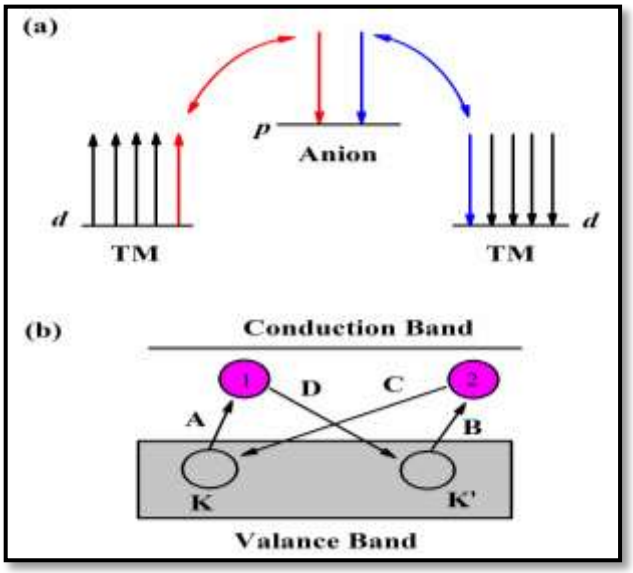

Figure 1.6.2.2: Schematic diagram of the four virtual transitions representing the superexchange ion-ion interaction.

1.6.2.3 Double Exchange

The double exchange mechanism occurs through coupling or paring of magnetic ions in different oxidation states by jumping of an electron from one ion to another ion and interaction with p-orbital is expressed as double exchange interaction shown in Figure 1.6.2.3 [58]. In this mechanism, there is no requirement of spin flips and it is dynamically good if both the ions have an equivalent magnetic structure. This method of exchange interaction is suitable to clarify the magnetism in spinel structure, manganite and Mn perovskites.

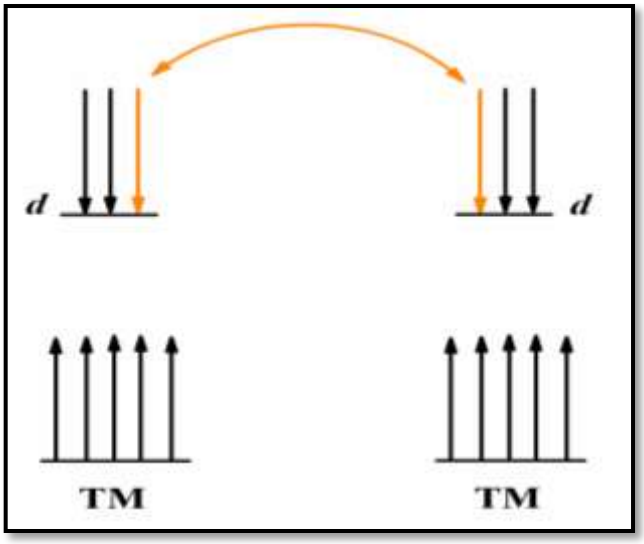

Figure 1.6.2.3: Systematic diagram of double exchange mechanism.

1.6.2.4 Bound Magnetic Polarons (BMP)

The BMP mechanism for long-range ferromagnetic ordering fails to elucidate the ferromagnetism by the mediation of free charge carriers, mainly when the charge carrier concentration is low and where ferromagnetism is seen at high temperature. In DMS materials many localized spins are due to the dopant transition metal ions which interact with a less number of weakly bound charge carriers. As a result, the magnetic moment gets polarized to produce significant magnetic moments in the donor/acceptor impurities area and is identified as bound magnetic polarons [59]. The fundamental idea of bound magnetic polarons is demonstrated in Figure 1.6.2.4. The polarons size enhances with decrease in temperature. Therefore, the contact and amount of overlapping between neighbour polarons boosts and the possibility of interaction with the dopant magnetic ions

results in forming polaron clusters which also gets increases. A ferromagnetic transition takes place when the cluster size of polaron is similar to that of the sample. This model explains the magnetism having low carrier density and can be relevant to both p- and n-type host materials [60]. In addition, the BMP model approach is the reverse to the mean field Zener model which talks about the carriers as quasi-localized states in an impurity band. The ferromagnetism is sorted out by donor electrons related to the defects such as oxygen vacancies to form bound magnetic polarons, which overlap to produce a spin – split band [61].

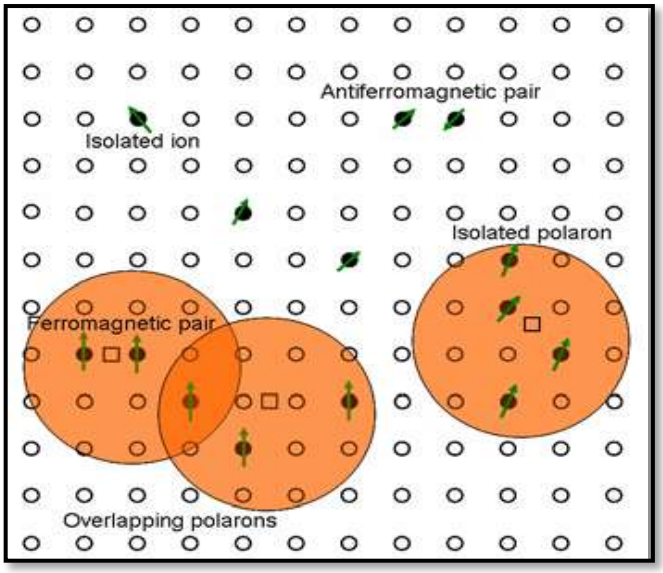

Figure 1.6.2.4 Systematic diagram of Bound Magnetic Polaron model [62].

1.7 Literature Review

Last two decades has seen a tremendous increase in research in the field of dilute magnetic semiconductor (DMS) materials. Currently lot of research work is going on DMS and especially on Oxide based DMS materials. Several reports are being published by researchers on the existence of room temperature ferromagnetism in DMS materials using different models.

A. Vanaja et.al. studied the structural, optical properties of Co doped ZnO Nanoparticles using Sol-gel method and found crystalline sizes of pure and Co doped ZnO to about 10.34 nm and 23.58 nm calculated from XRD data, SEM images showed sphere-shaped images due to the consequence of Co doping. Further FTIR spectra verify the presence of fundamental bands, the band gap decreases with increase in Co^{2+} concentration. Therefore, sol gel synthesis could

be considered as a successful synthesis to modify the properties of ZnO nanoparticles [63]. N. Mohamed Basith et.al. investigated the structural, morphological, optical, magnetic and antibacterial activity of Co-doped ZnO nanoparticles by using facile and rapid microwave-assisted combustion method. The XRD data calculation reviled that crystallite size varies in the range of 19 - 24 nm. SEM analysis shows that the morphology changes from grains to nanoparticles having hexagonal-like shape structure. Optical band gap decreases with increasing Co doping levels from 0 to 2.0 wt%, which is mainly attributed to the d-d transitions. PL spectra show a strong green emission band, RTFM is explained on the basis of BMP (Bound Magnetic Polarons) model. Antibacterial studies show that for higher Co-doped ZnO nanoparticles possess the most antibacterial effect [64]. R. Elilarassi et.al. studied the effect of Co doped ZnO nanoparticles on its structural, optical and magnetic properties synthesized using auto-combustion method and revealed the formation of hexagonal wurtzite structure without any secondary phase using XRD analysis. PL measurements show the UV, violet and orange-red emissions. The red shift in the UV emission may be attributed mainly because of the exchange interactions (sp–d exchange interactions). All the Co-doped samples exhibit ferromagnetism at room temperature [65]. V. Rajendar et.al. investigated the consequence of Co doped ZnO nanoparticles on its structural and magnetic properties prepared by Novel Combustion Synthesis and reviled that the crystallite size are in the range of 28 nm to 26 nm for the pure and Co doped ZnO nanopowder respectively calculated using XRD data. The magnetic measurements indicate that two magnetic phases were present, with a ferromagnetic phase dominating at high temperatures [66]. F. Ahmed et.al. studied structural and magnetic study of Co-doped ZnO ($Zn_{1-x}Co_xO$, x= 1, 3, 5, 7, 10%) nanoparticles synthesized by auto combustion method and revealed that all the synthesized Co-doped ZnO samples shows the presence of wurtzite structure without any secondary phase through XRD analysis. The TEM results revealed that the prepared Co-doped ZnO nanoparticles are nearly spherical in shape with particle size <50 nm. PL spectra of all the samples showed blue and green bands at 448 and 532 nm, respectively. Magnetic measurements studies conclude that the all Co doped samples showed room temperature ferromagnetism [67]. M. Ram et.al. synthesized $Zn_{1-x}Co_xO$ (x = 0,1,3 and 5%) using combustion method and studied the structural, microstructural and raman

spectroscopy. X-ray analysis confirms the formation of single phase nanoparticles and crystallite size were found to decrease with increase in Co concentration. Some organic impurities are observed in Co doped ZnO nanoparticle FTIR spectra which indicate that they are probably near surface impurities. Raman studies reveal wurtzite type hexagonal structure as all the prominent modes are present including its finger print mode at 439 cm^{-1} [68]. T.M. Hammad et.al. studied the effect of Co-doped ZnO nanoparticles on its structural, optical properties synthesized using combustion method and revealed that there is variation in XRD peaks which increase by Co concentration. It is shown that the average particle size decreases with increase in Co Content. The band-gap enhances from 3.32 eV to 4.12 eV due to the blue shifts of wavelength [69]. Nadia et.al. investigated structural, optical and magnetic properties of ZnO particles doped with Co using co-precipitation method and showed the formation of hexagonal structure from X-ray diffraction patterns without any secondary phase. The optical band gap decreases with increasing Co doping concentrations, indicating a clear red shift. All samples were found to exhibit room-temperature ferromagnetism [70]. M. A. Shafique et.al. investigated cobalt doping effect ZnO nanoparticles on its structural, optical, and magnetic properties using Co-precipitation method and revealed that for lower doping concentration no secondary peaks were observed but additional phases were present for higher doping confirmed through XRD data. Moreover VSM studies showed presence of room temperature ferromagnetism also revealed doping proportional properties [71]. A. Parra-palomino et.al. synthesised and characterised undoped and Fe doped ZnO nanoparticles (x = 0,1,3,5,8,10 %) using sol-gel technique and average crystallite size was found in the range of 11-13 nm. FT-IR analysis of the sample suggests the absorption of acetate species. Room Temperature squid analysis suggested that for x = 0.08 exhibits paramagnetic behaviour at high magnetic field [72]. S. Khatoon et.al. studied the optical and magnetic properties of Ni-doped ZnO nanoparticles and reviled that average particle size is of 23 nm, 14 nm and 12 nm respectively for 3.9, 8.3 and 12.4 weight %, Optical reflectance measurements showed an energy band gap of 3.27 eV, 3.2 eV and 3.15 eV, respectively, which decreases with increasing Ni content. All these samples show paramagnetic behavior with weak antiferromagnetic interactions [73]. J. K. Salem investigated structural and optical properties of Ni (0 %, 1 %, 3 % and 5 %) of Ni -doped ZnO

micro-spheres and showed that the crystallites in a wurtzite structure having size around 4–11 nm was estimated using XRD analysis. HRTEM micrograph shows the existence of spherical nanoparticles with 4 nm average diameters. The band gap decreases from 3.55–3.36 eV with Ni doping due to red shift which could be associated to the induction of Ni ions in the ZnO lattice [74]. J. Jadhav et.al. studied the structural and morphological properties of ZnO and Ni-doped ZnO ($Zn_{1-x}Ni_xO$ x = 0.01 to 0.05) and calcined at 400°C in ambient air reviled that crystallite size were found out to be 12 nm, 8 nm and 10 nm respectively using debye scherrer's formula. HRTEM images clearly show high crystalline order of nanoparticles having particle size in the range of 15- 18 nm. FTIR spectra of undoped and Ni-doped ZnO samples calcined at 400°C in ambient air shows Zn-O stretching 430-650 cm^{-1} and 650 ,651 to 660 cm^{-1} for Ni-doped ZnO. From VSM analysis it was observed that the resultant coercivity value decreases with the increase in the annealing temperature [75]. M. Bordbar et.al. studied the Optical and photocatalytic properties undoped and Mn-doped ZnO nanoparticles synthesized by hydrothermal method with the effect of annealing temperature and reviled that the average particle size range was in the range of 15-30 nm from SEM and XRD analysis. FTIR revealed that peaks at 450- 500cm^{-1} corresponds to Zn-O stretching vibration. The band of Mn-doped ZnO nanoparticles gap was found to increases and decrease upon increasing annealing temperature. Photocatalytic activity of Mn-doped ZnO has been attributed to the increase of surface-to-volume ratio, mean grain size, oxygen defects density and increase band gap relative to undoped ZnO [76]. B. H. Soni et.al. Studied the antimicrobial activity of undoped and Mn doped ZnO nanoparticles (with Mn content: 5 mol%, 10 mol% and 15 mol %) synthesized by microwave irradiation for 20 sec at 720 watt and reviled that EDAX spectrum analysis showed the purity of the samples with no contaminants in the prepared samples and TEM image concluded that the particle size decreases with the increase in Mn concentration. Selected area electron diffraction pattern (SAED) showed the ring pattern which confirms the polycrystalline nature of the nanoparticles and reflecting planes corresponds to the wurtzite structure of the nanoparticles. The enhanced Bioactivity of undoped and Mn doped (with Mn content: 5 mol%, 10 mol% and 15 mol%) ZnO nanoparticles dispersed in methanol medium are attributed to the higher surface area to volume ratio due to higher dispersion compared to water medium [77]. X. Wu et.al.

prepared Fe Doped ZnO nanoparticles using hydrothermal synthesis and studied the optical and magnetic properties. These studies reviled that Fe has successfully substituted in Zn lattice site confirmed via XRD analysis and also produce single-phase Fe Doped ZnO nanoparticles. The Raman spectra of the Fe Doped ZnO nanoparticles shows red shift, the UV emission and photoluminescence spectra is annihilated with the increase of Fe^{3+} concentration. All doped samples at room temperature showed ferromagnetic natures [78]. T. A. Abdel-Baset et.al. studied the structural and magnetic properties of $Zn_{1-x}Fe_xO$ (x = 0, 0.02, 0.04, 0.06, 0.08, and 0.1) using co-precipitation technique and reviled that by increasing concentration of the iron ion the particle size decreases within the range 31.4 nm - 29.2 nm . Magnetic measurements showed that declining in particle size enhances the ferromagnetism volume fraction [79].

M.S. Alshammari et.al. studied the Ferromagnetic ordering in Fe-doped In_2O_3 powder using solid state reaction method and reviled that Fe ion has successfully integrated in to In3 positions of In_2O_3 lattice with single phase cubic structure analyzed using XRD peaks. The magnetic measurement shows that sample has ferromagnetic ordering at room temperature. It was established that the saturation magnetization increases with Fe content, while the coercivity is independent of Fe. XPS results illustrate the existence of oxygen vacancies. Intrinsic defects provoked by the replacement of Fe ions into In position and are the most probable reason for having ferromagnetism in the material [80]. R.R. Ma et.al. investigated the consequences of oxygen vacancy and local spin on the ferromagnetic properties of Ni-doped In_2O_3 nanoparticles and reviled that ferromagnetism was obtained at room temperature in Ni-doped In_2O_3 nanoparticles using a solid-state reaction method with vacuum annealing process. XRD, and FC/ZFC measurements showed that there was no secondary phase present within the measured sensitivity in vacuum-annealed samples. The outcome indicates that oxygen vacancy and local spin are two crucial factors affecting the initiation of long-range ferromagnetic coupling in Ni-doped In_2O_3 samples [81]. B. Shanmuga Priya et.al. studied the hydrothermal synthesis of Ga-doped In_2O_3 nanoparticles and its structural, optical and photocatalytic properties synthesized using simple hydrothermal method and reviled the formation of single cubic crystal structure along (222) reflection plane using XRD analysis, the crystallite size decreases with increasing Ga concentration. The morphology transforms from irregular into

defined porous spindle-like nanostructure having particle size distribution of 9 to 18 nm, SAED patterns prove the good crystalline nature of the material. XPS results established that the doped gallium ions are in 3+ states. Band gap increases from 3.40 eV to 3.45 eV with increases in Ga doping, photoluminescence spectra showed violet, blue and green emissions. It is found that Ga-doped In_2O_3 nanoparticles exhibited good photo-catalytic activity by absorbed photo-excited electrons [82]. J. Chandradass et.al. studied structural, microstructural, magnetic properties of indium oxide nanoparticles and showed that prepared nanoparticles size is in the range of 12 nm calculated from XRD data. Material has Single-phase cubic structure shown by FTIR and Raman studies. Samples showed diamagnetic magnetic behaviour of indium oxide nanoparticles, from UV spectra the optical band gap energy was found to be 4.03 eV [83]. N. Sai Krishna et.al. studied the structural, optical, and magnetic properties of Iron doped Indium oxide nanoparticles with x = 0.00, 0.03, 0.05, and 0.07 were prepared using solid state reaction and annealing process and reviled that the saturation magnetization enhanced from 11.56 memu/g to 148.64 memu/g with the increase in Fe content from 0.03 to 0.07, suggesting room temperature ferromagnetism in $(In_{1-x}Fe_x)_2O_3$ powders and room temperature ferromagnetism was explained using F-centre model [84]. P. Vomáčka et.al. studied the catalytic degradation of Rhodamine B of tin doped copper oxide nanoparticles and reviled that samples were successfully synthesized at a low temperature via simple one-pot method. Sample showed gradual narrowing of CuO nanoparticles in the (010) direction analysed using XRD data, red shift of a band gap from 1.33 eV to 1.18 eV was observed by increasing Sn ions. Sn doping showed appearance of a new reactive surface species that were responsible for higher degradation efficiency [85]. M. Ponnar et.al. studied the influence of Ce doping on CuO nanoparticles prepared by using microwave irradiation method and the XRD analysis reviled that the sample posses monoclinic structure and the crystallite size increases with Ce concentration. Band gap decrease in with an increase in Ce content in the sample. The photoluminescence spectrum shows that Ce doped samples produces red colour radiation which may be helpful in optoelectronic devices. FT-IR and EDS analysis also trace of Cu, Ce, and O which are definitely present in the samples without any other impurity. Transformation of morphology is seen from TEM micrographs from spherical to rod-like structure with some defects. VSM analysis

shows that for higher Ce concentration doped in CuO samples the magnetization and coercivity decreases [86]. R.O. Yathisha Studied the effect of Zn^{2+} doping on optical and electrical properties of CuO nanoparticles prepared via microwave combustion method and reviled that Zn^{2+} ions have been substituted in CuO lattice with secondary phase above 8 mol% of Zn^{2+} doping content confirmed by XRD analysis. The FE-SEM, EDAX images shows the structural change that is due to the effect of Zn doping and confirmed the presence of Zn^{2+} ions in CuO lattice. Band gap decrease due to incorporation of Zn^{2+} ions in the CuO matrix. I-V characteristics investigation shows the dependency on the conductance and percentage of Zn^{2+} ions concentration in the CuO lattice. Therefore, the energy-gap and conductance of Zn-CuO nanoparticles has very potential use in the field of solar cells and optical devices [87]. N. Sharma et.al. studied weak ferroelectricity and ferromagnetism in Mn doped CuO nanostructures (x= 0 , 0.03 ,0.05 ,0.07) synthesized by the hydrothermal method and reviled the single monophasic phase formation for all samples confirmed from XRD pattern. FESEM images analysis show that the particle size dwindles from 116 to 40nm by enhancing the Mn concentration from x=0 to x=0.07 in CuO lattice. Polarization versus Electric field loops curves exhibit the conquer behaviour of capacitance for all samples. Additionally the value of dielectric constant reduces by increasing Mn concentration. M–H curves indicates the ferromagnetic behaviour upto x=0.03 sample and afterward sample showed paramagnetic behaviour that is for x=0.05 and x=0.07 sample [88]. N. Mohamed Basith studied the effect of Ni doped CuO nanoparticles on its structural, morphological, optical, and magnetic properties prepared via rapid microwave combustion method and reviled that formation of pure CuO monoclinic phase with Ni content up to 2.0wt%. The crystallite size varies from 20–26nm confirmed from X-ray diffraction patterns. SEM analysis shows the formation of self- aggregated nanoparticles. The optical band gap was found to increases from 3.9eV to 4.3eV with increasing Ni content which is due to the d-d transitions. PL spectrum displayed strong green emission band indicating increased density defects for Ni-doped CuO nanostructures. Samples exhibit a ferromagnetic behaviour at room temperature which is dependent on Ni doping concentration and the room temperature ferromagnetism which is caused by the intrinsic defects [89]. B. Anand et.al. prepared Ni doped CuO nanoparticles using Chemical precipitation synthesis and investigated optical and structural properties.

The XRD studies showed the formation of single monophasic phase Ni doped CuO nanoparticles. Increase in band gap was observed in Ni doped CuO nanoparticles because of quantum size effect. The vibration bonds for Ni doped CuO were observed using FT-IR spectra in the range from 400 cm^{-1} to 4000 cm^{-1}. SEM images showed non-uniform distribution of particles having some single particles with some clustered particles. The particle size was directly measured by TEM images which show nearly asymmetrical round shape particles [90].

Thus the published reports do not provide appropriate information about the correlation involved in the band gap variation, thermopower, resistivity, dielectric mechanism, magnetic variation etc. with the doping concentration of the magnetic ions. Hence an appropriate study on these materials was felt necessary to highlight the bridge gaps that were existed in these studies. With this motivation oxide based DMS nanomaterials were prepared and investigated for structural, optical, magnetic and electrical properties.

1.8 Aim And Objective of The Research Work

The conclusion drawn from the literature review of large number of research publication was that majority of the researcher have done research on either a single or few samples with low dopant concentrations in order to investigate the material properties. The work illustrates crumbling of findings that cannot be applied for large set of samples. As a result, large series of three different types of doped oxide samples with varying dopant concentrations was prepared, to understanding and explore the knowledge and interactions underlying the novel properties exhibited by these materials. In the current investigations nanoparticle DMS materials such as Co doped ZnO, Nd doped In_2O_3, Ni doped CuO were prepared by a simple method of materials preparation to investigate their structural, optical, electrical and magnetic properties.

Nanoparticles of $Zn_{(1-x)}Co_xO$ (x = 0.05, 0.10, 0.15, 0.20), $In_{(2-x)}Nd_xO_3$ (x =, 0.10, 0.15, 0.20), $Cu_{(1-x)}Ni_xO$ (x = 0, 0.05, 0.10, 0.15, 0.20, 0.25, 0.30) were prepared using auto-combustion method of sample preparation. The final exertion, explanation to investigative results and conclusions are presented in this thesis which includes eight chapters.

1.9 Organization of The Thesis

The content of the **eight** chapters included in the thesis is as follows:

❖ **Chapter 1: Introduction**

The introduction chapter is focused on preliminary topics like nanomatreial and nanotechnology, magnetic nanoparticles, dilute magnetic semiconductor, spintronics and origin of magnetism in dilute magnetic semiconductor. It includes a brief discussion on the properties of ZnO, In_2O_3 and CuO nanomaterial. This chapter also includes in-depth literature review on research work reported by researchers on DMS materials in nano form. Aim and objective of the work is also included in this chapter.

❖ **Chapter 2: Preparation of nanomaterials**

This chapter consists of detailed information on various method of sample preparation which has been employed by various researcher to prepare dilute magnetic semiconductor nanoparticles material. Moreover a comprehensive procedure engaged in auto-combustion synthesis route to prepare Co doped ZnO, Nd doped In_2O_3 and Ni doped CuO nanoparticles having chemical formula $Zn_{(1-x)}Co_xO$ (x = 0.05, 0.10, 0.15, 0.20), $In_{(2-x)}Nd_xO_3$ (x = 0, 0.10, 0.15, 0.20) and $Cu_{(1-x)}Ni_xO$ (x = 0, 0.05, 0.10, 0.15, 0.20, 0.25, 0.30) is also illustrated in this chapter.

❖ **Chapter 3: Characterization and Property measurement techniques**

This chapter provides a brief description of several investigative methods and instruments used for characterization and to study optical, magnetic and electrical properties of the materials. This chapter also includes basic principle and the standard procedure engaged in utilizing these sophisticated techniques.

❖ **Chapter 4: Characterization**

This chapter unfolds all the data that has been recorded using characterization techniques such as XRD, SEM, TEM, EDAX and FTIR, discussed carefully for all the prepared samples. It showcases the influence on structural parameter of Co^{2+} ions in ZnO matrix, Nd^{3+} ions in In_2O_3 matrix and Ni^{2+} ions in CuO matrix respectively. The results obtain from Rietveld refinement of XRD data of all the prepared samples, structural parameter estimated from XRD data such as

crystallite size, lattice parameter, cell volume etc. is given in this chapter. The crystallite size of all the prepared samples was calculated using Williamson-Hall method.

Monophasic wurtzite structure of $Zn_{(1-x)}Co_xO$ (x=0.05, 0.10, 0.15, 0.20) nanoparticles was confirmed from XRD data [JCPDS-79-2205]. The crystallite size't' shrinks from 25 nm to 17 nm and lattice parameter ('a' and 'c') was found to increase with the increase in Co^{2+} content. Development of single phase pure cubic bixbyite structure of $In_{(2-x)}Nd_xO_3$ nanoparticles with (x = 0, 0.10, 0.15 and 0.20) was confirmed from X-ray diffraction data [JCPDS card no. 71-2195]. Lattice constant '*a'* and Cell volume 'V' was found to increase with increasing Nd^{3+}content in the sample. The crystallite size '*t*' initiate to reduce from 52nm to 44nm with increase in Nd^{3+}content. Construction of monophasic monoclinic crystalline structure of $Cu_{(1-x)}Ni_xO$ (x = 0, 0.05, 0.10, 0.15, 0.20, 0.25, 0.30) was confirmed from X-ray diffraction data [JCPDS card no. 65–2309]. Lattice constant '*a*', '*b*', '*c*' and Cell volume 'V' was found to decrease with increasing Ni^{2+}content in the sample. The crystallite size '*t*' decrease from 78 nm to 48 nm with increase in Ni^{2+} concentration. This XRD analysis of all the prepared samples suggests that Co^{2+}, Nd^{3+} and Ni^{2+} ions have successfully substituted at Zn^{2+} , In^{3+} and Cu^{2+} site in ZnO, In_2O_3 and CuO matrix.

The surface morphology of samples was analyzed using SEM and the experimental particle size estimation of the prepared samples was done using SEM and TEM. Particle size found using TEM micrograph was found to agree with the crystallite size calculated using XRD data. The purity and the chemical composition analysis of the prepared samples were studied using EDAX. Moreover this chapter also gives supporting structural analysis data of FTIR spectroscopy that was utilized for the detection of functional groups present in the samples. The detailed analysis of the entire data recorded on the prepared nanoparticle samples is presented in this chapter.

❖ **Chapter 5: Optical properties**

This chapter includes recorded data on optical properties such as UV-Visible spectroscopy made on Co doped ZnO, Nd doped In_2O_3 and Ni doped CuO nanoparticles as well as Photoluminescence spectroscopy measurement made on Co doped ZnO, nanoparticles. UV-Visible spectrum was employed to determine

the energy band gap of all the prepared samples. The precise measurements of energy band gap were estimated from tauc's plot by using linear fit regression method. The band gap of Co doped ZnO, Nd doped In_2O_3 and Ni doped CuO nanoparticles were found to decrease with increase in doping concentration. The Photoluminescence (PL) emission spectra of the sample $Zn_{(1-x)}Co_xO$ (x = 0.05, 0.10, 0.15,0.20) obtained at room temperature with an excitation wavelength of 318 nm established the existence of defects Zn vacancies (V_{Zn}), O vacancies (V_O), interstitial Zn (Z_{ni}), interstitial O (Oi), and intermediate levels formed between valence band and conduction band due to Co^{2+} substitution at Zn^{2+} positions. Photoluminescence decay was analyzed to study the PL lifetime of the defects.

❖ **Chapter 6: Magnetic properties**

This chapter is focused on the magnetic data recorded on the samples. The magnetic properties such as magnetic hysteresis (M-H curves) and Field cooled and Zero field cooled (FC and ZFC) of Co doped ZnO, Nd doped In_2O_3 and Ni doped CuO nanoparticles were studied using vibrating sample magnetometer. M-H curves shows that the samples behaves as diamagnetic material at lower concentration of doping level and becomes ferromagnetic at room temperature as the doping concentration is increased. Further to confirm introduction of ferromagnetism in the materials field cooled and zero field cooled (FC and ZFC) measurement were done at 500 Oe.

❖ **Chapter 7: Electrical properties**

This chapter explores the data measurements and analysis made on electrical properties such as thermoelectric power, DC resistivity, dielectric properties with respect to frequency and temperatures and impedance analysis on Co doped ZnO, Nd doped In_2O_3 and Ni doped CuO nanoparticles. Prepared nanoparticles were grinded initially and used in a pallets form for all the electric measurements, additionally the measurement were done in the range from room temperature to 500 ^oC. Thermoelectric property of Co doped ZnO nanoparticles showed p-type semiconductor behavior for all the Co^{2+} concentrations with a first order transition from p-type to n-type behavior at 90^oC. Seebeck coefficient of Nd doped In_2O_3 showed n-type semiconductor behavior for entire temperature range, Seebeck

coefficient of Ni doped CuO showed both p-type and n-type semiconductor behaviour for different temperature.

DC resistivity of Co doped ZnO, Nd doped In_2O_3 and Ni doped CuO nanoparticles shows typical semiconductor type of behaviour with decreasing nature with increasing dopant concentrations. The activation energy for all the samples was calculated using Arrhenius equation from the resistivity plots.

The dielectric constant was found to decreases with increase in frequency in the initial stages and remained almost constant at higher frequency Co doped ZnO, Nd doped In_2O_3 and Ni doped CuO nanoparticles. Dielectric loss frequency shows a relaxation peaks in case of all the samples due to resonance phenomenon. Impedance analysis of Co doped ZnO, Nd doped In_2O_3 and Ni doped CuO nanoparticles showed a semicircular arc signifying the dominating nature of grain boundaries resistance in the material. Detailed explanations and discussions on these measurements are given in this chapter.

❖ **Chapter 8: Conclusion**

This chapter includes the summary of the entire work taken up for investigation. The results obtained and the overall conclusions on the influence of Co^{2+} ions in ZnO matrix, Nd^{3+} ions in In_2O_3 matrix and Ni^{2+} ions in CuO matrix on structural, optical, magnetic and electrical properties of the prepared nanoparticles are summarized here. Future scope in this research field has been also mentioned.

References:

[1] S. S Sanjay, A. C. Pandey, A Brief Manifestation of Nanotechnology, (2016) 47-63.

[2] Alagarasi, Inroduction to nanomaterials, (2011)1-76.

[3] T. Ribriro, C. Balezeizao, J. P. Farinha, Materials Journal 7(2014)3881-3900.

[4] J. Wu, J. Cao, W.Q. Han, A. Janotti and H.C. Kim, Springer publications, 149 (2012).

[5] M. F. Garcia, A. M. Arias, J. C. Hanson, J. A. Rodriguez, Chem. Rev. 104 (2004) 4063.

[6] X. Jiang, Y. Wang, and T. Herricks, J. Mater. Chem. 14 (2004) 695.

[7] I. Žutić, J. Fabian, and S. Das Sarma, Rev. Mod. Phys. 76 (2004) 323.

[8] S. S., Sarma D. D., Sanvito S, Nano Lett. 2 (2002) 605.

[9] R. Koferstein, T.Walther, D. Hesse, S. G. Ebbinghaus, J. Mater. Sci. 48 (2013) 6509.

[10] Xu Y. B. and Thompson S. M., Spintronic Materials and Technology, CRC, (2007).

[11] S.J. Pearton, C.R. Abernathy, D.P. Norton, A.F. Hebard, Y.D. Park, L.A. Boatner, J.D. Budai, Materials Science and Engineering, 40 (2003) 137–168.

[12] J. Fabian, A.M Abiague, C. Ertler, P. Stano, I. Z˘ utic´, acta physica slovaca, 57 (2007) 565 – 907.

[13] K. E. Drexler, Engines of Creation: The Coming Era of Nanotechnology; Doubleday (1986).

[14] P. Varshney, H. Agrawal, national conference on advances in technology and applied sciences, (2014).

[15] M. Makkar, R. Viswanatha, International Journal of Scientific and Research Publications, 2, (2012).

[16] M. Arucu, Turkish Journal of Physics, 41 (2017) 20 – 24.

[17] Z. Wilamowski and A. M. Werpachowska, Materials Science-Poland, 24 (2006).

[18] Y. B. Xu and S.M. Thompson, Taylor and Francis, (2006)

[19] R. P. Davies , C. R. Abernathy , S. J. Pearton , D. P. Norton , M. P. Ivill and F. Ren, Chem. Eng. Comm., 196 (2009) 1030–1053.

[20] R. Elilarassi, G. Chandrasekaran, Synthesis, American Journal of Materials Science, 2 (2012) 46-50.

[21] K. Y. Salkar, R.B. Tangsali, R.S. Gad, M. Jeyakanthan, U. Subramanian, Superlattices and Microstructures, 126 (2019) 158–173.

[22] H. Morkoç, Ü. Özgür, WILEY-VCH Verlag GmbH & Co. KGaA, Weinheim (2009).

[23] R. Asmatulu, H. Haynes, M. Shinde, Y. H. Lin, Y. Y. Chen, J. C. Ho, Hindawi Publishing Corporation Journal of Nanomaterials (2010) 3.

[24] H. Mushahid, K. Z. Husain, Advances in Nanomaterials, 79 (2016) XVIII, 429.

[25] S. Mehmood, M. A. Rehman, H. Ismail, B. Mirza, A. S Bhatti, International Journal of Nanomedicine, 10 (2015) 4521–4533.

[26] F. Ochanda, K. Cho, D. Andala, T.C. Keane, A. Atkinson, W.E. Jones, Langmuir 25, 7547–7552 (2009).
[27] J. Chaboy, R. Boada, c.Piquer, M.A. Laguna-Macro, M. Garcia-Hernandez, N. Carmona, J. Llopis, M. L. Ruiz-Gonzalez, J. Gonzalez-Calbet, J. F. Fernandez, M.Z. garcia, Physical review B, 82 (2010) 064411.
[28] A. A. Jacob, L. Balakrishnan, S. R. Meher, K. Shambavi, Z. C. Alex J. Alloys Compd., , 695 (2017) 3753.
[29] H.B. Carvalho, M.P.F. Godoy, R.W.D. Paes, M. Mir, A.O. Zevallos, F. Iikawa, M.J.S.P. Brasil, V.A. Chitta, W.B. Ferraz, M.A. Boselli, A.C.S. Sabioni, J. Appl. Phys. 108 (2010) 033914.
[30] Y. Wang, G. Duan, Y. Zhu, H. Zhang, Z. Xu, Z. Dai, W. Cai, Sensor and Actuators B- Chemical, 228 (2016) 74.
[31] A. Regoutz, R.G. Egdell, D.J. Morgan, R.G. Palgrave, H. Téllez, S.J. Skinner, D.J. Payne, G.W. Watson, D.O. Scanlon, Applied Surface Science 349 (2015) 970–982.
[32] H. Yang, J. Tian, Y. Bo, Y. Zhou, X. Wang, H. Cui, Journal of Colloid Interface Science, 487 (2017) 258.
[33] S. Zh. Karazhanov, P. Ravindran, P. Vajeeston, A. Ulyashin, T. G. Finstad, and H. Fjellvåg, Physical Review B, 76 (2007) 075129.
[34] D. Bruce Buchholz, Qing Ma, Diego Alducin, Arturo Ponce, Miguel Jose-Yacaman, Rabi Khanal, Julia E. Medvedeva and Robert P. H. Chang, Chemistry of materials, 26, (2014) 5401−5411.
[35] J. Du, Mino Yang, Seung Nam Cha, Danielle Rhen, Miwon Kang, Dae Joon Kang, Crystal Growth & Design, 8 (2008) 2313.
[36] A. Vomiero, Sebastiano Bianchi, Elisabetta Comini , Guido Faglia , Matteo Ferroni, Giorgio Sberveglieri, Journal of Crystal Growth, 7 (2007) 2500 - 2504.
[37] C.Y. Kuo, Shih-Yuan Lu, Te-Yu Wei, Journal of Crystal Growth, 285 (2005) 400 - 407.
[38] H. Zhou, W. Cai, L. Zhang, Material Research Bulletin, 34 (1999) 845–849.
[39] K. Anand, Jasmeet Kaur, Ravi Chand Singh, Rengasamy Thangaraj, Materials Science in Semiconductor Processing 39 (2015) 476 - 483.
[40] N. Bouazizi, R. Bargougui, A. Oueslati, R. Benslama, Adv. Mater. Lett. 6 (2015) 158–164.

[41] A. S. Zoolfakar, Rozina Abdul Rani, Anthony J. Morfa, Anthony P. O'Mullane and Kourosh Kalantar-zadeh, Journal of Materials Chemistry C (2014)
[42] A. Albert manoharan , R. Chandramohan , R. David prabu , S. Valanarasu , V. Ganesh, Mohd Shkir, A. Kathalingam, S. Al Faify, Journal of Molecular Structure 1171 (2018) 388-395.
[43] J. Singh, Gurjas Kaur and Mohit Rawat, Journal of Bioelectronics and Nanotechnology, 1 (2016) 9.
[44] M. Xu, F.Wang, M.Zhao, S.Yang, Z.Sun, X.Song, Physica E 44 (2011) 506–510.
[45] A. H. Morrish, The Institute of Electrical and Electronics Engineers, New York, (2001).
[46] R.T., Pardasani, P. Magnetic Properties of Paramagnetic Compounds, 31G (2017) XXXV, 913.
[47] Goldman, Alex Handbook of Modern Ferromagnetic Materials, 505 (1999), XIX, 649.
[48] L. Duò , Marco Finazzi , Franco Ciccacci, Verlag GmbH & Co. KGaA, (2010).
[49] D. Jilies, "Introduction to Magnetism and Magnetic Materials", Champman and Hall, London (1991)
[50] R. Cardias, A. Szilva, A. Bergman, I. Di Marco,M. I. Katsnelson, A. I. Lichtenstein, L. Nordström, A. B. Klautau, O. Eriksson & Y. O. Kvashnin, Scientific Reports 7 (2017) 4058.
[51] V.K. Thai, Hoang Anh Tuan, Proceeding National Conference Theoretical Physica, 36 (2011) 101-107.
[52] S. R. Power and Mauro S. Ferreira, Crystals, 3 (2013) 49-78.
[53] A. M. Werpachowska and Z. Wilamowski, Materials Science-Poland, 24 (2006).
[54] R. Skomski, J. Zhou, J. Zhang, and D. J. Sellmyer, Journal Of Applied Physics, 99 (2006).
[55] H. S. Kaushik, Anuradha Sharma, Mamta Sharma, International Journal of IT, Engineering and Applied Sciences Research (IJIEASR), 3 (2014).
[56] B. Belhadji, L Bergqvist, R Zeller, P H Dederichs, K Sato and H Katayama-Yoshida, Journal of Physics: Condensed Matter, 19 (2007) 12.
[57] B. E. Larson, K. C. Hass, H. Ehrenreich and A. E. Carlsson, 56 (1985) 347.

[58] P. M. Krstajić, F. M. Peeters, V. A. Ivanov, V. Fleurov, and K. Kikoin, Physical Review B, 70 (2004).
[59] A. C. Durst, R. N. Bhatt, P. A. Wolff, Physical Review B, 65 (2002).
[60] T.Dietl, (2001) 2176-2180.
[61] P. Senthilkumar, S. Dhanuskodi, J. Karthikeyan and P. Murugan, Physical Chemistry Chemical Physics, 21 (2019) 4032-4045.
[62] Y. Jiang, Wensheng Yan, Zhihu Sun, Qinghua Liu, Zhiyun Pan, Tao, Yao, Yuanyuan Li, Zemin Qi, Guobin Zhang, Pengshou Xu, Ziyu Wu and Shiqiang Wei, Journal of Physics: Conference Series 190 (2009).
[63] A. Vanaja, Karumuri Srinivisa Rao, Advances in Nanoparticles, 5 (2016) 83-89.
[64] N. Mohamed Basith, J. Judith Vijaya, L. John Kennedy, M. Bououdina, S. Jenefar, V. Kaviyarasan, Materials Science in Semiconductor Processing, 17 (2014) 110–118.
[65] R. Elilarassi and G. Chandrasekaran, Journal of Material Science Materials In Electronics, 24 (2013) 96–105.
[66] V. Rajendar, Kalagadda Venkateswara Rao, K. Shobhan, C.H. Shilpa Chakra, Journal of Nano- And Electronic Physics, 5 (2012) 01022.
[67] F. Ahmed, Shalendra Kumar, Nishat Arshi, M. S. Anwar, Bon Heun Koo Chan Gyu Lee, International Journal of Nanoscience, 10 (2011) 1025-1028.
[68] M. Ram , G. S. Arya , Kusum Parmar , R. K. Kotnala and N. S. Negi, International Journal of Advances in Engineering & Technology, 8 (2015) 329-336.
[69] T. M. Hammad, Jamil K. Salem, R. G. Harrison, Applied Nanoscience, 3 (2013) 133–139.
[70] N. F. Djaja, Dionisius Agung Montja, Rosari Saleh, Advances in Materials Physics and Chemistry, 3 (2013) 33-41.
[71] M. A Shafique, Saqlain A Shah, Muhammad Nafees, Khalid Rasheed Riaz Ahmad, International Nano Letters, (2012) 2-31.
[72] P. Palomino A., Perales-Perez O., Singhal R., , Tech Connect Briefs, 4 (2007) 297 – 300.
[73] S. Khatoon and T Ahmad, Journal of Materials Science and Engineering B, 2 (2012) 325-333.

[74] J. K Salem, Talaat M Hammad, Roger R Harrison Synthesis, Journal of Materials Science: Materials in Electronics 2013, 24, 1670-1676

[75] J. Jadhav, Mahesh Patange, Somnath Biswas, Carbon–Sci. Tech, 5 (2013) 269-274.

[76] M. Bordbar, Seyed Mohammad Vasegh, Somaye Jafari, Ali Yeganeh Faal, Iranian Journal of Catalysis, 5 (2015) 135-141.

[77] B. H. Sonia, M. P. Deshpandea, Sandip V. Bhatta , Sunil H. Chakia and Haresh Kaheria, Archives of Applied Science Research, 3 (2011) 173-179 .

[78] X. Wu, Zhiqiang Wei, Lingling Zhang, Xuan Wang, Hua Yang, and Jinlong Jiang, Journal of Nanomaterials, (2014) 6.

[79] T.A. Abdel-Baset, Yue-Wen Fang, B. Anis, Chun-Gang Duan, Mahmoud Abdel-Hafiez, Nanoscale Research Letters, (2016) 11-115.

[80] M. S. Alshammari , R. Alhathlool , A. Z. Al-Anzi , K. Y. Museery , M. A. Alkhunayfir , O.M. Lemine , M. Bououdina, Physica E: Low-dimensional Systems and Nanostructures, 108 (2019) 253-256.

[81] R. Rong Ma, Feng-Xian Jiang, Xiu-Fang Qin, Xiao-Hong Xu, Materials Chemistry and Physics, 132 (2012) 796–799.

[82] B. Shanmuga Priya, M. Shanthi, C. Manoharan, M. Bououdina, Materials Science in Semiconductor Processing, 71 (2017) 357–365.

[83] J. Chandradass, Dong Sik Bae, Ki Hyeon Kim, Advanced Powder Technology, 22 (2011) 370–374.

[84] N. Sai Krishna, S. Kaleemulla, G. Amarendra, N. Madhusudhana Rao, C. Krishnamoorthi, M. Kuppan, M. Rigana Begam, D. Sreekantha Reddy, I. Omkaram, Materials Research Bulletin, 61 (2015) 486–491.

[85] P. Vomácˇka, Václav Štengl, Jirˇí Henych, Martin Kormunda, Journal of Colloid and Interface Science, 481 (2016) 28–38.

[86] M. Ponnar, C. Thangamani, P. Monisha, S.S. Gomathi, K. Pushpanathana, Applied Surface Science (2018).

[87] R.O.Yathisha , Y. Arthoba Nayaka, P. Manjunatha , H.T. Purushothama , M.M.Vinay , K.V. Basavarajappa, Study on the effect of Zn^{2+} doping on optical and electrical properties of CuO nanoparticles, Physica E: Low-dimensional Systems and Nanostructures, (2018).

[88] N. Sharma, Gaur. A, and Kotnala R. K, Journal of Magnetism and Magnetic Materials, 377 (2015)183–189.

[89] N. Mohamed Basith, J. Judith Vijaya, L. John Kennedy, M. Bououdina, Materials Science in Semiconductor Processing, 17 (2014) 110–118.
[90] B. Anand, A. Muthuvel, V. Mohana, International Journal for Research in Applied Science & Engineering Technology (IJRASET), 5 (2017) 638-642.

CHAPTER 2
Method of Sample Preparation

2.1 Introduction

Sample preparation is one of the most important part of any materials research. One can carry out several investigations on structural properties of the material to establish the formation of the desired monophasic material. These measurements also facilitate to know or evaluate crystallite size, morphology, microstructure and chemical composition of the material formed. Since the emphasis is on preparation of nanoparticle material and all methods of materials preparation do not yield nanoparticles one has to carefully select or narrow done on a specific method of sample preparation to get required material. In general methodology of preparation of nanaoparticles is broadly classified into two main categories i.e. top-down method and bottom-up method. In top-down method the material is prepared in bulk using any standard method or readily available bulk material is taken and is downsized to nanometer scale by milling to produce nanoparticles [1-3]. In bottom-up method the nanoparticles are built up to produc the same from atomic level [4-6]. Both the methods of nanoparticle preparation play a very important role in this new era of nanotechnology. These different approaches/ methods have their own advantages and disadvantages. However the later method is more appropriate as it gives rise to quality nanoparticle material which evolves by itself from atomic level by assembly of atoms to give rise to the required structured material.

2.1.1 Top-to-Down Approach

Top-down method is usually based with the bulk material, additionally making the bulk material smaller and smaller. As a result breaking up big particles by utilizing physical methods such as crushing, milling or grinding [2,3]. Normally from top-down route it is very difficult to synthesize uniform shape and size nanoparticles. The major obstruction with this approach is the imperfections at the particle surface structure which produces noteworthy high impact on nanoparticles physical and surface related and other properties. Top-down method of materials preparation can harm the crystallographic pattern of nanostructures as

well as useful properties of the material. Top-down method is most likely to introduce internal stress with surface defects [5,6].

2.1.2 Bottom-Up Approach

Bottom-up method brings-up the formation of a material from the bottom, atom-by-atom, molecule-by-molecule, or cluster-by-cluster. The bottom-up method plays a significant role in the construction and processing of nanostructures and nanomaterials. Bottom-up method assures superior chance to acquire nanostructures with minimal defects, enhanced homogeneous chemical composition with good short and long range ordering. This is because of bottom-up method which is focused mainly on the reduction of Gibbs free energy, so the nanostructures and nanomaterials are produced in a state closer to thermodynamic equilibrium state.

2.2 Preparation of Nanoparticle DMS Materials.

The method of preparation of DMS nanoparticle materials itself has been a motivated area of investigation for a long because of their potential use in advanced spintronic applications [7]. Numerous reports have been presented on different types of methods used for nanoparticle DMS material preparation with varying properties. Methods like sol-gel method, co-precipitation method, precursor method, Chimie-Douce method, hydrothermal process, plasma synthesis, reverse micelle technique, sonochemical method, combustion method [8-17] etc. are utilized enormously to prepare numerous types of nanoparticles.

2.2.1 Sol-Gel Method

Sol-gel method of sample preparation is the multi-step technique comprising both chemical and physical processes like hydrolysis, polymerization, gelation, condensation, drying and densification respectively. Generally, this route is initiated by adding metal alkoxides or salts (in nitrate or acetate forms) in distilled water or in an appropriate solvent (normally an alcohol) at elevated temperatures. In sol gel method controlling of pH of the solution is significantly important to avoid the precipitation and to generate homogenous gel that could be attained by the adding base or acidic solutions. Organic compounds with hydrophilic functional groups like hydroxides or carboxylates, acid in small proportion such

as citric acid, succinic acid, oxalic acid and polymers such as polyacrylic acid (PAA) and polyvinyl pyrrolidone (PVP) can be utilized which are used to form ‘sol’ as well as to control the particle size and the crystalline nature of the end products. Chelation of metal ions is done by adding carboxylic acid into the solution which gives rise to a uniform distribution to the ions present in the gel. Meanwhile the gel is also heated at specific temperature to abolish excess water and volatile organic components. This result ultimately gives the dried gel. The crystalline nature of monophasic metal oxides is obtained after calcinating the dried gel at highly elevated temperatures, the temperature of calcination is dependent chemical nature of the precursor [18-21].

2.2.2 Co-Precipitation Method

In Co-precipitation method, the required metal cations are taken in from of a common medium such as hydroxides, carbonates, oxalates, formates etc. which usually gets co-precipitated. These precipitates are consequently calcinated at suitable temperatures to give the final product in nanopowder form. The better solubility of the precipitates gives high homogeneity and generates low particle size. However, this synthesis requires its own special conditions and precursor reactions. It is essential to control the solution concentration, pH, temperature and swiftness of mixture so as to obtain the end product with innovative properties [22-25].

2.2.3 Precursor Method

Precursor method of sample preparation has dragged the attention of researchers due to the production of nanomaterial with high purity and good homogeneity that could be increased by adding cations in the precursor itself. Consequently there is decrease in diffusion rate and minimization of the product formation temperature. To attain homogeneous product in less time and at low temperatures incorporation of constituent cations has to be made on atomic scale. This method engages a solid solution with metal ions in the required ratio, subsequently decomposing the precursor to give the end product. Precursor method is helpful due it produces material with outstanding stoichiometry, homogeneity and low impurity content [26-28].

2.2.4 Chimie-Douce Method

This method is an addition to precursor method of sample preparation. This process occurs at temperatures less than 500 ^{o}C, so as to form thermodynamically metastable phases. More often new phases are formed with curious structures and fascinating properties. The stable structures are gained via calcinations performed at higher temperature. This process engages steps like intercalation, in which ions are place in the structures that results in decrement of cations in the host material via electrochemical method. Reverse intercalation could be also carried out via electrochemical method. Intercalation is trailed by taking away the hydroxide group, which is achieved by using usual heating methods by maintaining temperature below 500^{o}C. Fine crystallite sizes of the specimen can be achieved upon calcinations at different temperatures. The calcination temperature can affect the particle size and other parameters like Curie temperature, dielectric properties, resistivity etc. [29-31].

2.2.5 Hydrothermal Process

This method of sample preparation is an efficient technique utilized for material synthesis and is based on the solubility of compound in hot water under high pressure. This technique is based on the fact that numerous oxides are soluble in an alkali solution and this method can be suitably applied to prepare ferrite materials. The big advantage in this method is that it allows the re-crystallization of the powder and it can also control the grain size and shapes, however this route is not quicker process to synthesize nanomaterial. Growth of the crystal is made in a setup having an autoclave that is normally a steel pressure vessel, wherein the chemicals are added with distilled water. A temperature gradient about 40^{o}C is kept at the two different terminals of the chamber consecutively to liquefy chemicals at hot terminal. A probable good point of this method over other techniques of crystal growth setup is that it owns the capability to produce crystalline phases which is unstable at the melting point. Moreover by using hydrothermal method the samples having high vapour pressure in the vicinity of their melting points can be prepared and by controlling the composition of the sample large amount of high quality crystals can be grown [32-35].

2.2.6 Plasma Synthesis

Plasma synthesis is one of the most efficient method of sample preparation to produce good yield nanopowder. It is possible to produce well crystalline nanomaterials using 50KW-3MHZ RF plasma torch. High power ball milled element powders, less than 10 micron size and desired stoichiometric proportion are utilized as metal ions in the plasma. Gas like Argon is employed as plasma gas and mixture of argon and hydrogen gas as a plasma stream gas. Precursor powders are injected via plasma jet stream by argon and using a carrier gas. Once the plasma is generated, air with high pressure is also forwarded in the reactor as an oxidizer. This method of sample preparation is highly frustrating and involves complicated system [36-38].

2.2.7 Reverse Micelle Technique

Reverse micelle procedure is a different method for the production of nanoparticles. Unlike other processes this technique can be also used to prepare DMS nanoparticles. Wet chemical method is carried out in Reverse micelle, where quantity of water is enclosed by surfactant molecules in an excess volume of oil which offers good control over size and morphology of the nanoparticles. During this process surfactant molecules restrict the particle growth as a result control on size and shape of particles are maintained. The basic principle for this technique is the use of surfactant molecule which makes aqueous droplet sizes stable in a medium having hydrocarbons. Structure of the surfactant and the size are capable to create a material with a wide range of grain sizes. It is important to maintain the pH and the electrochemical potential of the solution, consequently the starting ratio of metal precursors is customized to decrease the metals in the precipitate form and to fire the samples. In this route molar ratio of water is used to control micelle size, which is selected to yield a fine particle size in nanometer range. Subsequently ammonia solution is mixed in the metal salts solution and stirred constantly. This reaction is permitted to carry on for about an hour until particle flocculation is induced by adding extra methanol. Afterwards the particles are accumulated using centrifugation and washed with methanol to eliminate excess surfactant, next a methanol-water solution is added to remove any additional un-reacted ions if present. After ultimate centrifugation the material is

dried overnight in energetic vacuum, and then fired at highly elevated temperature for few hours under inert atmosphere to acquire the end product [39-41].

2.2.8 Sonochemical Method

In this method molecules experience chemical reactions because of applied powerful ultrasound radiation (approximately 20 KHz to 10 MHz). This method involves transitory sound waves of non varying frequency via solution of suspiciously chosen metal complex precursors. In a solvent vapour pressure of a definite threshold, development of discontinuous waves and compressions in the wave caused by cavities comes into view due to physical acoustic cavitation phenomenon that results in sonochemical process. Ultrasound power effects chemical changes happening because of cavitation phenomena which involves the development, enlargement, and disintegration of bubbles in liquid medium. This method has been utilized to manufacture various types of unstructured (amorphous) nanomaterials of metal, oxide, ferrite, and nitride [42-45].

2.2.9 Preparation of Co doped ZnO, Nd doped In_2O_3 And Ni doped CuO Dilute Magnetic Semiconductor Nanoparticles Using Combustion Method.

Combustion method of sample preparation is one of the uncomplicated method which is cost efficient, quick and yield efficient. As per reports [49-51], combustion method has been utilized successfully in preparing monophasic dilute magnetic semiconductor nanoparticles having fine particle size distribution and with superior structural, optical, electrical and magnetic properties. In current investigations we have prepared three different forms of DMS materials i.e. Cobalt doped Zinc Oxide, Neodymium doped indium Oxide and Nickel doped Copper Oxide, which were prepared discretely using combustion synthesis, the chemical formulae and the doping concentration are given as follows:

1) $Zn_{(1-x)}Co_xO$ with x = 0.05, 0.10, 0.15, 0.20
2) $In_{(2-x)}Nd_xO_3$ with x = 0, 0.10, 0.15, 0.20
3) $Cu_{(1-x)}Ni_xO$ with x = 0, 0.05, 0.10, 0.15, 0.20, 0.25, 0.30

Metal salts which were taken in stoichiometric proportions for the preparation of DMS nanoparticles includes:

1) Co doped ZnO

❖ Zinc acetate dehydrate [$C_4H_6O_4Zn.2H_2O$], Cobalt (II) acetate tetrahydrate [$(CH_3COO)_2.Co.4H_2O$] along with Nitrilotriacetic acid (NTA) [$C_6H_9NO_6$] and Glycine [$NH_2.CH_2.COOH$]

2) Nd doped In_2O_3

❖ Indium (III) nitrate hydrate [$In(NO_3)_3.xH_2O$], Neodymium (III) acetate hydrate [$Nd(CH_3CO_2)_3.xH_2O$] along with Nitrilotriacetic acid (NTA) [$C_6H_9NO_6$] and Glycine [$NH_2.CH_2.COOH$]

3) Ni doped CuO

❖ Cupric nitrate trihydrate [$Cu(NO_3)_2.3H_2O$], Nickel (II) nitrate hexahydrate [$Ni(NO_3)_2.6H_2O$] along with Nitrilotriacetic acid (NTA) [$C_6H_9NO_6$] and Glycine [$NH_2.CH_2.COOH$]

The metal salts as specified above taken in suitable stoichiometric proportions were mixed in double-distilled water. The solute in the solution was carefully dissolved using a magnetic stirrer with temperature maintained at 90 °C to achieve a homogeneous solution. The homogeneous solution was heated on the magnetic stirrer at 100 °C for the diminution of water content until it turns in to a thick gelatinous solution. The gelatinous solution was transferred on a shallow plate that was placed on a heater. The solution was stirred constantly to restrain the effect of the temperature gradient in the content. Prolong heating of the solution makes it glutinous turning it into a thick dry mass which self-ignites producing an ultrafine powder, which is the required sample.

References:

[1] V.M. Arole, S.V. Munde, Jaast: Material Science, 1 (2014) 89-93.

[2] E.L. Wolf, Nanophysics and Nanotechnology,Wiley-VCH Verlag Weinheim, (2004).

[3] H.V. Heeren, Nanotechnology lectures: enabling MNT, nanofabrication November (2006).

[4] P. Iqbal, Jon A. Preece, Paula M. Mendes, John Wiley & Sons, Ltd (2012).

[5] X. Zhang, Cheng Sun and Nicholas Fang, Journal of Nanoparticle Research, 6 (2004) 125–130.

[6] M. Singh, S. Manikandan and A.K. Kumaraguru, Nanoparticles, Journal of Nanoscience and Nanotechnology, (2010).

[7] B. Parveen, M. Hassan, S. Atiq, S. Riaz, S. Naseem, M. Asif Toseef, Materials International 27 (2017) 303–310.

[8] J. Livage, Sol-gel synthesis of solids, Encyclopedia of Inorganic Chemistry, R. Bruce King, John Wiley edition, Ney York, 3836-3851 (1994).

[9] S.k. Johny Basha, V. Khidhirbrahmendra, M. Avinash, U. Udayachandran Thampy, C.h. Venkata Reddy, J. Mater. Sci. Mater. Electron. 29 (2015) 6105-6112.

[10] L.Patron, I.Mindru, G.Marinescu, Encyclopedia of Nanoscience and Nano-technology, 1st ed., Marcel Dekker, New York, (2004) 1683–1699.

[11] N. Khan, TaimurAthar, H. Fouad, Ahmad Umar, Z.A.Ansari & S.G.Ansari, Application of pristine and doped SnO2 nanoparticles as a matrix for agro-hazardous material (organophosphate) detection, 7 (2017) 42510.

[12] W. J. Li, J. Mater. Sci. Letters, 20, 1381, 2001

[13] T.S. Ko, S. Yang, H.C. Hsu, C.P. Chu, H.F. Lin, S.C. Liao, T.C. Lu, H.C. Kuo, W.F. Hsieh, S.C. Wang, Materials Science and Engineering B, 134 (2006) 54–58.

[14] T. Ahmad, Ganguli. A. K, J. Mater. Res, 19 (2004) 2905-2912.

[15] J. Zhu, Yuri Koltypin, A. Gedanken, Chemistry of Materials, 12 (2000) 73-78.

[16] D. Paul Joseph, S. Naveenkumar, N. Sivakumar, C. Venkateswaran, Materials Chemistry and Physics 97 (2006) 188–192.

[17] K.Y. Salkar, R.B. Tangsali, R.S. Gad, M. Jeyakanthan, U. Subramanian, Superlattices Microstruct. 126, 158–173 (2019).

[18] P. Varshney, G. Srinet, and R. Kumar, Science in Semiconductor Processing, 15 (2012) 314–319.

[19] N. Bahadur, R. Pasricha, S.Chand, and R. K. Kotnala, Materials Chemistry and Physics,133 (2012) 471–479.

[20] A. Kumar, Nishtha Yadav, Monica Bhatt, Neeraj K Mishra, Pratibha Chaudhary and Rajeev Singh, Hindawi Publishing Corporation, Journal of Nanomaterials, (2015) 5.

[21] M.Z. Naik, A.V. Salker, Materials Chemistry and Physics, 212 (2018) 336-342.

[22] P. Kaur, Sanjeev Kumar, Anupinder Singh, S.M. Rao, J. Mater. Sci. Mater. Electron. 26 (2015) 9158-9163.

[23] O. D Jayakumar, H G Salunke, R MKadam, Manoj Mohapatra, G Yaswant and S K Kulshreshtha, Nanotechnology 17 (2006) 1278–1285.

[24] G. Venkata Chalapathi, M. Thaidun, D. Subramanyam, B. Srinivasa Rao, C. Balanarayana, B. Rajesh Kumar, Chalcogenide Letters,12 (2015) 181 – 190.

[25] Z. Karimi, Y. Mohammadifar, H. Shokrollahi, S.K. Asl, G. Yousefi, L. Karimi, J. Magn. Magn. Mater. 361 (2014) 150–156.

[26] S. Maensiri, Jakkapon Sreesongmuang, Chunpen Thomas, Jutharatana Klinkaewnarong, Journal of Magnetism and Magnetic Materials, 301 (2006) 422–432.

[27] B. Soni, Somnath Biswas, AIP Conference Proceedings 1953 (2018) 030267.

[28] S. Niasari. M., Davar, Material Letters, 63 (2009) 441-443.

[29] J. Gopalakrishnan, Chimie Douce Approaches to the Synthesis of Metastable Oxide Materials, Chemistry of Materials, 7 (1995).

[30] A. R. West, Solid state chemistry and its applications, John Wiley and sons (1984).

[31] Schleich, D.M., Solid State Ion. 1994, 70–71, 407–411.

[32] Y. Wang, Tingting Jiang, Dawei Meng, Dagui Wang, Meihua Yu, Applied Surface Science, 355 (2015) 191–196.

[33] T.Y. Jiang, Y.Q. Wang, D.W. Meng, X.L. Wu, J.X. Wang, J.Y. Chen., Applied Surface Science, 311 (2014) 602–608.

[34] N. Sharma, Anurag Gaur, R. K. Kotnala, Journal of Magnetism and Magnetic Materials, 377 (2015) 183–189.

[35] V. D. Keyson, D. Cavalcante L. Simoes, A. Joya, M. Longo, E. Varela, J. Pizani, P. Souza. A, Journal of Alloys and Compounds, 459 (2008) 537-542.

[36] Bagnall. D., Chen. Y., Shen. M, Zhu. Z, Goto. T, Yao. T, Journal of Crystal Growth, 1998, 184, 605-609.

[37] G. L. Liu, Q. Cao, J. X. Deng, P. F. Xing, Y. F. Tian, Y. X. Chen, S. S. Yan and L. M. Mei, Applied Physics Letters,90 (2007).

[38] N. M. Anukaliani A, Physica B, 406 (2011) 911–915.

[39] D. Kim, M. Miyamoto, and M. Nakayama, Journal of Applied Physics, 100 (2006).

[40] J. Chandradass, M. Balasubramanian, Dong Sik Bae, Hern Kim, Materials and Manufacturing Processes 12 (2012) , 1290-1294.

[41] B. A. Smith, Jin Z. Zhang, Alan Joly, Jun Liu., Physical Review B, *62* (2000) 2021-2028

[42] S.H. Jung, E. Oh, K.H. Lee, Y. Yang, C.G. Park, W. Park, S.H. Jeong, Crystal Growth Des, 8 (2008) 265–269.

[43] A.E. Kandjani, M.F. Tabriz, B. Pourabbas, Material Research Bulletin, 43 (2008) 645–654.

[44] L. B. Arruda, Douglas M.G. Leite, Marcelo O. Orlandi, Wilson A. Ortiz, Paulo Noronha Lisboa-Filho, Journal of Supercondtivity and Noval Magnetism, 26 (2013) 2515–2519.

[45] R.S. Yadav, P. Mishra, A.C. Pandey, Ultrasonic Sonochemical, 15 (2008) 863–868.

[46] C.N.R. Rao Kanishka Biswas, Ceramic Methods, Essentials of Inorganic Materials Synthesis (2015) 17–21.

[47] K. C. Patil, S. Sudar Manoharan and D.Gajapath, vol.1 (eds. Nicholas P.Cheremisinoff, Marcel Dekker, INC, New York) p.469.

[48] D. D Athayde, Souza, D. F., Silva, A. M. A., Vasconcelos, D., Nunes, E. H. M., Diniz da Costa, J. C., and Vasconcelos, W. L, Ceramics International, 42 (2016) 6555–6571.

[49] R. Krithiga, S. Sankar, G. Subhashree, J.spmi, 75 (2014) 621–633.

[50] V. Rajendar, K. Venkateswara Rao, K. Shobhan, C.H. Shilpa Chakra, Journal of Nano- And Electronic Physics, 5 (2012) 3.

[51] R.B.Tangsali, S.H.Keluskar, G.K.Naik, J.S.Budkuley ,Int.J.Nanosci, 3 (2004) 589–597.

CHAPTER 3

Characterization and Property Measurement Techniques

3.1 Introduction

Characterization of the prepared samples is the most important and fundamental technique involved in any research work. New generation advanced and improved instrument technology allows us to investigate and extract the noteworthy information about the structural, optical, magnetic and electrical properties from the material. These important pieces of information forms a central base of the research work and also assists in reporting the formation of the required material which have been prepared. After confirming the formation of the samples, the samples are taken for various properties measurement which involves several other sophisticated instruments. This chapter provides the vital information on the apparatus and procedures of special experimental techniques utilized for characterization, measuring optical, magnetic and electrical properties of as prepared Co doped ZnO, Nd doped In_2O_3 and Ni doped CuO nanoparticle samples having chemical formula $Zn_{(1-x)}Co_xO$ (x = 0.05, 0.10, 0.15, 0.20), $In_{(2-x)}Nd_xO_3$ (x = 0, 0.10, 0.15, 0.20) and $Cu_{(1-x)}Ni_xO$ (x = 0, 0.05, 0.10, 0.15, 0.20, 0.25, 0.30).

3.2 X-Ray Powder Diffraction

X-ray diffraction is the most significant technique employed to characterize the materials prepared. It is efficiently used for the structural confirmation, phase purity analysis, preferred orientation detection, to look in to order-disorder phenomenon and also calculate crystallite size of the crystals in the samples. The peak positions and the X-ray intensities are employed to identify the structure as well as phase of the prepared material. X-rays are produced by adopting the following procedure.

The X- ray tube consists of a filament, a Cathode and an Anode which holds a target material that could be copper, tungsten or any other material depending upon the energy or wavelength of X-rays required as shown in Figure 3.2.1. Electrons emitted by filament are accelerated by application of high voltage between the cathode and anode. The high energy electrons strike the target material (Cu or Mo) thereby knocking out tightly bound deep shell electrons (K

shell electrons) of the atoms in the target which results in fall of outer high energy shell electrons to inner shells to fill the vacancies created, by emission of photons of energy in X-ray region. Thus accelerated electrons strike the atoms present in the target material to produce X-rays with continuous spectrum termed as Bremsstrahlung radiation. X-ray photons are emitted with energy related to the target material (Cu or Mo) and the emitted X-ray photons are called as characteristic X-ray radiation [1].

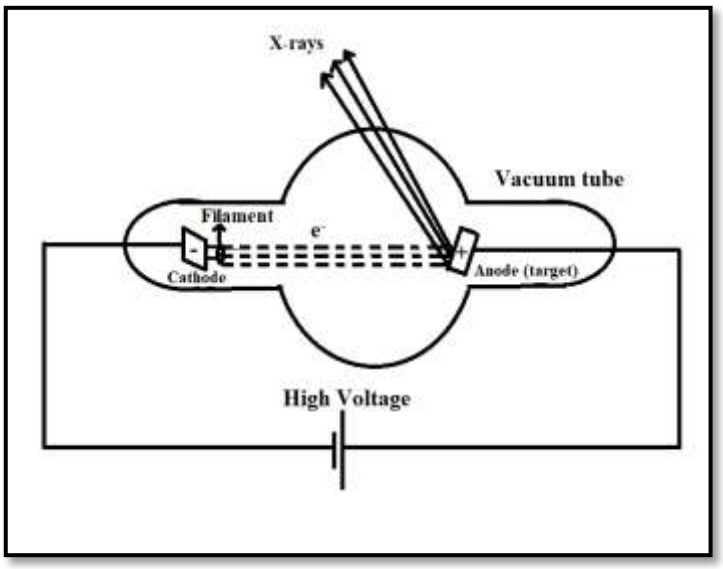

Figure 3.2.1: Production of X-rays.

Non amorphous materials that appear in nature or experimentally fabricated are made up of periodic array of atoms. So, X-ray scattering from these periodic arrangements shows way to the diffraction effect that follows a straightforward relationship known as Bragg's law a relation between the scattering angle, the wavelength of the radiation and the spacing between atomic planes. The distances between the atomic planes are reliant on the distribution and size of the atoms i.e. the structure of the material. Therefore XRD can be used for qualitative and quantitative phase identification of the material [2-5].

When X-ray beam (CuKα, MoKα) is incident on the crystal surface at an angle θ it gets reflected from the atomic planes as shown in Figure 3.2.2. Constructive interference occurs in crystalline material when the path difference between the reflected beams is an integral multiple of X-ray wavelength. This condition satisfies the bragg's law of diffraction as given in equation 3.2.1(a).

$$N\lambda = 2d\sin\theta \qquad 3.2.1(a)$$

Where N is an integer, d is the lattice spacing, θ is the diffraction angle, and λ is the wavelength of the incident X-ray beam. The sample is scanned at an angle of 2θ in all the possible direction of the lattice because of the random orientation of the powdered sample.

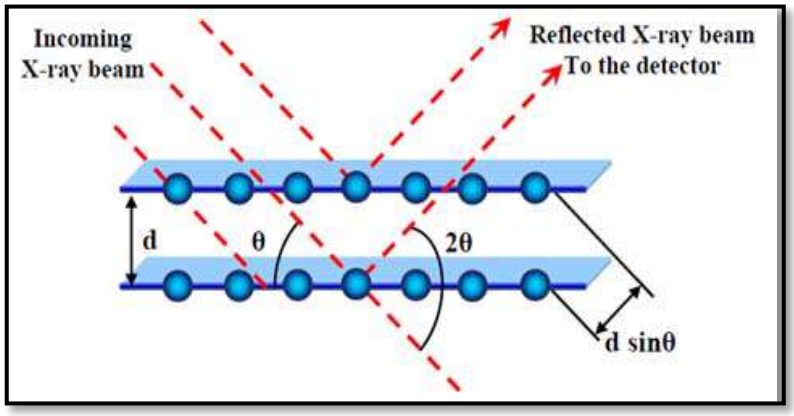

Figure 3.2.2: Diffraction of X-rays by atomic planes [6].

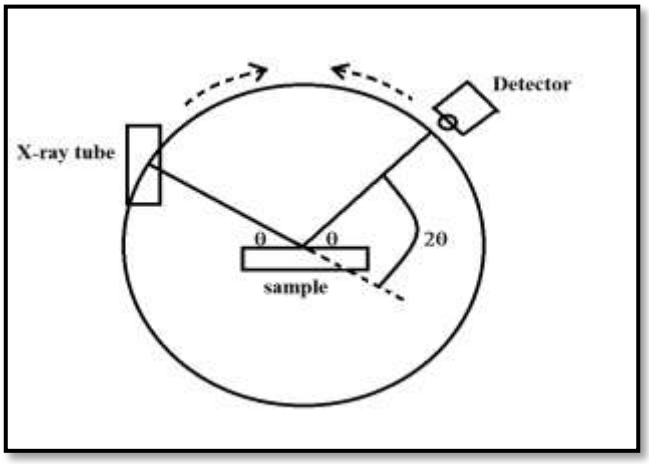

Figure 3.2.3: θ/2θ diffraction in Bragg-Brentano geometry.

Bragg- Brentano geometry is most commonly used for basic measurement geometry in X- ray diffraction instrument shown in Figure 3.2.3. In Bragg-Brentano geometry, the diffracted angle is 2θ defined as the angle between the incident beam and the detector angle, the incident angle is always half of the detector angle [6,7]. In this geometry X-ray tube is fixed, the sample is rotates at θ^o/min and the detector rotates at a rate of $2\theta^o$/min [8-10]. By converting the

diffraction peaks into d-spacing allows to identify the material under investigation because each material has unique d-spacing values. Comparing these values with the reference standard patterns the identification of the material can be attained. There are seven crystal structures available as listed in Table 3.2.1a with the Interplanar spacings d_{hkl} for different crystal arrangements along with their dependence on Miller indices *hkl*. Where *a, b* and *c* are the lattice parameters that corresponds to the lengths of the crystallographic unit cell, while α, β and γ are the angles between lattice parameters [11-13]. The X-rays diffraction patterns are then detected and processed.

Table 3.2.1a: Different crystal systems, constraints and their dependence on Miller indices *hkl*, Parameters *a, b, c,* α, β and γ.

Crystal System	**Constraints**	$\frac{1}{d_{hkl}^2} =$
Cubic	$a = b = c$ $\alpha = \beta = \gamma = 90^o$	$\frac{h^2 + k^2 + l^2}{a^2}$
Tetragonal	$a = b \neq c$ $\alpha = \beta = \gamma = 90^o$	$\frac{h^2 + k^2}{a^2} + \frac{l^2}{c^2}$
Orthorhombic	$a \neq b \neq c$ $\alpha = \beta = \gamma = 90^o$	$\frac{h^2}{a^2} + \frac{k^2}{b^2} + \frac{l^2}{c^2}$
Hexagonal	$a = b \neq c$ $\alpha = \beta = 90^o \gamma = 120$	$\left(\frac{4}{3}\right)\left(\frac{h^2 + k^2 + hk}{a^2}\right) + \left(\frac{l^2}{c^2}\right)$
Trigonal/ Rombohedral	$a = b = c$ $\alpha = \beta = \gamma \neq 90^o$	$\frac{(h^2 + k^2 + l^2)sin^2\alpha + 2(hk + hl + kl)(cos^2\alpha - cos\alpha)}{a^2(1 - 3cos^2\alpha + 2cos^3\alpha)}$
Monoclinic	$a \neq b \neq c$ $\alpha = \gamma = 90^o$ $\beta \neq 90^o$	$\frac{h^2}{a^2 sin^2\beta} + \frac{k^2}{b^2} + \frac{l^2}{c^2 sin^2\beta} + \frac{2hlcos\beta}{acsin^2\beta}$
Triclinic	$a \neq b \neq c$ $\alpha \neq \beta \neq \gamma$	$\frac{1}{V^2}(S_{11}h^2+S_{22}k^2+S_{33}l^2+2S_{12}hk+2S_{23}kl+2S_{13}hl)$ *Where, V = unit cell volume* $S_{11} = b^2c^2sin^2\alpha,$ $S_{22} = a^2c^2sin^2\beta,$ $S_{33} = a^2b^2sin^2\gamma,$ $S_{12} = abc^2(cos\alpha\ cos\beta - cos\gamma),$ $S_{23} = a^2bc\ (cos\beta\ cos\gamma - cos\alpha),$ $S_{13} = ab^2c\ (cos\gamma\ cos\alpha - cos\beta).$

The crystallite size can be determine from X-ray diffraction pattern using Debye-Scherrer equation given as

$$\boldsymbol{D = \frac{0.9\lambda}{\beta cos\theta}}$$

Where λ= Incident X-rays wavelength, β= Full width at half maximum and θ = Bragg angle.

Rietveld refinement method was utilized to classify and refine the crystal structure. If a structure of the trial material is known from the theoretical representation, the crystal structure of the material under research may be refined. The foundation of this process is based on the several steps for example creation of trial structure, powder diffraction profile calculation and evaluation of the same with computed profile. Different parameters, such as atomic positions, thermal parameters, site occupancies, peak shape parameters, etc. can be varied to alter the trial structure. The later stated parameters are varied till the finest fit is achieved [13-17].

Sample preparation for Powder X-ray diffraction

Finely grinded powdered samples, weighted around 0.5g each was used for obtaining X-ray diffraction patterns of $Zn_{(1-x)}Co_xO$ (x = 0.05, 0.10, 0.15, 0.20), $In_{(2-x)}Nd_xO_3$ (x = 0, 0.10, 0.15, 0.20) and $Cu_{(1-x)}Ni_xO$ (x = 0, 0.05, 0.10, 0.15, 0.20, 0.25, 0.30) samples. Figure 3.2.4 shows the Rigaku X-Ray diffractometer used for the purpose.

Figure 3.2.4: Rigaku X-Ray diffractometer.

Diffraction pattern was obtained using Rigaku X-Ray diffractometer with Mo-kα wavelength of 0.7093 Å for Co doped ZnO nanoparticles having chemical formula $Zn_{(1-x)}Co_xO$ (x = 0.05, 0.10, 0.15, 0.20). Whereas diffraction patterns for Nd doped In_2O_3 and Ni doped CuO nanoparticles with chemical formula $In_{(2-x)}Nd_xO_3$ (x = 0, 0.10, 0.15, 0.20) and $Cu_{(1-x)}Ni_xO$ (x = 0, 0.05, 0.10, 0.15, 0.20, 0.25, 0.30) were obtained by using Cu-kα wavelength of 1.5418Å over 2θ range of 20^o to 80^o in steps of 0.02^o and at scan rate of 2^o/min. FullProf suit software was used for rietveld refinement of XRD data obtained on all as prepared samples.

3.3 Fourier Transform Infrared Spectroscopy

The major goal of this spectroscopy is to investigate and to determine the chemical functional groups present in the sample. This method of characterization is nondestructive utilized in identification of compounds by matching the spectrum of unidentified compound with the reference spectrum. Infrared is a light with a longer wavelength and lower frequency than the visible light. IR region of electromagnetic spectrum could be classified into three different groups on the basis of their wavenumber as follows: (a) near infrared region (14000 cm^{-1} to 4000 cm^{-1}), (b) mid infrared region (4000 cm^{-1} to 400 cm^{-1}) and (c) far infrared region (400 cm^{-1} to 4 cm^{-1}) [18-19]. IR radiation do not have adequate amount of energy to induce electronic transition and absorption of IR radiation is limited to the compounds which are having rotational and vibrational modes with small energy difference. The main types of molecular vibrational modes associated with the compounds are stretching and bending mode. Stretching mode is observed in a compound due to change in inter atomic distance along the bond axis and shows symmetric or asymmetric mode. Bending mode is observed in a compound due to change in bond angle and shows twisting, scissoring, wagging or rocking type of motion. When IR radiation interacts with the compound, radiation is absorbed in specific frequency ranges and the associated energy enhances this kind of motions. This occurs when the frequency of the IR radiation matches with the vibrational frequency of the molecule. This absorption gives rise to the absorption bands in IR spectrum [20-22]. Analyzing the position, shape and the intensity of the absorption peak of the IR spectrum reveals the details of the sample molecular structure [23,24].

Figure 3.3.1: Shimadzu FTIR 8900 system.

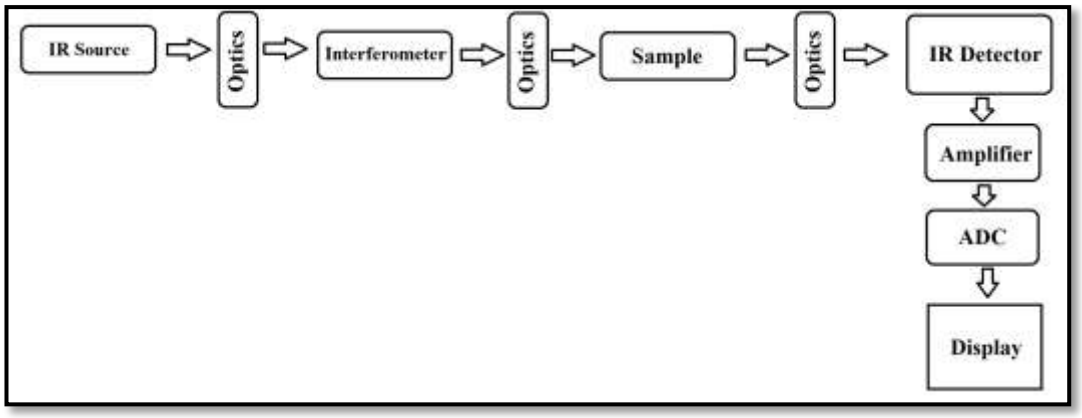

Figure 3.3.2: Diagram of basic components of an FTIR system.

In FTIR spectroscopy the basic idea is to utilize the interference of two beams in an interferometer. The change in optical path difference (OPD) of the two interfering beams produces characteristic interference pattern. The diagram of basic components of an FTIR system is displayed in Figure 3.3.2. The radiation from the interferometer is either transmitted or reflected by the sample that is focused on the detector. The detector amplifies the signal and converts it into a digital signal that is interfaced with a computer for Fourier transformation [25-27].

Material preparation for IR spectroscopy

To record FTIR spectra of nanoparticle samples, 100mg of KBr was weighed and pressed in to pallet with thickness of 1mm and radius 6mm. On this KBr pallet background spectrum was recorded. For recording of sample data 100mg of

KBr was mixed with 2mg nanosample and compressed into a pallet of similar dimensions. Similar procedure was followed and pallets of all the samples were prepared for recording of FTIR spectra.

3.4 Scanning Electron Microscopy (SEM)

Scanning electron microscopy (SEM) is a powerful technique extensively used for the surface imaging to investigate surface morphology of the material. SEM works on the basic principle of accelerated electrons. When accelerated electrons strike the sample the electron energy is dissipated on the sample by electron- sample interaction and various signals are produced. These signals include secondary electrons that generate SEM images, the backscattered electrons, generation of characteristic X-rays which are utilized for chemical composition analysis of the sample, continuum X-rays, visible light and heat. The equipment consists of electron gun that produces a monochromatic electron beam which is condensed and focused with the help of a set of magnetic condensing lens. A set of coils are used for the beam scanning and the objective lens is used to focus the scanning beam on the desired sample area as shown in Figure 3.4.2. The electron beam striking the sample produces secondary electrons that are collected by a secondary detector and applied to the display unit after converting it in to a voltage signal and amplifying the same. This gives rise to an intensity related light spot on the screen. The ultimate image contains thousands of these types of light spots with varying intensity on the display screen which corresponds to the samples morphology [28-32]. SEM micrograph shows two dimensional topographic view of the sample. Figure 3.4.1 presents Carl Zeiss EVO18 scanning electron microscope assembly.

Material preparation for scanning electron microscope

Micrographs of Co doped ZnO, Nd doped In_2O_3 and Ni doped CuO nanoparticles having chemical formula $Zn_{(1-x)}Co_xO$ (x = 0.05, 0.10, 0.15, 0.20), $In_{(2-x)}Nd_xO_3$ (x = 0, 0.10, 0.15, 0.20) and $Cu_{(1-x)}Ni_xO$ (x = 0, 0.05, 0.10, 0.15, 0.20, 0.25, 0.30) were obtained using Carl Zeiss EVO18 scanning electron microscope setup. Small amount of sample was dissipated on a conductive carbon adhesive tape and then subjected to Au/Pd coating as shown in Figure 3.4.3. The coated samples are placed in the scanning electron microscope to study the morphology.

Figure 3.4.1: Carl Zeiss EVO18 scanning electron microscope.

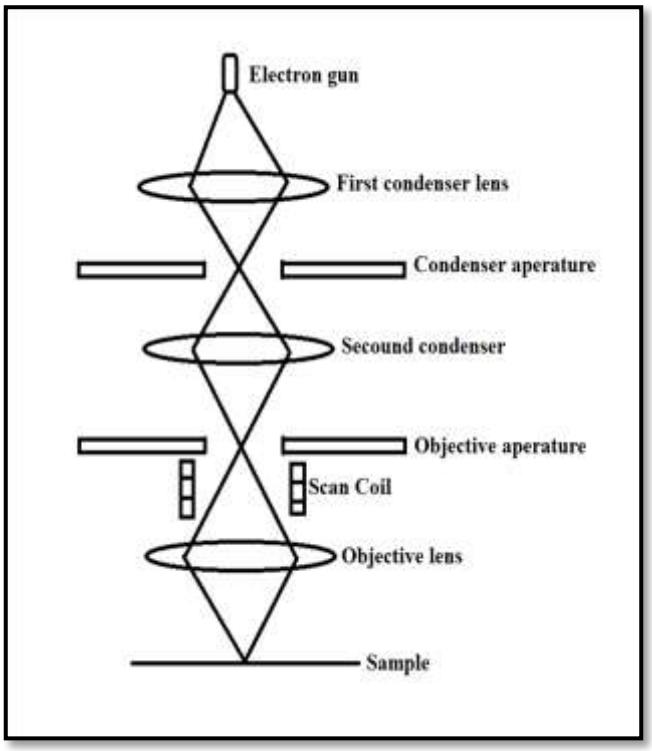

Figure 3.4.2: Basic assembly of scanning electron microscope.

Figure 3.4.3: Sputtering process using sputtering unit.

3.5 Transmission Electron Microscopy (TEM)

Transmission electron microscopy is a high resolution method that provides information about the morphology with good quality micrograph. It is very useful technique for the characterization of single crystal, crystalline materials, biological sample etc. In this technique sample is irradiated with high energy electron beam having uniform current density. Electrons are transmitted from an electron gun and illuminated on the sample through a condenser lens and aperture system. The electron intensity which is transmitted from the sample is magnified using three or four stages of lens system and seen on a fluorescence screen or on a photographic film as shown in Figure 3.5.1 [33-34]. TEM includes an electron gun, condenser system (lenses and apertures), sample chamber, objective lens system, projector lens system, image recording system as shown in Figure 3.5.1. Transmission electron microscopy in selected area diffraction mode gives a unique potential to determine the crystal structure of nanomaterial [35-38].

Material preparation for transmission electron microscope

Around 2-3 mg of Co doped ZnO, Nd doped In_2O_3 and Ni doped CuO nanoparticles having chemical formula $Zn_{(1-x)}Co_xO$ (x = 0.05, 0.10, 0.15, 0.20), $In_{(2-x)}Nd_xO_3$ (x = 0, 0.10, 0.15, 0.20) and $Cu_{(1-x)}Ni_xO$ (x = 0, 0.05, 0.10, 0.15, 0.20, 0.25, 0.30) nanoparticle samples were suspended in methanol, this solution was ultra-sonicated for 60 minutes. After ultra-sonication the samples were diffused on a copper grid for achieving TEM images.

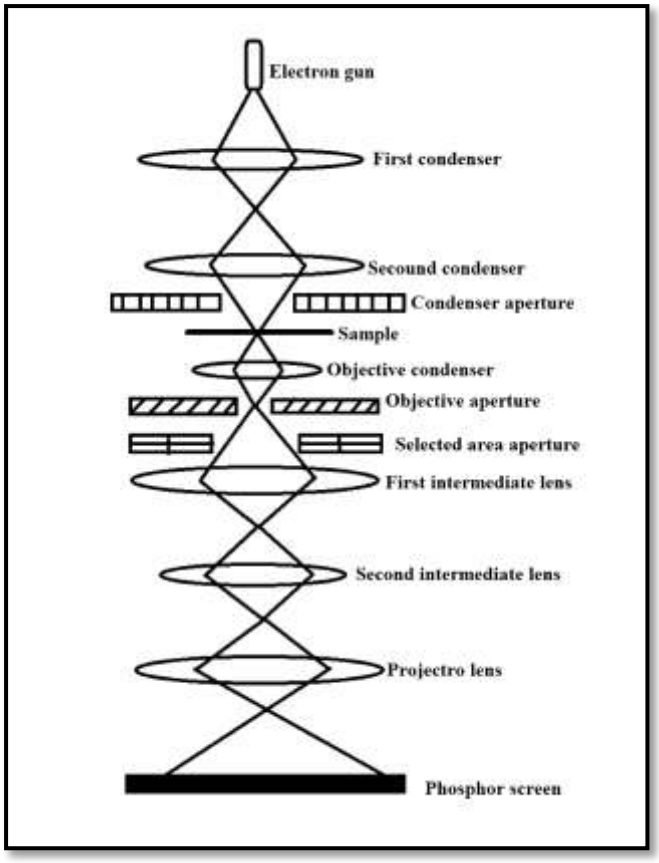

Figure 3.5.1: Basic assembly of tunneling electron microscope.

3.6 UV-Visible Spectroscopy

UV- Visible spectroscopy is a very useful and nondestructive technique used in determining the energy band gap of the material. Ultraviolet and visible light have sufficient energy to excite electrons to higher energy levels and usually applied to inorganic ions and molecules or composite materials [39-42]. For the liquid samples, this equipment has several features which are used for quantitative measurements. An incident beam of light from the source is made to fall on the grating, which is rotated with reference to an axis in such manner that the angle of incidence beam is progressively varied. The output beam from the grating will have several kinds of wavelengths and are separated spatially. Only one wavelength at a particular angle will pass from the slit such that the wavelength transmitted out from the slit will have monochromatic wavelength. Several wavelengths are produced with different incidence angles and a beam splitter is used to divide this beam. Beam passes through the reference and through the sample for which the absorption spectrum of the sample is to be recorded. The intensity and phase of the transmitted beams from both the sample and the

reference are detected. By evaluating these detected data through a phase responsive amplifier the absorption spectrum of the test sample is recorded and displayed. A block diagram and setup of an UV-Visible is as displayed in Figure 3.6.1(a) and Figure 3.6.1(c).

Diffusive reflectance spectroscopy is the powerful technique for the powdered materials. This technique gives vital information about the electron transition in the material. It is closely connected with the UV-Vis spectroscopy, because in both the techniques a visible light is utilized to excite the electrons from valence band to the conduction band within the sample. The only difference is that, in UV-Vis spectroscopy the relative change of transmittance of light when it passes through a solution is recorded, while in diffusive reflectance technique a relative change in the amount of reflected light from the powdered sample surface is recorded. Moreover in UV-Vis spectroscopy a dispersion medium is required for recording absorption spectra of the liquid sample, while this complexity is solved out in diffusive reflectance spectroscopy because it does not required any type of solvent for recording spectra. In this method, a incident light beam is made fall on the sample which gets scattered in different directions corresponds to the diffuse reflection, while light beam which is reflected symmetrically corresponds to specular reflection (mirror like reflection) as shown in Figure 3.6.1(b).

The ultra-violet region is divided into two spectral regions i.e the range between 2000 to 4000 Å known as the near ultra violet region and the region less than 2000Å as far or vacuum ultra violet region. Two classes of spectra can be recorded, the emission and absorption spectra. An emission spectrum is produced by analyzing the light released from luminous source. An absorption spectrum is attained by the spectroscopic investigation of the transmitted light from absorbing medium that is positioned between the light source and the detector. Once the light is incident on a sample with energy hν the absorption occurs within the energy band (Eg) of the material [43-45]. When hν is less than Eg the light passes from all the way through the sample with little absorption. As the energy of the radiation increases such that hν ~ Eg a fine increase or a rise in the absorption occurs. The straightforward and easy method to resolve the band structure of semiconductors is by estimating the absorption spectrum. Absorption is conveyed in terms of a coefficient α (hυ), that is linked to the energy gap (Eg) in agreement with the following equation.

$$\alpha (h\nu) = A (h\nu - Eg)^n$$

Where A is a constant, h is the planks constant, ν is the incident beam light frequency and n is equal to ½ for a direct band gap and 2 for an indirect gap.

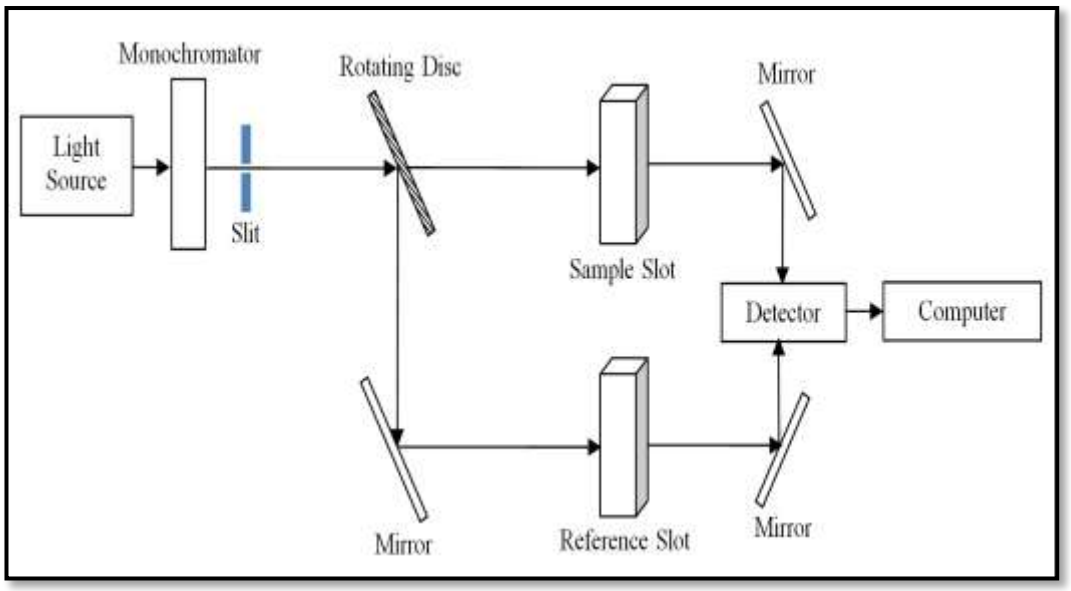

(a)

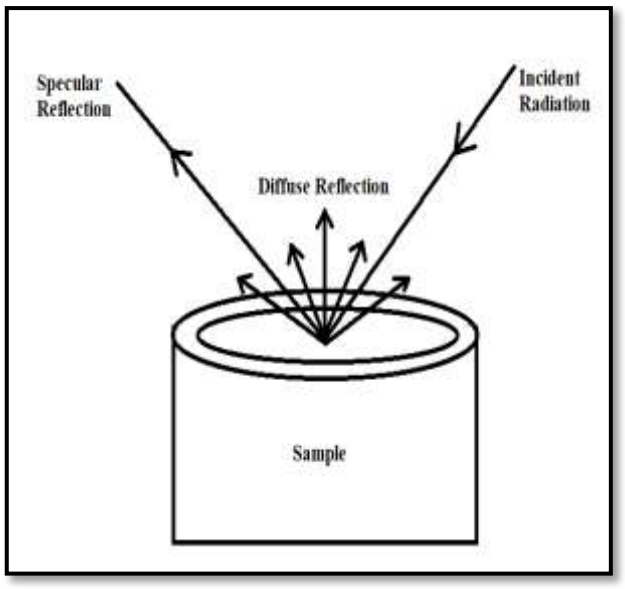

(b)

(c)

Figure 3.6.1: (a) A block diagram of an UV-Visible [45], (b) Scattering of incident light beam from a solid sample (c) UV-Visible setup.

Material preparation for UV-Visible spectroscopy

Nanoparticles of Co doped ZnO, Nd doped In_2O_3 and Ni doped CuO nanoparticles having chemical formula $Zn_{(1-x)}Co_xO$ (x = 0.05, 0.10, 0.15, 0.20), $In_{(2-x)}Nd_xO_3$ (x = 0, 0.10, 0.15, 0.20) and $Cu_{(1-x)}Ni_xO$ (x = 0, 0.05, 0.10, 0.15, 0.20, 0.25, 0.30) respectively were grinded manually in a motor pestle. A sample quantity of 2-3 grams of powder is required to fill the sample holder. The powder was filled into the holder by applying adequate amount of pressure using a cylindrical crystal piece, so that the powder may not fall down. Then the holder containing sample was mounted in the machine and the required data was obtained in reflectance mode using Shimadzu 2401 PC UV Spectrophotometer.

3.7 Photoluminescence Spectroscopy

Photoluminescence (PL) emission is observed when spontaneous light is emitted by the material, under precise optical excitation. The excitation energy and intensity can be selected to analyze different types of excitations of the sample. PL technique is nondestructive and this method requires very small sample quantity. When light radiation with adequate amount of energy is illuminated on a material, photons are absorbed and electronic excitations are produced. When these excitations are relaxed, photons are released. The PL data

can be put together and analyzed to give information about the photo-excited states. The PL spectrum reveals the information about the transition energies and the intensity determines the relative rates of radiative and non-radiative recombination [46-50]. Deviation of the PL intensity with change of external parameters such as temperature, excitation energy, excitation power, can be utilized for further characterization of electronic states and this technique also can be used to describe a variety of materials parameters, which are established respectively as follows:

(1) Band gap calculation the most general radiative transition in semiconductor material involving levels in the conduction and valence bands. Determination of band gap is predominantly helpful when working with semiconductor compounds.

(2) Detection of impurity levels and defect states transitions in semiconductor compounds also revelling localized defect levels. Energy of PL is associated with these levels which can be utilized to categorize the specific defects; moreover the PL intensity could be used to verify compounds concentration.

(3) Recombination mechanisms as conferred above, the returning of electrons to its equilibrium states identified as "recombination" which holds both radiative and nonradiative processes. The PL intensity depends on the photo-excitation states and temperatures are directly associated to the recombination process. Investigation of PL helps to understand the fundamental recombination mechanism.

(4) Non radiative methods are related with localized defect levels, whose existence is determines uniqueness and quality of the material. As a result, material quality can be measured by the radiative recombination calculation. The usual PL experimental set-up is displayed in Figure 3.7.1.

Material preparation for PL spectroscopy

Co doped ZnO nanoparticles with chemical formula $Zn_{(1-x)}Co_xO$ (x = 0.05, 0.10, 0.15, 0.20) was pressed into pallets of thickness ranging between 3 mm to 3.5 mm with diameter of 12 mm. Variation of intensity was recorded for all these samples over the wavelength range from 400 nm to 600 nm with excitation wavelength of 318nm using PTI Spectrofluorometer QM-40.

Figure 3.7.1: PL experimental set-up.

3.8 Vibrating Sample Magnetometer (VSM)

The process of vibrating sample magnetometer (VSM) is mainly based on the Faraday's Law of Induction. According to this law a varying magnetic field will generate an electric field that can be used to evaluate the data as a function of varying magnetic field. VSM is enormously used to determine the magnetic behavior of magnetic materials. For recording the magnetic behavior of a sample, the sample kept in a steady magnetic field initially, gets magnetized by aligning the magnetic domains with the field. The amount of magnetization in the sample is proportional to the magnitude of applied field. The dipole moment of the sample is responsible for magnetization of the sample. Since the sample is surrounded by the pick-up coil up and down movement of the sample brings about change in magnetic flux linked to the pick-up coil which induces an emf or a voltage in the pick-up coil. The induced voltage is used to measure the magnetization produced in the sample.

VSM system is used to examine the magnetic properties of materials with respect to magnetic field and temperature. The alternating magnetic field produces an electric field in the pick-up coils in agreement with the Faraday's Laws of induction and the current generated is proportional to the sample magnetization. If the magnetization is large the induced current will also be high [51-53]. The Quantum Design Versa Lab’s 3Tesla Vibrating Sample Magnetometer (VSM) a reliable, fastest and delicate DC magnetometer was used to measure Magnetic properties of the samples. In this instrument the temperature of the sample can be lowered to 50K and can be move up to 400 K. It uses a cryogen free cryo-cooler

device to reach cryogenic temperatures. In this VSM system magnetic field is produced by a superconducting niobium-titanium (NbTi) solenoid placed in the cryostat vacuum. The typical magnet provides magnetic field of 3T at 20A of current and is cooled by solid conduction. Magnetic noise isolation is ensured by placing a magnet shield in the VSM system [54].

Figure 3.8.1: Quantum Design's Versa Lab 3 Tesla Vibrating sample magnetometer (VSM).

Material preparation for Vibrating sample magnetometer (VSM)

Figure 3.8.2: VSM sample holder and the sample wrapped in Teflon tape.

Quantum Design's Versa Lab 3T vibrating sample magnetometer (VSM) were used to investigate magnetic properties sequentially of Co doped ZnO, Nd doped In_2O_3 and Ni doped CuO nanoparticles having chemical formula $Zn_{(1-x)}Co_xO$ (x = 0.05, 0.10, 0.15, 0.20), $In_{(2-x)}Nd_xO_3$ (x = 0, 0.10, 0.15, 0.20) and $Cu_{(1-x)}Ni_xO$ (x = 0, 0.05, 0.10, 0.15, 0.20, 0.25, 0.30) , 5mg of sample was wrapped up

in Teflon tape and was placed on sample holder as shown in Figure 3.8.2 for obtaining hysteresis measurement. The corrected data was obtained after eliminating the contribution of Teflon tape which was determined initially prior to loading of the sample. Zero field cooled (ZFC) and Field cooled (FC) magnetic moment data on the sample was obtained on the same VSM setup. For ZFC magnetic data, the sample was first cooled down from room temperature to 50K in absence of magnetic field, and then precise magnetic moment of the sample was recorded by enhancing the temperature of the sample in presence of constant applied magnetic field of 500 Oe. For obtaining FC magnetic data, the sample was cooled from room temperature to 50K with a magnetic field of 500 Oe and the required data was recorded as the sample warms up. The complete measurement is automated and computer controlled through a software program which is adjusted by feeding in the required parameter.

3.9 Thermopower

The temperature difference between the two ends of a semiconductor material produces an electromotive force (emf) known as thermo emf (V). Thermopower analysis are widely useful in understanding the conduction mechanism is the semiconductor material and DMS materials due to low mobility. The quantification of thermo-emf is very straightforward and its sign provides very important information regarding conduction mechanism whether the conduction in the material is due to electrons or holes and also explores the behavior of the material whether it is p-type or n-type. Moreover the main significance of thermo-emf is that it permits one to calculate the Fermi energy and carrier concentration values. The experimental set-up of thermo-emf is displayed in Figure 3.9.1 It has upper point contact probe that forms a hot junction and a bottom point contact which makes a cold junction when the sample is placed in between [55-58].

Material preparation for thermopower

The samples under investigation were pressed into pallets having thickness between from 2.5mm to 3mm with the diameter of 10 mm. The pallets were painted with silver paste on both sides to establish good ohmic contact. Thermoelectric power measurements were carried for all the samples over a temperature range of room temperature to 500^{o}C.

Figure 3.9.1: Thermopower setup.

3.10 DC Resistivity

Resistance of the semiconductor material can be measured by using two different methods i.e. the fixed voltage two probe method [59-63] and a four probe fixed current method. A typical block diagram is shown in Figure 3.10.1, which consists of two electrodes made of silver. The DC resistivity setup employed for measurements is shown in Figure 3.10.2. The temperature of the sample was determined with the help of calibrated thermocouple attached to the controller and the temperature was directly displayed on the monitor. The resistance of sample was determined by varying the temperature, during each measurement plenty of time was given to reach the required temperature [64]. On escalating the temperature thermal agitation of the electrons enhances, electrons attain energy larger than E_g and hop into conduction band. The electrons in conduction band are called as free electrons and the vacancies left behind in the valence band are called as holes. For semiconductors resistivity decreases as the temperature increases because more and more charge carries move in to conduction band at higher temperatures.

Material preparation for DC Resistivity

Nanoparticles of Co doped ZnO, Nd doped In_2O_3 and Ni doped CuO nanoparticles having chemical formula $Zn_{(1-x)}Co_xO$ (x = 0.05, 0.10, 0.15, 0.20), $In_{(2-x)}Nd_xO_3$ (x = 0, 0.10, 0.15, 0.20) and $Cu_{(1-x)}Ni_xO$ (x = 0, 0.05, 0.10, 0.15, 0.20,

0.25, 0.30) respectively were pressed into pallets of thickness ranging between 2.5mm to 3mm with the a diameter of 10 mm. The pallets were painted with silver paste on both sides for creating good ohmic contact with the electrodes. Variation of current was recorded for all these samples over the range from room temperature up to 500 ^{o}C using two probe resistivity setup shown in Figure 3.10.1.

Figure 3.10.1: Two probe D.C. Resistivity setup with data acquisition system.

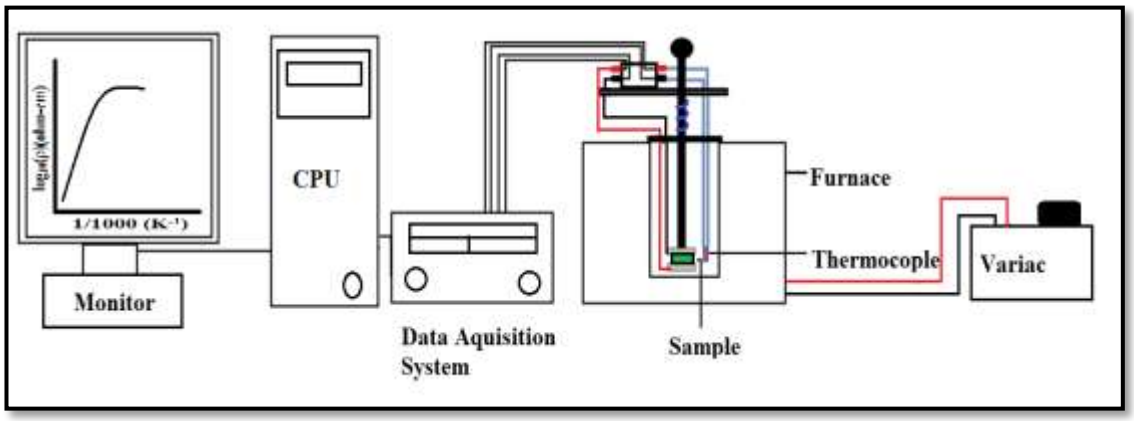

Figure 3.10.2: Block diagram of two probe D.C. Resistivity setup with data acquisition system.

3.11 Dielectric Measurements

A dielectrics material exhibits insulating nature having an important property of electrical polarization which is a good feature. A dielectric material attains polarized when it is placed into an electric field. Figure 3.11.1a displays a dielectric material without any application of electric field while Figure 3.11.1b

displays a dielectric material polarization with an application of electric field. This occurrence of polarization is known as dielectric polaraztaion. Clausius [65] and Mossotti [66] have successfully interconnected the specific inductive capacity to microscopic structure of the material, a macroscopic feature of the insulator was studied by Faraday [67] which is now commonly termed as dielectric constant.

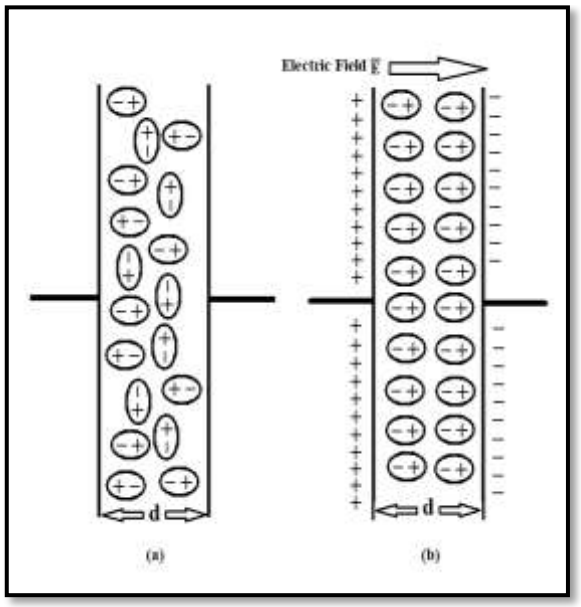

Figure 3.11.1: a) Dielectric material in the absence of electric field, b) Dielectric in the presence of electric field.

Michael Faraday initiated that if a parallel plate capacitor of value C_0 is kept under vacuum and loaded with a dielectric material, the charge storage capacitance of the material enhances to a value C. The 'χ' ratio of the capacitance increase given by

$$\boldsymbol{\chi = \frac{c - c_o}{c_o} = \frac{\Delta c}{c_o}} \qquad 3.11.1(a)$$

'χ' is termed as the electrical susceptibility or dielectric permittivity of the dielectric.

$$\boldsymbol{\varepsilon_r = \frac{c}{c_o}} \qquad 3.11.1(b)$$

For this reason the dielectric constant of a material is a dimensionless quantity. In highly crystalline and well structured materials the dielectric constant is sturdily dependent on applied field frequency. Materials with fairly high dielectric constants can be used efficiently in fabricating proficient microwave

devices. The dielectric natures of nanoparticles are extremely dependent on the method of sample preparation, elemental composition and substitution, size, structure and doping concentration.

Dielectric loss

The dielectric constant of a material has real and imaginary part mathematical symbols denoted as ε_r and ε respectively. The imaginary part gives the detail information about energy loss through the dielectric material when AC signal is passed through the material. Moreover the real part of permittivity is expressed as the dielectric constant which specifies the connection between the transmission of AC signal and the capacitance of dielectric material. The imaginary part measures the amount of electric field which is dissipated as heat during the polarization process in presence of alternating electric field [68-70] known as dielectric loss and is given by following equation.

$$\boldsymbol{tan\delta = \frac{\varepsilon''}{\varepsilon}} \qquad 3.11.1(c)$$

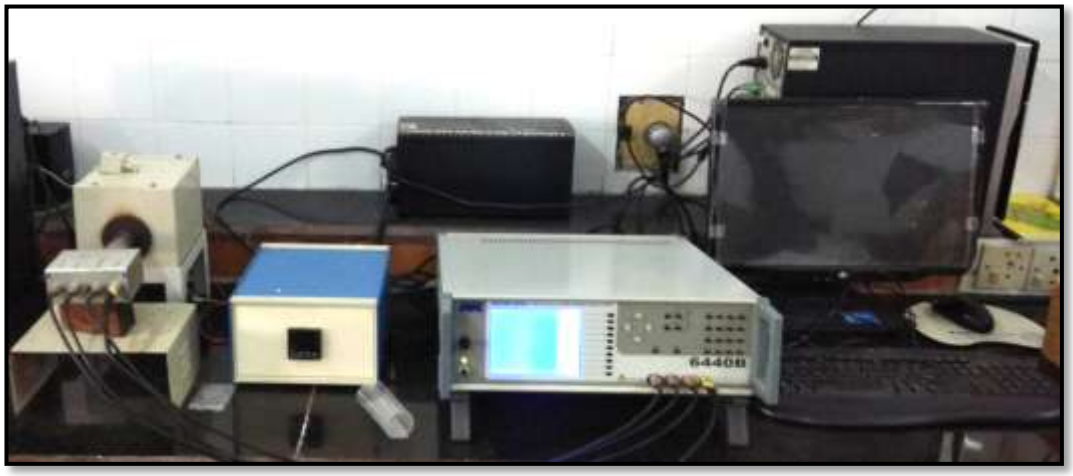

Figure 3.11.2: Wayne Kerr precision component analyzer 6440B.

Impedance measurement

When A.C. current is passes through the circuit that consists of inductors, capacitors and resistors, and the complex resistance of the LCR circuit known as Impedance comprises of real part and imaginary part. Capability of circuit to resist the applied current is given by real part and the capability of circuit to hoard electrical energy is revealed by imaginary part of the impedance [71,72]. Complex impedance is expressed as Z = Z' – jZ", where Z' is the real part of the impedance,

Z" is the imaginary part of the impedance and imaginary factor j = $\sqrt{-1}$. Real part and Imaginary part of the complex impedance was determined using equation 3.11.1(d) and 3.11.1(e). Where Z is the complex impedance and θ is the phase angle.

$$Z' = Z \cos \theta \qquad 3.11.1(d)$$

$$Z'' = Z \sin \theta \qquad 3.11.1(e)$$

Material preparation for dielectric property and impedance measurements

Co doped ZnO, Nd doped In_2O_3 and Ni doped CuO nanoparticles having chemical formula $Zn_{(1-x)}Co_xO$ (x = 0.05, 0.10, 0.15, 0.20), $In_{(2-x)}Nd_xO_3$ (x = 0, 0.10, 0.15, 0.20) and $Cu_{(1-x)}Ni_xO$ (x = 0, 0.05, 0.10, 0.15, 0.20, 0.25, 0.30) nanoparticles respectively were pressed into pallets of thickness ranging between 2.5mm to 3mm with diameter of 10 mm. Silver paint was applied on both the sides of the pallets for creating good ohmic contacts with electrodes. Capacitance and dielectric loss of the materials were recorded with respect to frequency over the range of 20Hz to 3MHz. Temperature dependence of capacitance and the dielectric loss was recorded over a range of 300K to 773K. The complex impedance and phase angle of the materials were recorded as a function of frequency over the range of 20Hz to 3MHz using Wayne Kerr precision component analyzer 6440B shown in Figure 3.11.2. The complex impedance configuration can be modelled as a parallel combination of resistance and capacitor. Dielectric constant was determined using the following equation

$$\varepsilon_r = \frac{Cd}{\varepsilon_0 A}$$

Where C = Capacitance, d = Thickness of the pallet, ε_0 = Absolute permittivity of free space (8.85x10-12 $C^2m^{-2}N^{-1}$), A = Area of the pallet.

References:

[1] W.C. Roentgen, Ann. Phys. Chem., 64(1898)1–11.

[2] G. Von Hevesey, McGraw-Hill, New York, (1932).

[3] S.F. Bartram, X-Ray analysis, Vol. 4 (1960).

[4] L.S. Birks, American Chemical Society Centennial, Washington DC, (1976).

[5] H.G.J. Moseley, Philosophical Magazine, 26, (1912)1024–1034.

[6] Y. T. Prabhu, K. Venkateswara Rao, V. Sesha Sai Kumar, B. Siva Kumari, International Journal of Engineering and Advanced Technology (IJEAT), 2 (2013) 2249 – 8958.

[7] M. Birkholz, C. Genzel, T. Jung, Journal of Applied Physics, 96 (2004) 7202.

[8] R. Jenkins, D. J. Haas, F. R. Paolini, Norelco Reporter, 18, (1971)1–16.

[9] C.L. Mallory, R.L. Snyder, Advances in X-Ray Analysis, 22, (1979)121–132.

[10] B. E. Warren, X-Ray Diffraction, Addison-Wesley, Reading, MA, (1969).

[11] B. D. Cullity, Elements of X-Ray Diffraction, Addison-Wesley, (1967).

[12] V.D. Mote, Y. Purshotham, B. N. Dole, Journal of Theoretical and Applied Physics, 6-6(2012) 2251–7235.

[13] T. Taguchi, Powder Diffraction, 21 (2006) 97-101.

[14] X. Hong Deng, Qing Li, Xun Peng, Jinping Wang, Chen, Yadong Li, Angewandte Chemie, 117, (2005) 2842–2845.

[15] C. Venkataraju, G. Sathishkumar, K. Sivakumar, Journal of Magnetism and Magnetic Materials, 322 (2010) 230–233.

[16] A. R. Bueno, Maria L. Gregori, Maria C. S. Nobrega, Material Chemistry and Physics, 105 (2007) 229–233.

[17] R. Chatterjee, A. Verma, Journal of Magnetism and Magnetic Materials,306 (2006) 313–320.

[18] B. Stuart, Infrared Spectroscopy: Fundamentals and Applications Chichester: Wiley (2004).

[19] H.Gunzler, H. U. Gremlich, IR Spectroscopy: An Introduction Weinheim: Wiley (2002).

[20] R. J. Bell, Introductory Fourier Transform Spectroscopy New York: Academic (1972).

[21] T. Vo-Dinh, Handbook of Spectroscopy, WILEY-VCH (2003)

[22] M. Vollmer, K-P Möllmann, The Physics Teacher, 46 (2008) 114–7.

[23] J. Kauppinen, Fourier Transforms in Spectroscopy Berlin: Wiley (2001).

[24] W. S. Lau, IR Characterization for Microelectronics, World Scientific (1999).

[25] E. D. Palik, Handbook of Optical Constants of Solids Boston, MA: Academic (1985).

[26] H. M Heise, J Fritzsche, H Tkatsch, F Waag, K Karch, K Henze, S Delbeck, J

Budde, European Journal of Physics, 34 (2013) 139–59
[27] M Vollmer, K-P Möllmann, Infrared Thermal Imaging: Fundamentals, Research and Applications, Weinheim: Wiley (2010).
[28] R. F. Egerton, Physical Principles of Electron Microscopy: An Introduction to TEM, SEM, and AEM, Springer: New York (1986).
[29] J. Goldstein, D. Newbury, D. Joy, C. Lyman, C.; Echlin, P.; Lifshin, E.; Sawyer, L.; Michael, J. Scanning Electron Microscopy and X-Ray Microanalysis, 3rd ed., Kluwer: New York (2003).
[30] M.T. Postek, K.S. Howard, A.H. Johnson and K.L. McMichael, Ladd Research Ind., Inc.Williston, VT (1980).
[31] C.E. Lyman, D.E. Newbury, J.I. Goldstein, D.B. Williams, A.D. Romig, J.T. Armstrong, P. Echlin, C.E. Fiori, D.C. Joy, E. Lifshin, Klaus-Ruediger Peters, Plenum Press. New York, N.Y. (1990).
[32] J.I. Goldstein, H. Yakowitz, D.E. Newbury, E. Lifshin, J.W. Colby, J.W. Colby, J.R. Coleman, J.I. Goldstein and H. Yakowitz, Pelnum Press. New York, N.Y (1975).
[33] Thomas LaGrange, Introduction: Basics of Transmission Electron Microscopy (TEM), TEM Doctoral Course MS-637 (2016).
[34] S. J. B. Reed, Electron Microprobe Analysis Cambridge Univ. Press. Second edition (1993).
[35] S. J. B. Reed, Electron Microprobe Analysis and Scanning Electron Microscopy in Geology by Cambridge Univ. Press. (1996).
[36] M. Von Heimendahl, W. Bell, G. Thomas, Journal of Applied Physics 35 (1964) 3614.
[37] C. Richard Brundle, Charles A. Evans Jr, Shaun Wilson. Encyclopedia of materials characterization, Butterworth-Heinemann publications (1992).
[38] J. Mayer, Lucille A. Giannuzzi, Takeo Kamino, Joseph Michael, TEM Sample Preparation and FIB-Induced Damage. Bulletin, volume 32, (2007).
[39] D. A. Skoog, F. J. Holler, S. R. Crouch, Principles of Instrumental Analysis, 6th Ed., Thomson Brooks/Cole (2007).
[40] J. P. Sibilia, Materials Characterization and Chemical Analysis, 2nd Ed., Wiley-VCH, New York (1996) 3.
[41] D. C. Harris, Quantitative Chemical Analysis, 7th Ed., Freeman, New York (2007).

[42] G. R. Chatwal, S. K. Anand Instrumental methods of chemical analysis, Himalaya Publishing House (1979).

[43] C.N.R. Rao, Butterworths Publication, London, (1961).

[44] E.A. Braude, Academic Press, New York, 1955 A

[45] R. John, Dyer, Prentice Hall (1971).

[46] D.R. Luminescence of solids Plenum Press NewYork (1998).

[47] C.Fouassier, Luminescence-Encyclopedia of Inorganic Chemistry Accademic Press New York (1984).

[48] M. Omar and Howard H Patterson, Luminescence theory - Encyclopedia of Spectroscopy, Academic Press New York (1999).

[49] L. Marton, Methods of experimental Physics - Solid state of physics. Academic Press New York 6 (1959).

[50] S. Mathew, A.K. Prasad, T. Benoy, P.P. Rakesh, M. Hari, T.M. Libish, P. Radhakrishnan, V.P.N. Nampoori, C.P.G. Vallabhan, Journal of Fluorescence, 22 (2012) 1563.

[51] A. Hubert, R. Schäfer. Magnetic Domains. Springer-Verlag, Berlin Heidelberg, (1998).

[52] B. D. Cullity, C. D. Graham, Introduction to Magnetic Materials. John Wiley & Sons, New Jersey (2009)

[53] O' Handley, R. C. Modern magnetic materials: principles and applications. John Wiley & Sons, New York (2000).

[54] Quantum Design's Versa lab 3 Tesla VSM user manual, part no. 1300-001.

[55] B. L. Gallagher and P. N. Butcher, Handbook on semiconductors, Amsterdam; Elsevier, 1 (1992) 721-816.

[56] C.M. Bandari and D.M. Rowe, Thermal conduction in semiconductors, Wiley Estern Ltd, New Delhi (1988).

[57] F.J. Blatt, P.A.Schroeder, C.L.Foiles and D. Greig, Thermoelectric power of metals, Plenum Press, New York, (1976).

[58] S.M. Puri, and T.H. Geballe, Semiconductors and Semimetals, Eds. R. K. Willardson and A. C. Beer, Academic Press, New York (1966) 203.

[59] D. Kumar, K.C Mouli, International Journal of Nanotechnology and Applications, Volume 4, No.1 (2010) 51-59.

[60] S. Thakur and S. C. Katyal M. Singh, Applied Physics Letters, 91, (2007) 262501.

[61] A. A.Samokhvalov, A.G.Rustamov, Soviet Physics Solid state, 6, (1964) 749.
[62] A.A.Samokhvalov, A.G. Rustamov, Soviet Physics Solid state, 7, (1965) 961.
[63] L. G. Van Uitert, Proc.I.R.E. 44 (1956) 1294.
[64] Yu V Petrov, N A Inogamov, A V Mokshin and B N Galimzyanov, Journal of Physics: Conf. Series 946 (2018) 012096.
[65] R.Clausius, Volume 2 Vieweg Braunschweigh (1879).
[66] M. Faraday, Phil. Trans 128:1 79 (1837)265.
[67] O. F. Mossoti, Bibl. univ. modena 6, (1847) 193.
[68] Anthony R. West, Solid State Chemistry and its Applications, 534-537.
[69] A. J. Dekker, Solid State Physics, 148, 149.
[70] A.K. Jonscher, Dielectric relaxation in solids, 306.
[71] H. Semat, Robert Katz, Research Papers in Physics and Astronomy Robert Katz Publications, 157 (1958) 461-487.
[72] S. Devi, A K Jha, Bull. Mater. Sci. 33 (2010) 683–690.

CHAPTER 4

Structural Characterization of Co doped ZnO, Nd doped In_2O_3 & Ni doped CuO Dilute Magnetic Semiconductor Nanoparticles

Introduction

Characterization of the materials prepared is essential in order to understand their structural properties as it provides vital information about formation of required materials thereby confirming the suitability of the sample preparation method adopted. Characterization has explores the structural detail and the parameters which are linked to properties and performance of the materials. Atomic structure of the material notifies how the atoms in a material are bonded together, which helps to classify the materials. Similarly, characterization of the materials may also reveal the features of individual's elemental composition. Structure and crystallite size of the material yields important information related to materials properties such as optical, magnetic and electrical properties. In current chapter details and outcome of characterization methods such as XRD, SEM, TEM, EDS and FTIR immoderately used in present investigation for obtaining qualitative and quantitative information of Co doped ZnO, Nd doped In_2O_3 and Ni doped CuO nanoparticles samples have been provided. Experimental techniques which are used in this work scrutinizes the materials characterization with regard to crystal structure, phases, crystallite size, lattice parameter, cell volume, micro-structural morphology, the chemical composition, and absorption wavelengths of vibrational bonds, are presented and quantitatively discussed.

4.1 Co doped ZnO, $Zn_{(1-x)}Co_xO$ (x = 0.05, 0.10, 0.15, 0.20)

4.1.1 X-Ray Diffraction Analysis

Characteristic of X-ray diffraction patterns obtained on the samples $Zn_{(1-x)}Co_xO$ (x = 0.05, 0.10, 0.15, 0.20) are displayed in Figure 4.1.1.1. The rietveld refinement of XRD patterns were done using FullProf suite for all the samples and are shown in Figure 4.1.1.2. The X-ray beam produced by Molybdenum target having wavelength λ=0.7093Å was used for obtaining the diffraction patterns of these samples. The inter planer spacing '*d*' was calculated from the XRD data and the '*d*' values achieved from the standard data (JCPDS-79-2205) are list in Table 4.1.1(a).

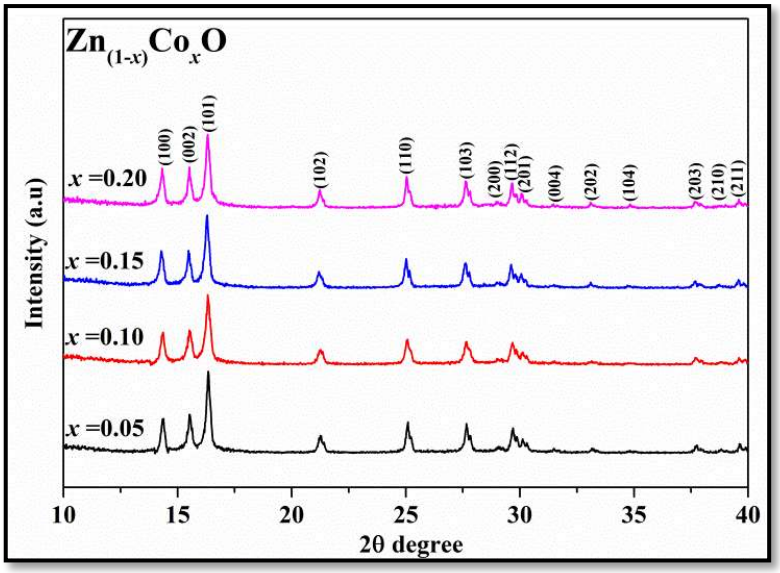

Figure 4.1.1.1: X-ray diffraction pattern of $Zn_{(1-x)}Co_xO$ with x = 0.05, 0.10, 0.15, 0.20.

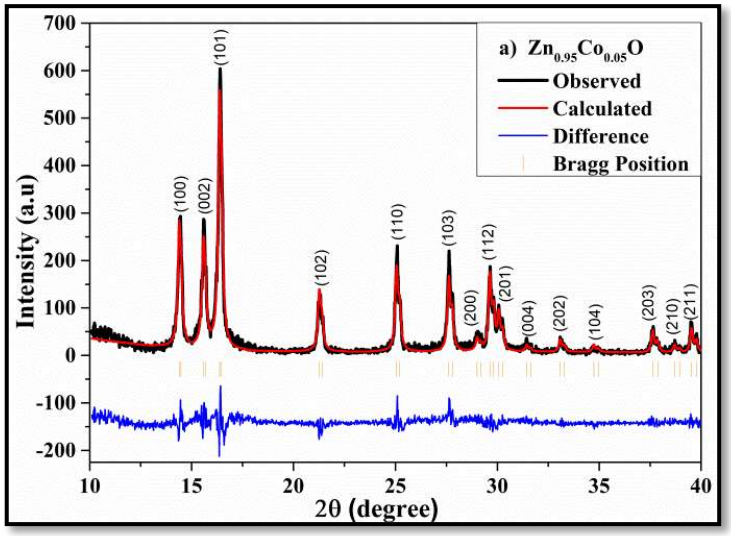

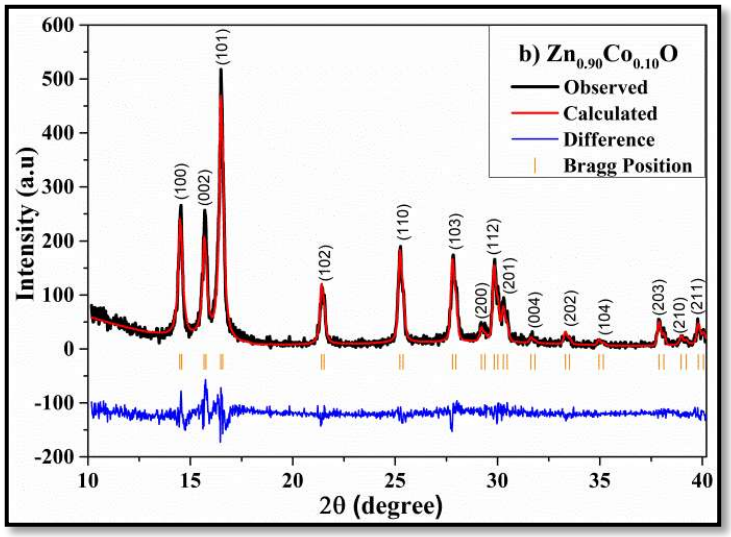

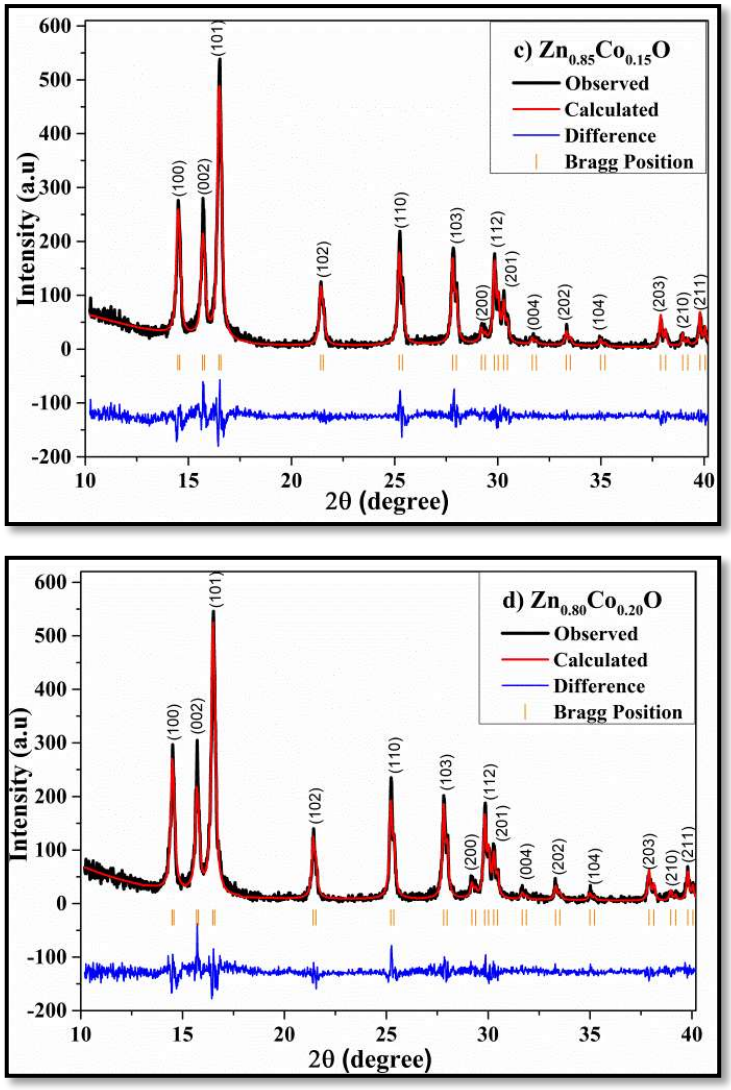

Figure 4.1.1.2: Rietveld refined XRD patterns of (a) $Zn_{0.95}Co_{0.05}O$, (b) $Zn_{0.90}Co_{0.10}O$, (c) $Zn_{0.85}Co_{0.15}O$, (d) $Zn_{0.80}Co_{0.20}O$.

Variation of lattice constant values '*a*' and '*c*', bond lengths '*l*' and cell volume 'V' are displayed in Figure 4.1.1.3, Figure 4.1.1.4, Figure 4.1.1.5 respectively. These are found to be in excellent agreement with the reported data [1-3]. Resemblance in the values of the inter planer distance'*d*', the lattice constants and the bond length with reported data authenticates the formation of monophasic wurtzite phase samples. This also verifies the successful substitution of Co^{2+} ions in place of Zn^{2+} ions sites in the ZnO matrix [1, 2, 4]. Dominance of <101> peak in all XRD patterns having higher intensity than that of the other peaks suggests superior growth of <101> direction along c-axis [5,6].

Table 4.1.1a: Comparison of '*d*' spacing from JCPDS-79-2205 with Rietveld refinement data obtained on nanoparticle $Zn_{(1-x)}Co_xO$ (x= 0.05, 0.10, 0.15, 0.20).

hkl	***d*** **spacing in Å**	***d* spacing in Å (Rietveld refinement)**			
		***x*= 0.05**	***x*= 0.10**	***x*= 0.15**	***x*= 0.20**
100	2.814	2.835	2.838	2.851	2.854
002	2.606	2.627	2.627	2.631	2.634
101	2.478	2.497	2.499	2.502	2.504
102	1.912	1.923	1.923	1.928	1.928
110	1.626	1.633	1.634	1.638	1639
103	1.478	1.484	1.484	1.486	1.489
200	1.408	1.413	1.416	1.417	1.421
112	1.379	1.384	1.385	1.388	1.388
201	1.359	1.243	1.308	1.247	1.310
004	1.302	1.096	1.100	1.099	1.101
202	1.239	1.046	1.049	1.049	1.049

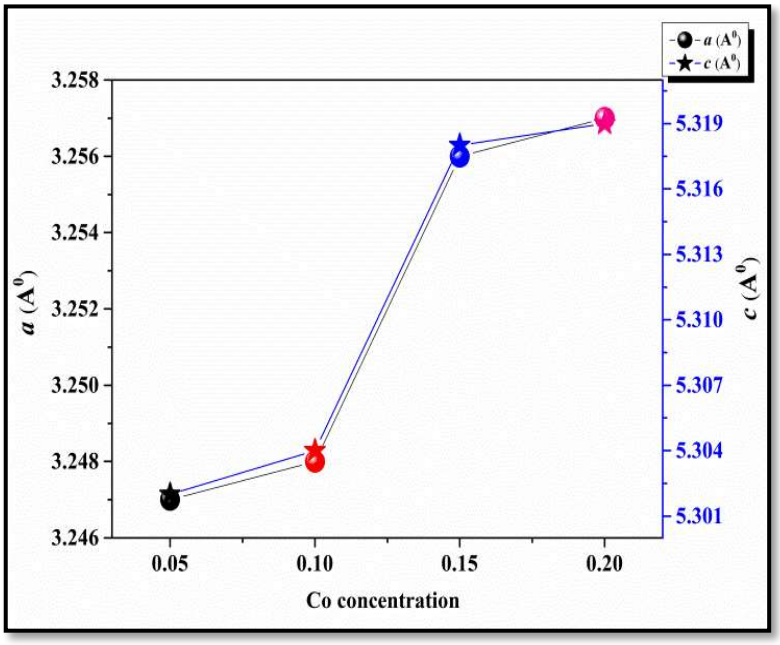

Figure 4.1.1.3: Variation of lattice constant *'a'* and *'c'* with Co concentration.

The sensitive variation of lattice parameters *'a', 'c'* with Co concentration '*x*' are presented in Figure 4.1.1.3. There is a small increase in both the lattice

constants *'a'* and *'c'* when '*x'* enhances from 0.05 to 0.10 and 0.15 to 0.20. However, there is a sturdy amplification in their values when *'x'* changes from 0.10 to 0.15 which is unique and fascinating behavior, such type of behavior are far from reported results. This type of variation is also observed in bond length parameter shown in Figure 4.1.1.4 and in cell volume as shown in Fig. 4.1.1.5. As per the Hermann–Mauguin information, the wurtzite structure ZnO has a hexagonal unit cell with lattice parameters *'c'* and *'a'* with the ratio of *c*/*a* = $(8/3)^{1/2}$ = 1.633 in an ideal case and affiliated to $P6_3mc$ space group. In the current analysis the *c*/*a* ratio equals to 1.632 for all the samples and is in excellent agreement with the ideal value. Rising mode of both the parameters *'a'* and *'c'* reveals that Co^{2+} has entered into the octahedral site in the wurtzite structure thereby giving rise to a disorder in the otherwise standard lattice. It may be noted that when Co^{2+} is in the octahedral state, the low spin state, it has ionic radius of 0.65Å but when in high spin state it has an ionic radius of 0.745Å both are larger than Zn^{2+} ionic radius of 0.60Å [4, 7].

The internal parameter *'u',* nearest neighbor Zn-O bond length '*l*', in wurtzite structure and the unit cell volume 'V' for the hexagonal structure are calculated using equation 4.1.1(a), 4.1.1(b) and 4.1.1(c).

$$\boldsymbol{u} = \frac{\mathbf{1}}{\mathbf{3}}\left(\frac{\boldsymbol{a^2}}{\boldsymbol{c^2}}\right) + \frac{\mathbf{1}}{\mathbf{4}} \qquad 4.1.1(a)$$

$$\boldsymbol{l} = \sqrt{\frac{\boldsymbol{a^2}}{\mathbf{3}} + \left(\frac{\mathbf{1}}{\mathbf{2}} - \boldsymbol{u}\right)^{\mathbf{2}} \boldsymbol{c^2}} \qquad 4.1.1(b)$$

$$\mathbf{V} = \frac{\mathbf{3}\sqrt{\mathbf{3}}}{\mathbf{2}}\ \boldsymbol{a^2 c} \qquad 4.1.1(c)$$

Bond length '*l*' and the unit cell volume 'V' variation with '*x*' are represented in Figure 4.1.1.4 and Figure 4.1.1.5. It may be seen that '*l*' increases from 1.988 Å to 1.994 Å whereas 'V' enhances from 145.263 $Å^3$ to 146.617 $Å^3$ as '*x*' increases from 0.05 to 0.20. The flare-up in these values with augmentation in '*x'* is essentially due to Co^{2+} mending in high spin state in octahedral state of the wurtzite structure during the material development process [8,9]. A close assessment of bond length *'l'*, cell volume 'V', and the lattice constants *'a'*, '*c'* reveals an identical increasing behavior as '*x'* enhances from 0.05 to 0.20 in the samples. This vital information provides the required conclusive validation that all of Co^{2+} added goes in to high spin state in the material.

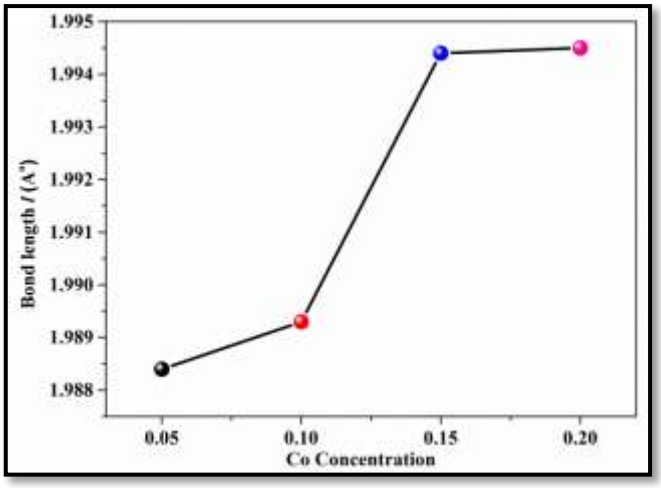

Figure 4.1.1.4: Variation of Bond length '*l*' with Co concentration.

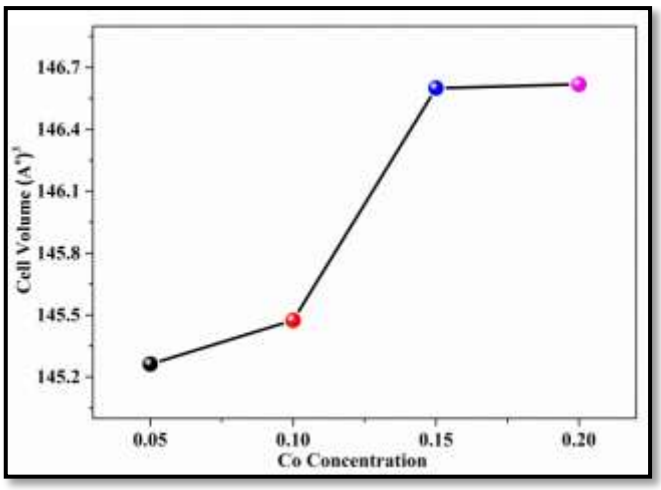

Figure 4.1.1.5: Variation of Unit Cell Volume 'V' with Co concentration.

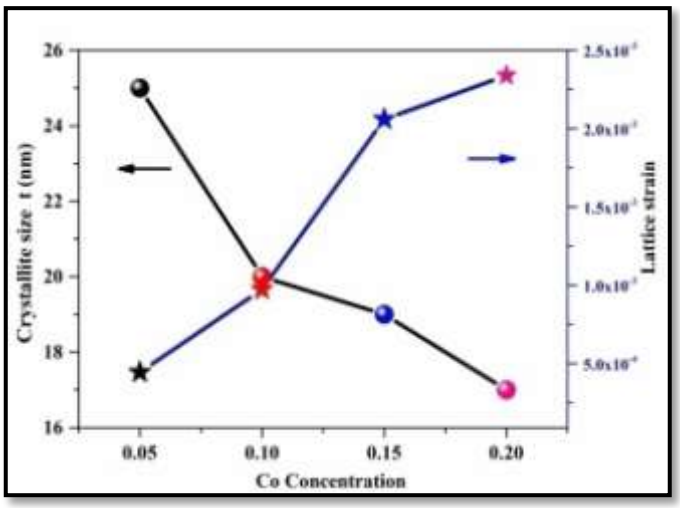

Figure 4.1.1.6: Variation of Crystallite size '*t*' and Lattice strain with Co concentration.

The crystallite size was determined using Williamson-Hall analysis and size-strain plot method using equation 4.1.1(d).

$$\boldsymbol{\beta cos\theta = \frac{k\lambda}{t} + 4\varepsilon sin\theta} \qquad 4.1.1(d)$$

Where, β is the X-ray diffraction peaks full width at half the maximum intensity in radians, θ is half of the angle 2θ at peak position in degrees, k is the shape factor and λ is the X-rays wavelength, *'t'* is the crystallite size in nm and ε is the strain. The values of $\beta cos\theta$ were plotted as a function of $4sin\theta$ and the intercept was employed to attain the crystallite size (t) [10,11]. The crystallite size *'t'* shown in Figure 4.1.1.6 with respect to '*x'* seems to decline with '*x'* which may be due to the fact that, the development of nanoparticles during the formation of the samples is weakened by slowing down the movement of the grain boundaries following increased pinning effect of fine pores in the samples [12,13]. When the moving boundaries attaches to the pores, the particle growth is stalled by generating a retarded force, a phenomenon termed as Zener-pinning effect. The retarding force created at the boundary is proportional to the boundary length connected to these ions and the pores. The highest force produced by a single pore on such a moving boundary is $F_{max} = \Pi r_p \gamma_b$, where γ_b is the grain boundary energy and r_p is the obstacle radius [13]. Thus the particle growth is halted when the retarded force overwhelms the driving force enforcing grain growth. Consequently the addition of Co^{2+} ions in the ZnO matrix creates obstructions for grain growth which enhances with Co concentration thereby subordinating grain size as shown in Figure 4.1.1.6. Therefore the enhancement of doping concentration indirectly assists in keeping a lower particle size.

4.1.2 Particle Size Estimation from SEM, TEM Micrographs and EDS Analysis

Scanning electron microscopy (SEM) and Transmission electron microscopy (TEM) are crucial instruments which give information about microstructure and assist in estimating the average particle size of the material. Room temperature SEM micrographs of the samples $Zn_{(1-x)}Co_xO$ (x = 0.05, 0.10, 0.15, 0.20) are displayed in Figure 4.1.2.1. The micrographs show agglomerates of the nanoparticles that are spherical in shape having typical particle size ranging from 25 nm to 55 nm. However an average particle size of 21±3 nm was obtained from

the TEM micrograph of the sample $Zn_{0.85}Co_{0.15}O$ shown in Figure 4.1.2.1 (e) estimated by using Image J software, over an ensemble size of 50 particles which is in good agreement with crystallite size obtained from XRD data. This analysis of SEM and TEM micrographs authenticates the formation of nanoparticle material.

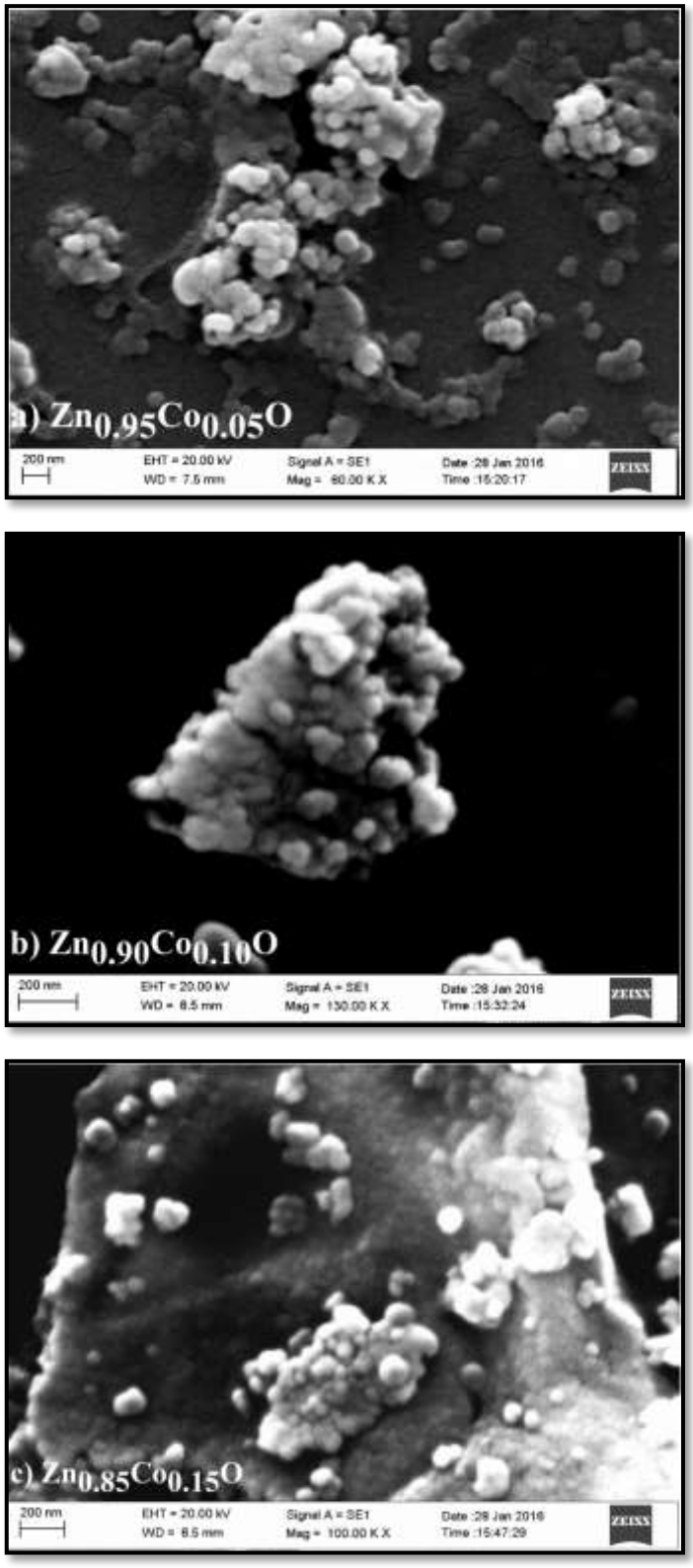

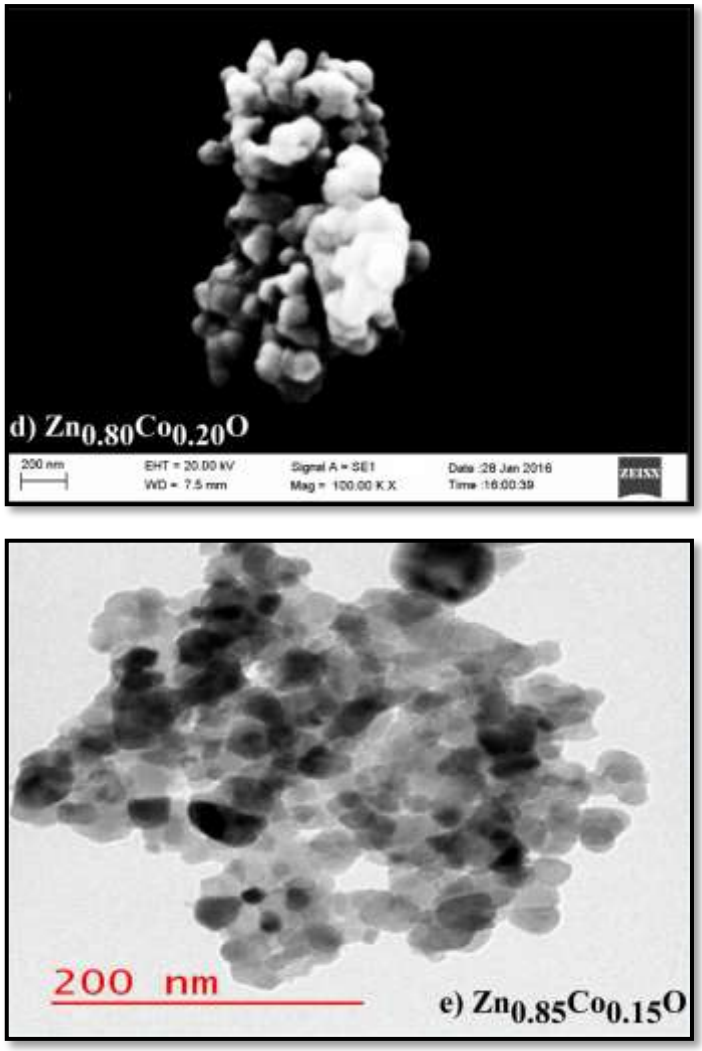

Figure 4.1.2.1: SEM micrographs of $Zn_{(1-x)}Co_xO$ with (a) x= 0.05, (b) x= 0.10, (c) x= 0.15, (d) x= 0.20 and e) TEM image of $Zn_{0.85}Co_{0.15}O$ at room temperature.

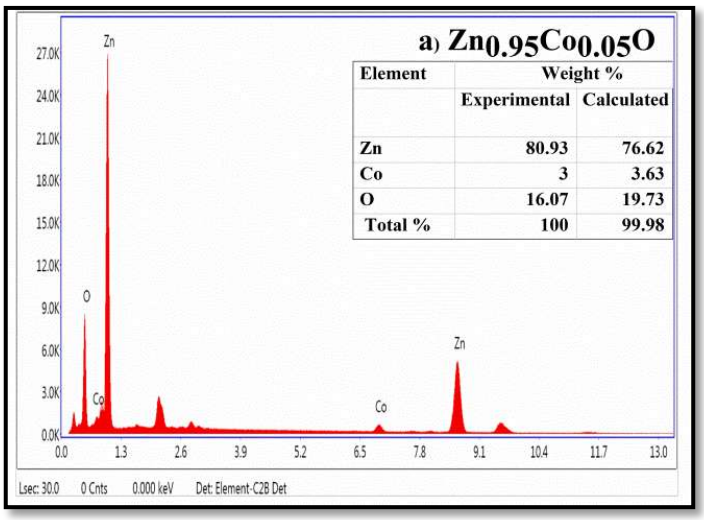

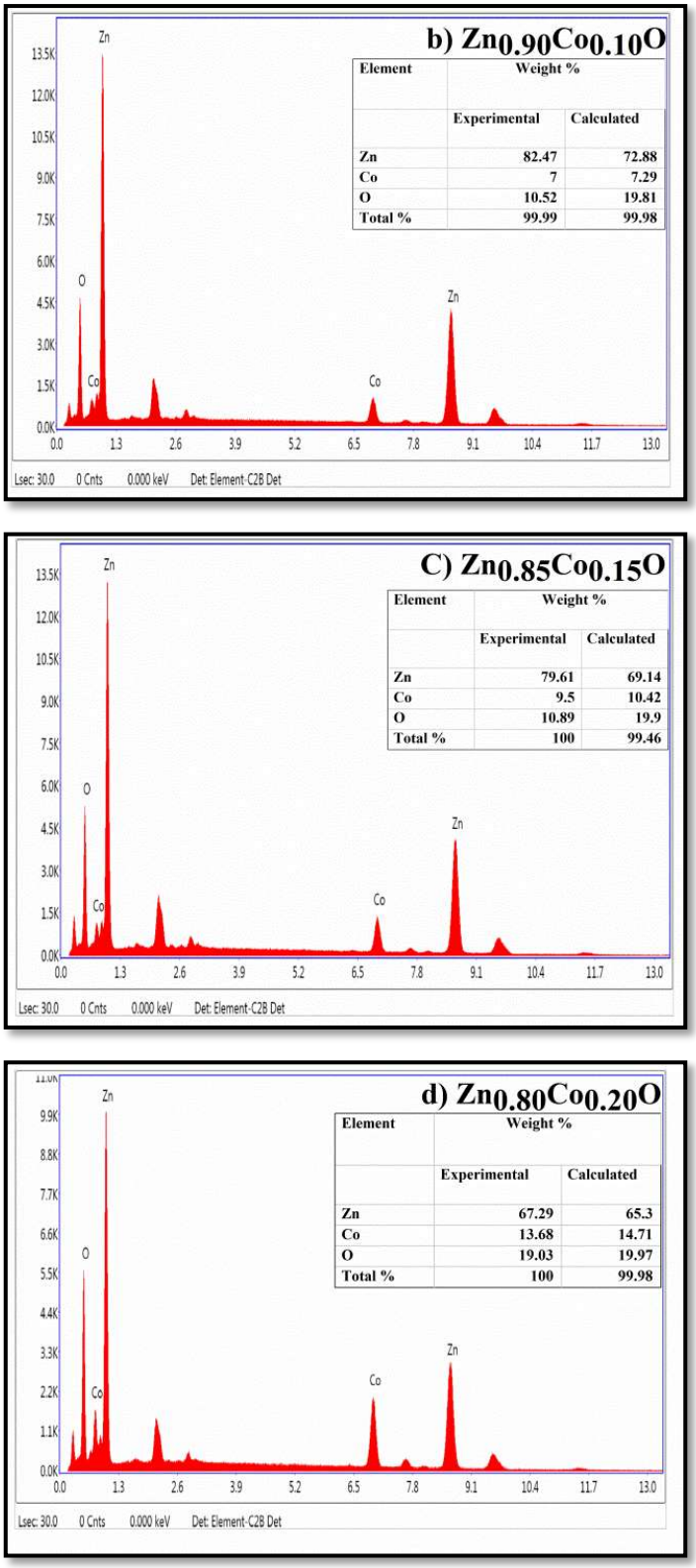

Figure 4.1.2.2: EDS analysis of $Zn_{(1-x)}Co_xO$ with (a) $Co_{0.05}O$, (b) $Co_{0.10}$, (c) $Co_{0.15}$, (d) $Co_{0.20}$.

The elemental composition of $Zn_{(1-x)}Co_xO$ with (a) x= 0.05, (b) x= 0.10, (c) x= 0.15, (d) x= 0.20 has been scrutinized using the energy dispersive spectroscopy

(EDS). Figure 4.1.2.2 displays the EDS spectra obtained on all the samples. The EDS pattern confirms the existence of Zn, Co and O elements with no other impurity element in the nanosamples. Experimental and calculated elemental weight percentages in all the samples showed in the inserts Figure 4.1.2.2 are in good agreement within the limits of experimental errors. Additionally EDS pattern also provides the required proof of successful substitution of Co^{2+} ions into the ZnO matrix ruling out the possibility of additional trace impurities entering the material.

4.1.3 Fourier Transform Infra-red Spectroscopy

Fourier Transform Infra-red spectroscopy (FTIR) is a fundamental tool in materials characterization which is proficient for identifying the presence of impurity traces in the freshly prepared materials. Different elemental bonds that exist in compounds vibrate/rotate at different frequencies that fall in infra-red region. Introduction of these types of materials to IR energy gives rise to resonance absorption bands in the FTIR spectra. KBr pellet method was used to record FTIR spectra of $Zn_{(1-x)}Co_xO$ (x = 0.05, 0.10, 0.15, 0.20) at room temperature. Several stretching and vibrational bonds can be known from the FTIR spectra presented in Figure 4.1.3.1.

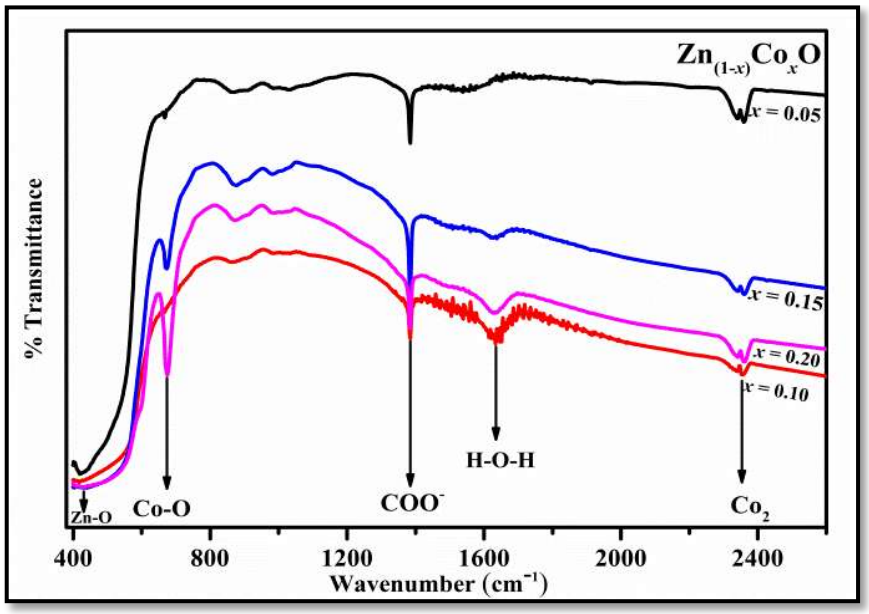

Figure 4.1.3.1: Fourier transforms infra red spectra for $Zn_{(1-x)}Co_xO$ (x= 0.05,0.10,0.15,0.20) at room temperature.

One can spot two main absorption bands first one in the range of 400 cm^{-1} to 576 cm^{-1} and the second in the range of 650 cm^{-1} - 700 cm^{-1}. These bands are credited to the Zn-O stretching bonds and Co-O vibrational bonds in the lattice. The appearance of second band is due to addition of Co^{2+} into the Zn−O lattice [14,15]. Additionally another set of three small absorption bands in the range of 1385 cm^{-1} to 1400 cm^{-1}, 1550 cm^{-1} – 1680 cm^{-1}, and 2280 cm^{-1} to 2390 cm^{-1}, can be also identified. The absorption band in between 1385 cm^{-1} to 1400 cm^{-1} corresponds to the asymmetrical and symmetrical stretching vibration of the carboxylate group (COO^-) that can be initiated from fuel Glycine [$NH_2.CH_2.COOH$] [3,16]. The sample for FTIR spectra was prepared by mixing it with hygroscopic KBr which results in an absorption band between 1550 cm^{-1} – 1680 cm^{-1} due to H-O-H bending vibration [17]. Absorption band in the range 2280 cm^{-1} to 2390 cm^{-1} corresponds to the bending of CO_2 molecule which is present in the air [17,18]. Therefore recognition of bonds like Zn-O and Co-O along with its characteristic vibrational frequencies from FTIR spectra confirms formation of impurity free monophasic sample.

4.2 Nd doped In_2O_3, $In_{(2-x)}Nd_xO_3$ (x = 0, 0.10, 0.15, 0.20)

4.2.1 X-Ray Diffraction Analysis

The sample phase purity and crystallite size calculations of $In_{(2-x)}Nd_xO_3$ with x = 0, 0.10, 0.15, 0.20 nanoparticles were done using X-ray diffraction data. Typical X-ray diffraction patterns for all the samples are shown in Figure 4.2.1.1 and rietveld refined XRD patterns obtained on the samples are shown in Figure 4.2.1.2. All the indexed XRD peaks shown in figure match well with the JCPDS card no. 71-2195, this proves the crystalline nature of the samples and authenticates the formation of monophasic cubic bixbyite or C type rare earth doped oxide structure (Space group Ia3) with no impurity peaks which could be analogous to existence of secondary phase [24].

The lattice constant values '*a*' and cell volume 'V' obtained on the samples are shown in Figure 4.2.1.3(a) and Figure 4.2.1.3(b) which is in good agreement with the reported data [20,21]. Consistency in the lattice constants '*a*' values with reported data confirms the formation of monophasic cubic phase samples, This also ensures the successful substitution of Nd^{3+} ions in place of In^{3+} ions sites inside In_2O_3 matrix [21,23].

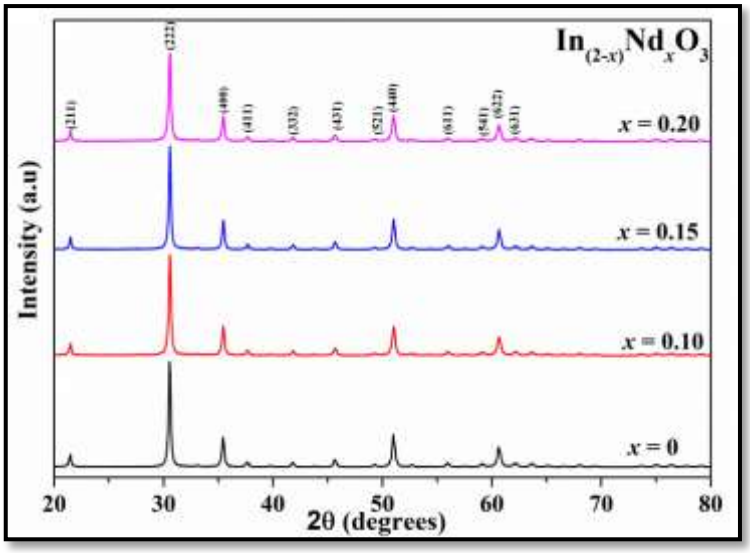

Figure 4.2.1.1: X-ray diffraction pattern for $In_{(2-x)}Nd_xO_3$ (x= 0, 0.10, 0.15, 0.20).

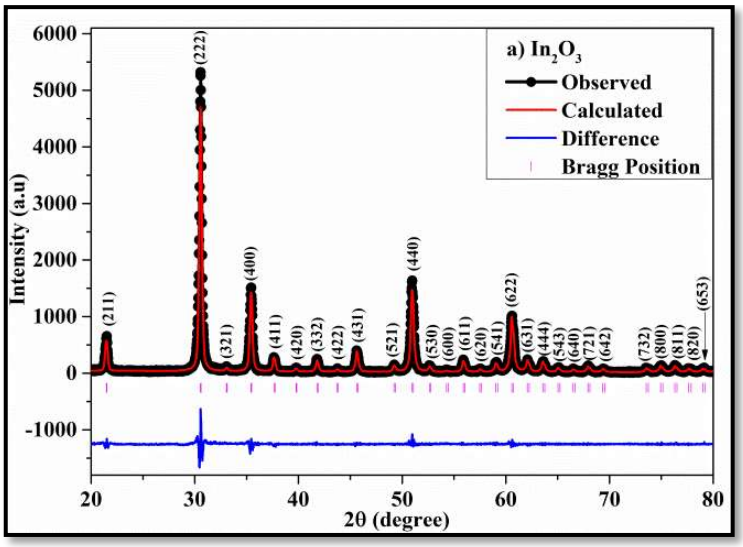

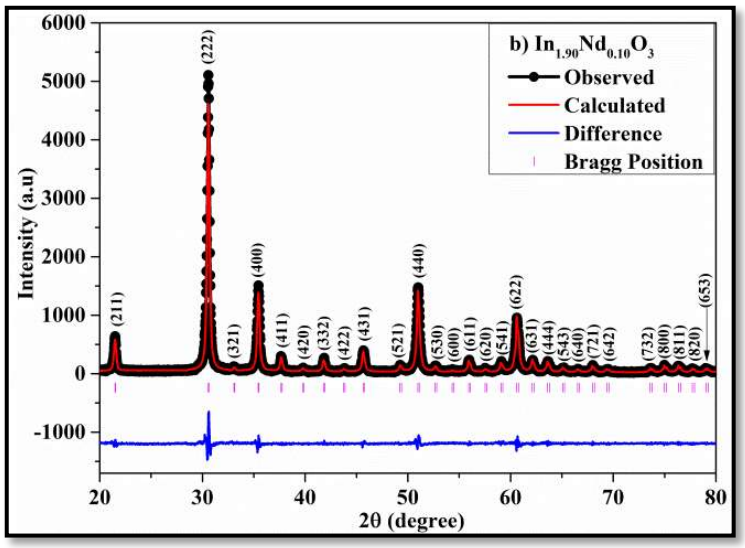

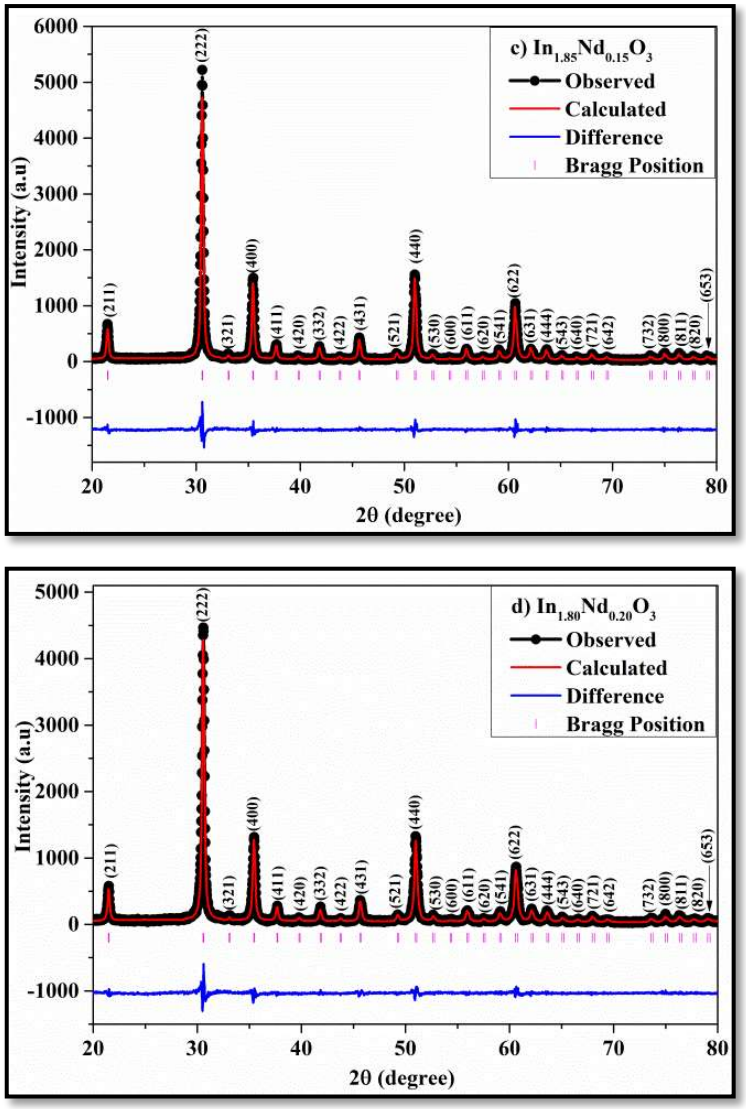

Figure 4.2.1.2: Rietveld refined X-ray of diffraction pattern of (a) In_2O_3, (b) $In_{1.90}Nd_{0.10}O_3$, (c) $In_{1.85}Nd_{0.15}O_3$, (d) $In_{1.80}Nd_{0.20}O_3$.

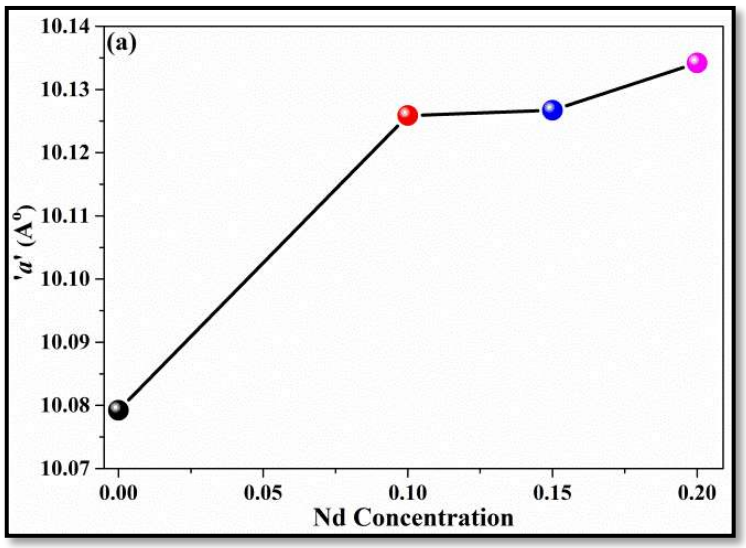

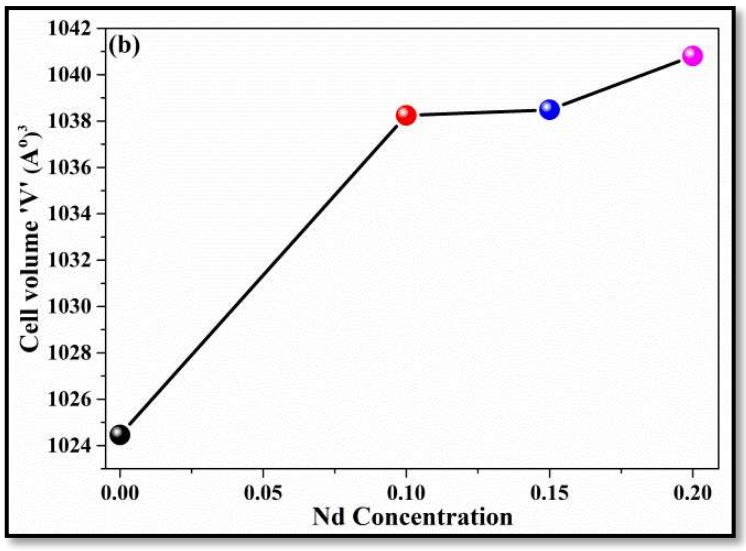

Figure 4.2.1.3: (a) Variation of lattice constant '*a*' with Nd concentration and (b) Variation of Cell volume 'V' with Nd concentration.

The lattice parameters *'a'* (*a*=*b*=*c*) Å for cubic bixbyite structure were calculated using equation 4.2.1(a) and is shown in Figure 4.2.1.3(a).

$$\frac{1}{d_{hkl}} = \frac{\sqrt{h^2 + k^2 + l^2}}{a} \qquad 4.2.1(a)$$

It may be seen from Figure 4.2.1.3(a) that the lattice parameters *'a'* enhance from 10.079 Å to 10.134 Å with increase in Nd^{3+} concentration '*x*'. This enlargement in lattice parameter '*a*' can be attributed to Nd^{3+} (1.12 Å) having larger ionic radii as compared to that of In^{3+} (0.94Å) [24]. The Cell volume of cubic structure were calculated using relation $\mathbf{V} = \boldsymbol{a^3}$. The cell volume was found to increases from 1024.45 $Å^3$ to 1040.80 $Å^3$ with increase in Nd^{3+} concentration as shown in Figure 4.2.1.3(b). This increase in cell volume 'V' specifies that cell volume is entirely dependable on the lattice parameter. Therefore this close inspection of both structural parameters having increasing trend of lattice parameter '*a*' and the cell volume 'V' with increase in '*x*' confirms successful substitution of Nd^{3+} into In_2O_3 cubic structure leading to a systematic structural disorder in the In_2O_3lattice [24].

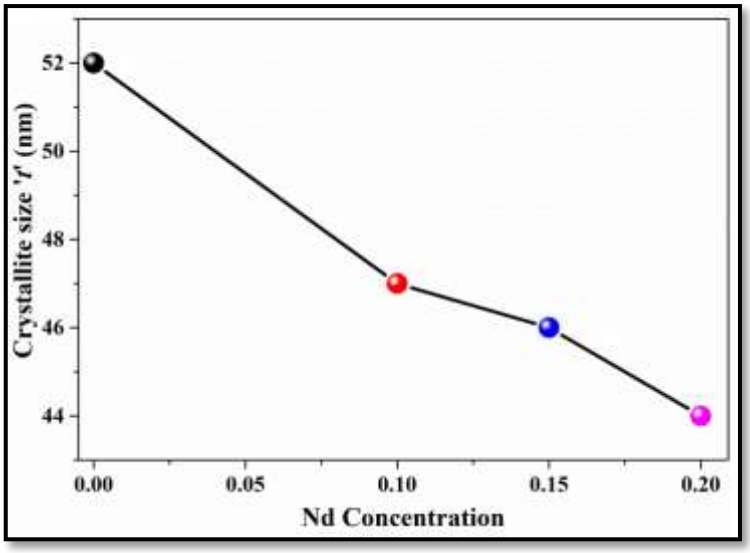

Figure 4.2.1.4: Variation of Crystallite size '*t*' with Nd Concentration.

$$\boldsymbol{\beta cos\theta = \frac{k\lambda}{t} + 4\varepsilon sin\theta} \qquad 4.2.1(b)$$

The Crystallite size was determined using Williamson-Hall method using equation 4.2.1(b) where, '*β'* is the full width at half the maximum FWHM intensity of the diffraction peaks in radians, and '*θ'* is the peak site angle in degrees, *k* is the shape factor, *λ* is the wavelength of X-rays (Cu K_α = 1.5418Å), *'t'* is the crystallite size in nm and '*ε'* is the strain [25]. Crystallite size calculation was made by plotting βcosθ verses *4sinθ*, in which the intercept was exploited to achieve the crystallite size '*t'*. Figure 4.2.1.4 shows dwindling of crystallite size behavior from 52 nm to 44 nm with raise in Nd^{3+} concentration. The reduction in crystallite size 't' could be due to the difficulty in the grain growth of the crystallites during sample formation process. This course of action can be explained by zener-pinning effect [12,13].

4.2.2 Particle Size Estimation From SEM, TEM Micrographs and EDS Analysis

SEM micrographs of $In_{(2-x)}Nd_xO_3$ with x = 0.10, 0.20 nanoparticles obtained at room temperature are shown in Figure 4.2.2.1(a) and Figure 4.2.2.1(b). The SEM micrographs show agglomerates of spherically shaped nanoparticles having particle size ranging from 60 nm to 70 nm. However TEM micrograph in Figure 4.2.2.1(c) displays In_2O_3 nanoparticles with an average particle size of 54±3 nm

achieved by using Image J software for an ensemble of 40 particles, which is in concurrence with crystallite size achieved from XRD data.

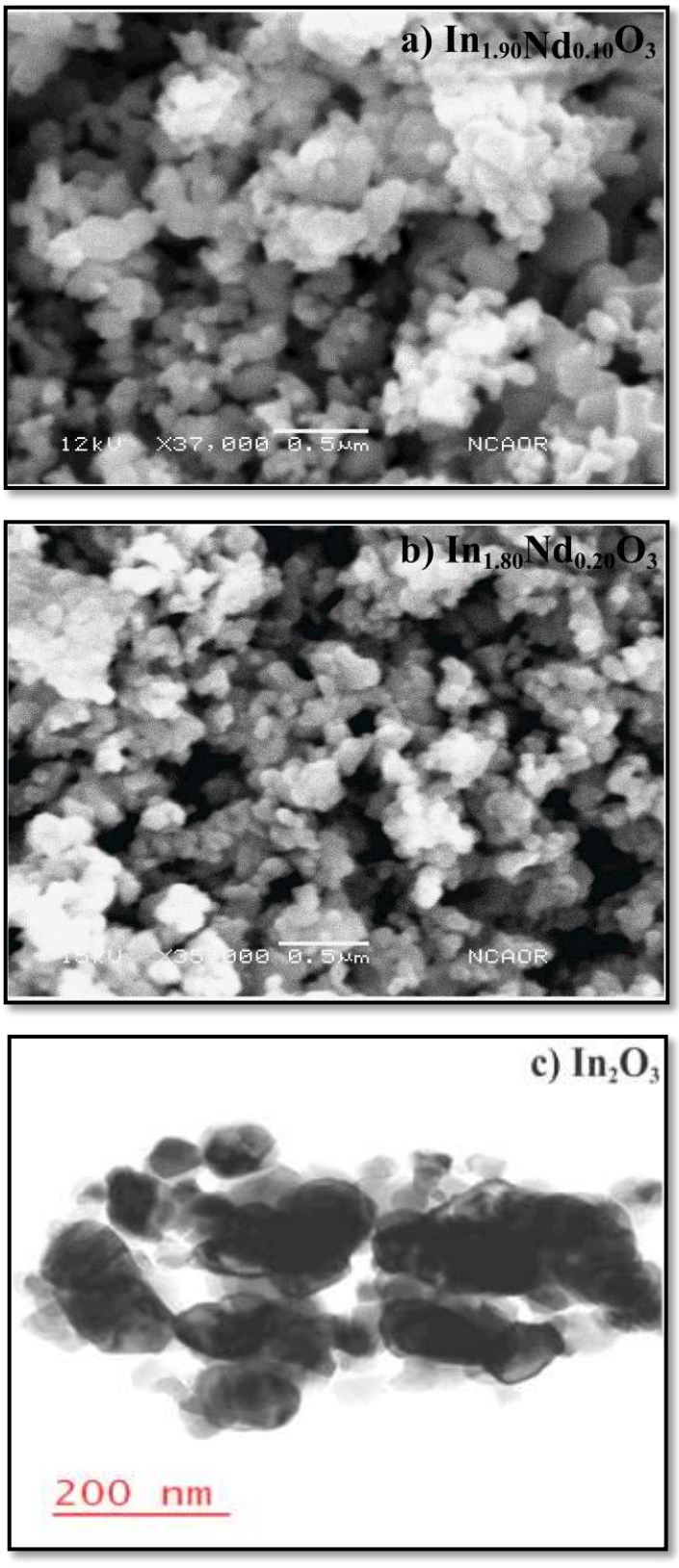

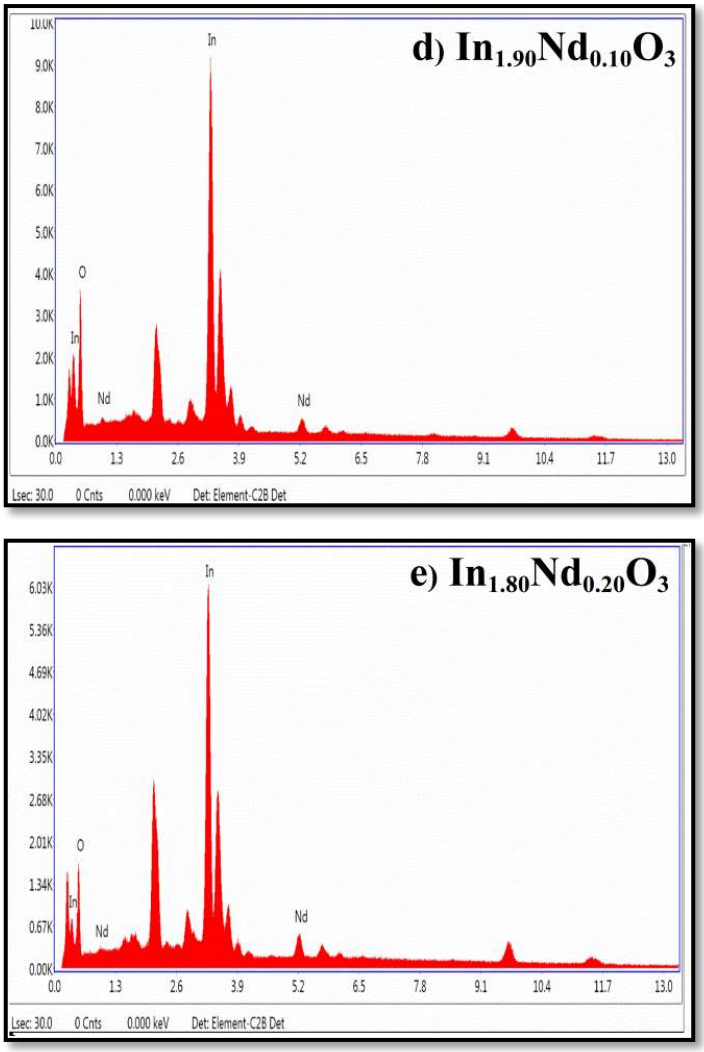

Figure 4.2.2.1: SEM micrographs of (a) $In_{1.90}Nd_{0.10}O_3$, (b) $In_{1.80}Nd_{0.20}O_3$, (c) TEM image of In_2O_3 and EDS analysis of (d) $In_{1.90}Nd_{0.10}O_3$, (e) $In_{1.80}Nd_{0.20}O_3$ at room temperature.

The elemental composition of $In_{(2-x)}Nd_xO_3$ with x = 0.10, 0.20 nanosamples examined using the energy dispersive X-ray spectroscopy (EDX) is given in Figure 4.2.2.1(d) and Figure 4.2.2.1(e). The EDX spectrum shows the presence of In, Nd and O elements in the prepared samples. The extra peaks obtained are Au and Pd peaks that occur because of sputtering of these materials on the samples for obtaining EDX spectra. Elemental weight percentages obtained from EDX spectra and theoretically calculated values of all the samples shown in Table 4.2.1(a) and are found to be in good agreement for Nd however percentages for In and O differ which could be due to EDX technique itself. Reports suggest that error occurs as EDX is a surface based technique which does not provide full

information of the entire sample. Thus the identification of the compositional elements in the samples by EDX spectra confirms absence of impurity elements in all the samples. Thus EDX analysis confirms successful substitution of Nd^{3+} ions into the In_2O_3 matrix without any traces of impurity.

Table 4.2.1a: Experimental and Calculated weight percentage values for $In_{(2-x)}Nd_xO_3$ with x = 0.10, 0.20

$In_{1.90}Nd_{0.10}O_3$			**$In_{1.80}Nd_{0.20}O_3$**		
Elements	**Weight %**		**Elements**	**Weight %**	
	Experimental	**Calculated**		**Experimental**	**Calculated**
In	63.82	77.75	**In**	67.12	72.89
Nd	5.27	5.14	**Nd**	11.61	10.17
O	30.46	17.10	**O**	21.26	16.92
Total %	99.55	99.99	**Total %**	99.99	99.98

4.2.3 Fourier Transform Infra-Red Spectroscopy

Figure 4.2.3.1(a) represents the Fourier transform infrared spectrum of $In_{(2-x)}Nd_xO_3$ (x = 0, 0.10, 0.15, 0.20) nanoparticles. Broad band in the range of 408 cm^{-1} - 505 cm^{-1} and well resolved absorption bands at 536 cm^{-1}, 563 cm^{-1}, and 601 cm^{-1} can be observed which are the characteristic bands of cubic phase in cubic bixbyite In_2O_3 structure shown in Figure 4.2.3.1(b). Bands in the range of 408 cm^{-1} - 505 cm^{-1}, at 536 $cm^{-1}$and 563 cm^{-1} are attributed to the In–O stretching bands [26, 27], in addition to these peaks band at 601 cm^{-1} is observed which is attributed to In–O bending band in cubic bixbyite In_2O_3 structure [27]. The appearance of intense band in the range of 628 cm^{-1} - 634 cm^{-1} are due to addition of Nd^{3+} into the In_2O_3 lattice [28]. This insight examination of FTIR spectroscopy verifies that Nd^{3+} ions have successfully substituted at In^{3+} ions position in the In_2O_3 matrix with impurity free monophasic sample. Furthermore, an additional four set of absorption bands from 1480 cm^{-1} to 1520 cm^{-1}, 1620 cm^{-1} - 1676 cm^{-1}, 2303 cm^{-1} to 2410 cm^{-1} and 3333 cm^{-1} to 3556 cm^{-1} could be also identified. The absorption band in between 1480 cm^{-1} to 1520 cm^{-1} corresponds to the asymmetrical and symmetrical stretching vibration of the carboxylate group (COO^-) that might be originating from fuel (Glycine) [29]. As the sample for

FTIR spectra is organized by mixing prepared sample with KBr which is hygroscopic there is always some amount of H_2O present which appears as an absorption band between 1620 cm^{-1} - 1676 cm^{-1} due to H-O-H bending vibration in the spectra [30]. Absorption band in the range 2303 cm^{-1} to 2410 cm^{-1} corresponds to the bending of CO_2 molecule and weak band observed in the range 3333 cm^{-1} to 3556 cm^{-1} which is assigned to the stretching and bending vibrations due to presence of the O-H molecule in the air [31,32].

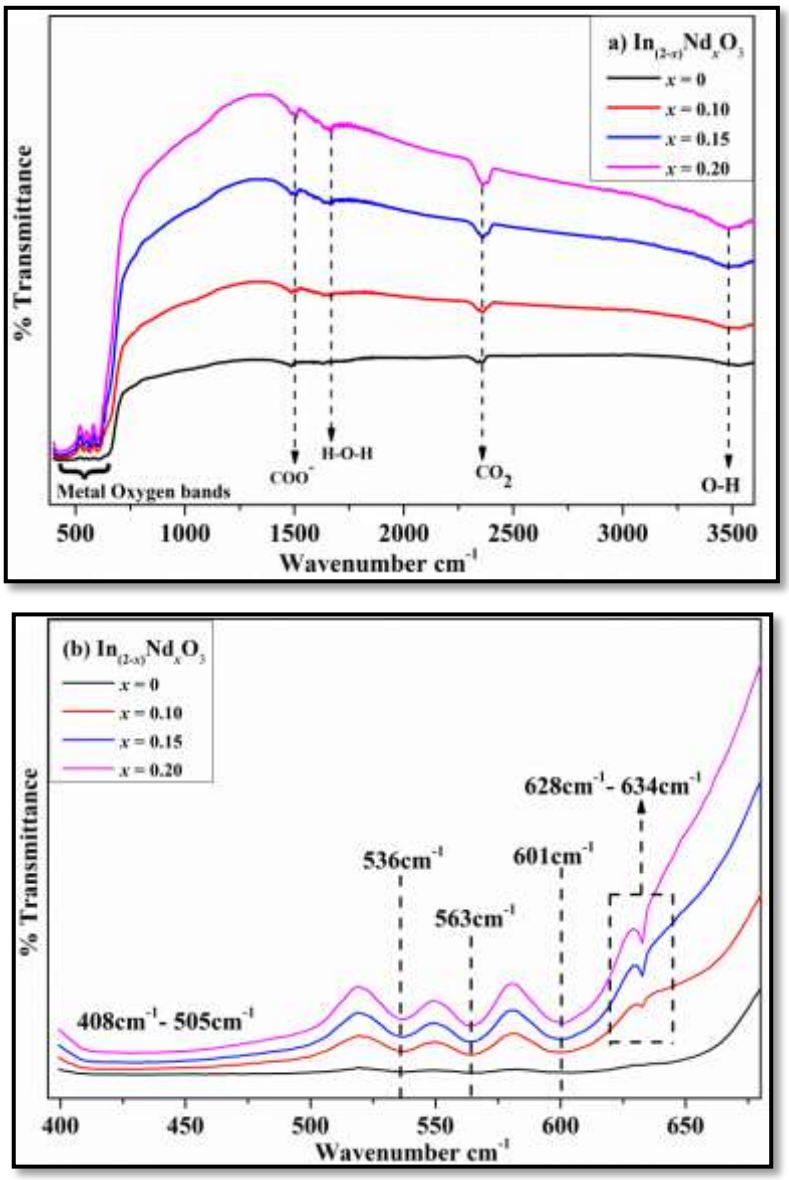

Figure 4.2.3.1: (a) Fourier transforms infra red spectra for $In_{(2-x)}Nd_xO_3$(x= 0, 0.10, 0.15, 0.20) at room temperature and (b) Fourier transforms infra red spectra in the fingerprint region for $In_{(2-x)}Nd_xO_3$ (x= 0,0.10,0.15,0.20).

4.3 Ni doped CuO, $Cu_{(1-x)}Ni_xO$ (x = 0, 0.05, 0.10, 0.15, 0.20, 0.25, 0.30)

4.3.1 X-Ray Diffraction Analysis

X-ray diffraction investigation of $Cu_{(1-x)}Ni_xO$ (x = 0, 0.05, 0.10, 0.15, 0.20, 0.25, 0.30) nanoparticles were carried out to study the crystalline nature and the purity of the samples. Figure 4.3.1.1 shows the XRD patterns of all the samples and the rietveld refinement of XRD patterns done using FullProf suite of all the samples are shown in Figure 4.3.1.2. All the indexed XRD peaks match well with the JCPDS card No. 65–2309 that confirms the formation of monophasic monoclinic crystalline structure with space group C2/c [33,34]. Metallic traces such as NiO, Cu_2O or Cu_3O_4 were not observed in the XRD pattern which confirms that the prepared samples are impurity free samples. This XRD analysis suggests that Ni^{2+} ions have successfully substituted at Cu^{2+} site in CuO matrix [35].

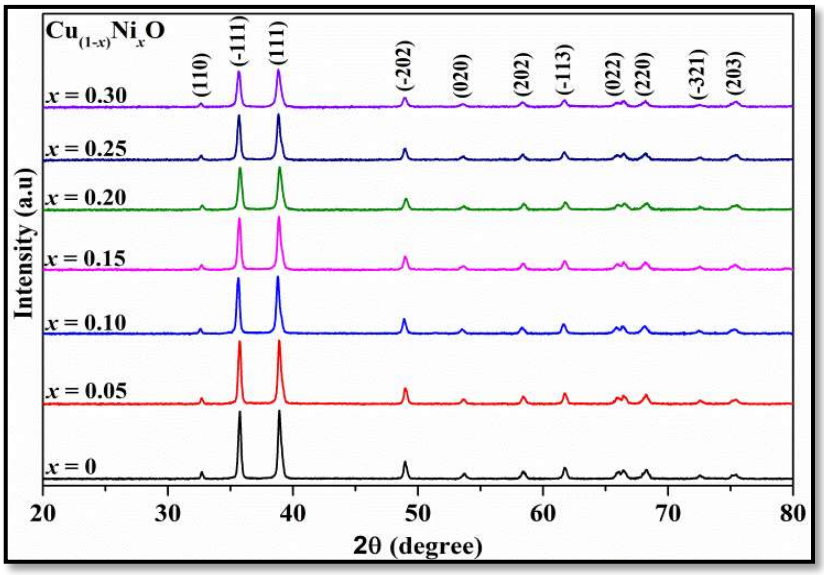

Figure 4.3.1.1: X-ray of diffraction pattern of $Cu_{(1-x)}Ni_xO$ with x = 0, 0.05, 0.10, 0.15, 0.20, 0.25, 0.30.

The lattice parameter '*a*', '*b*', '*c*' and the Cell volume 'V' variation of the monoclinic crystal structure of all the samples are shown in Figure 4.3.1.3 and Figure 4.3.1.4. The calculation of lattice parameter values was done using Rietveld profile fitting technique for all the samples as shown in Figure 4.3.1.3 and the Cell volume 'V' was calculated using equation 4.3.1(a).

$$\mathbf{V} = \boldsymbol{abc}\sin\boldsymbol{\beta} \qquad 4.3.1(a)$$

Where '*a*', '*b*', '*c*' are lattice parameter and 'β' is the interfacial angle.

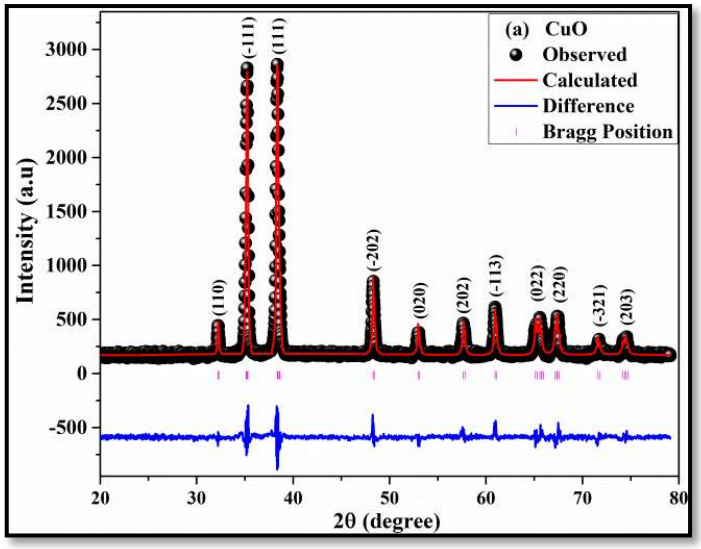
(a) CuO
Observed
Calculated
Difference
Bragg Position
Intensity (a.u)
2θ (degree)
(110)
(-111)
(111)
(-202)
(020)
(202)
(-113)
(022)
(220)
(-321)
(203)

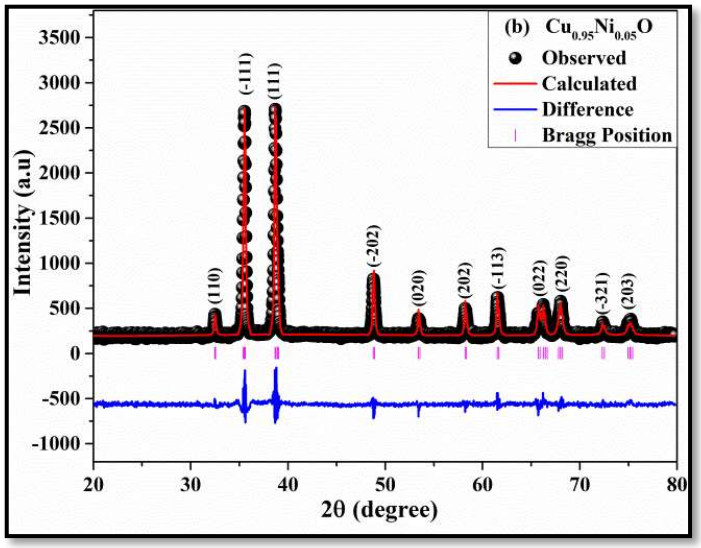
(b) Cu0.95Ni0.05O
Observed
Calculated
Difference
Bragg Position
Intensity (a.u)
2θ (degree)
(110)
(-111)
(111)
(-202)
(020)
(202)
(-113)
(022)
(220)
(-321)
(203)

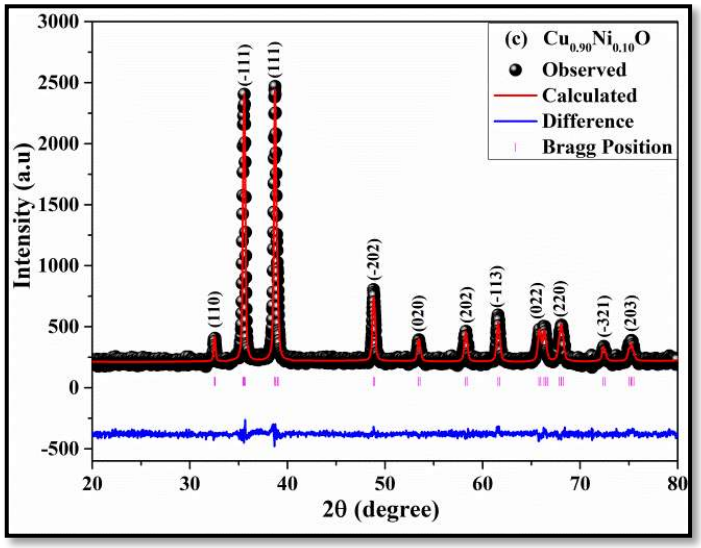
(c) Cu0.90Ni0.10O
Observed
Calculated
Difference
Bragg Position
Intensity (a.u)
2θ (degree)
(110)
(-111)
(111)
(-202)
(020)
(202)
(-113)
(022)
(220)
(-321)
(203)

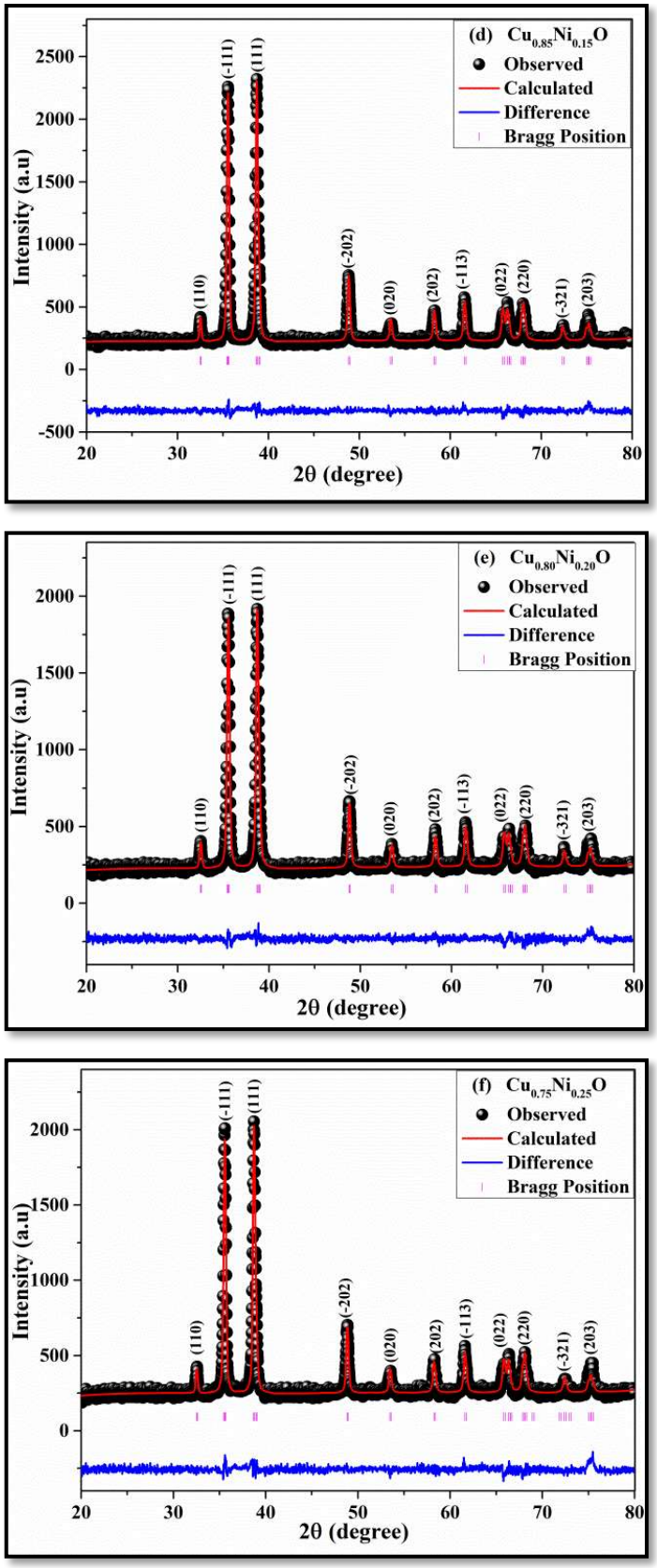
(d) Cu0.85Ni0.15O
Observed
Calculated
Difference
Bragg Position
Intensity (a.u)
2θ (degree)
(110)
(-111)
(111)
(-202)
(020)
(202)
(-113)
(022)
(220)
(-321)
(203)
(e) Cu0.80Ni0.20O
Observed
Calculated
Difference
Bragg Position
Intensity (a.u)
2θ (degree)
(f) Cu0.75Ni0.25O
Observed
Calculated
Difference
Bragg Position
Intensity (a.u)
2θ (degree)

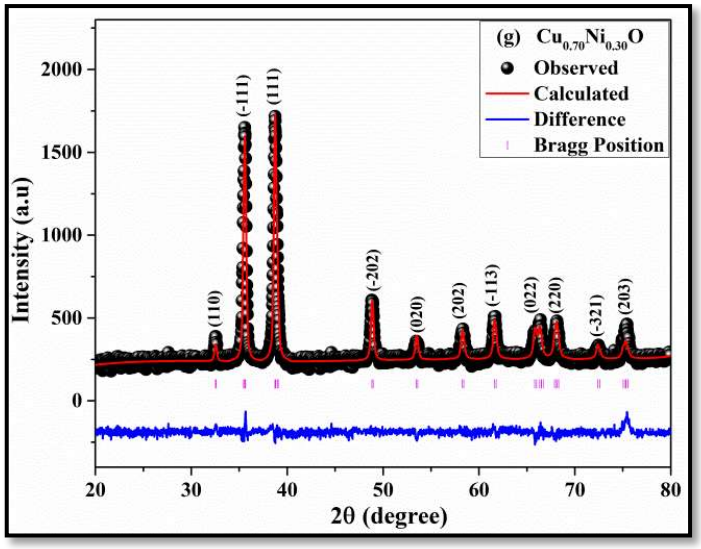

Figure 4.3.1.2: Rietvield refined X-ray of diffraction pattern of (a) CuO, (b) $Cu_{0.95}Ni_{0.05}O$, (c) $Cu_{0.90}Ni_{0.10}O$, (d) $Cu_{0.85}Ni_{0.15}O$, (e) $Cu_{0.80}Ni_{0.20}O$, (f) $Cu_{0.75}Ni_{0.25}O$, (g) $Cu_{0.70}Ni_{0.30}O$.

Increment or reduction of the crystal lattice depends on the ionic radii of the magnetic dopant ions and the host ions. The reduction in lattice parameter with increase in Ni^{2+} concentration is due to the substitution of Ni^{2+} ions (0.69Å) which is having smaller ionic radii with Cu^{2+} ions (0.73Å) which is having larger ionic radii [36,37]. Furthermore it may be observed from Figure 4.3.1.4 that the Cell volume reduces from 81.39 $Å^3$ to 81.14 $Å^3$ as the Ni^{2+} content increases from 0 to 0.30. Since the cell volume is dependent on the lattice parameter '*a*', '*b*', '*c*' and the interfacial angle '*β*', as a result the Cell volume reduces with Ni^{2+} concentration. The variation of interfacial angle '*β*' with Ni^{2+} concentration is shown in inset of Figure 4.3.1.4. The subordination of lattice parameter and the cell volume with Ni^{2+} concentration confirms the successful doping of Ni^{2+} ions in CuO matrix [38,39].

$$\boldsymbol{\beta cos\theta = \frac{k\lambda}{t} + 4\varepsilon sin\theta} \qquad 4.3.1(b)$$

The Crystallite size was determined using Williamson-Hall method using equation 4.3.1(b) where, '*β*' is the full width at half the maximum FWHM intensity of the diffraction peaks in radians, and '*θ*' is the peak site angle in degrees, *k* is the shape factor, *λ* is the wavelength of X-rays (Cu K_α = 1.5418Å), '*t*' is the crystallite size in nm and '*ε*' is the strain. Crystallite size estimation was done by plotting βcosθ verses *4sinθ*, and the intercept was utilized to obtain the

crystallite size *'t'*. Figure 4.3.1.5 shows the decreasing crystallite size behavior from 78 nm to 48 nm with raise in Ni^{2+} concentration. The decreases in crystallite size't' can be due to the difficulty in the grain growth of the crystallites during sample formation process. This course of action can be explained by zener-pinning effect [12,13].

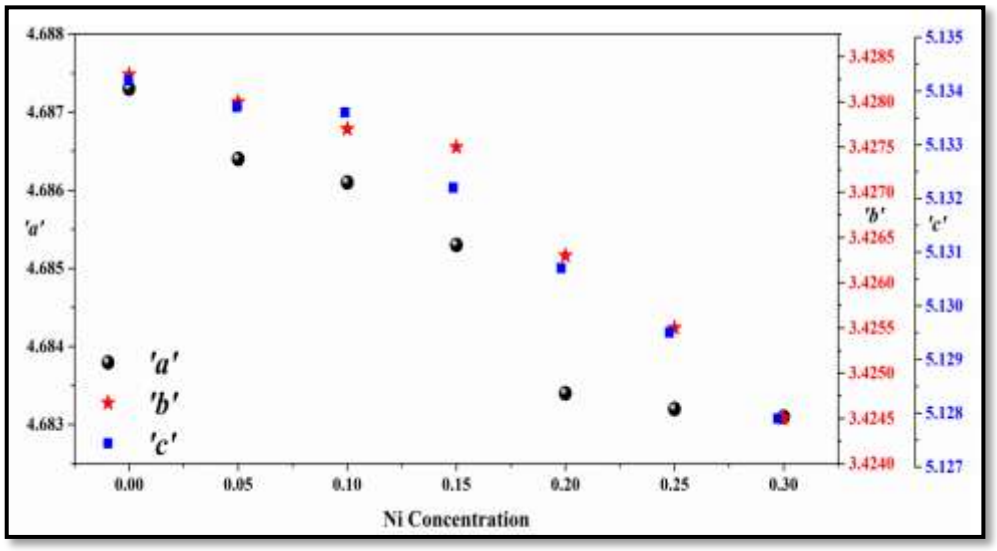

Figure 4.3.1.3: Variation of lattice parameter *'a', 'b', 'c'* with Ni concentration.

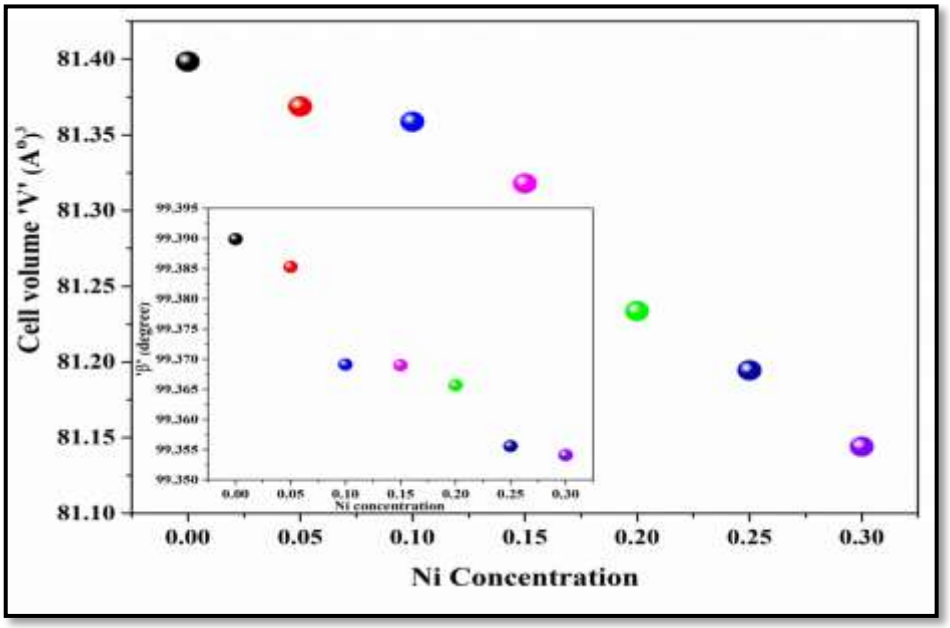

Figure 4.3.1.4: Variation of Cell Volume 'V' with Ni concentration.

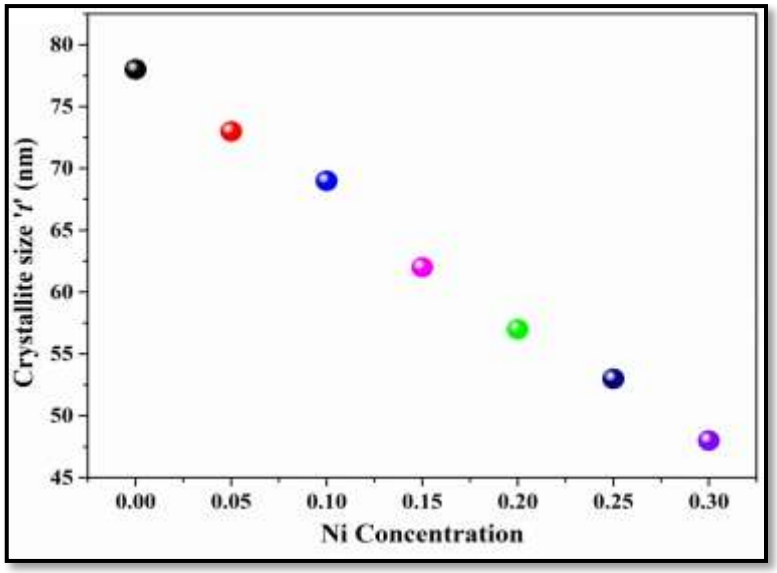

Figure 4.3.1.5: Variation of crystallite size *'t'* with Ni concentration.

4.3.2 Particle Size Estimation from SEM, TEM Micrographs and EDS Analysis

Room temperature SEM micrographs of the sample $Cu_{(1-x)}Ni_xO$ (x = 0.10 and 0.20) are shown in Figure 4.3.2.1(a) and Figure 4.3.2.1(b). The SEM micrographs shows agglomerates of the nanoparticles which are spherical in shape with typical particle size ranging from 80 nm to 70 nm, this estimation were made using Image J software, over an ensemble size of 40 particles is in good agreement with crystallite size obtained from XRD data. The elemental composition of $Cu_{0.90}Ni_{0.10}O$ and $Cu_{0.80}Ni_{0.20}O$ has been analyzed using the energy dispersive spectroscopy (EDS).

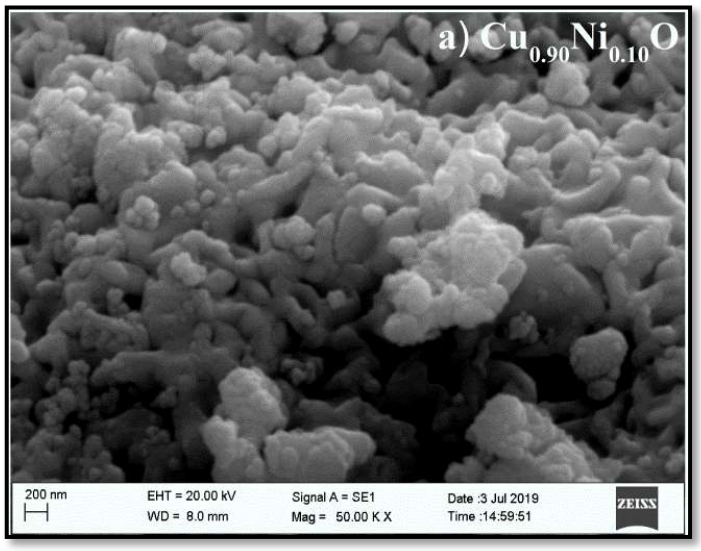

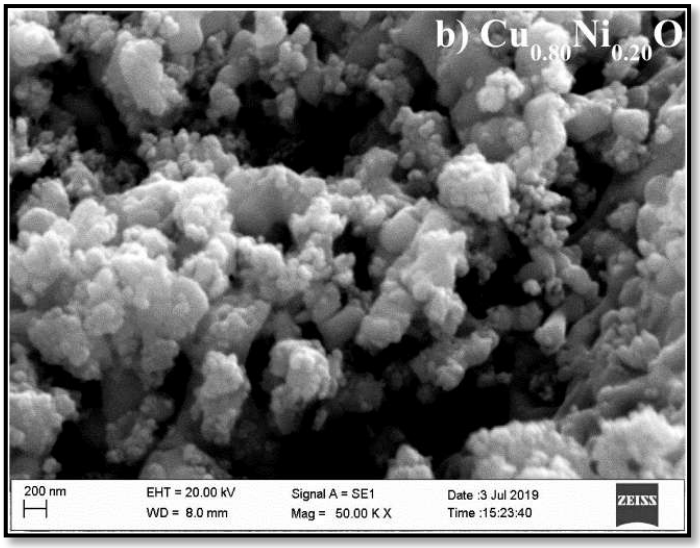
b) $Cu_{0.80}Ni_{0.20}O$
200 nm
EHT = 20.00 kV
WD = 8.0 mm
Signal A = SE1
Mag = 50.00 K X
Date :3 Jul 2019
Time :15:23:40
ZEISS

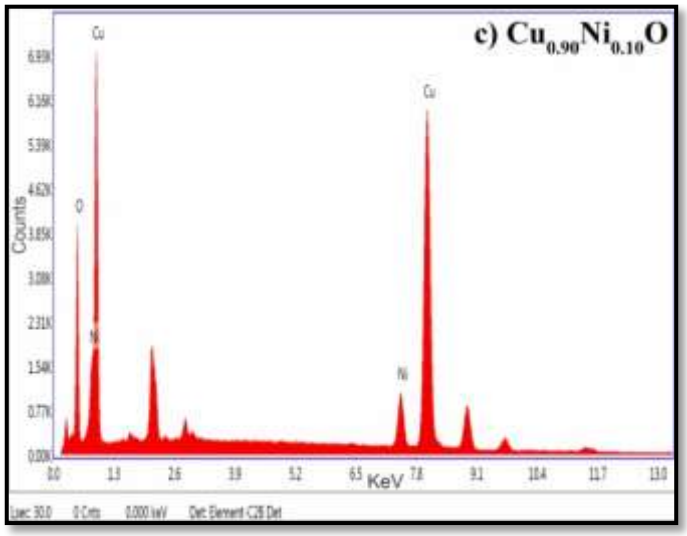
c) $Cu_{0.90}Ni_{0.10}O$
Cu
O
Ni
Cu
Ni
Counts
KeV

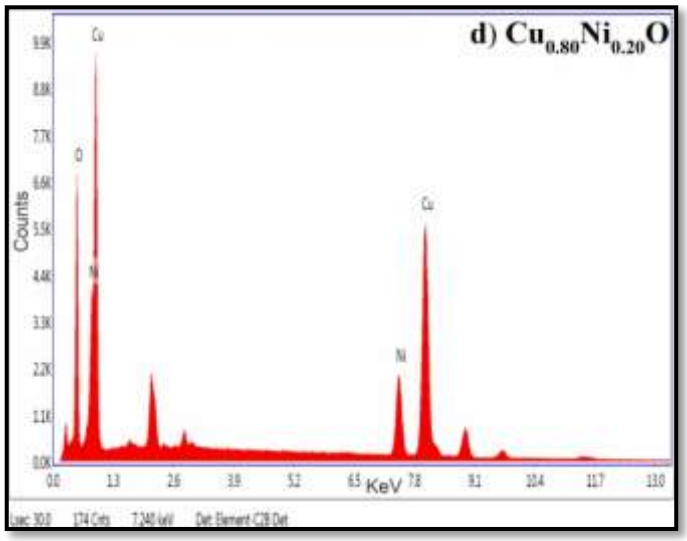
d) $Cu_{0.80}Ni_{0.20}O$
Cu
O
Ni
Cu
Ni
Counts
KeV

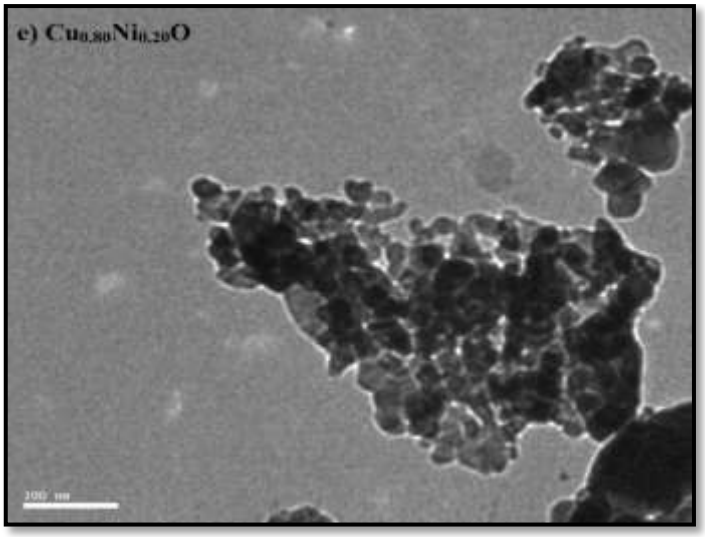

Figure 4.3.2.1: SEM micrographs of (a) $Cu_{0.90}Ni_{0.10}O$, (b) $Cu_{0.80}Ni_{0.20}O$, and EDS analysis of (c) $Cu_{0.90}Ni_{0.10}O$, (d) $Cu_{0.80}Ni_{0.20}O$ (e) TEM image of $Cu_{0.80}Ni_{0.20}O$.

The EDS spectra obtained on all the samples are shown in Figure 4.3.2.1(c) and Figure 4.3.2.1(d). The EDS pattern verifies the presence of Cu, Ni and O elements with no other impurity element in the nanosamples. Experimental and calculated elemental weight percentages values for all the samples are tabulated in Table 4.3.1(a) which are in good agreement within the limits of experimental errors. SEM and EDS pattern further gives the evidence of successful substitution of Ni^{2+} ions into the CuO matrix with no additional impurity trace within the EDS resolution limit. The TEM micrograph in Figure 4.3.2.1(e) shows $Cu_{0.80}Ni_{0.20}O$ nanoparticles with an average particle size of 42±3 nm as attained by using Image J software for an cluster of 50 particles, which is in good agreement with crystallite size calculated from XRD data.

Table 4.3.1a: Experimental and Calculated weight percentage values for $Cu_{(1-x)}Ni_xO$ with x = 0.10, 0.20

$Cu_{0.90}Ni_{0.10}O$			**$Cu_{0.80}Ni_{0.20}O$**		
Elements	**Weight %**		**Elements**	**Weight %**	
	Experimental	**Calculated**		**Experimental**	**Calculated**
Cu	69.82	72.34	**In**	52.81	64.70
Ni	8.16	7.42	**Nd**	14.38	14.93
O	22.02	20.23	**O**	32.81	20.36
Total %	100	99.99	**Total %**	100	99.99

4.3.3 Fourier Transform Infra-red Spectroscopy

Figure 4.3.3.1 (a) shows the Fourier transform infrared spectrum of $Cu_{(1-x)}Ni_xO$ (x = 0, 0.05, 0.10, 0.15, 0.20, 0.25, 0.30) nanoparticles. The strong absorption band around 513 cm^{-1} to 532 cm^{-1} and broad absorption band in the range of 567 cm^{-1} to 600 cm^{-1} and 660 cm^{-1} to 673 cm^{-1} assign to the stretching vibration band of Cu-O [40, 41]. The absorption band in the range of 443 cm^{-1} to 461 cm^{-1} related to the Ni-O vibration band [42] which occurs due to replacement of Cu^{2+} ions by Ni^{2+} ions in the CuO matrix as shown in Figure 4.3.3.1 (b). Furthermore, another two set of absorption bands could be also identified in the range of 1359 cm^{-1} to 1396 $cm^{-1}$and 2337 cm^{-1} to 2386 cm^{1}. The absorption band in between 1359 cm^{-1} to 1396 cm^{-1} corresponds to Corresponds to the asymmetrical and symmetrical stretching vibration of the carboxylate group i.e COO^- could be due to the presence of partially burnt fuel [16]. Absorption band seen in the range of 2337 cm^{-1} to 2386 cm^{1}corresponds to the bending vibration of CO_2 molecule that is present in the air [18]. Therefore the above information authenticates the formation of monophasic Ni-doped CuO nanoparticles.

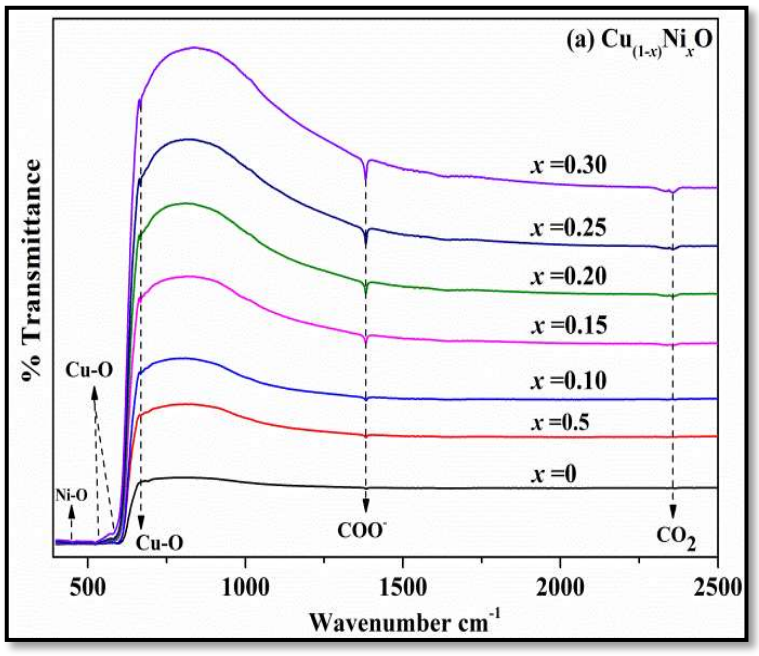

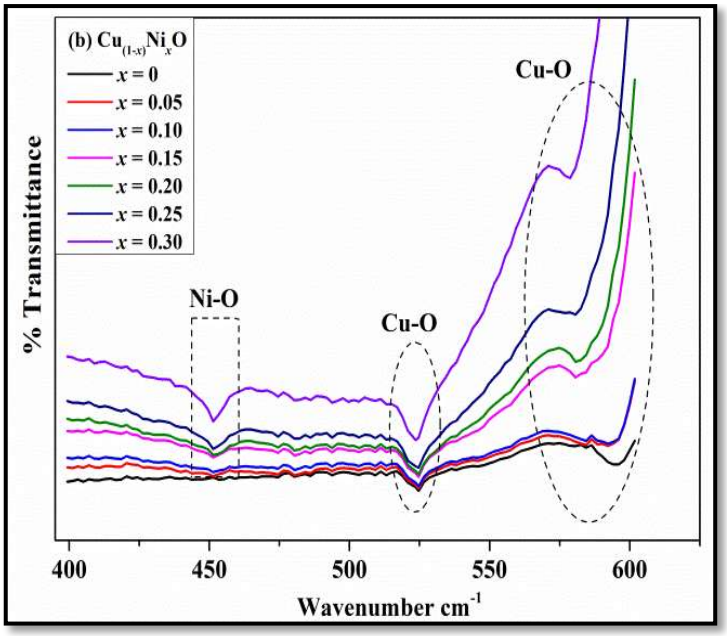

Figure 4.3.3.1: (a) Fourier transforms infra red spectra for $Cu_{(1-x)}Ni_xO$ (x = 0, 0.05, 0.10, 0.15, 0.20, 0.25, 0.30) at room temperature and (b) Fourier transforms infra red spectra in the fingerprint region for $Cu_{(1-x)}Ni_xO$ (x = 0, 0.05, 0.10, 0.15, 0.20, 0.25, 0.30).

References:

[1] M. Nirmala, Anukaliani, Physica B 406 (2011) 911–915.

[2] V.Pazhanivelu, A. Paul Blessington Selvadurai, Yongsheng Zhao, R. Thiyagarajan, R. Murugaraj, Physica B 481 (2016) 91–96.

[3] H. Rongliang, Bin Tang, Cuong Ton-That, Matthew Phillips, Takuya Tsuzuki, J Nanopart Res 15 (2013).

[4] U. Godavarti, V.D. Mote, Journal of Asian Ceramic Societies (2017).

[5] J. Liang Zhao, J. Mater. Res 21 (2006) 2185–2190.

[6] S. Kumar, C.L. Chen, C.L. Dong, Y.K. Ho, J.F. Lee, T.S. Chan, R. Thangavel, T.K. Chen, B.H. Mok, S.M. Rao, M.K. Wu, J mater sci 48 (2013) 2618–2623.

[7] O.D. Jayakumar, I.K. Gopalakrishnan, S.K. Kulshreshtha, J. Mater. Chem. 15 (2005) 3514–3518.

[8] S. Udayakumar, V. Renuka, K. Kavitha Structural, J. Chem. Pharm. Res. 4 (2) (2012) 1271–1280.

[9] A.K. Srivastava, R. Gakhar, P. Dua, K. Senthil, J.S. Tawale, K.N. Sood, K. Yong, Microscopy: Science, Technology, Applications and Education, (1820).

[10] K. Hellal Harbbi, Ahmed alaa Ihsan, Advances In Physics Theories And App lications 49 (2015).
[11] H. Sarma, K.C. Sarma, International Journal of Scientific And Research Publications 4 (2014).
[12] S. Singhal, Japinder Kaur, Tsering Namgyal, Rimi Sharma, Physica B 407 (2012) 1223–1226.
[13] R.W. Kelsall, I.W. Hamley, M. Geoghegan, Nanoscale Science and Technology, John Wiley & Sons, 2006.
[14] H. Kumar, Renu Rani, Physics and Astronomy 14 (2013) 26–36.
[15] P. Davide Cozzoli, M. Lucia Curri, andAngela Agostiano, J. Phys. Chem. B 107 (2003) 4756−4762.
[16] G. Xiong, U. Pal, J.G. Serrano, K.B. Ucer, R.T. Williams, Phys Stat Sol C 3 (2006) 3577–3581.
[17] A. B. Lavand, Yuvraj S. Malghe, Journal Of King Saud University – Science (2016).
[18] H. Yao-Ming, Shi-Yun Lou, Shao-Min Zhou, Rui-Jian Yuan, Gong-Yu Zhu, Li Ning, Nanoscale Research Letters 7 (2012) 100.
[19] R. Mukherji, Vishal Mathur, Arvind Samariya, Manishita Mukherji, journal of nano- and electronic physics, 9 (2017) 3.
[20] N. Sai Krishna , S. Kaleemulla, G. Amarendra, N. Madhusudhana Rao, C. Krishnamoorthi, M. Kuppan, M. Rigana Begam, D. Sreekantha Reddy, I. Omkarame, Materials Research Bulletin, 61 (2015) 486–491.
[21] M. Thirumoorthi, J. Thomas Joseph Prakash, Journal of Asian Ceramic Societies, 4 (2016) 124–132.
[22] S. Dussan , M. K. Singh , A. Kumar & R. S. Katiyar, 125 (2011) 155–161.
[23] G. Z. Xing, J. B. Yi, F. Yan, T. Wu, and S. Li, Applied Physics Letters 104 (2014) 202411.
[24] L. Zhanpeng, Junran Zhang, Wei Niu, Minhao Zhang, Li Song, Hairong Zhu and Xuefeng wang, Chinese physics B, 25 (2016) 9.
[25] K. Y. Salkar, R.B. Tangsali, R.S. Gad, M. Jeyakanthan, Uma Subramanian, Superlattices and Microstructures 126 (2019) 158–173.
[26] P. Song, Dan Han, Huihui Zhang, Jia Li, Zhongxi Yang, Qi Wang, Sensors and Actuators B 196 (2014) 434–439.

[27] E. Nirmala, I. Kartharinal Punithavathy, S. Johnson Jeyakumar and M. Jothibas, J. Nano. Adv. Mat, 5 (2017) 11-16.

[28] S. Mortazavi-Derazkola, Sahar Zinatloo-Ajabshir, Masoud Salavati-Niasari, J Mater Sci: Mater Electron (2015).

[29] M. Z. Naik, S. N. Meena, S. C. Ghadi, M. M. Naik, A. V. Salker, Med Chem Res, 25 (2016) 381–389.

[30] E.C.C. Souza, J.F.Q. Rey, E.N.S. Muccillo, Applied Surface Science, 255 (2009) 3779–3783.

[31] A. A. Resheedi, Norah Saad Alhokbany, Refaat Mohammed Mahfouz, Acetate Materials Research, 17 (2014) 346-351.

[32] Z. Fang, H. Assaaoudi, R. I.L. Guthrie, J.A. Kozinski, J. Am. Ceram. Soc, 90 (2007) 2367–2371.

[33] N. Kumaresan , K Ramamurthi, S Mathuri , M Maria Angelin Sinthiya , T Manimozhi , Mahesh Mudaliar Margoni , R Rameshbabu, International Journal of ChemTech Research, 7 (2014-2015) 1598-1602.

[34] M.Z. Sahdan, M.F. Nurfazliana, S.A. Kamaruddin, Z. Embong, Z. Ahmad, H. Saim, Procedia Manufacturing, 2 (2015) 379 – 384.

[35] A. E. Morsy , M. Rashad, N. M. Shaalan and M.A. Abdel-Rahim, Micro and Nanosystems, 11 (2019).

[36] S. Al-Amri, M. Shahnawaze Ansari , Saqib Rafique , Musab Aldhahri , Sawsan Rahimuddin , Ameer Azam and Adnan Memic, Current Nanoscience, 11 (2015).

[37] S. Baturay, Ahmet Tombak, Derya Kaya, Yusuf Selim Ocak, Murat Tokus, Murat Aydemir, Tahsin Kilicoglu, J Sol-Gel Sci Technol, 78 (2016) 422–429.

[38] N.M. Basith, Vijaya JJ, Kennedy LJ, Bououdina M, Material Science and Semiconductor Processing, 17 (2014) 110–118.

[39] A.K. Prakash Chand, Anurag Gaur, Applied Science Letter, 1 (2015) 115–124.

[40] F. M Khan, S.B Rahman, Jamal A, Umar A, Material Letters, 2011, 65(9), 1400-1403.

[41] D.P. Dubal, Gund G.S, Lokhande C.D, Holze R, Mater. Res. Bull., 2013, 48(2), 923-928.

[42] F. Davar, Zeinab Fereshteha, Masoud Salavati-Niasari Nanoparticles, Journal of Alloys and Compounds 476 (2009) 797–801.

CHAPTER 5

Optical properties of Co doped ZnO, Nd doped In_2O_3 & Ni doped CuO Dilute Magnetic Semiconductor Nanoparticles

Introduction

UV visible spectroscopy is a useful technique as one can obtain important information about energy band gap of the semiconductor material. In the current chapter we have reported energy band gap studies of Co doped ZnO, Nd doped In_2O_3 and Ni doped CuO nanoparticles samples. Besides, outcome of photoluminescence and photoluminescence lifetime studies carried out on Co doped ZnO nanoparticle samples which are considered to be a DMS material of utmost importance are also explicated here.

5.1 Co doped ZnO, $Zn_{(1-x)}Co_xO$ (x = 0.05, 0.10, 0.15, 0.20)

5.1.1 UV-Visible Spectroscopy

Room temperature UV absorption spectra of the samples $Zn_{(1-x)}Co_xO$ (x = 0.05, 0.10, 0.15, 0.20) measured in the wavelength range from 300nm - 800nm is shown in Figure 5.1.1.1 (a). These measurements were carried out to explore the consequence of Co^{2+} doping on the band gap of the material ZnO with an added advantage of confirming the substitution of Co^{2+} in the ZnO structure. It is seen that UV absorbance is highest for lower Co^{2+} concentration and decreases slowly on escalating Co^{2+} concentration in ZnO matrix. It is well-known that the overall UV absorbance depends on factors like lattice strain, crystallite size, oxygen deficiency, impurity centers, surface roughness, agglomeration of the nanoparticles etc [1]. It was seen from Figure 4.1.1.6 in chapter IV that there is an increase in lattice strain with increase in Co^{2+} concentration 'x' which restricts the crystallite growth thereby reducing the crystallite size in the sample. Therefore decrease in crystallite size ultimately results in decline in UV absorption and the same is reflected in the energy band gap of the material. Secondly PL investigation shows reduction in peak intensities with increasing 'x' that implies that oxygen deficiency in the samples dwindles as Co^{2+} content increases in the samples. Additionally, X-ray and EDS supports the formation of impurity free samples. As a result these assessments provide satisfactory evidence of reduction in UV absorbance with increasing Co^{2+} concentrations in the samples [1,2].

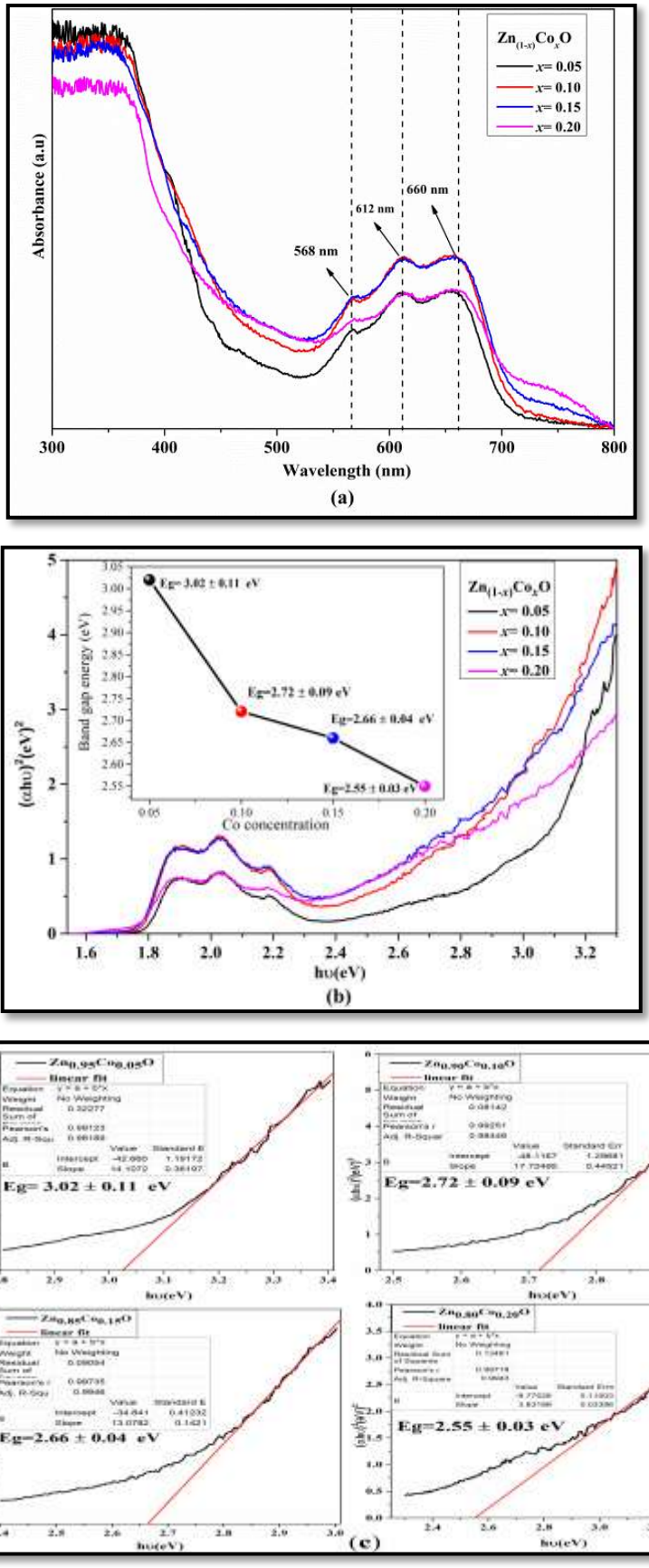

Figure 5.1.1.1: (a) UV absorbance spectra, (b) Plots of $(\alpha h\nu)^2$ versus photon energy (hν), (c) linear regression fit for $Zn_{(1-x)}Co_xO$ (x = 0.05, 0.10, 0.15, 0.20).

It may be seen that additional three humps at 568 nm (2.18eV), 612 nm (2.03eV) and 660 nm (1.88eV) are observed for all samples as shown in Figure 5.1.1.1 (a). Occurrence of these three humps can indisputably attributed to d-d electronic transitions which take places from the ground state $^4A_2$ to $^2A_1$, $^4T_1$ and $^2E_1$ state for the tetrahedral Co^{2+} ions [3,4]. The existence of Co^{2+} in high spin state at tetrahedral environment is known to create lattice distortion which is furthermore confirmed by X-ray studies [5]. The existence of these three peaks in the visible region indicates the successful inclusion of Co^{2+} ions in the Zn^{2+} tetrahedral sites of the ZnO matrix [3-5]. A random UV absorption effect is observed in case of absorption by d-d transition levels in the samples. Samples with x = 0.05, 0.20 show lower absorption then samples with x = 0.10, 0.15. This variation in absorbance may be due to factors like particle size, reduction in impurity centers, surface roughness and agglomeration of particles that cannot be controlled by any nanoparticle materials preparation method.

The energy band gap for Co-doped ZnO samples was estimated from Tauc's plots as per equation 5.1.1 (a) in which A is constant, hυ the photon energy, E_g is the energy band gap, n = ½ and n = 2 for allowed direct and indirect transitions respectively [6].

$$(\alpha h\upsilon) = A\,(h\upsilon - Eg)^n \qquad 5.1.1(a)$$

Figure 5.1.1.1 (b) displays Tauc's plots $(\alpha h\upsilon)^2$ Vs $h\upsilon$ for the samples with the inset showing corresponding direct band gap energy values obtained. These accurate band gap values of Co-doped ZnO were obtained using linear regression fit at higher energy values taken from tauc's plots as shown in Figure 5.1.1.1 (c). The highest energy band gap value E_g=3.02 ± 0.11 eV at x=0.05 was found to decrease linearly to a value of E_g=2.55 ± 0.03 eV at x=0.20 therefore increasing the optical wavelength which is an signal of a red shift in the band gap [7,8]. The lessening in energy band gap with Co^{2+} concentration [insert in Figure 5.1.1.1 (b)] is attributable to the exchange interaction among the d-localized electrons of Co^{2+} atoms and the s-p band electrons of ZnO [9, 10].

5.1.2 Photoluminescence Analysis

Room temperature photoluminescence (PL) emission spectra of the sample $Zn_{(1-x)}Co_xO$ (x = 0.05, 0.10, 0.15,0.20) obtained with an excitation wavelength of 318 nm is shown in Figure 5.1.2.1. Generally, the overall PL intensities trail a

decreasing pattern as the Co^{2+} concentration enhances in the sample. The sample $Zn_{0.95}Co_{0.05}O$ shows most intense PL spectra with a wide broadening in the greenish-yellow area. The emission spectrum for higher values of Co^{2+} concentration are improved and found to explain specific peaks in different colour regions in place of a broad spread seen between 500nm to 600nm. The emission wavelengths and its peak intensities are seen to become sharper and separate with a minor slide down in overall intensities. The dissimilarity of the most intense peak intensities for wavelengths namely 410nm, 466nm, 547 – 550 nm and 579nm as a function of Co^{2+} concentration '*x'* are shown in Figure 5.1.2.2. The dwindle in PL intensity observed is due to the formation of defect states below the conduction band that shrinks with increasing '*x*' in the ZnO matrix. Some of the electrons excited from valence band slow down at the defect states without reaching the conduction band [11] ending up in decreased PL intensity. It can be seen that for a particular concentration, green emission is the most intense emission except for sample with $x = 0.05$ where greenish-yellow emission takes the maximum intensity.

The PL emission peaks in three different regions namely violet, blue and green given in Table 5.1.1(a), have been observed for all the samples. Zinc oxide by itself has a large band gap (3.3 eV) which goes on declining from 3.02 ± 0.11 eV to 2.55 ± 0.03 eV due to the adding up of Co^{2+} in the ZnO matrix. The PL emission peaks in three different regions namely violet, blue and green given in Table 5.1.1(a), have been observed for all the samples.

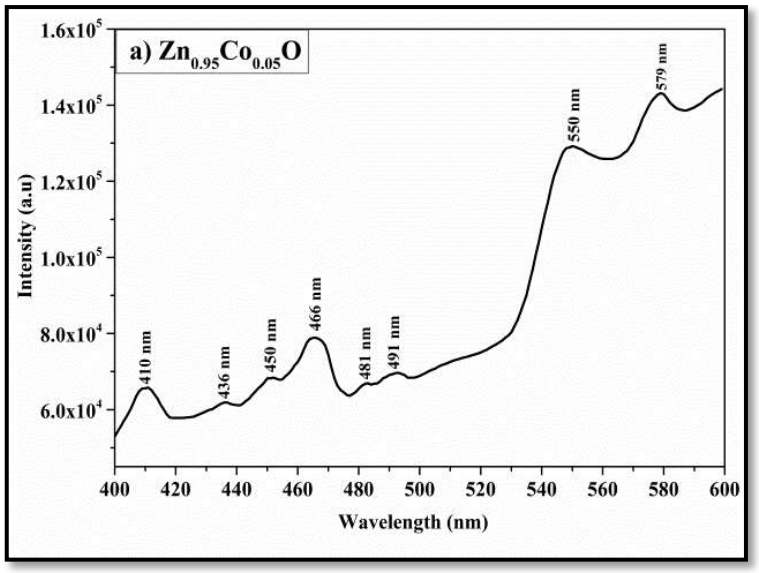

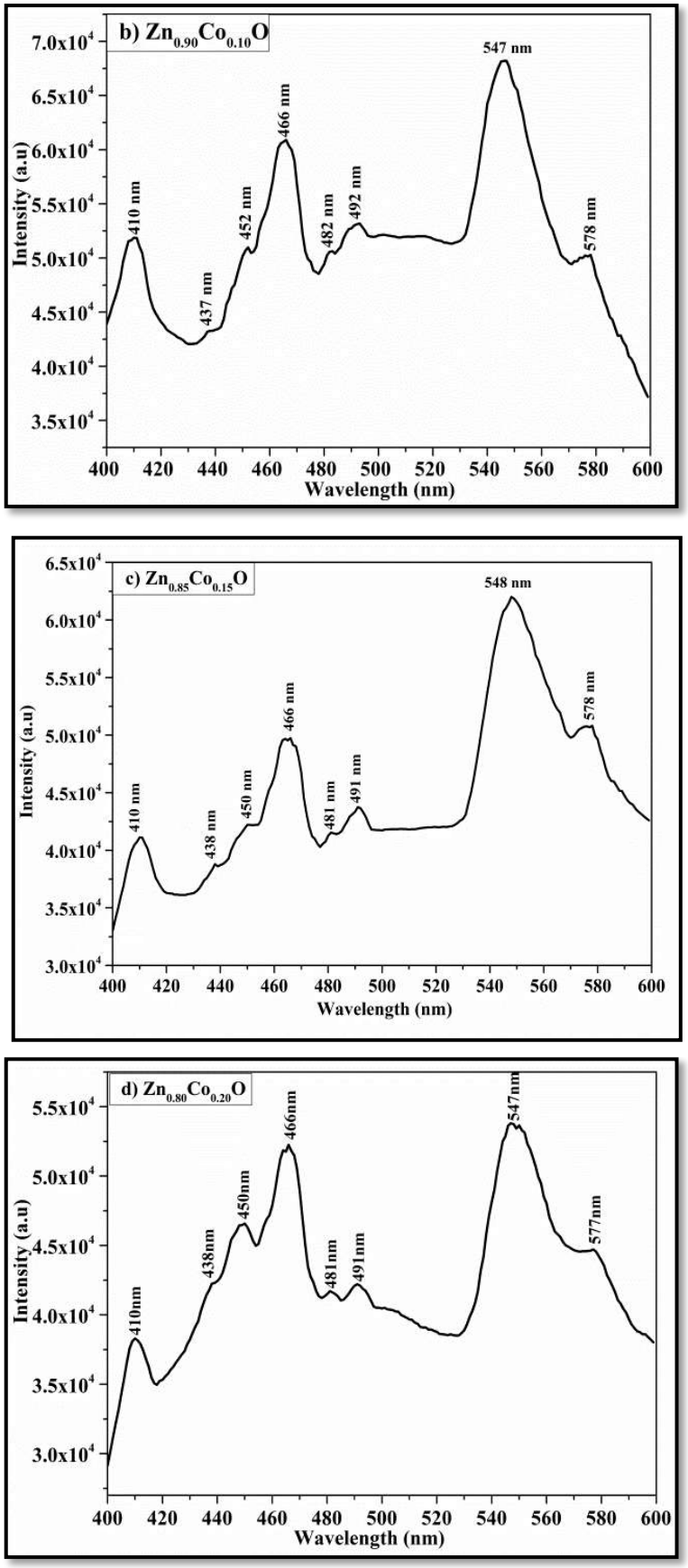

Figure 5.1.2.1: Room temperature PL spectra of $Zn_{(1-x)}Co_xO$ with (a) $Co_{0.05}$ (b) $Co_{0.10}$ (c) $Co_{0.15}$ (d) $Co_{0.20}$.

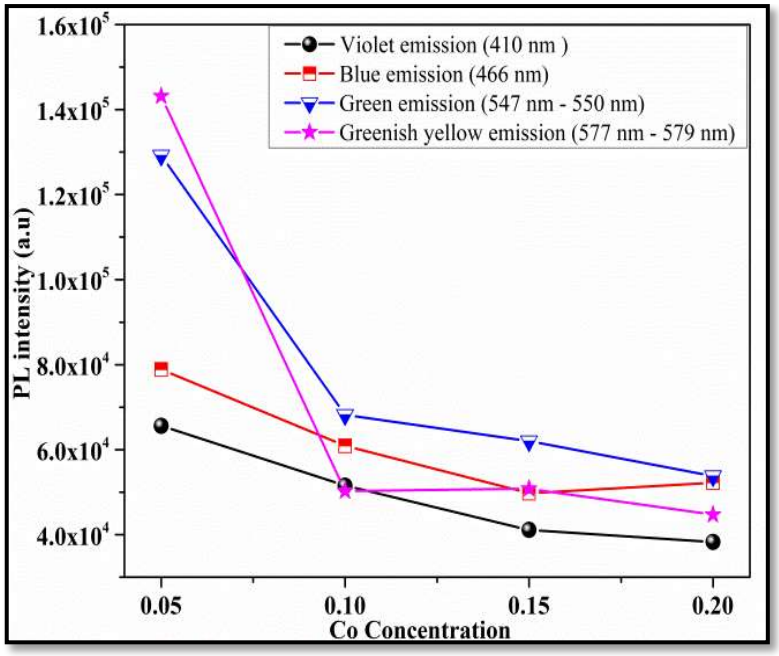

Figure 5.1.2.2: Variation of PL intensity with Co concentration.

Zinc oxide by itself has a large band gap (3.3 eV) which goes on declining from 3.02 ± 0.11 eV to 2.55 ± 0.03 eV due to the adding up of Co^{2+} in the ZnO matrix. Reports propose that these emissions in the visible region are product of intrinsic defects created in the samples, that include Zn vacancies (V_{Zn}), O vacancies (V_O), interstitial Zn (Zn_i), interstitial (O_i), and O intermediate levels formed between valence band and conduction band due to Co^{2+} substitution at Zn^{2+} positions [2, 12]. The emission peak observed in violet region at 410 nm for all the samples, is attributable to the existence of defects such as interstitial Zn (Zn_i) and Zn vacancies (V_{Zn}) related to interface traps existing at the grain boundaries of the nanoparticles [13,14]. Five emission peaks observed in blue region (436 nm – 492 nm) for all the samples could be due to transition from interstitial Zn (Zn_i) to the valence band or transition from the bottom of the conduction band to the interstitial O (O_i) level [12,15]. Two main observable emission peaks observed in green region (547 nm to 579 nm) for all the samples, may be ascribed to the existence of different types of defects that may be present prevalent to oxygen vacancies (V_O) and zinc vacancies (V_{Zn}) in the samples [16, 17].

Table 5.1.1a: PL emission wavelengths and intensities of $Zn_{(1-x)}Co_xO$ (x = 0.05, 0.10, 0.15 ,0.20) at room temperature obtained with excitation wavelength of 318nm.

***x* =**	**Violet Emission wavelength (nm)**	**Intensity (a.u)**	**Blue Emission wavelength (nm)**	**Intensity (a.u)**	**Green Emission Wavelength (nm)**	**Intensity (a.u)**
0.05	410	65602	436	61919	550	129213
			450	68197	579	143152
			466	78858		
			481	66280		
			491	69312		
0.10	410	51868	437	43208	547	68206
			452	50977	578	50277
			466	60902		
			482	50572		
			492	53115		
0.15	410	41120	438	38781	548	62003
			450	42214	578	50803
			466	49746		
			481	41536		
			491	43753		
0.20	410	38309	438	42242	547	53804
			450	46588	577	44718
			466	52254		
			481	41708		
			491	42206		

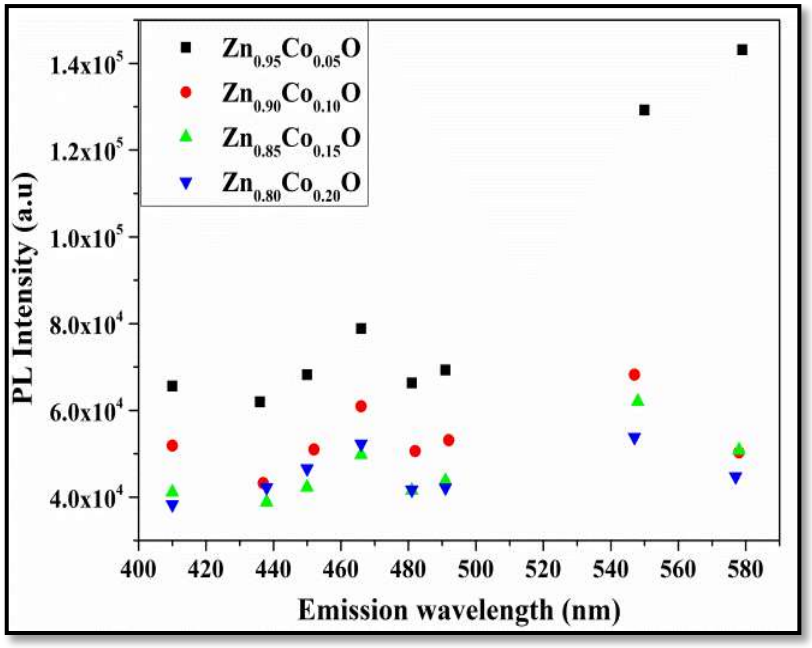

Figure 5.1.2.3: Variation of PL intensity with emission wavelength for Co concentration x = 0.05, 0.10, 0.15 and 0.20.

It may be seen from Figure 5.1.2.3 that the PL peak positions i.e emission wavelengths do not change with variation of Co^{2+} concentration in the samples. But for any given wavelength the peak intensity reduces with increasing Co^{2+} concentration. This imperative observation implies that the numbers of defect states or intermediate energy states are subordinated on increasing Co^{2+} concentration in the sample. Secondly enhancement in emission intensity at higher wavelengths suggests that the defect centers or the unoccupied energy states at higher energy level close to conduction band are in smaller amount as number compared to similar states at low energy level close to valence band. Therefore it may be seen that there is no increase in the number of defect states with raise in Co^{2+} concentration in the sample.

Photoluminescence Lifetime

Photoluminescence (PL) lifetime spectra for the sample $Zn_{(1-x)}Co_xO$, (x = 0.05, 0.10, 0.15, 0.20) was recorded at room temperature. The samples were excited with excitation wavelength of 318 nm and decay times for four major emission wavelengths between 410 nm to 579 nm were recorded. The PL decay curves given in Figure 5.1.2.4 were fitted with single exponential function as specified by equation 5.1.1 (b).

$$\mathbf{I = A \exp(-t/\tau) + I_0} \qquad 5.1.1(b)$$

Where I_0 and I are the initial and instantaneous luminescence intensities, A is a constant, t the measurement time and τ represents the lifetime of the PL emission [18].

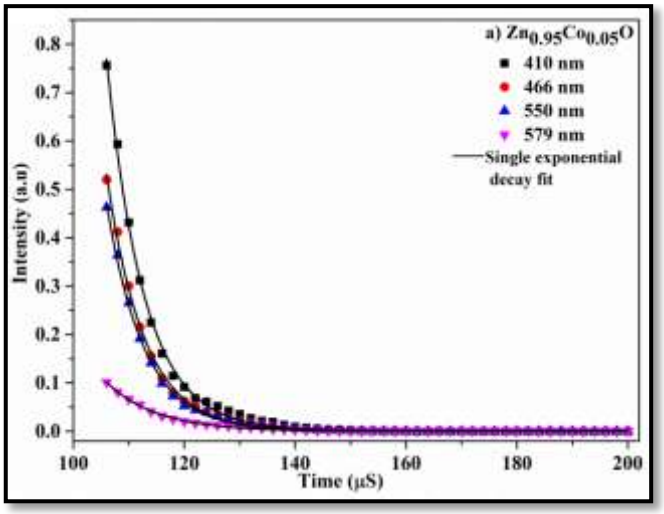

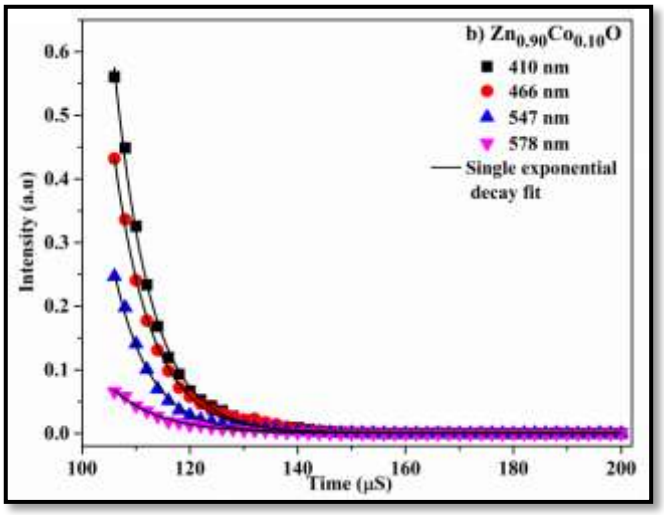

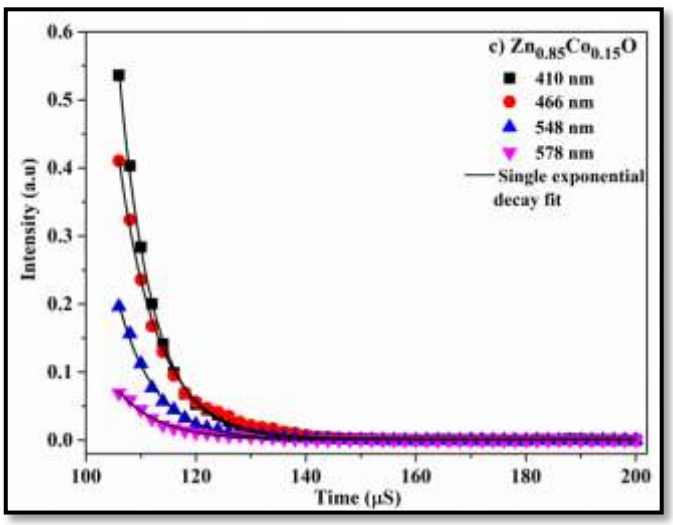

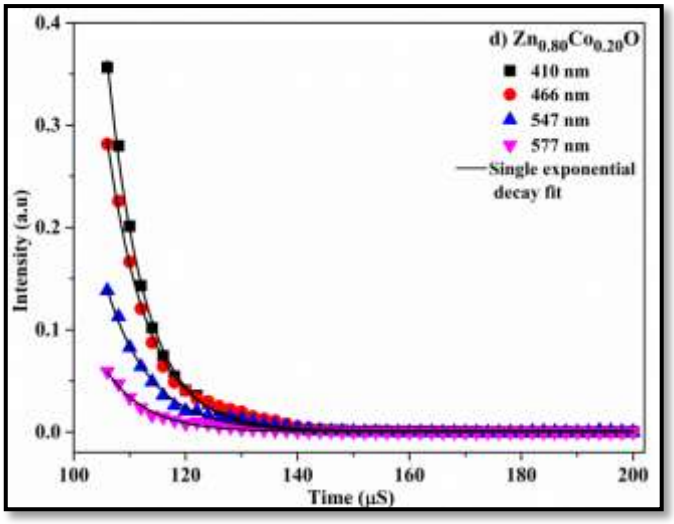

Figure 5.1.2.4: PL lifetime of $Zn_{(1-x)}Co_xO$ (x = 0.05, 0.10, 0.15 ,0.20) at room temperature with excitation wavelength 318nm.

Table 5.1.1b: Room temperature PL lifetimes observed for $Zn_{(1-x)}Co_xO$ (x = 0.05, 0.10, 0.15,0.20) with excitation wavelength of 318nm.

$Zn_{0.95}Co_{0.05}O$			**$Zn_{0.90}Co_{0.10}O$**		
Emission wavelength λ (nm)	**I_o (a.u)**	**Lifetime τ(μS)**	**Emission Wavelength λ (nm)**	**I_o (a.u)**	**Lifetime τ(μS)**
410	0.756	6.738 ± 0.041	410	0.560	6.637 ± 0.052
466	0.520	6.742 ± 0.040	466	0.432	6.762 ± 0.041
550	0.463	6.758 ± 0.038	547	0.247	6.962 ± 0.045
579	0.102	9.086 ± 0.048	578	0.066	8.951 ± 0.086
$Zn_{0.85}Co_{0.15}O$			**$Zn_{0.80}Co_{0.20}O$**		
Emission wavelength λ (nm)	**I_o (a.u)**	**Lifetime τ (μS)**	**Emission Wavelength λ (nm)**	**I_o (a.u)**	**Lifetime τ(μS)**
410	0.536	6.138 ± 0.034	410	0.356	6.611 ± 0.039
466	0.410	7.126 ± 0.056	466	0.281	6.712 ± 0.044
548	0.196	7.403 ± 0.097	547	0.138	7.280 ± 0.068
578	0.069	7.969 ± 0.081	577	0.059	7.814 ± 0.097

The calculated values of PL lifetime τ tabulated in Table 5.1.1(b) are in microseconds. Figure 5.1.2.5 (a) and (b) respectively shows the variation of τ and I_o with emission wavelength for the samples. It is observed that τ for the samples show a mixed behavior. The PL lifetimes on an average are seen to increase with enhancement in the emission wavelengths for each individual sample however the order is not maintained with concentration '*x*' in the samples. The short lifetime decay may be attributed to the radiative recombination of near-surface excitons due to the existence of surface defects [19,20]. The long lifetime decay for emission wavelengths in the range 466 nm to 579 nm, can be due to donor-acceptor pair recombination [21]. Initial Intensity I_o decreases with increase in Co^{2+} content and rise in emission wavelength is shown in Figure 5.1.2.5 (b).

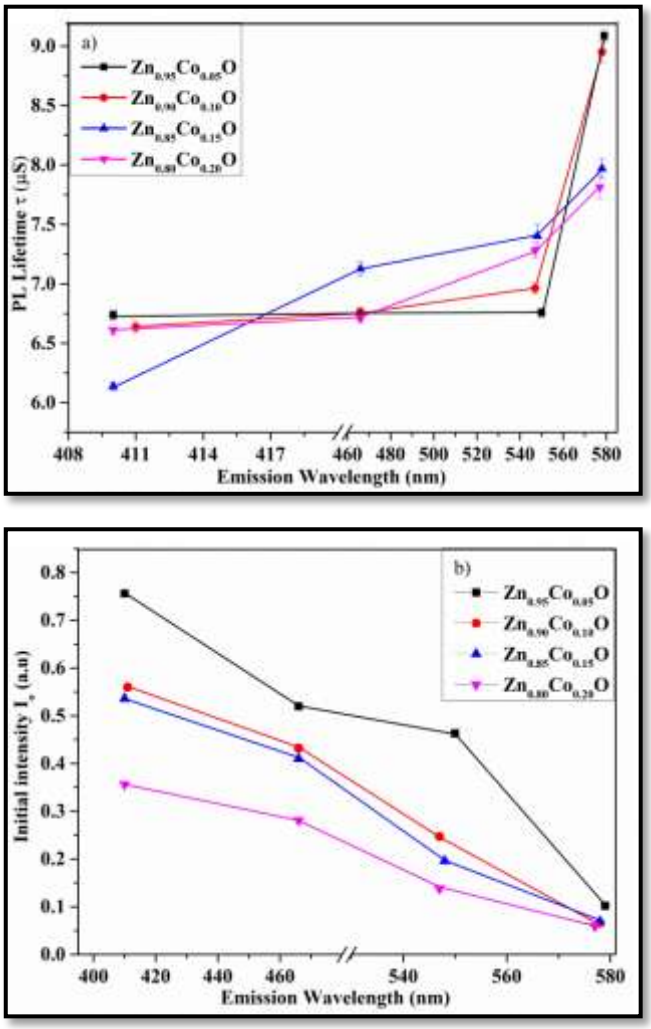

Figure 5.1.2.5: (a) Variation of PL lifetime τ (μS) and (b) Variation of PL Initial intensity I_o with emission wavelength for $Zn_{(1-x)}Co_xO$ with x = 0.05, 0.10, 0.15, 0.20

5.2 Nd doped In_2O_3, $In_{(2-x)}Nd_xO_3$ (x = 0, 0.10, 0.15, 0.20)

5.2.1 UV-Visible Spectroscopy

Figure 5.2.1.1 (a) shows the room temperature UV absorption spectra of the $In_{(2-x)}Nd_xO_3$ (x= 0, 0.10, 0.15, 0.20) nanosamples. UV absorbance measurement were done in the wavelength range of 250 nm to 800 nm to examine the influence of Nd^{3+} on the band gap of the material and to verify the substitution of Nd^{3+} in the In_2O_3 structure. Tauc's plots plotted as per equation 5.2.1 (a) where A is a constant, hυ is the energy of the photon, E_g is the energy band gap and for direct transitions n = ½ [6] are shown in Figure 5.2.1.1 (b) with inset correspond to direct energy band gap values.

$$(\alpha h\upsilon)=A(h\upsilon - Eg)^n \qquad 5.2.1(a)$$

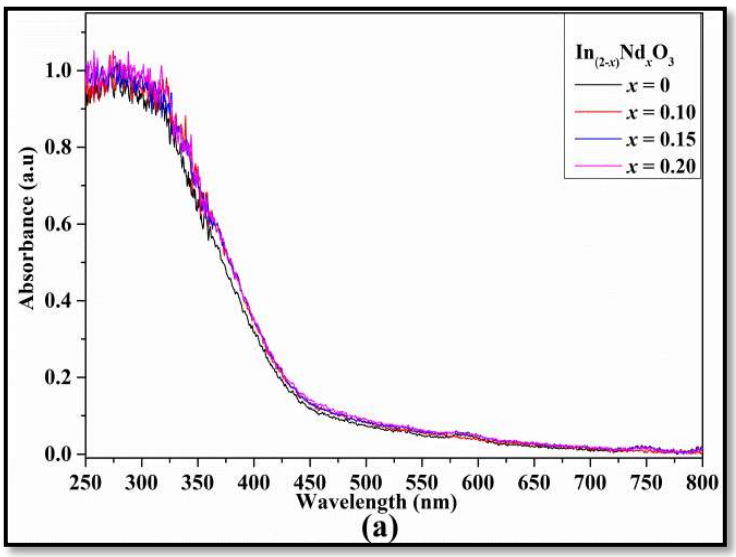

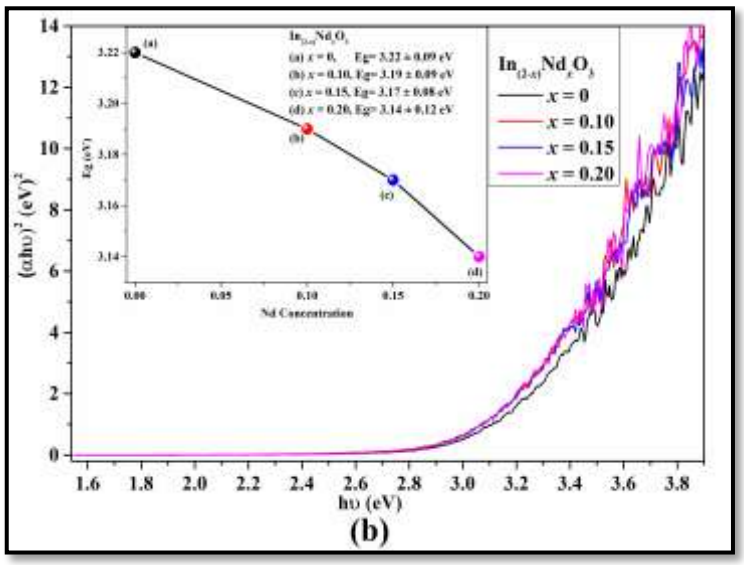

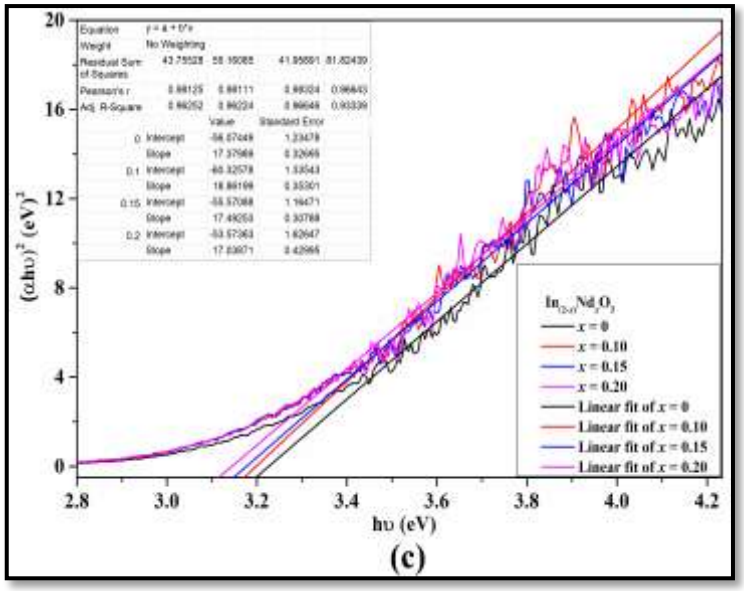

Figure 5.2.1.1: (a) UV absorbance spectra, (b) Plots of $(\alpha hv)^2$ versus photon energy (hν), (c) linear regression fit for $In_{(2-x)}Nd_xO_3$ (x= 0, 0.10, 0.15, 0.20).

The exact energy band gap values were obtained using linear regression fit at higher energy taken from tauc's plots as shown in Figure 5.2.1.1 (c). The highest energy band gap value E_g=3.22± 0.09 eV at x=0 was found to decrease linearly to a value of E_g=3.14 ± 0.12 eV at x=0.20 thus increasing the optical wavelength which is an implication of a red shift in the band gap [22]. This consequence could be due to phenomenon known as band bending. In doped semiconductors, ionization of dopant atoms in the vicinity of the interface develops an electric field causing shifts in energy levels. The (localized) valence band and delocalized (conduction) band are moved as a function of Fermi level and the process is termed as band bending [23-25]. The main cause of band bending in nanomaterial doped semiconductor is related to decrease of crystallite size. Nanomaterials are known to possess large surface to volume ratio. This ratio keeps on enhancing with decrease in crystallite size [25]. The resulting large surface area and large number of ionized dopant atoms at the interface keeps on escalating with increase in dopant concentration. Therefore band shifting would be more with larger dopant concentration thereby reducing the energy band gap of the material.

5.3 Ni doped CuO, $Cu_{(1-x)}Ni_xO$ (x = 0, 0.05, 0.10, 0.15, 0.20, 0.25, 0.30)

5.3.1 UV-Visible Spectroscopy

UV absorbance measurement were done in the wavelength range of 250 nm to 800 nm to examine the influence of Nd^{3+} on the band gap of the CuO and to study the influence of Ni^{2+} in the CuO matrix, Tauc plots of the $Cu_{(1-x)}Ni_xO$ (x = 0, 0.05, 0.10, 0.15, 0.20, 0.25, 0.30) nanoparticles is shown in Figure 5.3.1.1. Tauc's plots are plotted as per equation 5.2.1(a). The exact energy band gap values were obtained using linear regression fit at higher energy taken from tauc's plots as shown in Figure 5.3.1.2 and the variation of energy band gap with Ni concentration is shown in Figure 5.3.1.3. The highest energy band gap value E_g=3.33± 0.19 eV at x=0 was found to decrease linearly to a value of E_g=2.51 ± 0.33 eV at x=0.30 thereby increasing the optical wavelength which is an implication of a red shift in the band gap. This effect could be due to phenomenon known as band bending as stated earlier [24,25]. In addition the decreasing of band gap could be attributed to sp-d (s-d and p-d) exchange interaction which is the exchange interaction between the localized 'd' electrons of Ni^{2+} atoms and the 'sp' band electrons of CuO [26,27].

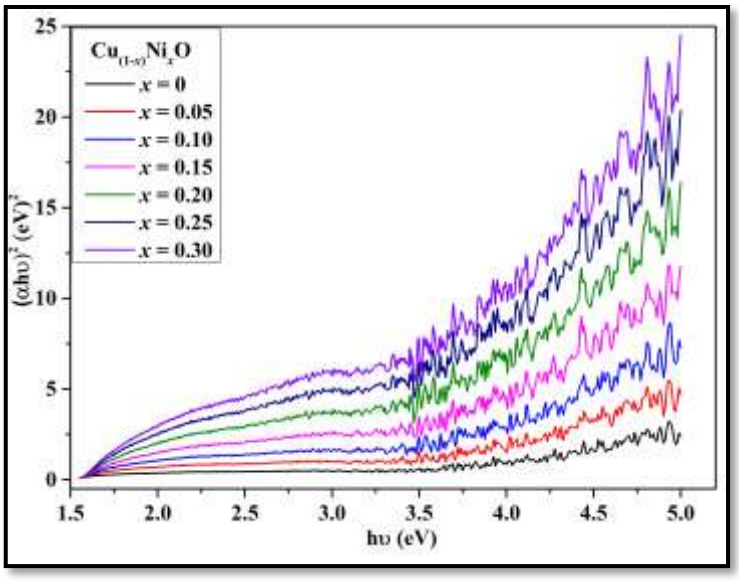

Figure 5.3.1.1: Tauc Plots of $(\alpha h\nu)^2$ versus photon energy (hν) for $Cu_{(1-x)}Ni_xO$ (x = 0, 0.05, 0.10, 0.15, 0.20, 0.25, 0.30).

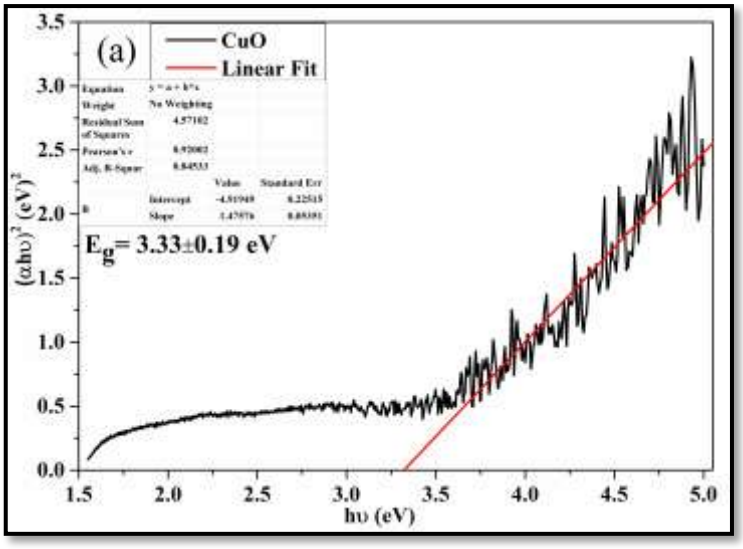
(a)
CuO
Linear Fit
Eg= 3.33±0.19 eV
(αhυ)² (eV)²
hυ (eV)

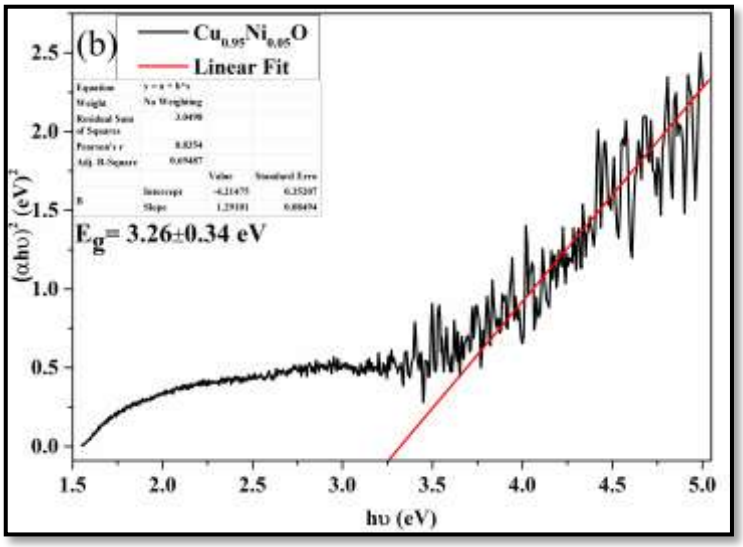
(b)
Cu0.95Ni0.05O
Linear Fit
Eg= 3.26±0.34 eV
(αhυ)² (eV)²
hυ (eV)

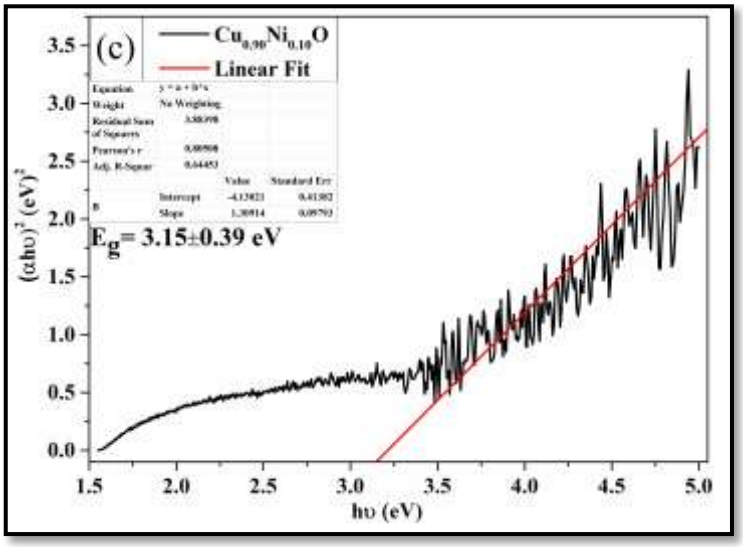
(c)
Cu0.90Ni0.10O
Linear Fit
Eg= 3.15±0.39 eV
(αhυ)² (eV)²
hυ (eV)

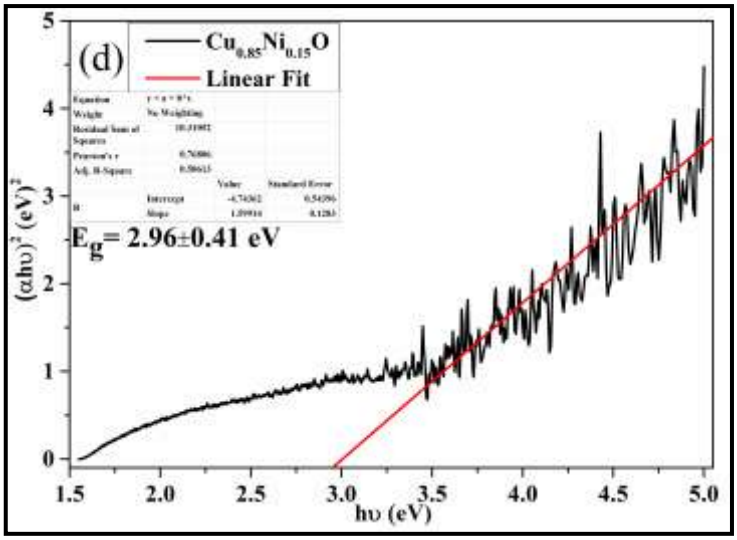
(d)
$Cu_{0.85}Ni_{0.15}O$
Linear Fit
E_g= 2.96±0.41 eV
$(\alpha h\upsilon)^2$ (eV)^2
hυ (eV)

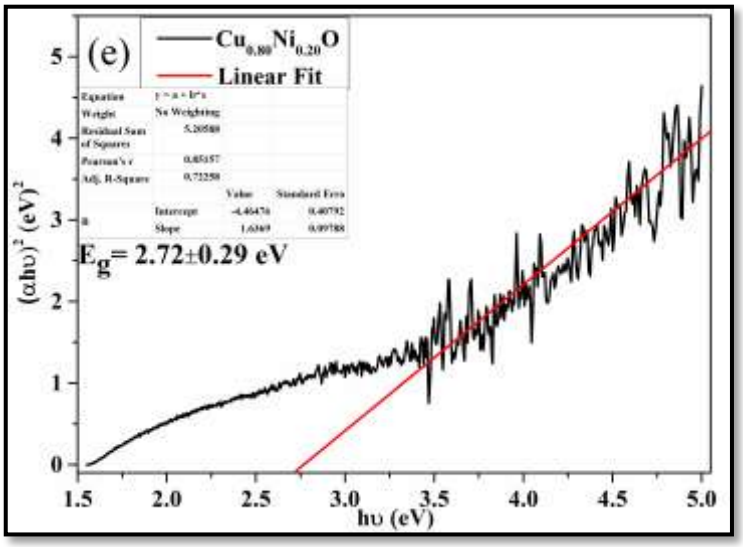
(e)
$Cu_{0.80}Ni_{0.20}O$
Linear Fit
E_g= 2.72±0.29 eV
$(\alpha h\upsilon)^2$ (eV)^2
hυ (eV)

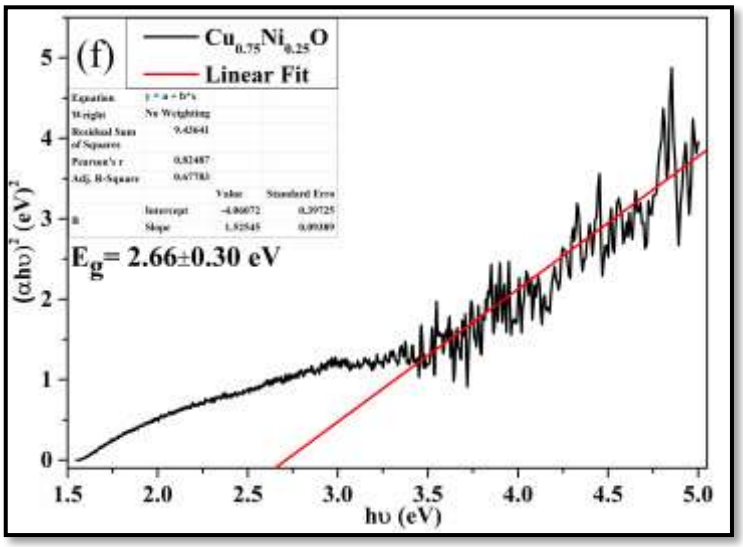
(f)
$Cu_{0.75}Ni_{0.25}O$
Linear Fit
E_g= 2.66±0.30 eV
$(\alpha h\upsilon)^2$ (eV)^2
hυ (eV)

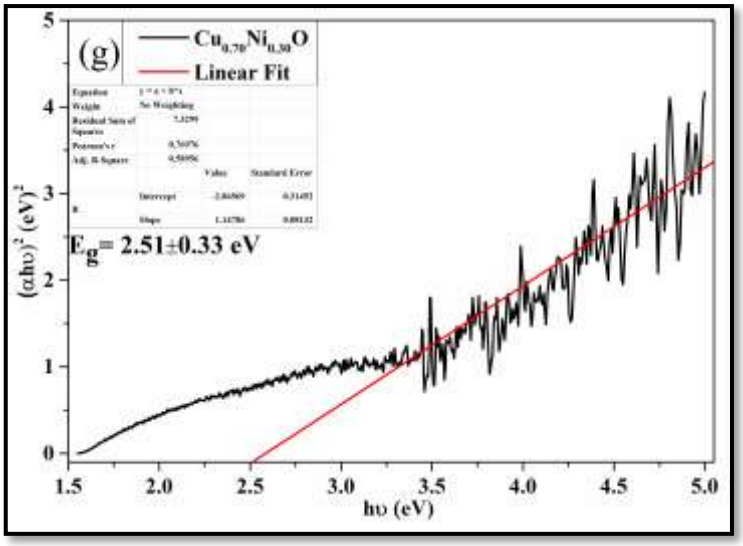

Figure 5.3.1.2: Linear regression fit for (a) CuO, (b) $Cu_{0.95}Ni_{0.05}O$, (c) $Cu_{0.90}Ni_{0.10}O$, (d) $Cu_{0.85}Ni_{0.15}O$, (e) $Cu_{0.80}Ni_{0.20}O$, (f) $Cu_{0.75}Ni_{0.25}O$, (g) $Cu_{0.70}Ni_{0.30}O$.

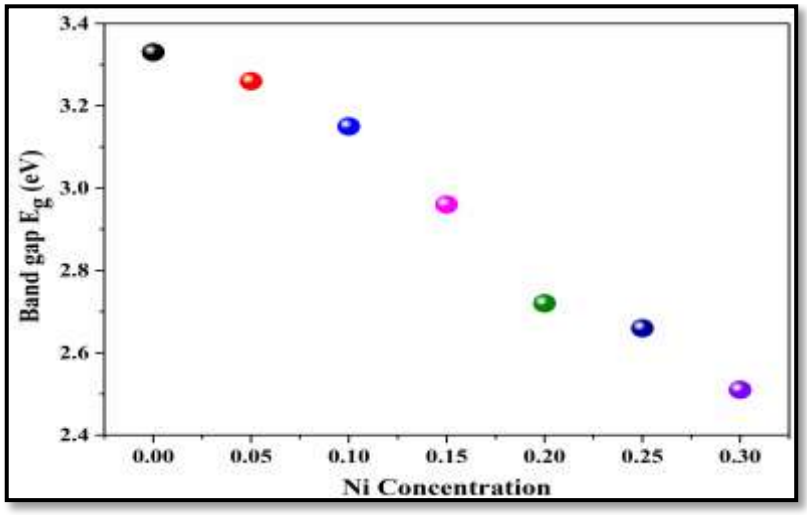

Figure 5.3.1.3: Variation of Bang gap 'E_g' with Ni concentration.

References:

[1] J. Singh, A. Chanda, S. Gupta, P. Shukla, V. Chandra, AIP Conference Proceedings 1731 (2016) 050091.

[2] A. Parveen, Shraddha Agrawal, Ameer Azam, Optical Materials 76 (2018) 21–27.

[3] B.T Rong lianghe, cuong ton-that, j nanopart res 15 (2013) 1–8.

[4] S. Lakshmi Reddy, Tamio Endo, G. Siva Reddy, INTECH, 2012.

[5] R. Elilarassi, G. Chandrasekaran, J Mater Sci: Mater Electron 24 (2013) 96–105.

[6] A. Tumuluri, K. Lakshun Naidu, K.C. James Raju, thin films international journal of chemtech research coden (USA) 6 (2014) 3353–3356.

[7] A. Anna Jacob, L. Balakrishnan, K. Shambavi, Z.C. Alex, RSC Adv 7 (2017) 39657.

[8] T. Thangeeswari, Ann Tresa George and A. Arun Kumar, Indian journal of science and technology (2016) 9.

[9] M. Naeem, S.K. Hasanain, A. Mumtaz, J. Phys.: Condense Matter 20 (2008).

[10] A.G. Ali, Francis B. Dejene, Hendrik C. Swart, Cent. Eur. J. Phys 10 (2) (2012) 478–484.

[11] A. L. Linsebigler, Guangquan Lu, John T. Yates Jr., Chem. Rev 95 (1995) 735–758.

[12] G. Vijayaprasath, R. Murugan, Y. Hayakawa, G. Ravi, Journal of Luminescence 178 (2016) 375–383.

[13] S. Taguchi, T. Tayagaki, Y. Kanemitsu, Materials Science and Engineering 6 (2009) 012029.

[14] F.S. Husairi, Syahirah Mhd Ali, A. Azlinda, M. Rusop, S. Abdullah, Hindawi Publish. Corp. J. Nanomater. 7 (2013).

[15] P.S. Xu, Y.M. Sun, C.S. Shi, F.Q. Xu, H.B. Pan, Sci. China,Ser 44 (2001) 1252–1253.

[16] T. Hammad, Jamil K. Salem, R.G. Harrison, Appl Nanosci 3 (2013) 133–139.

[17] R. Raji, K.G. Gopchandran, journal of science: advanced materials and devices 2 (2017) 51–58.

[18] X. Jiang, X. Zhao, L. Duan, H. Shen, H. Liu, T. Hou, F. Wang, Ceram. Int. 42 (2016) 15160–15165.

[19] G. xiong, u. Pal, j. Garcia serrano, journal of applied physics 101 (2007) 024317.

[20] S. Baruah, Sudarson Sekhar Sinha, Barnali Ghosh, Samir Kumar Pal, A.K. Raychaudhuri, Joydeep Dutta, Journal Of Applied Physics 105 (2009) 074308.

[21] H. chander, santa chawla, bull. Mater. Sci. 31 (2008) 401–407.

[22] S. Parhoodeh, Mohammad Kowsari, Physica B, 498 (2016) 27–32.

[23] H. J Lewerenz., J. Electroanal. Chem.**,** 356 (1993) 121-143.

[24] Z. Zhang, John T. Yates Jr., Chem. Rev., 112 (2012) 5520−5551.

[25] D. Beena, K. J. Lethy, R. Vinod kumar, A. P. Detty, V. P. Mahadevan pillai, V. Ganesana, Optoelectronics and advanced materials – rapid communications, 5 (2011) 1 – 11.
[26] M. Ponnar, C. Thangamani, P. Monisha, S.S. Gomathi, K. Pushpanathan, Applied Surface Science, (2018).
[27] S. Rehman, A. Mumtaz, S. K. Hasanain, Journal of Nanoparticle Research 13 (2011) 2497–2507.

CHAPTER 6

Magnetic properties of Co doped ZnO, Nd doped In_2O_3 & Ni doped CuO Dilute Magnetic Semiconductor Nanoparticles

Introduction

The magnetic properties of any particular material can be understood by investigating its response to external magnetic fields. However, it is also found that the magnetic properties of DMS material are strongly dependent on the existence of unpaired electrons in the material. In the current chapter we have reported complete exploration of important magnetic properties of Co doped ZnO, Nd doped In_2O_3 and Ni doped CuO nanoparticles samples using magnetic measurements such as Hysteresis curves at room temperature, Zero field cooled (ZFC) and Field cooled (FC) Plots under constant magnetic field of 500 Oe.

6.1 Co doped ZnO, $Zn_{(1-x)}Co_xO$ (x = 0.05, 0.10, 0.15, 0.20).

6.1.1 Magnetic Properties

Figure 6.1.1.1 shows the results of hysteresis curves measured at room temperature for all the samples. The insert in the figure display the enlarged vision of the hysteresis curves near origin. The sample with lowest Co^{2+} concentration holds the diamagnetic behavior of ZnO while the other three samples having higher Co^{2+} concentration show ferromagnetic behavior. This signifies that induction of trace amount of Co (x = 0.05) cannot alter the diamagnetic behavior of the sample [1]. The foremost magnetic moment is observed for sample with highest Co^{2+} concentration [2, 3]. The magnetization of these samples proceeds linearly above 2-3 kOe of the applied field. The linear enhancement of magnetization in the M-H loops could be explained on the basis of strong in d-d exchange interaction coupled with Co^{2+} ions which increases with increase in Co^{2+} doping. At low level (x = 0.05) of Co^{2+} doping d-d exchange interaction is very weak and limits the sample from going into a ferromagnetic state. Thus the Co^{2+} doped samples at this concentration stage do not exhibit ferromagnetism. The origin of increasing magnetization in the M-H loops at higher concentrations of x = 0.15, 0.20 can be elucidated on the basis of Co^{2+} going in the high spin state. Co^{2+} ($4s^0 3d^7$) ions in high spin state arrangement has three unpaired electrons as shown in Figure 6.1.1.2, this produces a high spin environment in the wurtzite

structure leading to enhancement in the magnetization [11]. Thus for samples with x = 0.15 and 0.20 the high spin environment and strong d-d exchange interaction quickly enhances the magnetization giving rise to ferromagnetism in these samples. Although the samples with x =0.10, 0.15, 0.20 exhibit ferromagnetism which is higher in magnitude, the samples are far from attaining a stable saturation state [4, 5].

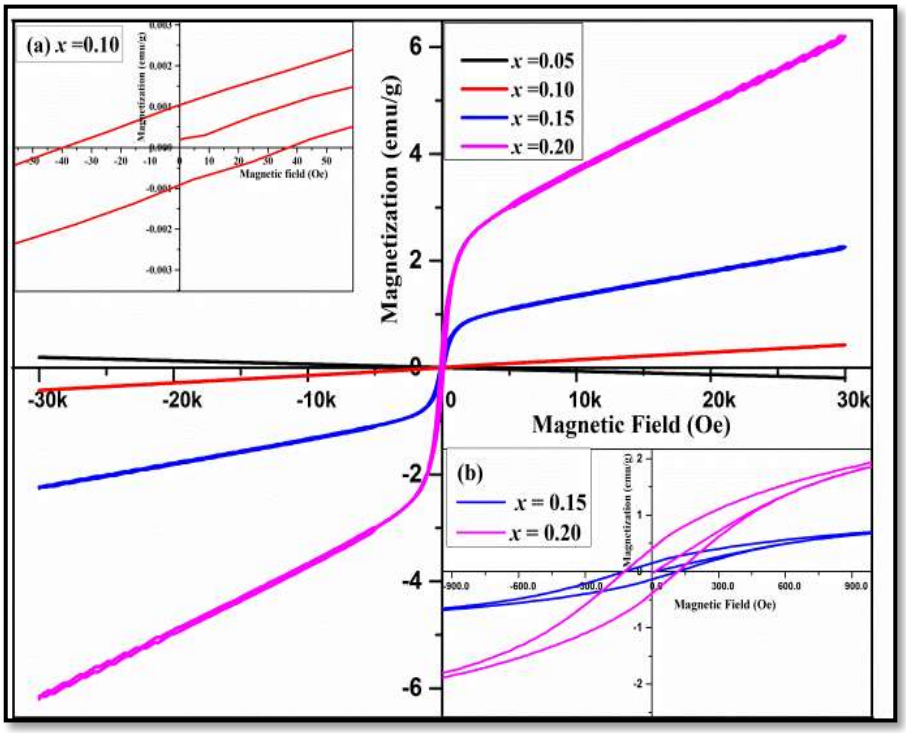

Figure 6.1.1.1: Hysteresis loop of $Zn_{(1-x)}Co_xO$ (x = 0.05, 0.10, 0.15, 0.20) at room temperature.

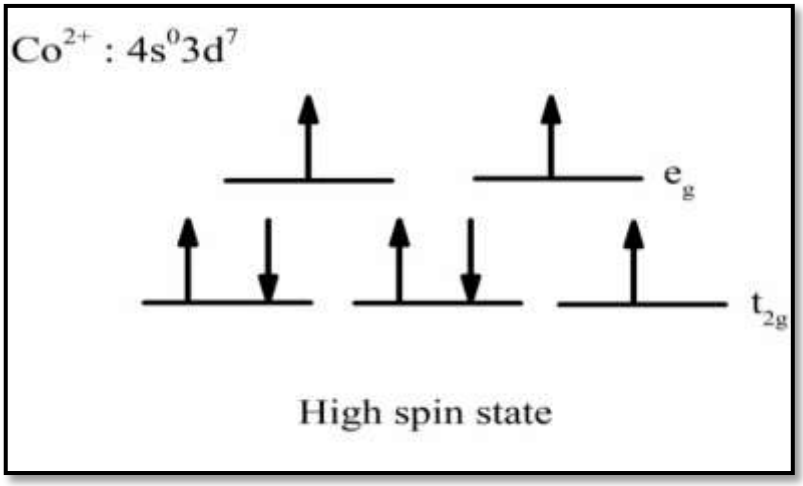

Figure 6.1.1.2: Co^{2+} ($4s^0 3d^7$) high spin electronic configuration.

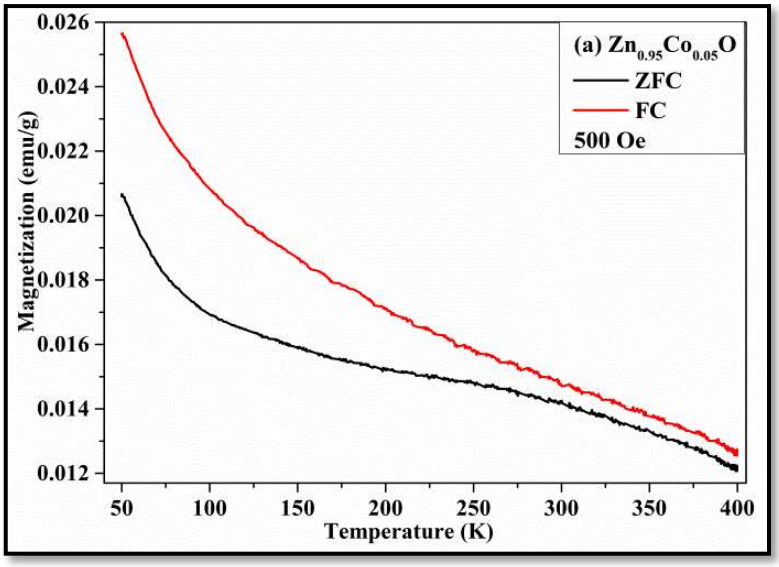
(a) $Zn_{0.95}Co_{0.05}O$
ZFC
FC
500 Oe
Magnetization (emu/g)
Temperature (K)
0.026
0.024
0.022
0.020
0.018
0.016
0.014
0.012
50
100
150
200
250
300
350
400

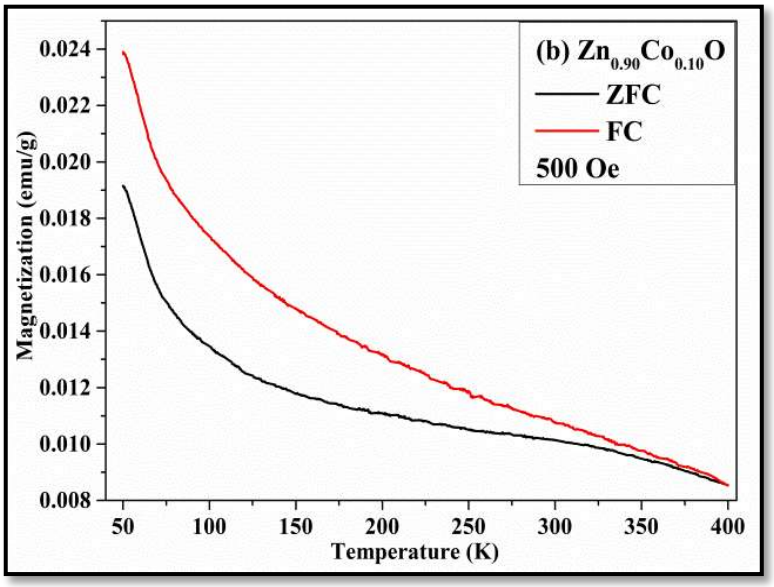
(b) $Zn_{0.90}Co_{0.10}O$
ZFC
FC
500 Oe
Magnetization (emu/g)
Temperature (K)
0.024
0.022
0.020
0.018
0.016
0.014
0.012
0.010
0.008
50
100
150
200
250
300
350
400

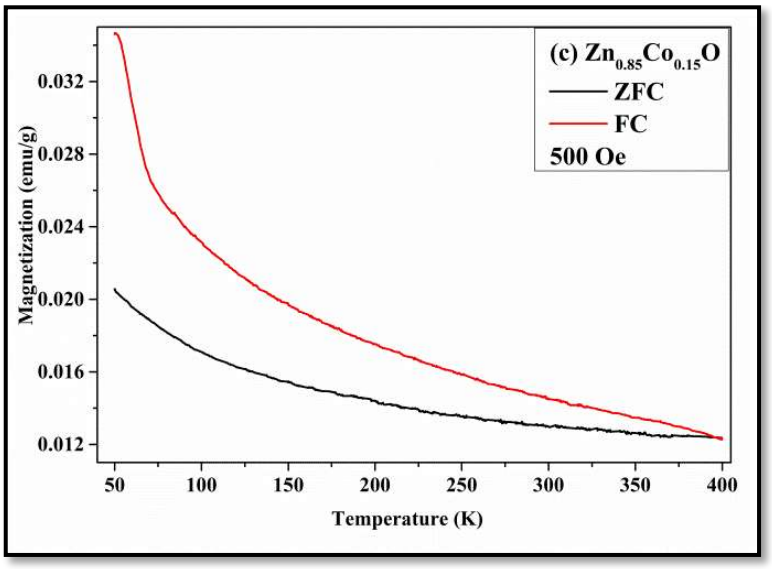
(c) $Zn_{0.85}Co_{0.15}O$
ZFC
FC
500 Oe
Magnetization (emu/g)
Temperature (K)
0.032
0.028
0.024
0.020
0.016
0.012
50
100
150
200
250
300
350
400

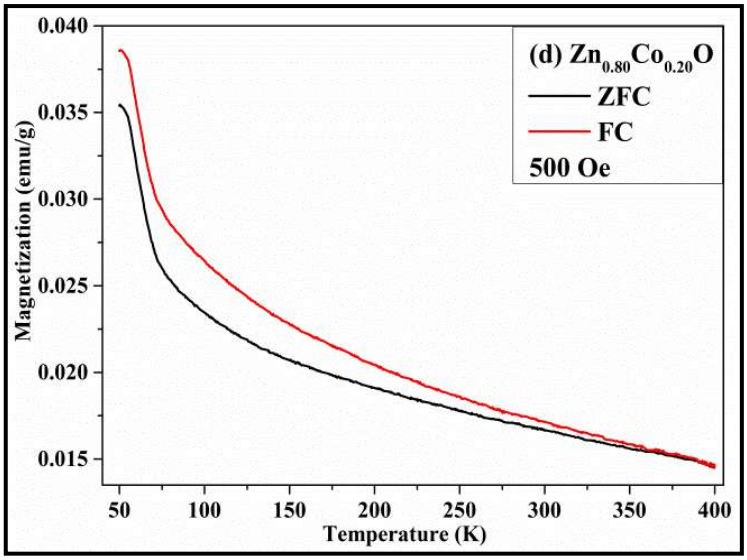

Figure 6.1.1.3: Zero field cooled (ZFC) and Field cooled (FC) Plots for (a) $Zn_{0.95}Co_{0.05}O$, (b) $Zn_{0.90}Co_{0.10}O$, (c) $Zn_{0.85}Co_{0.15}O$, (d) $Zn_{0.80}Co_{0.20}O$ under 500 Oe.

To examine the perspective aspect about the magnetic behavior in DMS nanomaterials, change of magnetization with respect to temperature (M-T curves) were attained under zero field cooled and field cooled conditions with an applied magnetic field of 500 Oe. The magnetization of the samples as seen from Figure 6.1.1.3 is found to decrease with increasing temperature. This is attributed to increase in thermal agitation of the atoms that result in non-alignment of the atoms in the magnetic field. Generally a decrease in magnetization with increasing temperature is an indication of the paramagnetic behavior of a material [6]. But at a given temperature, the difference between the corresponding magnetization value on FC and ZFC curves gives the net ferromagnetic contribution of the sample by deducting paramagnetic and diamagnetic contributions at that temperature [7]. In the present case, the distinct separation between FC and ZFC curves with the presence of irreversibility temperature of 398 K, 395 K and 389K for last three samples indicates presence of ferromagnetic ordering in these samples. It may be seen that decrease of irreversibility temperature with increase in Co^{2+} concentrations is an indicator of an increase in ferromagnetic ordering. This behavior can very clearly be seen in the hysteresis curves given in Figure 6.1.1.1.

For a sample with x = 0.05 irreversible temperature could not be seen till 400K which is the limit of the instrument. This may be due to the low value of

doping concentration which can be also visible from the M-H curve in Figure 6.1.1.1. Moreover, the smooth fall of ZFC and FC curves with rising temperature without any cusp indicates absence of characteristic FM to SPM or FM to PM transition [8,9]. Since the samples are free from impurity phases such as CoO or Co_3O_4, no antiferromagnetic ordering was observed that normally rampant in presence of these kinds of impurities which annihilates ferromagnetism in materials [10]. Thus the natures of FC and ZFC curves supports formation of impurity free material and justify induction of ferromagnetism in the samples which is exclusively caused by the exchange interactions among the localized d-electrons in Co^{2+} atoms.

6.2 Nd doped In_2O_3, $In_{(2-x)}Nd_xO_3$ (x = 0, 0.10, 0.15, 0.20)

6.2.1 Magnetic Properties

Magnetization versus Magnetic field (M-H) curves obtained for $In_{(2-x)}Nd_xO_3$ (x= 0, 0.10, 0.15, 0.20) samples with a maximum applied field of 30kOe at room temperature are shown in Figure 6.2.1.1. It may be seen that the un-doped sample with x = 0 exhibits diamagnetic behavior [8] whereas the doped samples show ferromagnetic behavior which enhances with increasing Nd^{3+} concentration. Thus maximum magnetic moment is observed for sample having highest Nd^{3+} concentration. The hysteresis plots in the figure shows that the magnetization of the doped samples raises almost linearly with a minor curvature approximately above ±5 kOe of the applied magnetic field. The magnetization of the samples increases with increase in Nd^{3+} concentration indicating presence of ferromagnetic nature in the samples. The ferromagnetism in the sample is due to exchange interaction between the localized f electrons in Nd^{3+} atoms [12]. This measurement provides sufficient confirmation about the existence of ferromagnetism in the samples.

To understand better about induction of ferromagnetism in the materials, temperature dependent magnetization measurements under (ZFC) zero field cooled and field cooled (FC) conditions at 500 Oe were carried out as shown in Figure 6.2.1.2. The overall magnetization of the samples is seen to reduce with increasing temperature as a result of increased thermal agitation of the atoms which is an outcome of non alignment of the atoms in the magnetic field.

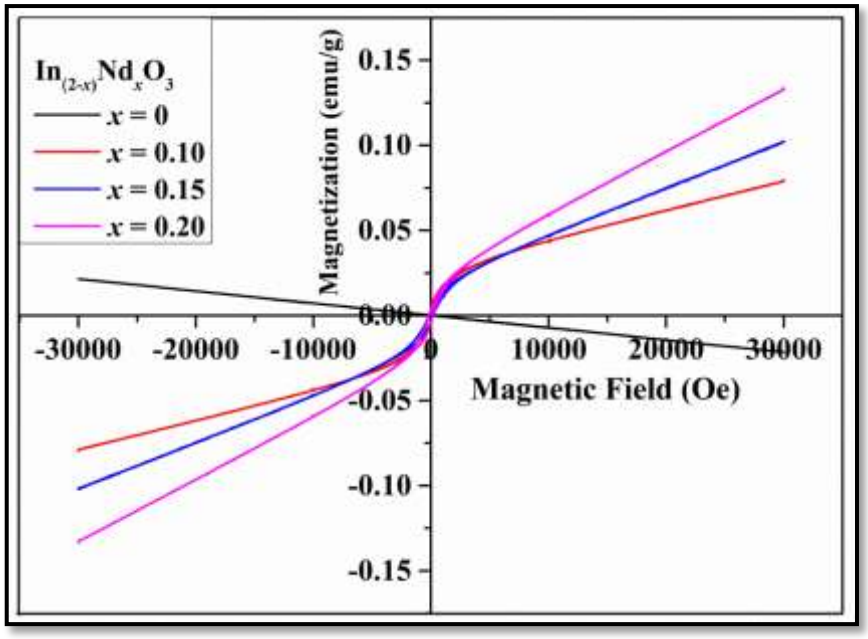

Figure 6.2.1.1: Hysteresis loop of $In_{(2-x)}Nd_xO_3$ (x= 0, 0.10, 0.15, 0.20) at room temperature.

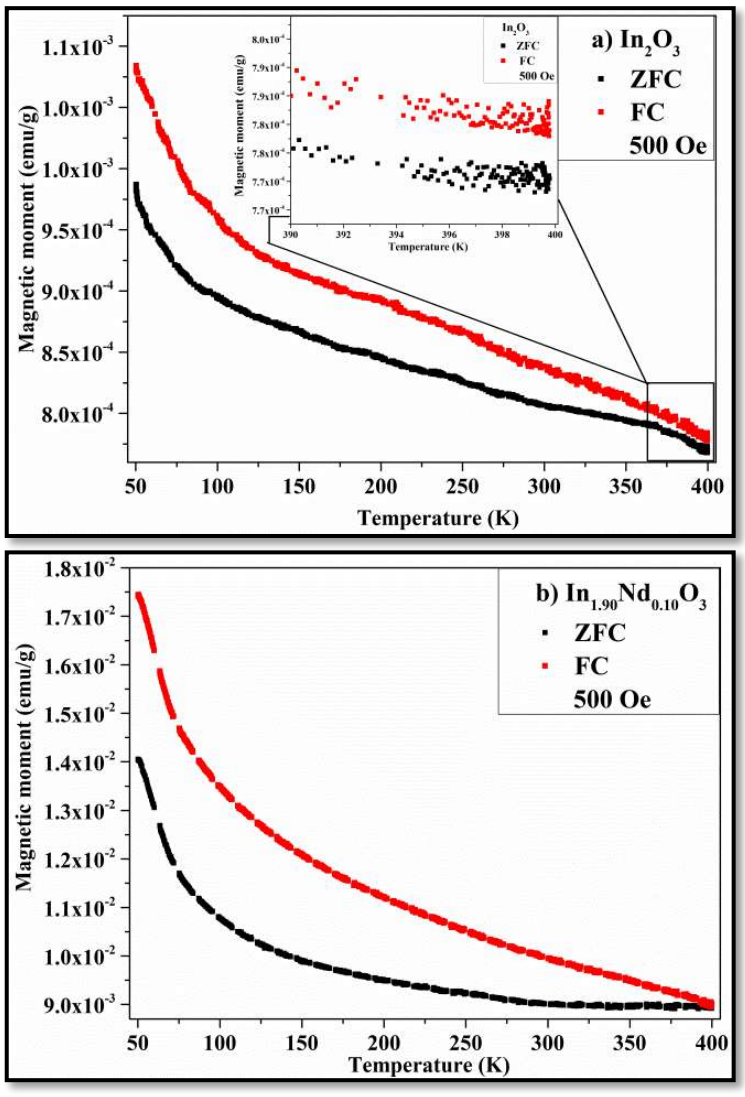

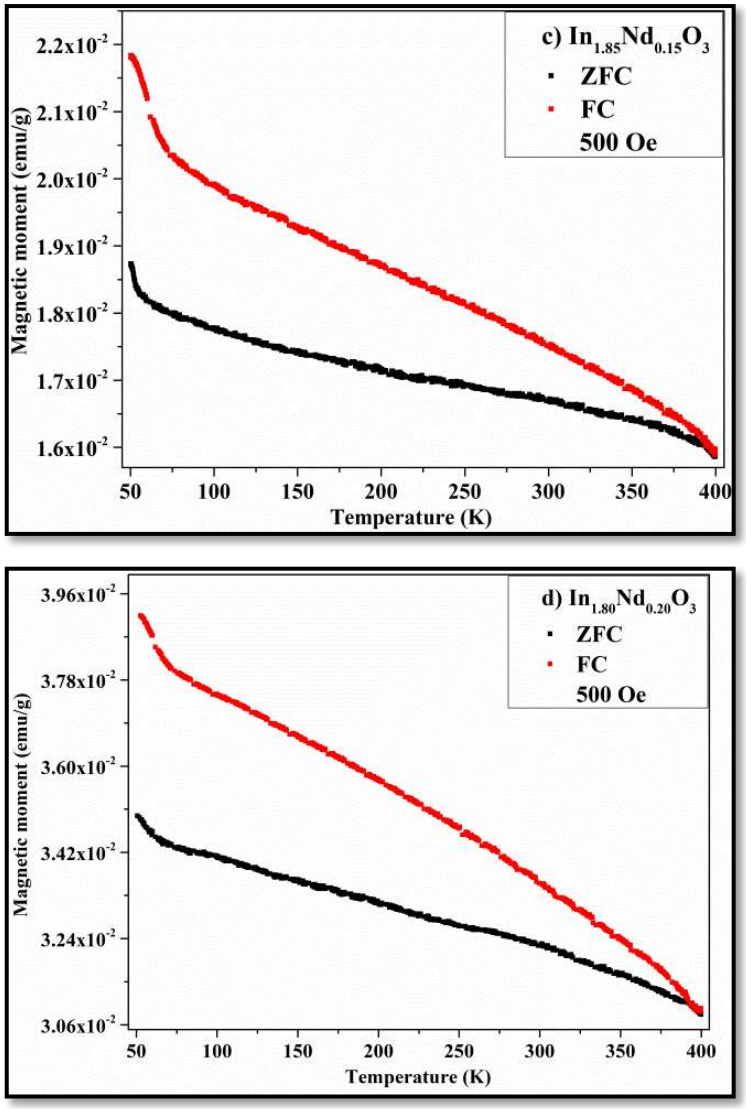

Figure 6.2.1.2: Plots of ZFC and FC measurements for (a) In_2O_3, (b) $In_{1.90}Nd_{0.10}O_3$, (c) $In_{1.85}Nd_{0.15}O_3$, (d) $In_{1.80}Nd_{0.20}O_3$ under 500 Oe.

Generally the difference between FC and ZFC magnetization values provides the total ferromagnetic contribution in the sample by eliminating paramagnetic and diamagnetic contributions [7]. FC and ZFC curves for x = 0 does not show any irreversibility temperature as displayed in the inset of Figure 6.2.1.2 (a). This implies that the sample is purely diamagnetic in nature [8]. Moreover the distinct separation between FC and ZFC curves with presence of irreversibility temperatures at 396 K, 394 K and 392 K for samples with x= 0.10, 0.15 and 0.20 respectively under 500Oe indicate the existence of ferromagnetic ordering in the samples. It is observed that the irreversibility temperature of the sample reduces with increase in Nd^{3+} concentration which signifies an augmentation of

ferromagnetic ordering in the samples as observed in the hysteresis curves. Secondly no uncharacteristic behavior like a cusp, indicating transition from ferromagnetic to paramagnetic or ferromagnetic to super-paramagnetic state or presence of antiferromagnetic ordering, is observed in ZFC and FC curves [9,15]. This also establishes the fact that Nd^{3+} has entered the In_2O_3 matrix forming a pure phase and has not formed a mixed impurity state like Nd_2O_3 within the material there by forming a mixture of the two oxides [14]. Thus FC and ZFC curves give clear confirmation of introduction of pure ferromagnetic phase in the samples which is due to exchange interaction between the localized *f* electrons in Nd^{3+} atoms in the sample [12].

6.3 Ni doped CuO, $Cu_{(1-x)}Ni_xO$ (x = 0, 0.05, 0.10, 0.15, 0.20, 0.25, 0.30)

6.3.1 Magnetic Properties

Magnetization versus Magnetic field (M-H) curves obtained for $Cu_{(1-x)}Ni_xO$ (x= 0, 0.05, 0.10, 0.15, 0.20, 0.25, 0.30) samples with a maximum applied field of 20kOe at room temperature are shown in Figure 6.3.1.1. All the samples exhibit ferromagnetic behavior that elevates with increase in Ni^{2+} concentration the samples. The ferromagnetism in these DMS materials could be due to the existence of unpaired spin electrons, surface size effect and the impurity/secondary phase in the sample. However the prepared samples are formed in single phase, without any trace of impurity/secondary phase as conformed from X-ray analysis discussed in the chapter 4. It may be seen from inset of Figure 6.3.1.1 that for x = 0 sample shows feeble ferromagnetic behavior [17]. The ferromagnetism present in x = 0 sample must be due to the oxygen vacancies created in the CuO matrix [17]. Moreover superiority of ferromagnetic behavior increases with increase in Ni^{2+} content in the sample. From the figure it is noticed that maximum magnetic moment is detected for sample having highest Ni^{2+} content. The ferromagnetism in the doped samples may be due to the variation of the magnetic moment of Ni^{2+} ions when it is substituted with Cu^{2+} ions. The magnetic moment of Ni^{2+} is 2.83 μB which is larger than the magnetic moment of Cu^{2+} that is 1.73 μB [18]. Therefore, increase of Ni^{2+} content results in amplification of the ferromagnetic spin-spin interaction among the nickel and copper atoms [18].

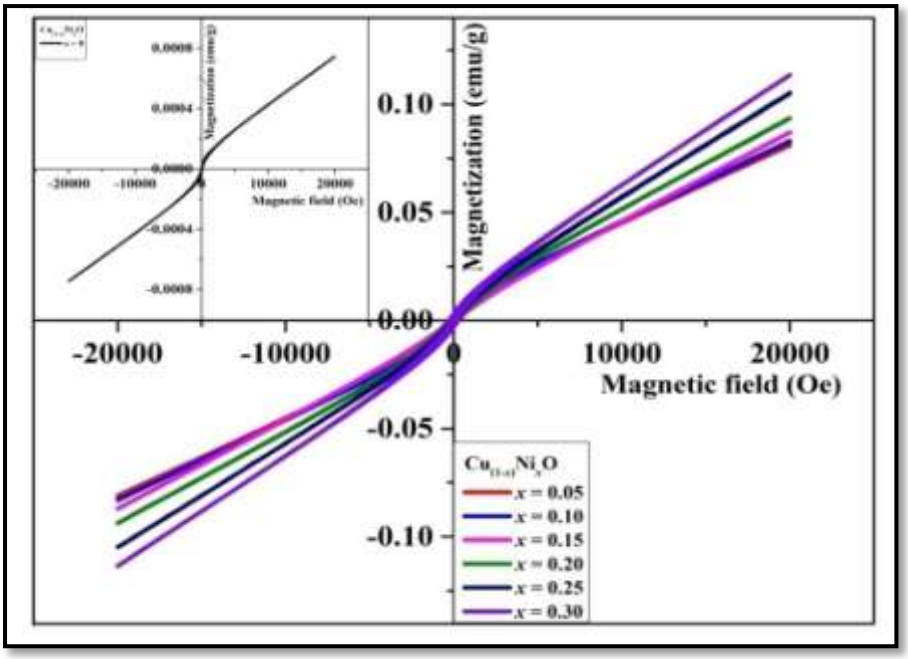

Figure 6.3.1.1: Hysteresis loop of $Cu_{(1-x)}Ni_xO$ (x = 0, 0.05, 0.10, 0.15, 0.20, 0.25, 0.30) at room temperature.

In order to find out more information about the magnetic behavior of the Ni-doped CuO nanoparticles, the field-cooled and zero field-cooled magnetization curves were measured from 50 K to 400 K under applied magnetic field of 500 Oe. It can be seen from Figure 6.3.1.2 that initially the zero field-cooled magnetization increases, subsequently the magnetization decreases with increases in temperature and Field cooled magnetization decreases with increases in temperature.

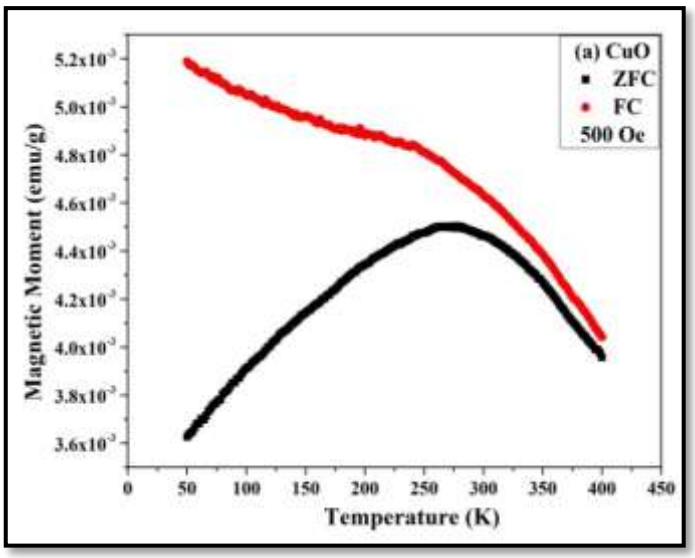

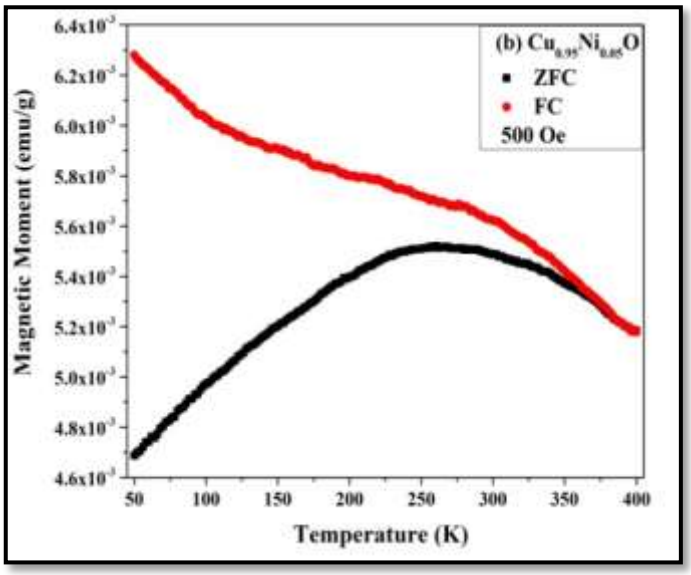
(b) $Cu_{0.95}Ni_{0.05}O$
ZFC
FC
500 Oe
Magnetic Moment (emu/g)
Temperature (K)

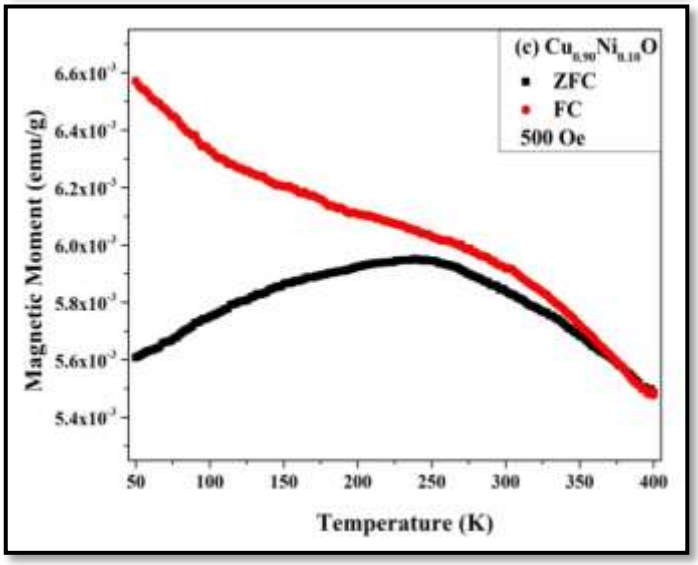
(c) $Cu_{0.90}Ni_{0.10}O$
ZFC
FC
500 Oe
Magnetic Moment (emu/g)
Temperature (K)

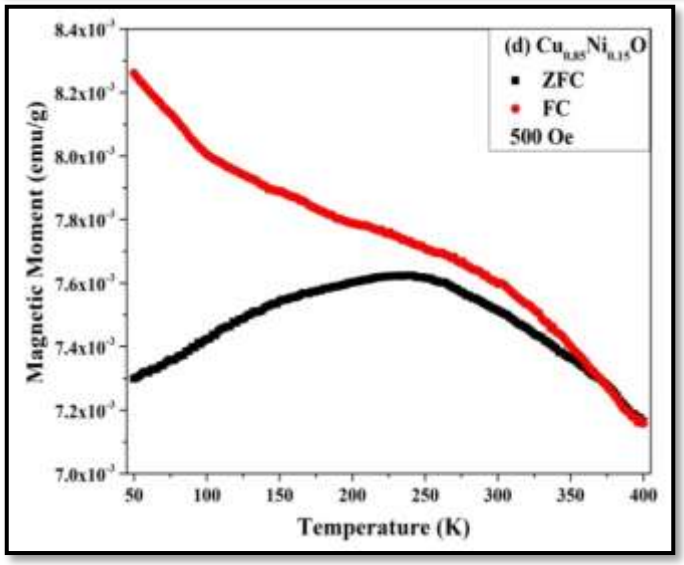
(d) $Cu_{0.85}Ni_{0.15}O$
ZFC
FC
500 Oe
Magnetic Moment (emu/g)
Temperature (K)

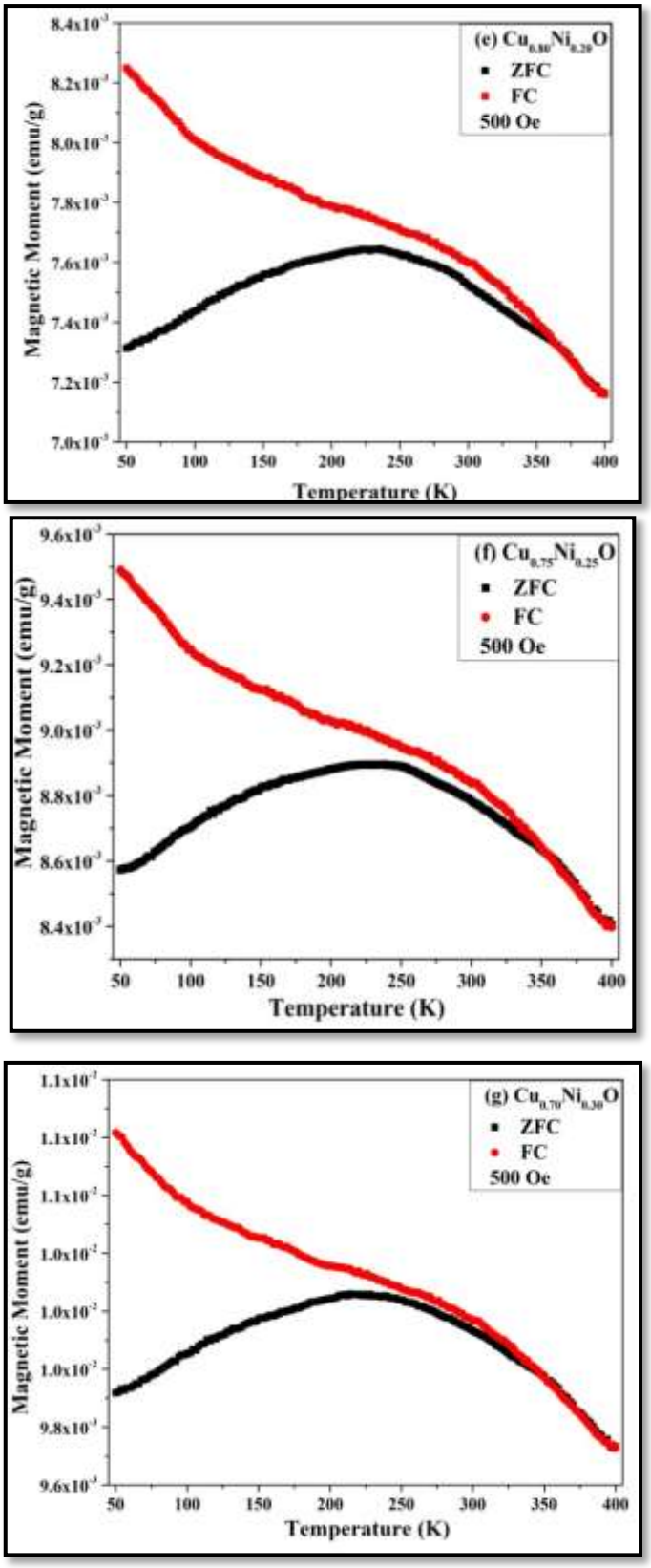

Figure 6.3.1.2: Plots of ZFC and FC measurements for (a) CuO, (b) $Cu_{0.95}Ni_{0.05}O$, (c) $Cu_{0.90}Ni_{0.10}O$, (d) $Cu_{0.85}Ni_{0.15}O$, (e) $Cu_{0.80}Ni_{0.20}O$, (f) $Cu_{0.75}Ni_{0.25}O$, (g) $Cu_{0.70}Ni_{0.30}O$ under 500 Oe.

The variation in FC and ZFC curve signifies a typical behavior of ferromagnetic nanoparticles [19]. Moreover presence of irreversible temperature is observed for x = 0.05 at 386 K, x = 0.10 at 378 K, x = 0.15 at 370 K, x = 0.20 at 364 K, x = 0.25 at 352 K and x = 0.30 at 346 K under 500 Oe. The irreversible temperature decreases with increase in Ni^{2+} content signifying enhancement of ferromagnetic ordering in the samples. FC and ZFC curves for x = 0 do not show irreversibility temperature as displayed in Figure 6.3.1.2 (a). This implies that the sample have low ferromagnetic ordering in the sample [20]. It can be seen from Figure 6.3.1.2 that for all the samples ZFC curves magnetization increases, reaches to a maxima and then decreases. The point where the magnetization is maximum is called as blocking temperature [21]. The blocking temperature signifies the presence of superparamagnetism in the samples and the blocking temperature is dependent on the crystallite size [21,22]. The blocking temperature observed for x = 0 at 264 K, x = 0.05 at 258 K, x = 0.10 at 246 K, x = 0.15 at 242 K, x = 0.20 at 236 K, x = 0.25 at 230 K and x = 0.30 at 222 K, which decreases with increasing the Ni^{2+} content. The superparamagnetism arises when the crystallite size becomes small [22] and it is confirm from our structural analysis that the crystallite size decreases with increases in Ni^{2+} concentration. This analysis shows that the blocking temperature is in the temperature range of 222K - 264K which indicates presence of superparamagnetic grains in the samples. Moreover with increase in temperature the Ni^{2+} samples showed irreversible temperature indicating existence of ferromagnetism in the samples. This analysis ascertains the fact that Ni^{2+} has entered in the CuO matrix and has not formed an impurity state like NiO in the material thus from FC and ZFC curves provides a clear confirmation of ferromagnetism in the samples [14].

References:

[1] K Hyodo, S Morimoto, T Yamazaki, T Ishikawa, J Utsumi, and Y Ichiyanagi, AIP Conference Proceedings, 020004 (2016) 1709 .

[2] S. Deka, P.A. Joy, Solid State Communications, 142 (2007) 190–194.

[3] J. Wojnarowicz, Sylwia Kusnieruk , Tadeusz Chudoba , Stanislaw Gierlotka , Witold Lojkowski , Wojciech Knoff , beilstein j. Nanotechnol. 6 (2015)1957–1969.

[4] X. F. Wang, Xu. J. B, Zhang. B, Yu. H. G, Wang. J, Zhang. X, Yu J. G, Li. Q, Adv. Mater. 18 (2006) 2476−2480.

[5] S. Fabbiyola, L. John Kennedy, Udaya Aruldoss , M. Bououdina, Powder Technology, 286 (2015) 757–765.

[6] S. S. Abdullahi, Yuksel Koseogˇlu, Sadik Guner , Sinan Kazan , Bayram Kocaman, Chifu E. Ndikilar, Superlattices and Microstructures, 83 (2015) 342–352.

[7] Y. Köseoˇglu, J Supercond Nov Magn, (2014).

[8] L. B. Duan, G. H. Rao, J. Yu, Y.C. Wang, Solid State Communications, 145 (2008) 525–528.

[9] A. Chand, Shipra Gupta, M. Vasundhara, Shalik R. Joshi, Geeta R. Muttae and Jai Singh,RSC Adv, 7 (2017) 50527–50536.

[10] A. Franco Jr, H.V.S. Pessoni, P.R.T. Ribeiro, F.L.A. Machado, 426 (2017) 347–350.

[11] R. Elilarassi, G. Chandrasekaran, J Mater Sci: Mater Electron, 24 (2013) 96–105.

[12] G. Z. Xing, J. B. Yi, F. Yan, T. Wu, and S. Li, Applied Physics Letters 104 (2014) 202411.

[13] M. Naeem, K. Kamran, S. Qaseem, S. Rizwan Ali, and S. Imran Ali, Journal of Basic & Applied Sciences, 13 (2017) 370-374.

[14] Z. Lv, Junran Zhang, Wei Niu, Minhao Zhang, Chin. Phys. B, 25 (2016) 097502.

[15] S. Matteppanavar, Sudhindra Rayaprol, Anupama A.V. Basavaraj Angadia, Balaram Sahoo, Ceramics International. 41 (2015) 11680-11686.

[16] C. Thangamani, Surface Review and Letters (2019).

[17] M. Ponnar, C. Thangamani, P. Monisha, S.S. Gomathi, K. Pushpanathan, Applied Surface Science 449 (2018) 132–143.

[18] S. Ramya, G. Viruthagiri R. Gobi N. Shanmugam N. Kannadasan, J Mater Sci: Mater Electron 27 (2016) 2701–2711.

[19] S. Layek and H. C. Verma, Journal of Nanoscience and Nanotechnology, 13 (2013) 1848–1853.

[20] X. G. Zheng, T. Mori, K. Nishiyama, W. Higemoto, and C. N. Xu, Solid State Commun. 132 (2004) 493.

[21] P.P. Gauns Dessai, V. M. S. Verenkar, Journal of Materials Science: Materials in Electronics, 29 (2018) 6924–6936.
[22] C. DX, Sanchez A, Taboada E, Journal of Applied Physics 105 (2009) 083924.

CHAPTER 7

Electrical properties of Co doped ZnO, Nd doped In_2O_3 & Ni doped CuO Dilute Magnetic Semiconductor Nanoparticles

Introduction

Electrical transport properties of DMS materials are generally used to understand the conduction mechanisms involved in DMS materials. This information is also useful in deciding the suitability of the materials for particular type of application. Oxide based DMS materials are the most versatile materials having numerous spintronic applications. These materials find applications in solar cells, logic devices, spin polarized light emitting diodes, nonvolatile memory storage, spin field effect transistors. A detailed study of the important electrical properties like thermo-power, resistivity, dielectric constant and dielectric loss with respect to frequency and temperature of Co doped ZnO, Nd doped In_2O_3 and Ni doped CuO nanoparticles is discussed here. The fundamental of electrical parameters and a model explaining the dielectric properties briefly is also mentioned in this Chapter.

7.1 Co doped ZnO, $Zn_{(1-x)}Co_xO$ (x = 0.05, 0.10, 0.15, 0.20).

7.1.1 Thermoelectric Power

Thermopower measurements on the samples were carried out in the temperature range of 300K (27 ^oC) to 773K (500 ^oC). The plots obtained for Seebeck coefficient 'S' (V/K) variation with respect to the temperature 'T' (^oC) are shown in Figure 7.1.1.1 (a) for all the samples. The 'S' was calculated using equation 7.1.1 (a) and the charge carrier concentrations were estimated using equation 7.1.1 (b) and 7.1.1 (c).

$$\boldsymbol{S = \frac{\Delta V}{\Delta T}} \qquad \text{7.1.1 (a)}$$

$$\boldsymbol{n = 2\left(\frac{2\pi e_m KT}{h^2}\right)^{3/2} \exp\left[-\frac{(E_c - E_f)}{KT}\right]} \qquad \text{7.1.1 (b)}$$

$$\boldsymbol{p = 2\left(\frac{2\pi h_m KT}{h^2}\right)^{3/2} \exp\left[-\frac{(E_f - E_v)}{KT}\right]} \qquad \text{7.1.1 (c)}$$

Where, in equations 7.1.1a and in equations 7.1.1c, ΔV is the thermo-electro motive force (e.m.f) , ΔT is the temperature difference between hot and the cold

junction; 'h_m' and 'e_m' are the rest mass of the charge carriers (holes and electron), 'K' is the Boltzmann constant, '*h*' is the Planck's constant and 'S' is the Seebeck coefficient. E_c is the bottom energy level of the conduction band, E_v is the upper energy level of the valence band and E_f is the position of the fermi energy level.

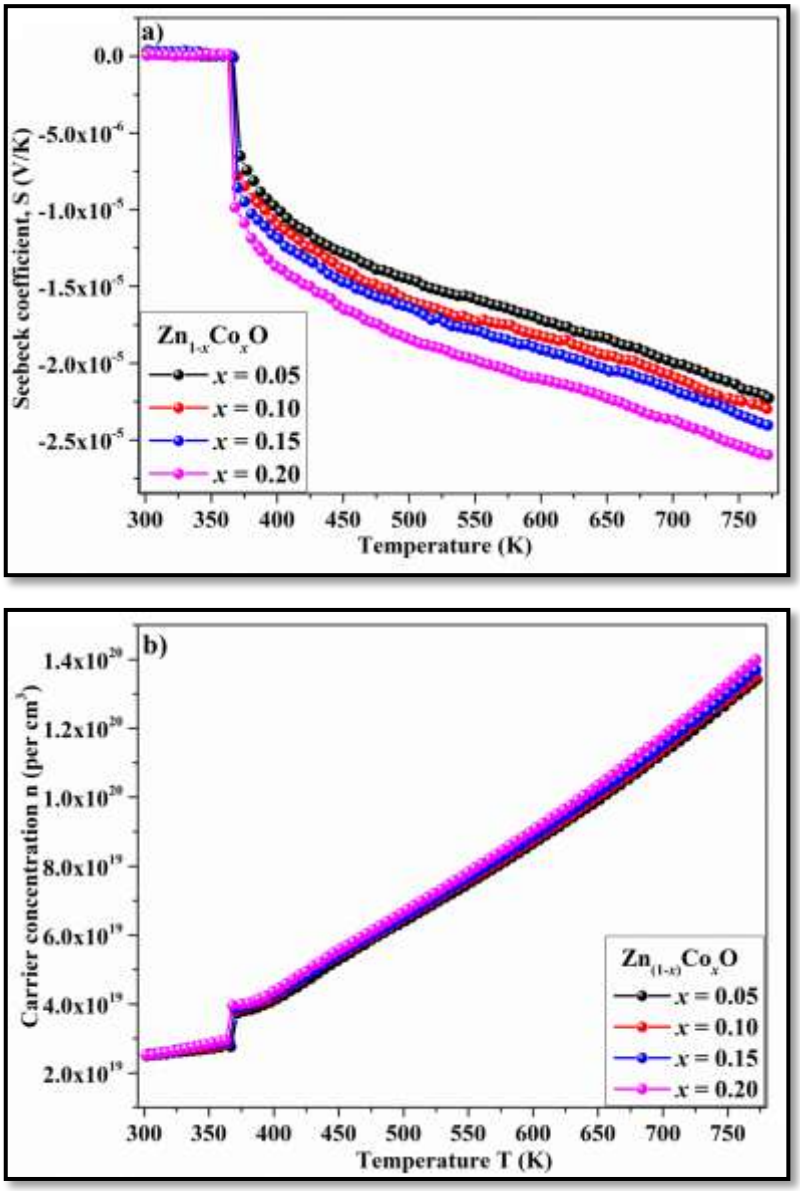

Figure 7.1.1.1: (a) Seebeck coefficient variation with respect to temperature and (b) Variation of Carrier concentration with respect to temperature for Co doped ZnO.

The material type (p-type or n-type) information is provided by the polarity signal of the Seebeck coefficient that gives the charge carriers (holes or electron) nature [1]. For all the samples Seebeck coefficient 'S' displays a positive value

that stays steady for lower range temperature up to 363K (90 ^{o}C) representing a p-type semiconductor behavior. Figure 7.1.1.1 (b) shows that there is a negligible raise in carrier concentration in this range of temperature. Near about 363K (90^{o}C) a signal of change in the nature of semiconductor behavior (p-type to n-type charge carriers) occurs all of a sudden due to a first order charge polarity transition. A large enhancement in charge carrier concentration (n-type) is noticed due to this transition. Therefore from room temperature to about 363K (90^{o}C) the samples acts as p-type semiconductors and from a temperature little higher than 363K (90^{o}C) onwards the samples acts as n-type of semiconductors with electrons replacing the holes as majority charge carries employed in conduction mechanism [1,2]. A charge carrier concentration trends with respect to temperature are displayed in Figure 7.1.1.1 (b). The charge carrier concentration enhances from room temperature approximate value of $2.53x10^{19}$ per cm^3 to a value of $1.35x10^{20}$ per cm^3 at 363K (500^{o}C). At elevated temperature conduction electrons which are thermally activated electrons plays an important character in Seebeck coefficient. It may be seen that for all the Co^{2+}concentrations increase in charge carrier population results in decrease in the seebeck coefficient value. At elevated temperatures charge carriers are thermally activated and those carriers which attains adequate amount of energy jump from valance band into the conduction band. 'S' values decreases due to increment of charge carriers (electrons) in the conduction band which enhances the charge carrier collisions at high temperature [3]. However what is interesting is the first order transition from p-type of semiconductor to n-type of semiconductor at a temperature of 363K (90 ^{o}C) which can be very useful for application.

7.1.2 DC Resistivity

In addition to thermopower of a material the electrical resistivity provides significant information about the conduction process in solid material and also determines how strongly the material will resists the flow of electric current. $\log_{10}$ ρ (Ω cm) v/s 1000/T (K^{-1}) plots are shown in Figure 7.1.2.1 (a) for $Zn_{(1-x)}Co_xO$ with x = 0.05, 0.10, 0.15 and 0.20. The resistivity 'ρ' was calculated at different temperatures using equation 7.1.2 (a).

$$\boldsymbol{\rho} = \left(\frac{\mathbf{VA}}{\mathbf{It}}\right) \qquad 7.1.2\ (a)$$

Where ‘V’ is the applied voltage, ‘A’ is pellet area, ‘I’ is Current and ‘t’ is pellet thickness.

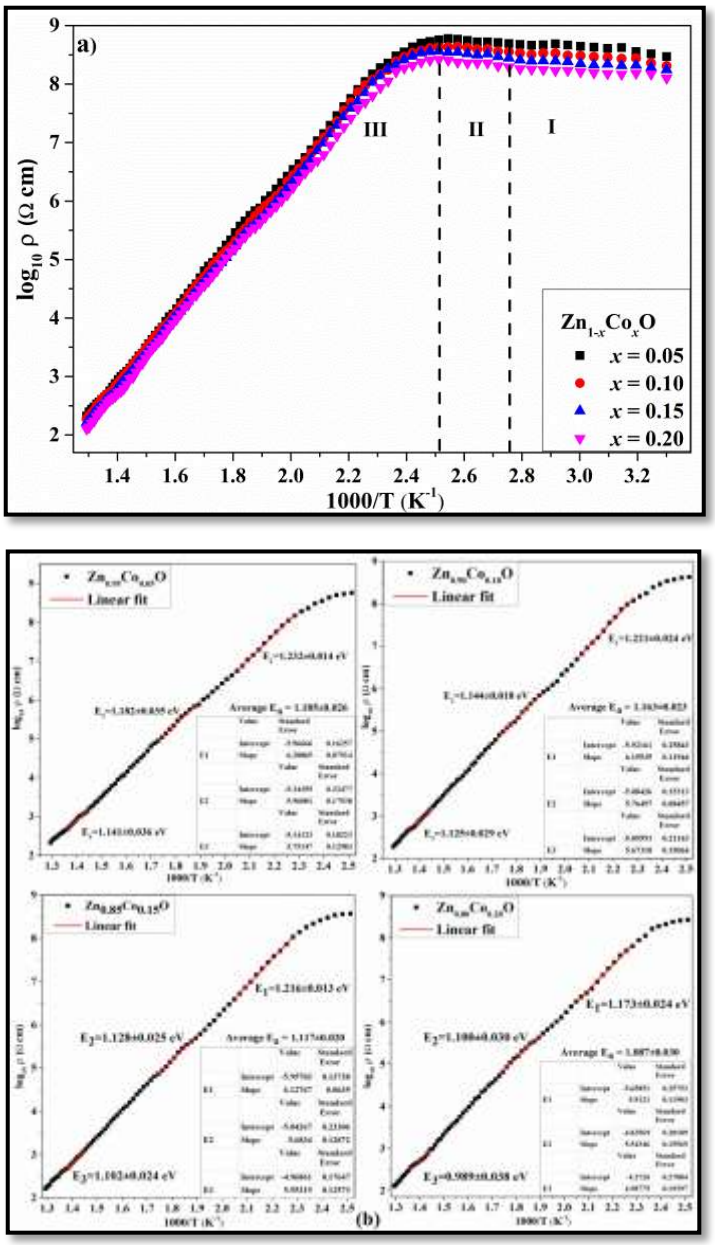

Figure 7.1.2.1: (a) Variation of resistivity with respect to temperature and (b) Arrhenius fitted curves at elevated temperature region for Co doped ZnO nanoparticles.

The resistivity curves over the temperature range from room temperature to 773K (500 ^{o}C) are separated into three different regions, that is the region I is between 300K (27^{o}C) - 363K (90^{o}C), region-II between 363K (90^{o}C) – 398K (125^{o}C) and region-III is between 398K (125^{o}C) – 773K (500^{o}C) respectively as

shown in Figure 7.1.2.1 (a). It is noticeable that there is a little increase in the resistivity values which rises with temperature from 300K (27^{o}C) to 363K (90^{o}C) as displayed in region I. Generally resistivity enhances in region I due to activation of phonon vibrations and phonon induced scattering of charge carriers consequently reducing the mean free path of the free charge carriers [4,5]. However, enhancement of resistivity in the current materials due to phonon vibrations is enormously less as compared to the reports published on similar materials [6,7]. This implies two things, for occurrence of multiple scattering of charge carriers either the phonon vibration are not so intense or the there are less amount of charge carriers in the sample at these temperatures. Since the samples show high resistivity values in this region which is of the order around 10^{8} Ohm-cm and above it means that there is less number of charge carriers for conduction. It may be also seen that the resistivity from room temperature to about 363K (90^{o}C) positive charge carriers (holes) are dominated in the system as shown in 7.1.1.1 (a), generally in semiconductors movement of holes is different from electron movement as a result huge effect of phonons will not be there in the conduction of holes in this region. First order phase transition around at 363K (90^{o}C) can be obviously noticeable from Figure 7.1.1.1 which shows the Seebeck coefficient and charge carrier concentration curves with respect to temperature. At this particular temperature there is sufficient thermal energy to vacant some valance electrons into the conduction band. At this particular temperature electron concentration is of the order of 3.79x10^{19} per cm^{3} that normally exists in a semiconductor. A slight increase in resistivity is observed because of charge carrier scattering in the temperature region II that is from 363K (90^{o}C) to about 398K (125^{o}C) phonons become active due to change in charge carrier and its result can be observed in Figure 7.1.2.1 (a). Steep fall of resistivity in region III of the materials can be seen in Figure 7.1.2.1 (a) which implies that in this region maximum thermal energy is available for the ejection of charges that goes on rising and enhancing the electron charge carrier population in the conduction band. From Figure 7.1.1.1 (b) it is seen that in region II the concentration of charge carriers gradually enhances with temperature till around 398K (125^{o}C). After initial transition at 363K (90^{o}C), the charge carrier concentration progressively increases and can be observed in region II. Charge carrier concentration value at temperature 398K (125^{o}C) is 4.21x10^{19} per cm^{3} enhances

rapidly with rising temperature to approach $1.35x10^{20}$ per cm^3 at 773K (500^oC) in region III. From this analysis it appears that resistivity and thermopower are reliant on Co^{2+} content. As Co^{2+} content is enhanced from $x = 0.05$ to $x = 0.20$ the resistivity shows a descent decline, on the other side thermo power and carrier concentration shows a growing behavior.

The activation energy in region III has been calculated using Arrhenius equation 7.1.2 (b) for all the samples.

$$\rho = A \exp\left(\frac{E_a}{kT}\right) \qquad 7.1.2(b)$$

Where ρ is the resistivity, T is the temperature, A is the constant, E_a is the activation energy and k is the Boltzmann constant. For all the samples in high temperature region III Arrhenius plots are fitted linearly to attain E_a as displayed in Figure 7.1.2.1 (b). Some major factors which are dependent on the activation energy as per the reports are nature of the material (crystalline or amorphous), size of the crystallite and the temperature at which the measurements are obtain [8,9]. Usually activation energy is the energy that required to hop the charge carriers (electrons) from valance to the conduction band [8,10]. At high temperature large amount of thermal energy exists for the charge carriers which results in decreasing the activation energy [11]. These assists in accelerating the charge transport process as more and more electrons are moved in to conduction band therefore dropping the resistivity of the material. This is obvious from the activation energy estimation done at various temperatures between 398K (125 ^oC) and 773K (500 ^oC). Figure 7.1.2.2 shows the activation energy values (E_a) with inset displaying the average activation energy estimated using equation 7.1.2 (b) about three different temperatures from the resistivity curves. It may be noted that with increase in temperature the E_a values reduces which authenticates the information mentioned earlier regarding decreasing of activation energy with increasing temperature. As the Co^{2+}content increases the activation energy continues to decline as shown in Figure 7.1.2.2. Lowering of 'E_a' could be understood on the basis of band gap decrement with increase of Co^{2+} content. It has been reported that with raises in Co^{2+} concentration the band gap decreases [14]. By increasing Co^{2+} content in the sample the density of the charge carrier increases as the Fermi level is shifted near to the conduction band. Therefore with increasing Co^{2+} concentration the energy gap between the donor level and the conduction band of

the material goes on decreasing [11,12]. So energy required for the charge carrier in valance band to hop into conduction band reduces continuously. Consequently addition of more charge carriers at elevated temperature in the conduction and decreases the samples resistivity from around 2.95×10^{8} Ωcm at room temperature to about 2.19×10^{2} Ωcm at 773K (500^{o}C).

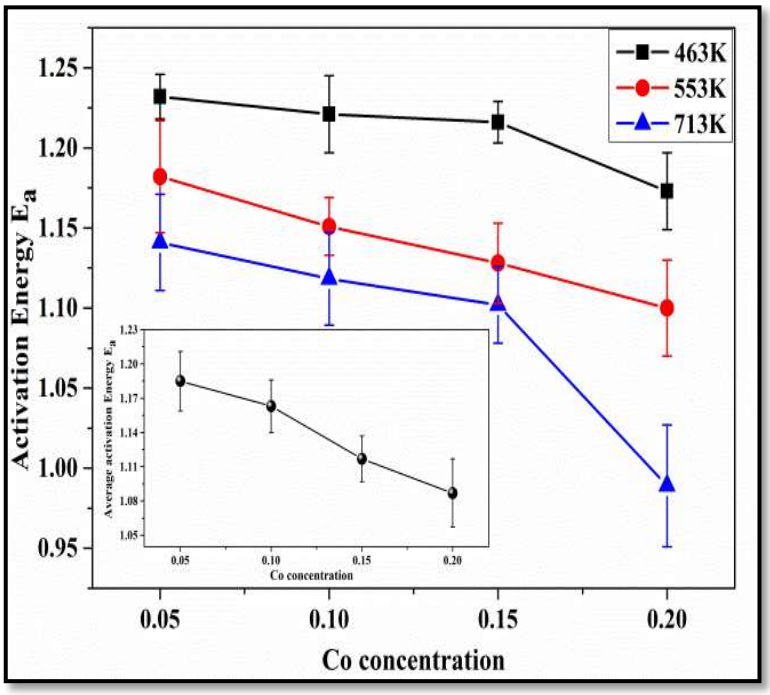

Figure 7.1.2.2: Variation of 'E_a' with Co^{2+} concentration at temperatures 463K (190 ^{o}C), 553K (280 ^{o}C) and 713K (440 ^{o}C).

Figure 7.1.2.3 shows the variation of resistivity that is (Δρ/ΔT) with respect to temperature at various Co^{2+} content and at different temperatures. It is seen that Δρ/ΔT displays similar declining trend with increase in Co^{2+} content in the sample at different temperatures signifying reduction in resistivity. Δρ/ΔT calculated at 313K (40^{o}C) and 363K (90^{o}C) are positive for all the specified Co^{2+} content, while Δρ/ΔT are negative at 398 K (125^{o}C), 463 K (190^{o}C), 553K (277^{o}C) and 713K (440^{o}C) for all the specified Co^{2+} content as shown in Table 7.1.1 (a). Since all the plots of Δρ/ΔT display an identical behavior which indicates that the fall of resistivity with temperature is similar for all Co^{2+} content

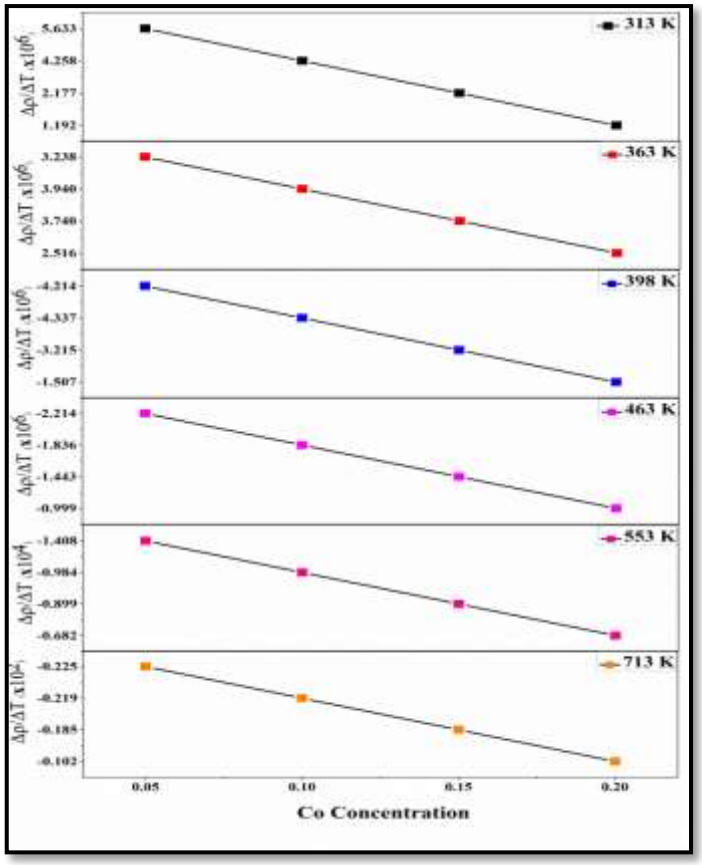

Figure 7.1.2.3: Variation of (Δρ/ΔT) with respect to Co^{2+} concentration at various temperatures.

Table 7.1.1 (a) Δρ/ΔT values at different temperature and Co^{2+} concentrations.

$\frac{\Delta\rho}{\Delta T}$						
Sample	**313K ($x10^6$)**	**363K ($x10^6$)**	**398K ($x10^6$)**	**463K ($x10^6$)**	**553K ($x10^4$)**	**713 K ($x10^2$)**
0.05	5.633	3.238	-4.214	-2.214	-1.408	-0.225
0.10	4.258	3.940	-4.337	-1.836	-0.984	-0.219
0.15	2.177	3.740	-3.215	-1.443	-0.899	-0.185
0.20	1.192	2.516	-1.507	-0.999	-0.682	-0.102

7.1.3 Dielectric Properties

Figure 7.1.3.1 (a) displays the variation of dielectric constant (ε) as a function of frequency for $Zn_{(1-x)}Co_xO$ with x = 0.05, 0.10, 0.15 and 0.20 nanoparticles at room temperature. Equation 7.1.3 (a) was used to calculate the dielectric constant 'ε'.

$$\varepsilon = \frac{\mathbf{Cd}}{\varepsilon_o \mathbf{R}} \qquad 7.1.3\ (a)$$

Where, 'C' is the capacitance, 'd' is the thickness of the pallet, 'R' is the area of the pallet and 'ε_o' is the permittivity of free space [ε_o= 8.85 x 10^{-14} (F/cm)]. From the Figure 7.1.3.1 (a) it is noticeable that initially the dielectric constant values shrinks very quickly with increasing frequency for all the Co^{2+} concentrations and further on escalating the frequency dielectric constant 'ε' values gradually decreases. This falling trend in dielectric constant with respect to frequency could be clarified on the basis of Maxwell-Wagner interfacial polarization model [13]. According to this model, it is assumed that dielectric medium is made-up of conducting grains which are separated by poor conducting grain boundaries. In presence of applied external electric field, charge carriers with reverse polarity moves inside the grain in opposite directions. The moving charges collected at the grain boundaries due to separation of poor conducting grain boundaries. Therefore in presence of applied external electric field, the grain functions as an electric dipole termed as space charge polarization or interfacial polarization. This type of polarization shows high dielectric constant value for all the samples at lower frequency [14,15]. It can be seen that with increases in Co^{2+} content in the sample the overall 'ε' increases due to increases in density of charge carrier that reliant on both the Co^{2+} concentration in the sample and the applied frequency. For lower frequencies as well as at higher Co^{2+} concentration a high value of dielectric constant is noticeable.

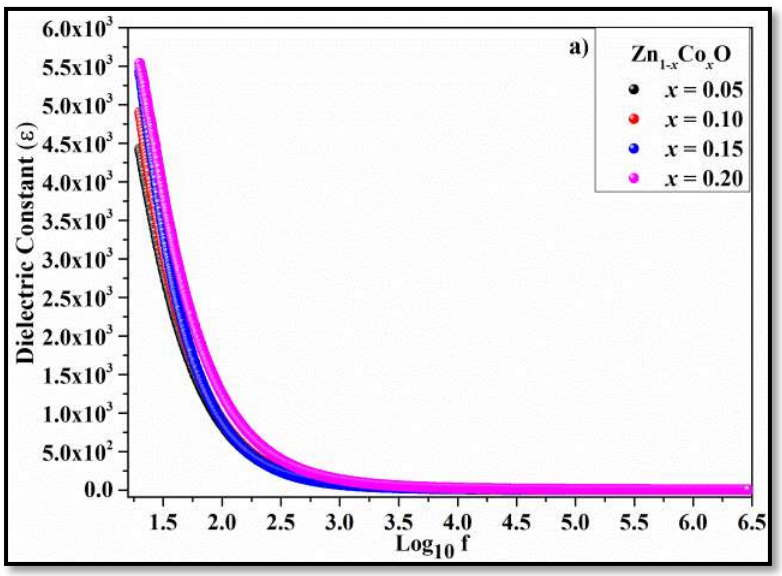

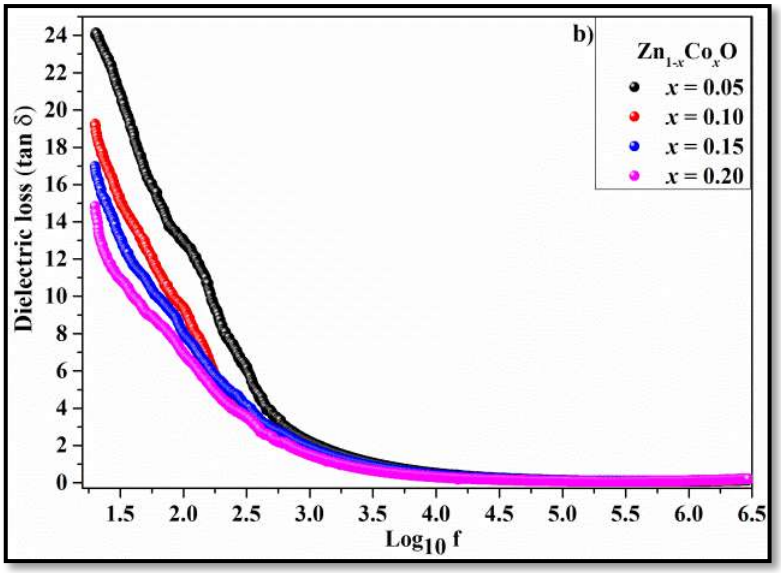

Figure 7.1.3.1: Room temperature variation of (a) Dielectric constant (ε) and (b) Dielectric loss (tanδ) with respect to frequency for Co doped ZnO nanoparticles.

Additionally in dielectric constant (ε) crystallite size also plays very crucial role [16,17]. Our result on structural analysis shows that with increase in Co^{2+} concentration the crystallite size of the material decreases. It is clear that dwindling in crystallite size can enhance the amount of crystallites per unit volume. Consequently dielectric constant of the material is increased at low frequencies. Thus reduction in crystallite size enhances grain boundary of the crystallites per unit volume and also the surface to volume ratio. Due to increased Co^{2+} content results in increasing the grain boundary and also amplifies the concentration of charge carrier which gives raise in dielectric constant at lower frequencies [18]. As the frequency is increased the value of dielectric constant (ε) falls continuously. This may be attributed to the sluggishness of dipole movements which are not capable to follow the high applied frequency that is associated with the Co^{2+} and Zn^{2+} ions hopping rate. Consequently the contribution due to polarizability lags back with respect to the applied external electric field at higher frequencies [13,15].

Figure 7.1.3.1 (b) shows room temperature Dielectric loss (tan δ) with respect to frequency. It is noticeable that initially 'tan δ' declines quickly with increase in frequency and as the applied frequency further increases 'tan δ' decreases slowly. This diminishing trend of 'tan δ' shows similar variation like 'ε'. Normally, polar dielectric molecules require little amount of electric energy to adjust in the

direction of applied frequency to surmount the internal forces. Movement of molecules from one place to another place and the rotary motion of dipole molecules in existence of applied electric field uses fraction of electric energy that results in energy loss. Dielectric loss is highest for x = 0.05 sample and lowest for x = 0.20 sample at lower frequency which is clearly seen from the figure. Factors such as crystallite size, grain boundary effects and the ions hopping rate may influence the dielectric loss in the materials. Our investigation made on structural properties shows that with increase in Co^{2+} content results in decrease in crystallite size in the samples. Reduction in crystallite size amplifies the surface to volume ratio that enhances the number of crystallite per unit volume consequently surface charge polarization increases. As a result the energy required for the dipoles to orient themselves in the direction of applied electric field is mainly depends on the Co^{2+} content and therefore become lower at lower frequency for higher Co^{2+} content [4]. High dielectric constant is displayed by the sample having high Co^{2+} content with low grain size. It is seen from Figure 7.1.3.1 (b) that 'tan δ' curves continues to decline with rise in Co^{2+} content because of the reasons stated above. In the lower frequency region a wide hump is noticeable for all the tan δ curves. That may be referred as a relaxation peak that decreases smoothly with rise in Co^{2+} content. A relaxation peak is generally seen when the hopping frequency of the charge carrier externally matches with the applied electric field frequency [16]. Shrinking of 'tan δ' with Co^{2+} content and applied electric field implies that these materials could be utilized for spintronic applications in high frequency devices [19].

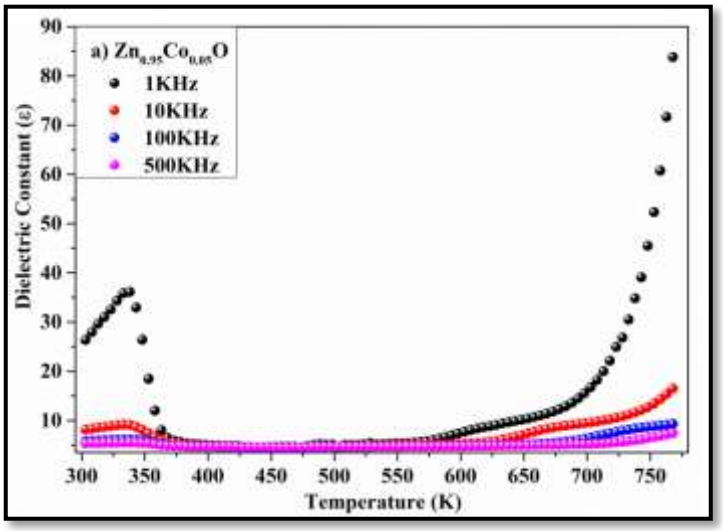

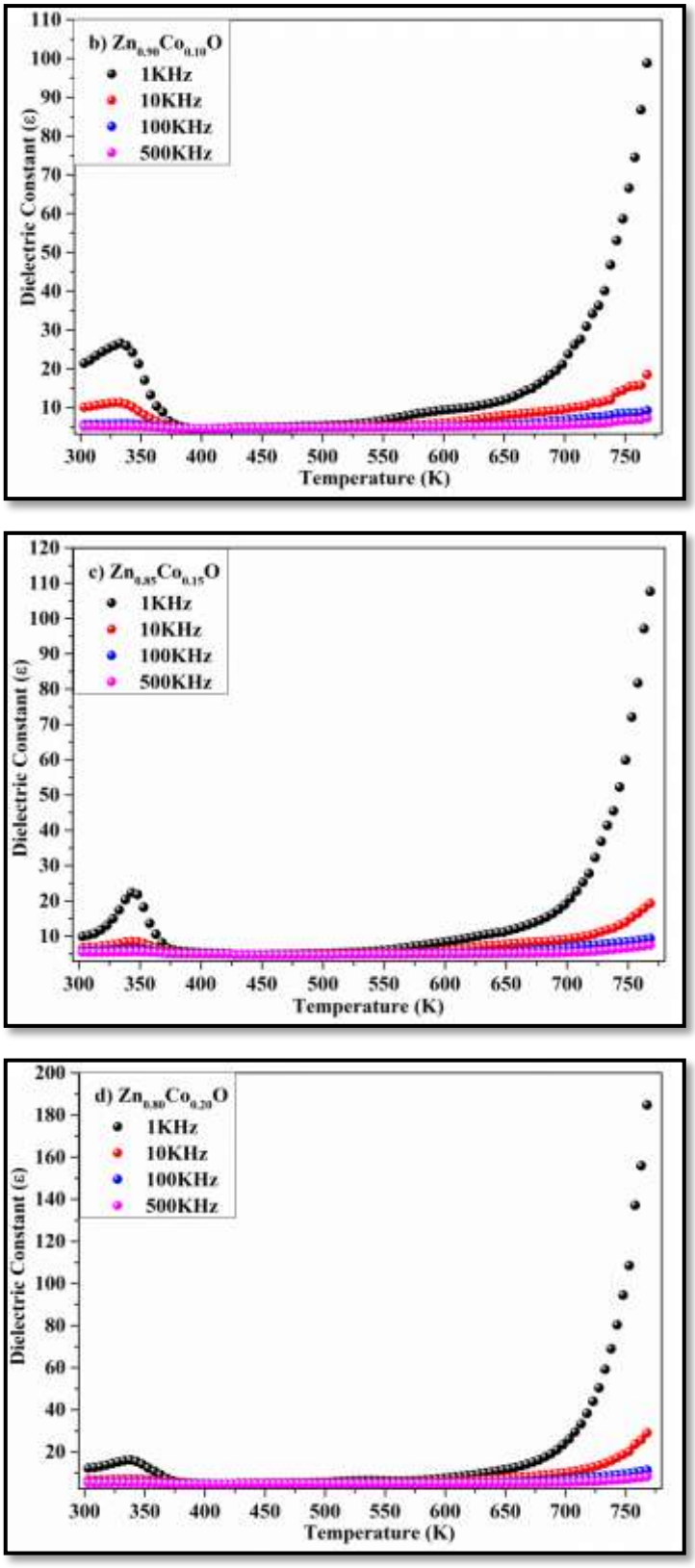

Figure 7.1.3.2: Variation of dielectric constant ('ε') with temperature for (a) $Zn_{0.95}Co_{0.05}O$, (b) $Zn_{0.90}Co_{0.10}O$, (c) $Zn_{0.85}Co_{0.15}O$, (d) $Zn_{0.80}Co_{0.20}O$.

Dielectric constant of a dielectric material with frequency is very sensitive to temperature. 'ε' of all the samples was recorded at different frequencies from room temperature to 773K (500^{o}C). The corresponding plots obtained are shown in Figure 7.1.3.2. Initially all the samples displays a peaking behavior in the lower temperature region (300K and 400K) for all the frequencies. From the structural investigations it was observed that the crystallite size is dependent on the Co^{2+} content in the sample, hence one can easily co-relate the link between magnitudes of peak height with the material particle size. The peaks are identified as relaxation peaks that are dependent on frequency as these are produced due to the relaxation time, which is the time taken by the electric dipoles to orient in the direction of applied electric field. Resonance phenomenon occurs when the relaxation time matches with the applied field time period, wherein there is a maximum energy transfer from the applied ac field. Appearance of similar peaks in dielectric loss v/s temperature curves as shown in Figure 7.1.3.3 testifies this reasoning. The relaxation peak spread and the peak height of both dielectric constant and dielectric loss decrease with increasing ac field frequency finally to become flat at higher frequency of 500 KHz. The relaxation peak at higher frequency and lower temperature disappear due to charge carrier localization [11,18]. But with increase in the temperature there is increased in thermal energy which increases the hopping rate of charge carrier resulting in amplified charge carrier mobility thus increasing the material conductivity. Therefore there is augmentation of dipole polarization that is dependent on applied frequency [11,10], and Co^{2+} content in the sample. The tan δ curves shown in Figure 7.1.3.3 displays similar behavior as shown by dielectric constant curves illustrated in Figure 7.1.3.2. In the crystalline material, When the dielectric polarization lags back the applied frequency dielectric loss occurs which is mainly due to grain boundary effect. The dielectric properties in the case of nanoparticle samples may depend on factors such as sample preparation method, structure, size of the crystallite, chemical composition and preparative conditions [10].

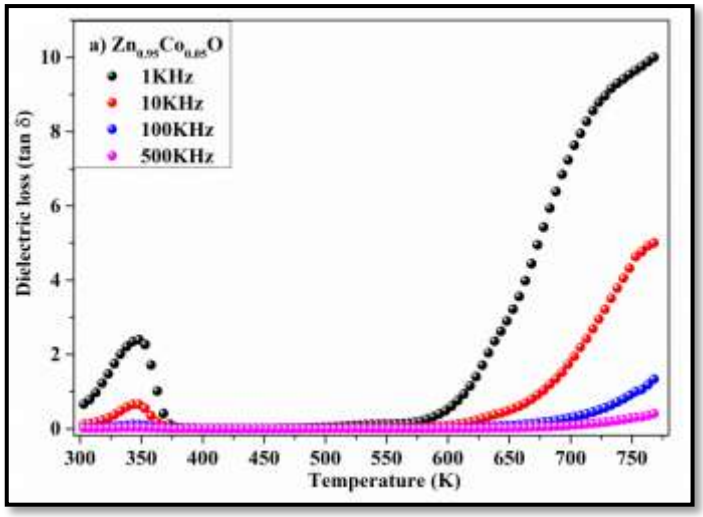
a) $Zn_{0.95}Co_{0.05}O$
1KHz
10KHz
100KHz
500KHz
Dielectric loss (tan δ)
Temperature (K)

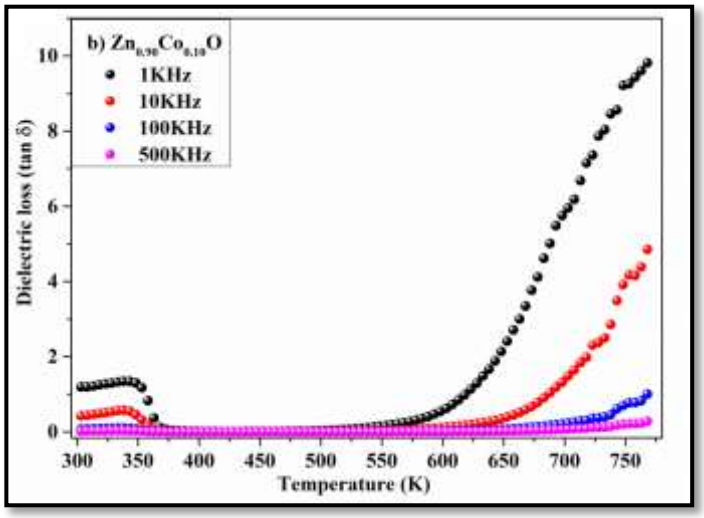
b) $Zn_{0.90}Co_{0.10}O$
1KHz
10KHz
100KHz
500KHz
Dielectric loss (tan δ)
Temperature (K)

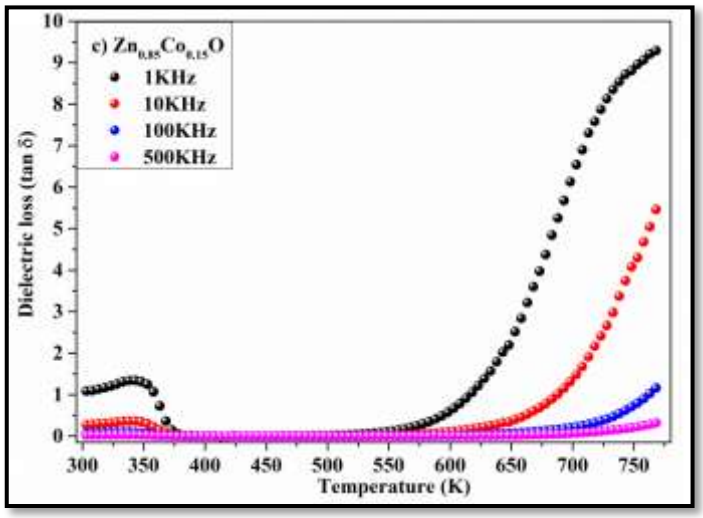
c) $Zn_{0.85}Co_{0.15}O$
1KHz
10KHz
100KHz
500KHz
Dielectric loss (tan δ)
Temperature (K)

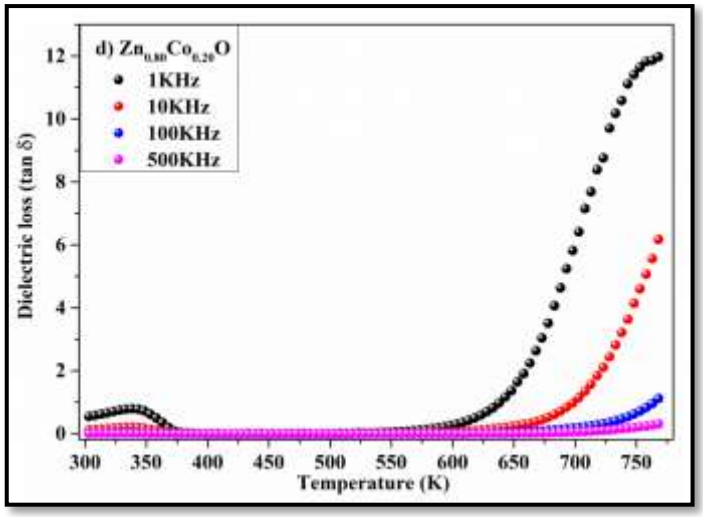

Figure 7.1.3.3: Variation of dielectric loss (tan δ) with temperature for (a) $Zn_{0.95}Co_{0.05}O$, (b) $Zn_{0.90}Co_{0.10}O$, (c) $Zn_{0.85}Co_{0.15}O$, (d) $Zn_{0.80}Co_{0.20}O$.

7.1.4 Impedance Analysis

Impedance investigation is very useful technique to study the grains and grain boundaries effects in the samples, as grain boundaries and the grains play important role in the electrical transport properties of the material [49, 50]. Figure 7.1.4.1 displays the cole-cole plot for $Zn_{(1-x)}Co_xO$ (x = 0.05, 0.10, 0.15, 0.2) nanoparticles. The real part of the complex impedance Z' and the imaginary part of the complex impedance Z" is the calculated using equation 7.1.4 (a) and equation 7.1.4 (b) respectively. Where Z is the complex impedance and θ is the phase angle.

$$Z' = |Z| \cos\theta \qquad 7.1.4\ a$$

$$Z'' = |Z| \sin\theta \qquad 7.1.4\ b$$

Normally cole-cole graphs shows various semicircular arcs that belong to the different electrically active regions [50, 51], the first semi-circle in cole-cole plot at lower frequency is due to the grain boundaries resistance and the second semicircle at higher frequency gives the grains contribution of the material [51]. In present case only the first semicircular arcs are observed for all the samples as shown in Figure 7.3.4.1. Moreover the cole–cole plots shows in the figure indicates dominating nature of grain boundaries resistance in the material. Furthermore it is observed that the size or the diameter of semicircular arc decreases which implies that the grain boundaries resistance decreases with increase in Co^{2+} content. The decrement in grain boundaries resistance is due to

replacement of Zn^{2+} ions by Co^{2+} ions in ZnO matrix [52,53]. On increasing Co^{2+} content in the ZnO matrix the number of charge carrier (electron) concentration increases for conduction process which results in decrease in electrical resistance of the sample [54]. Impedance analysis shows typical nature of semiconductor wherein the resistivity decrease which signifies that there is increase in conductivity with increase in Co^{2+} content in the samples.

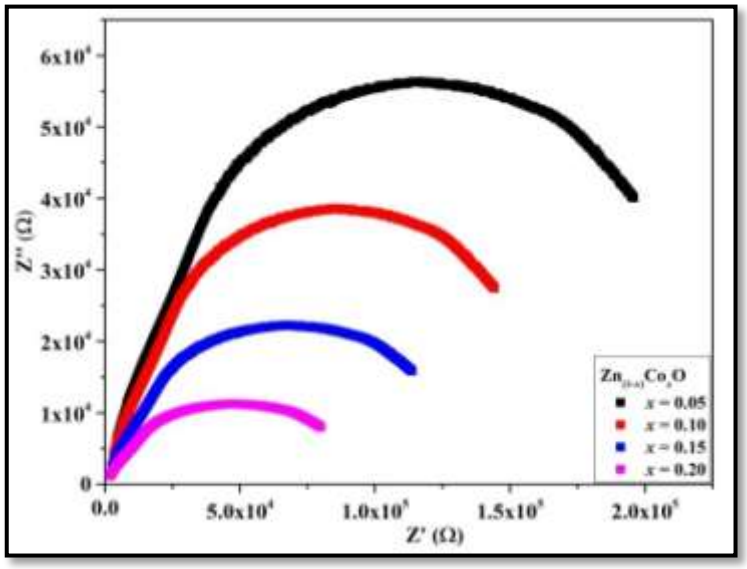

Figure 7.1.4.1: Cole-Cole plot for Co doped ZnO nanoparticles.

7.2 Nd doped In_2O_3, $In_{(2-x)}Nd_xO_3$ (x = 0, 0.10, 0.15, 0.20)

7.2.1 Thermoelectric Power

Figure 7.2.1.1 (a) displays the variation of Seebeck coefficient 'S' (V/K) as a function of Temperature 'T' (^oC) for $In_{2-x}Nd_xO_3$ (x = 0, 0.10, 0.15, 0.20) nanoparticles. The 'S' for all the samples was calculated using equation 7.1.1 (a) and the charge carrier concentrations 'n' were calculated at different temperature using equation 7.1.1 (b). Figure 7.2.1.1 (a) displays that for all the samples seebeck coefficient 'S' curves shows n-type behavior over the entire temperature range. For x = 0 seebeck coefficient 'S' shows n-type behavior with low 'S' values which is due to intrinsic defects mainly produced by the oxygen vacancies [7,20-22] and as the Nd^{3+} concentration is increased from 0.10 to 0.20 the seebeck coefficient 'S' values increases which signifies that majority of the charge carries are electrons taking place in conduction process [23,29].

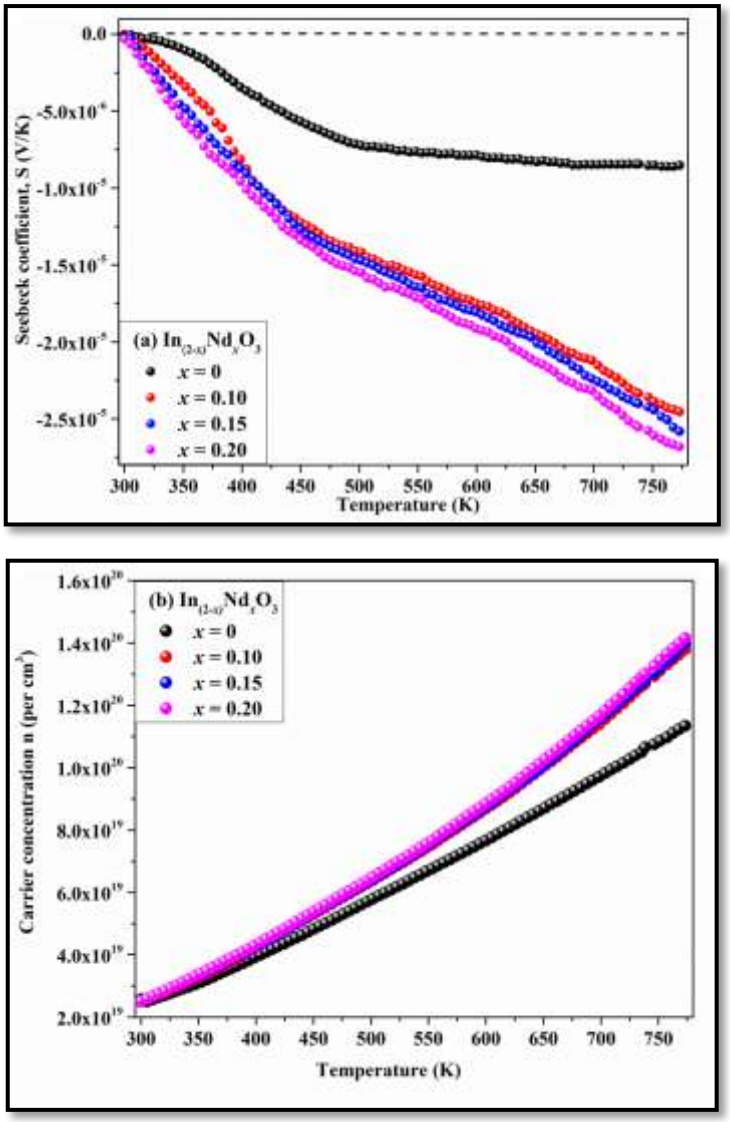

Figure 7.2.1.1: (a) Variation of Seebeck coefficient as a function of temperature and (b) Variation of Carrier concentration as a function of temperature for Nd doped In_2O_3 nanoparticles.

Figure 7.2.1.1 (b) displays the curves of charge carrier concentration '*n*' vs. temperature of the hot junction. A carrier concentration curve demonstrates that with increasing Nd^{3+} concentration and with the increasing hot junction temperature the charge carrier concentration increases. Seebeck coefficient 'S' values, the charge carrier concentration values at room temperature and at 773K (500 ^oC) for all samples are tabulated in Table 7.2.1 (a). It is seen that the 'S' values reduces for all the Nd^{3+} content with increase in carrier concentration because at high temperatures thermally activated electrons gains adequate amount of energy to hop the electrons from valance band to the conduction band.

Intensification of electrons (charge carrier) in the conduction band boosts the charge carrier collisions and result in lowering the 'S' values [25].

Table 7.2.1 (a): Calculated values of Seebeck coefficient 'S' values, charge carrier concentration '*n*' at room temperature and at 500^{o}C for Nd doped In_2O_3 nanoparticles.

Samples	Seebeck coefficient 'S'		charge carrier concentration '*n*'	
	RT	773K	RT	773K
In_2O_3	-2.92×10^{-8}	-8.52×10^{-6}	2.57×10^{19}	1.13×10^{20}
$In_{1.90}Nd_{0.10}O$	-5.05×10^{-8}	-2.45×10^{-5}	2.50×10^{19}	1.37×10^{20}
$In_{1.85}Nd_{0.15}O$	-1.19×10^{-7}	-2.58×10^{-5}	2.50×10^{19}	1.39×10^{20}
$In_{1.80}Nd_{0.20}O$	-3.04×10^{-7}	-2.68×10^{-5}	2.51×10^{19}	1.41×10^{20}

7.2.2 DC Resistivity

Figure 7.2.2.1 shown the plot of $\log_{10}$ ρ v/s 1000/T for $In_{2-x}Nd_xO_3$ (x = 0, 0.10, 0.15, 0.20) nanoparticles. The resistivity 'ρ' for the samples at different temperature was calculated using equation 7.1.2 (a). It is seen from the Figure 7.2.2.1 (a) that all the resistivity curves exhibits two regions in the temperature range from 300K (27^{o}C) to 773K (500^{o}C) i.e. region-I from 300K (27^{o}C) to 333K (60 ^{o}C), region-II from 333K (60 ^{o}C) to 773K (500 ^{o}C) respectively. In the first region the resistivity plots shows enrichment in the resistivity values as the temperature is enhanced from 300K (27^{o}C) to 333K (60 ^{o}C). Initially the overall resistivity values are of the order of 10^8 Ohm-cm for all the samples. But at 333K (60 ^{o}C) sample with x = 0 shows high resistivity values of the order 10^9 Ohm-cm whereas for x = 0.20 displays lower resistivity values of the order 10^8 Ohm-cm. This decrease in resistivity values at 333K (60 ^{o}C) could be possibly due to the increase of Nd^{3+} content in the In_2O_3 matrix. This behavior of increasing resistivity at lower temperature is observed for all the samples which are mainly due to the activation of phonon vibrations and phonon induced scattering of charge carriers [7]. In second region that is from 333K (60 ^{o}C) to 773K (500 ^{o}C) the resistivity value gradually dwindles with increases in temperature. It is seen from the graph that the resistivity values decreases up to the order of 10^5 Ohm-cm at 773K (500 ^{o}C) for all the samples as the Nd^{3+} concentration is increased in from x = 0 to x = 0.20. This could be due to the replacement of Nd^{3+} ions in place of

In^{3+} ions in the In_2O_3 matrix which enhances the carrier concentration in the sample and also could be due to the temperature effect which plays an important role in the resistivity, as a result resistivity decreases and conductivity of a material enhances [26].

For $x = 0$ decrease in resistivity as the temperature increases is due to intrinsic defects created by the oxygen vacancies [27]. Because of these defects donor states are created between the forbidden band and the conduction band. This creation of new levels gives rise to conducting behavior as a result the conductivity increases. In this type of materials the electrical properties are governed by the intrinsic defects [27-29]. However for samples with $x = 0.10$, 0.15, 0.20, as the temperature of the samples increases there is increase in lattice vibration which helps the electrons in the matrix to move with each other and scatter. At higher temperature electron hopping mechanism amplifies and the electrons jump from valance band to conduction band, to enhance the conduction process in the material. The drift mobility of charge carrier increases which shrinks the resistivity and amplifies the conductivity in the material [30]. Thermal excitations of electrons are the major reason for decrease in resistivity in this region.

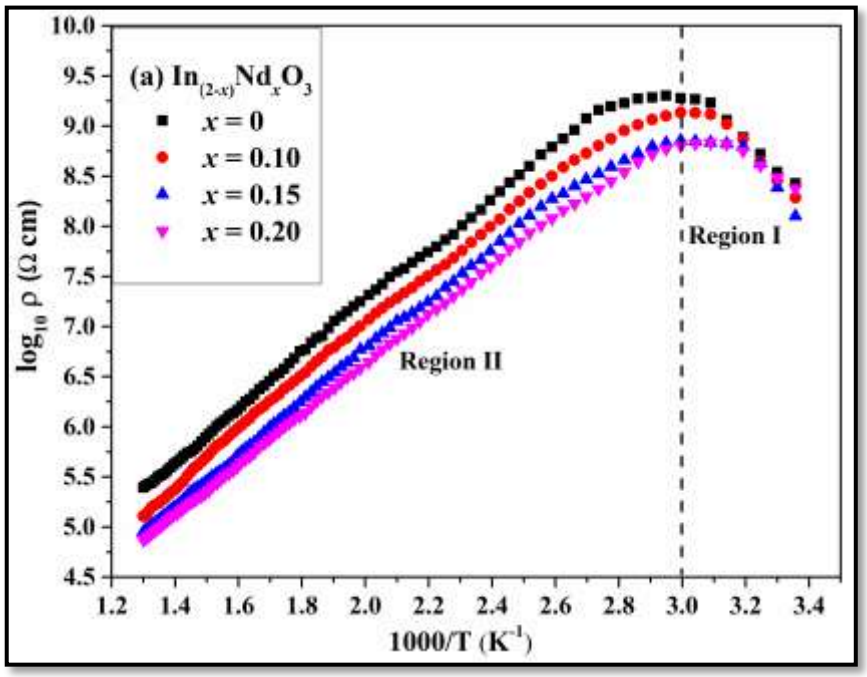

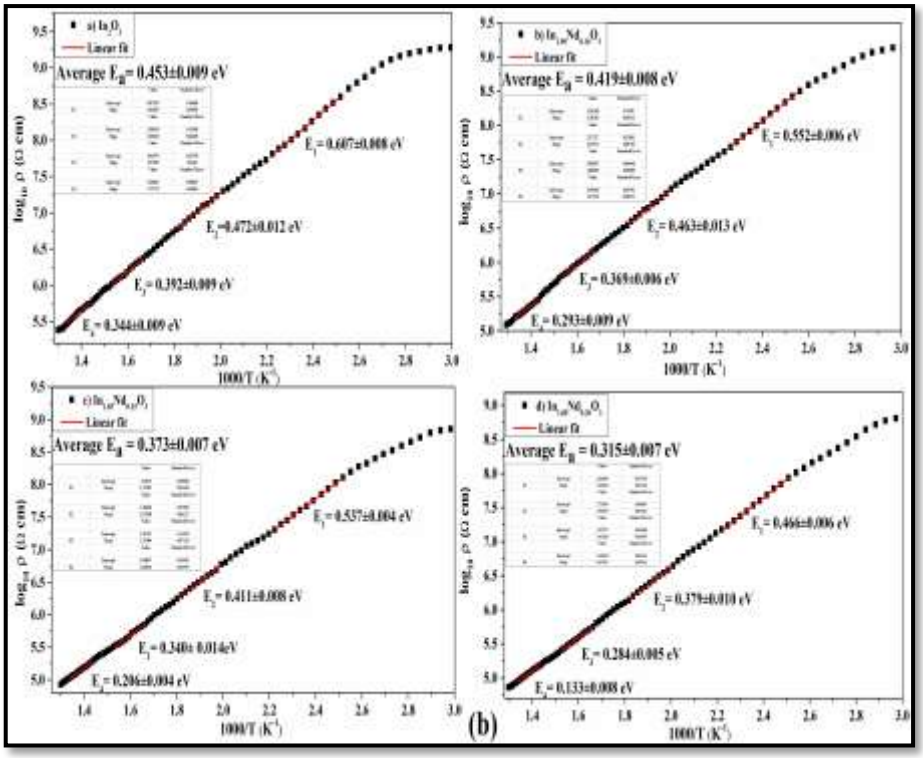

Figure 7.2.2.1: (a) Plot of $\log_{10}$ ρ v/s 1000/T and (b) Arrhenius plot at different temperature region for Nd doped In_2O_3 nanoparticles.

The Activation energy 'E_a' has been calculated using Arrhenius equation 7.1.2 (b) for all the samples in the temperature region that is from 333K (60^{o}C) to 773K (500^{o}C). The Arrhenius plots are fitted linearly in order to attain activation energy as shown in Figure 7.2.2.1 (b). As per available information, the activation energy mainly depends on the crystalline nature of the material, size of the crystallites and the temperature at which the measurements are done [8,9]. In general the 'E_a' is the energy that is required for the electron to jump from valance band to the conduction band in the semiconductor material [8]. Decrease in activation energy at elevated temperature is due the existence of high amount of thermal energy for the charge carriers [11]. This is obvious from the activation energy estimation made at different temperatures in the interval between room temperature to 773K (500^{o}C) that is at 423K (150^{o}C), 523K (250^{o}C), 623K (250^{o}C), 723 K (450^{o}C) respectively as shown in Figure 7.2.2.1 (b). Variation of Activation energy values (E_a) around temperatures 423K (150^{o}C), 523K (250^{o}C), 623K (250^{o}C), 723 K (450^{o}C)respectively are displayed in Figure 7.2.2.2 (a) and the variation of average activation energy with Nd^{3+} concentration shown in Figure 7.2.2.2 (b).

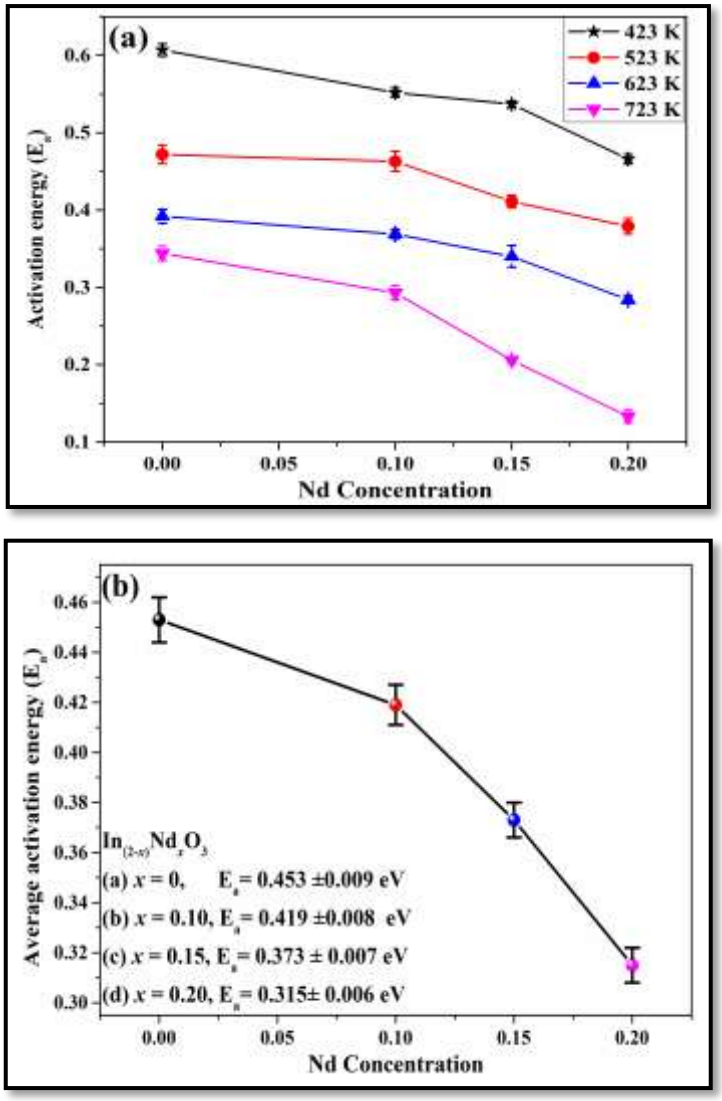

Figure 7.2.2.2: (a) Variation of activation energy (E_a) with Nd concentration at different temperature and (b) Variation of average activation energy (E_a) with Nd concentration.

It can be seen from Figure 7.2.2.2 (a) that the 'E_a' reduces with increasing Nd^{3+} concentration in the sample. On the basis of band gap reduction the decreases in 'E_a' can be identify with increasing Nd^{3+} content in the sample. The Fermi level is shifted near to the conduction band by increasing the amount of Nd^{3+} concentration in the sample which results in increasing the density of donor charge carrier. As a result escalating the Nd^{3+}concentration the energy band gap goes on falling between the donor level and the conduction band [11,12] and consequently the required energy for the charge carriers in the valance band to jump into the conduction band reduces continuously.

7.2.3 Dielectric Properties

Figure 7.2.3.1 (a) displays dielectric constant (ε) as a function of frequency taken at room temperature for $In_{(2-x)}Nd_xO_3$ with x = 0, 0.10, 0.15 and 0.20 nanoparticles and the dielectric constant 'ε' was estimated using equation 7.1.3 (a). It is obvious that for all the Nd^{3+} concentrations initially dielectric constant 'ε' values are found to be high and reduces rapidly with raise in frequency. On the basis of Maxwell-Wagner model the dielectric constant decreasing trend as a function of frequency could be explained [31,32]. Generally Space charge polarization at lower frequencies provides high values of dielectric constant for all the samples [15]. As the Nd^{3+} content in the sample increases the dielectric constant increases which implies that dielectric constant is systematically depends on 'x' content in the sample. This escalation of 'ε' specifies amplification of charge carrier density which dependents on both frequency and the concentration of doping of Nd^{3+} ions into In_2O_3 lattice. Furthermore crystallite size also plays an crucial role in dielectric constant of the material [16,17]. In the structural analysis results reduction of crystallite size was observed with increase of Nd^{3+} content in the In_2O_3 matrix. It is understandable that the number of crystallites per unit volume increases with decrease in crystallite size. As a result, there is augmentation in dielectric constant at lower applied frequencies of the material. So the reductions in crystallite size and increase in surface to volume ratio increases the overall grain boundary surface area of the crystallites, per unit volume that increases the overall surface charge polarization. Therefore this increase in grain boundary and charge carrier concentration is due to increase in Nd^{3+} content which provides high dielectric constant at lower frequencies [18,36]. As the applied frequency increases dielectric constant 'ε' value goes on deteriorating because the orientation of dipole becomes slow and cannot follow the path of applied electric field, associated with the hopping rate of Nd^{3+} and In^{3+} ions and therefore with at higher frequencies the electric polarizability lags behind [31,15].

Figure 7.2.3.1 (b) shows the room temperature dielectric loss 'tan δ as a function of frequency. It can be seen from the figure that for all tan δ curves a broad hump is observed in the lower frequency region, referred as relaxation peak. A relaxation peak is viewed normally in those materials in which the hopping

frequency of charge carrier matches with the frequency of applied external electric field [16].

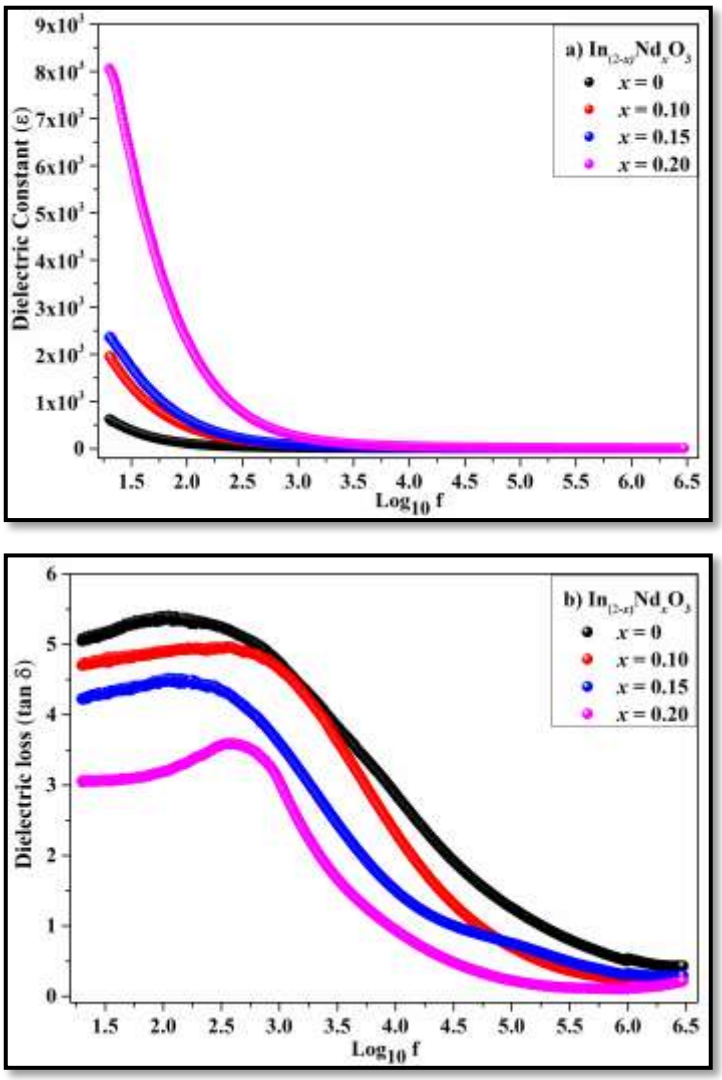

Figure 7.2.3.1: Variation of room temperature (a) Dielectric constant (ε) and (b) Dielectric loss (tanδ) as a function of frequency for Nd doped In_2O_3 nanoparticles.

It is noticeable from the graph that as the applied frequency increases 'tan δ' decreases quickly and on further increasing the applied frequency 'tan δ' decreases slowly. The dielectric loss can be explain as, in presence of applied frequency polar dielectrics molecules orient themselves in the direction of applied frequency which requires small amount of electric energy to surmounts the internal forces. Movement of molecule from one site to another and the rotating motion of dipole moment in existence of applied electric field uses a fraction of electric energy that results in dielectric loss. From Figure 7.2.3.1 (b) it is

noticeable that the dielectric loss is maximum for $x = 0$ and minimum for $x = 0.20$ in lower frequency region. Grain boundary effects, ions hopping rate and crystallite size are some factors which influences the dielectric loss in material. Our analysis made on structural properties reviled that the crystallite size decreases with increased in as the Nd^{3+} content in the sample. Reduction in crystallite size enhances the surface to volume ratio that amplifies the number of crystallite per unit volume as a result surface charge polarization increases. Consequently the energy required for the dipoles to adjust themselves in the direction of applied electric field is generally depends on the Nd^{3+} concentration and therefore become lower at lower frequency for higher Nd^{3+} concentration [17, 38, 39]. High dielectric constant is displayed by the sample having high Nd^{3+} content with low grain size. It is seen from Figure 7.2.3.1 (b) that 'tan δ' curves continues to decline with rise in Nd^{3+} concentration due to the reasons stated above.

Figure 7.2.3.2 shows the variation of dielectric constant with temperature from room temperature to 500^{o}C (773K) at different applied frequencies. It is noticeable from the graph that dielectric constant significantly increases with increases in temperature. The variation of dielectric constant with temperature can be explained on the basis of thermal energy. At lower temperature, the thermal energy is not sufficient to increase the charge carrier mobility and the charge carriers are unable to orient themselves in the direction of applied field. However at high (elevated) temperature the thermal energy is large and it enhances the charge carrier hopping rate and consequently the mobility of charge carrier increases so that they are effortlessly able to orient themselves in the direction of field [40,41]. Therefore the dielectric polarization increases and leads to increase in the dielectric constant of the material. The 'tan δ' curves displayed in Figure 7.2.3.3 shows similar kind of variation as shown by dielectric constant curves presented in Figure 7.2.3.2. Loss in dielectric material occurs when the dielectric polarization lags behind the applied field which is usually because of grain boundary effect in the crystalline material. The properties of a dielectric material may depends on factors like sample preparation technique, structure of the material, crystallite size, chemical composition and preparative condition in case of nanoparticle material [41].

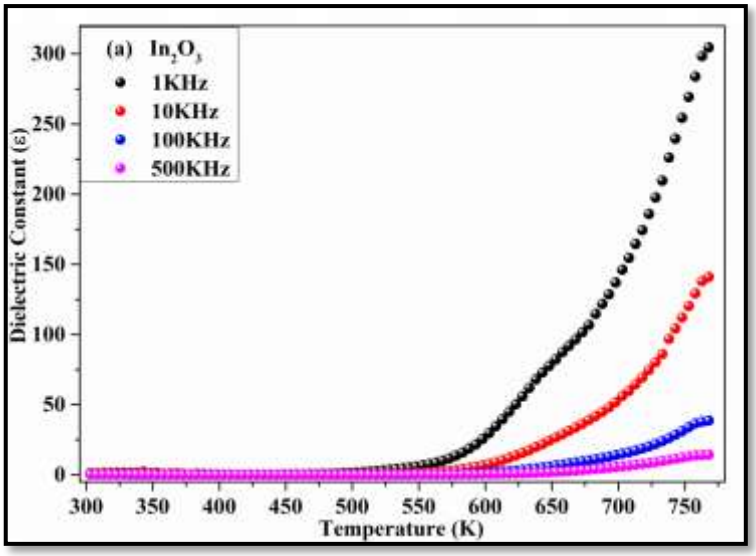
(a) In2O3
1KHz
10KHz
100KHz
500KHz
Dielectric Constant (ε)
Temperature (K)

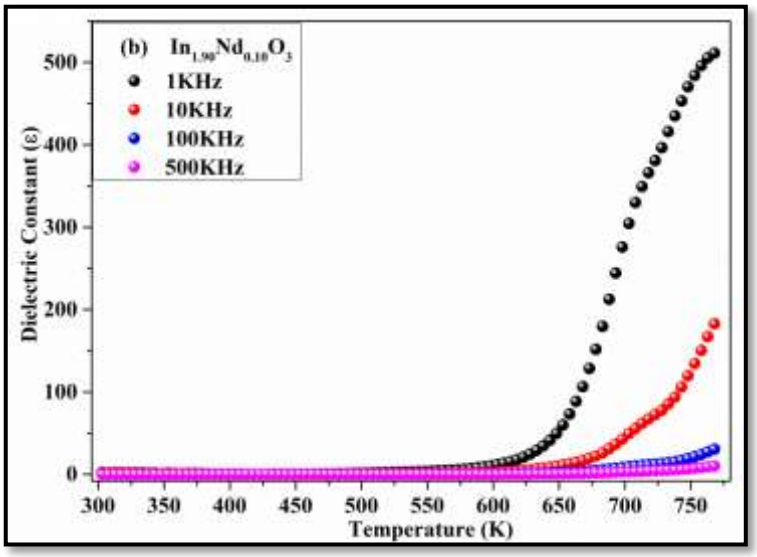
(b) In1.90Nd0.10O3
1KHz
10KHz
100KHz
500KHz
Dielectric Constant (ε)
Temperature (K)

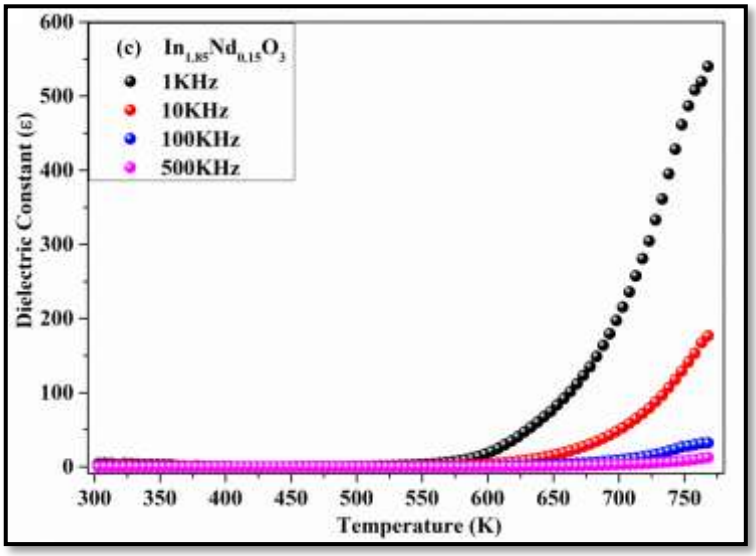
(c) In1.85Nd0.15O3
1KHz
10KHz
100KHz
500KHz
Dielectric Constant (ε)
Temperature (K)

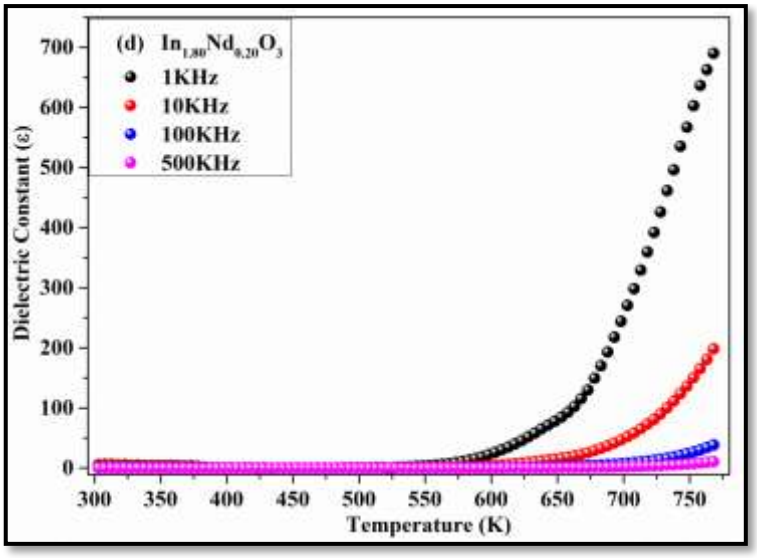

Figure 7.2.3.2: Variation of dielectric constant ('ε') with temperature for (a) In_2O_3, (b) $In_{1.90}Nd_{0.10}O_3$, (c) $In_{1.85}Nd_{0.15}O_3$, (d) $In_{1.80}Nd_{0.20}O_3$.

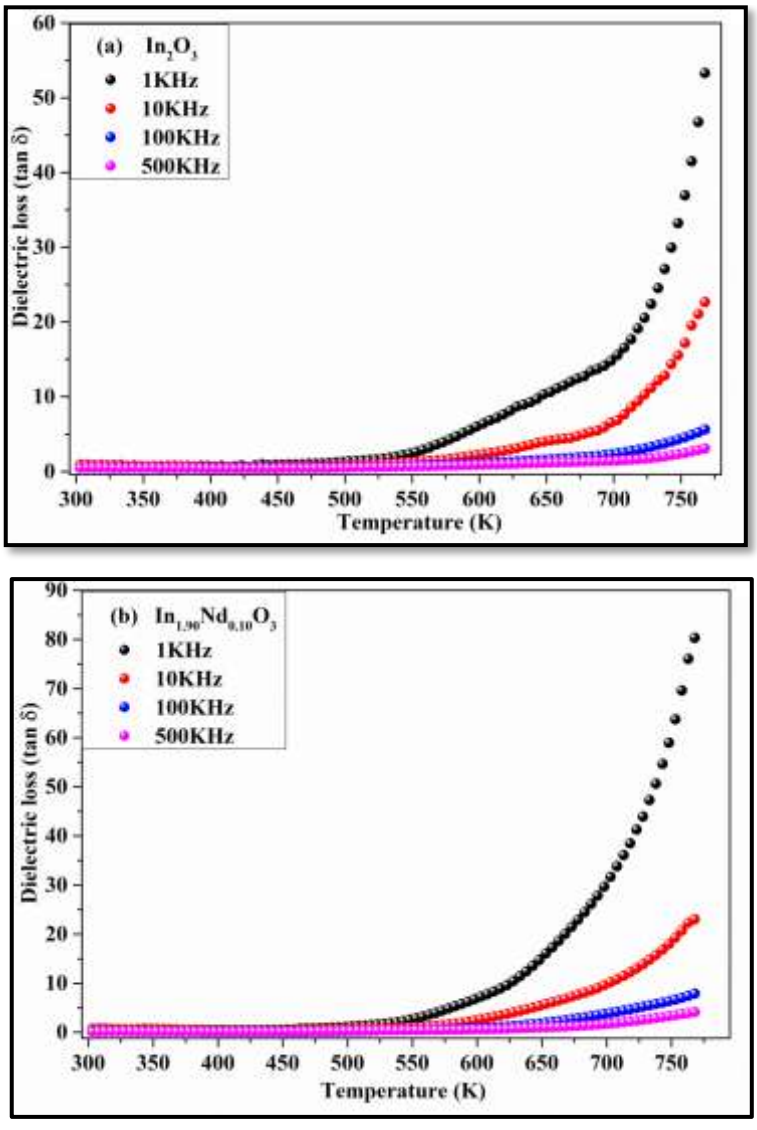

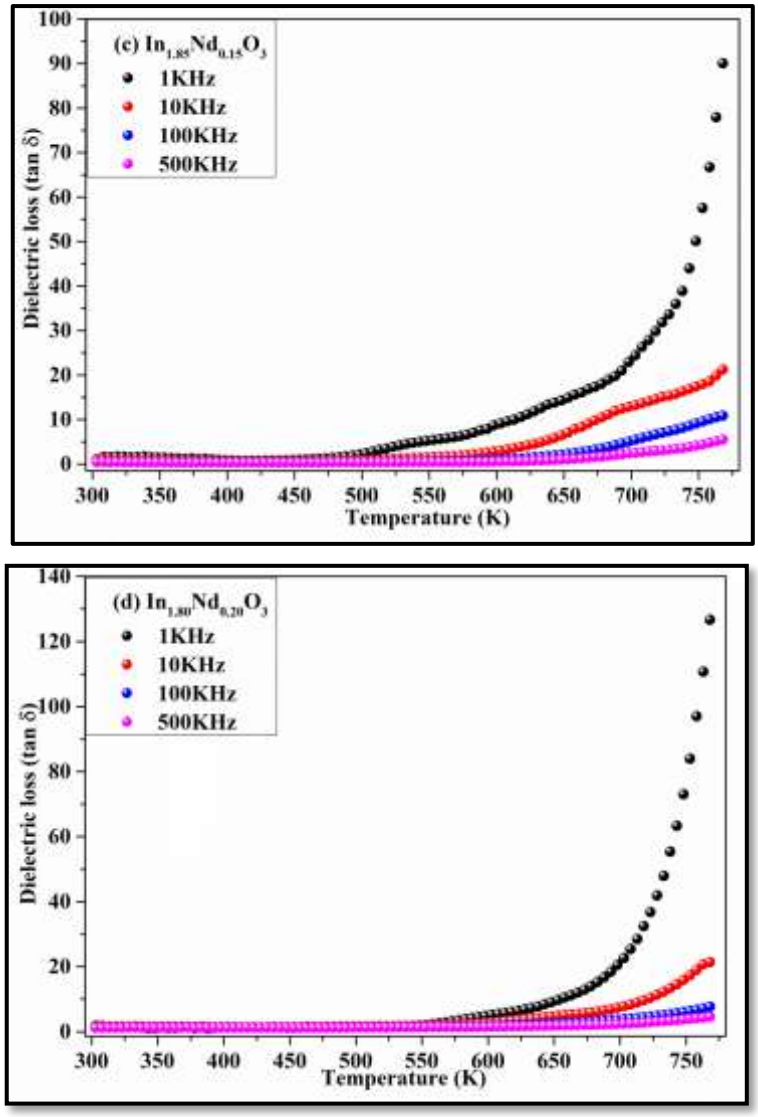

Figure 7.2.3.3: Variation of dielectric loss (tan δ) with temperature for (a) In_2O_3, (b) $In_{1.90}Nd_{0.10}O_3$, (c) $In_{1.85}Nd_{0.15}O_3$, (d) $In_{1.80}Nd_{0.20}O_3$.

7.2.4 Impedance Analysis

Figure 7.2.4.1 displays the cole-cole plot for $In_{(2-x)}Nd_xO$ (x = 0, 0.10, 0.15, 0.20) nanoparticles. The real part of the complex impedance Z' and the imaginary part of the complex impedance Z" is the calculated using equation 7.1.4 (a) and equation 7.1.4 (b) respectively. cole-cole plot shows semicircular regions which belongs to the different electrically active regions [50, 51]. In the cole-cole plots the first semi-circle at lower frequency is due to the grain boundaries resistance and the second semicircle at higher frequency gives the grains contribution of the material [51]. Furthermore it is seen from the Figure 7.2.4.1 that only the first semicircular arcs are observed for all the samples which shows the dominating

nature of grain boundaries resistance in the material. It is observed from the figure that the semicircular arcs decreases with increase in Nd^{3+} content in the sample which signifies that the grain boundaries resistance decreases. The decrement in grain boundaries resistance is due to replacement of In^{3+} ions by Nd^{3+} ions in In_2O_3 matrix [52,53]. By increasing Nd^{3+} content the number of charge carrier concentration increases which results in decrease in electrical resistance of the sample [54]. Impedance studies displays the typical nature of semiconductor wherein the resistivity decrease which signifies that there is increase in conductivity with increase in Nd^{3+} content in the samples.

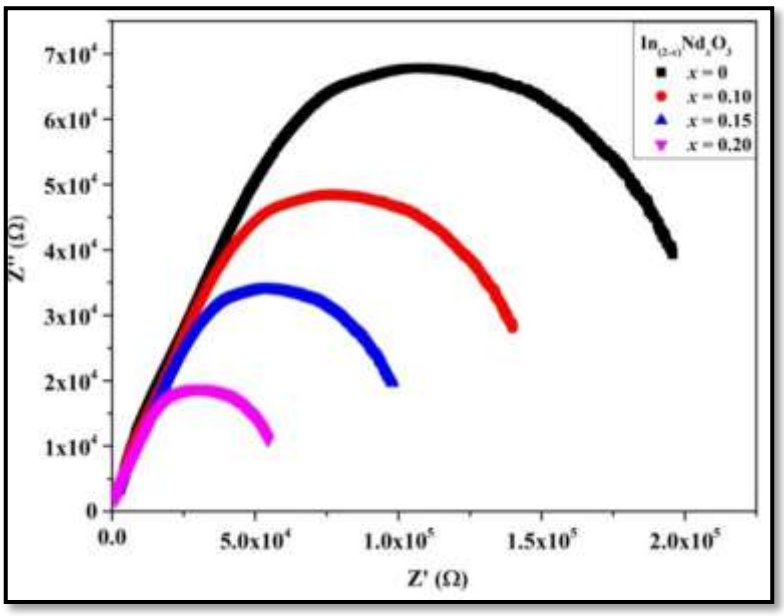

Figure 7.2.4.1: Cole-Cole plot for Nd doped In_2O_3 nanoparticles.

7.3 Ni doped CuO, $Cu_{(1-x)}Ni_xO$ (x = 0, 0.05, 0.10, 0.15, 0.20, 0.25, 0.30)

7.3.1 Thermoelectric Power

Figure 7.3.1.1 (a) displays the variation of Seebeck coefficient 'S' (V/K) with 'T' (^oC) the temperature for all the samples. Equation 7.1.1 (a) was applied to calculate the Seebeck coefficient 'S' and equation 7.1.1 (b) and equation 7.1.1 (c) were used to calculate the charge carrier concentrations at different temperatures.

It is noticeable from Figure 7.3.1.1 (a) that at room temperature all the samples shows positive Seebeck coefficient 'S' values and continues to show positive 'S' values around 423K (150^oC) signifying p-type semiconductor behavior. Around 423K (150^oC) a polarity charge transition from p-type to n-type charge carriers

was observed signifying first order charge polarity transition with significant increase in n-type charge carrier concentration. Semiconducting p-type behavior was observed from room temperature to about 423K (150^{o}C) and from 423K (150^{o}C) onwards the samples behaved like n-type semiconductor material.

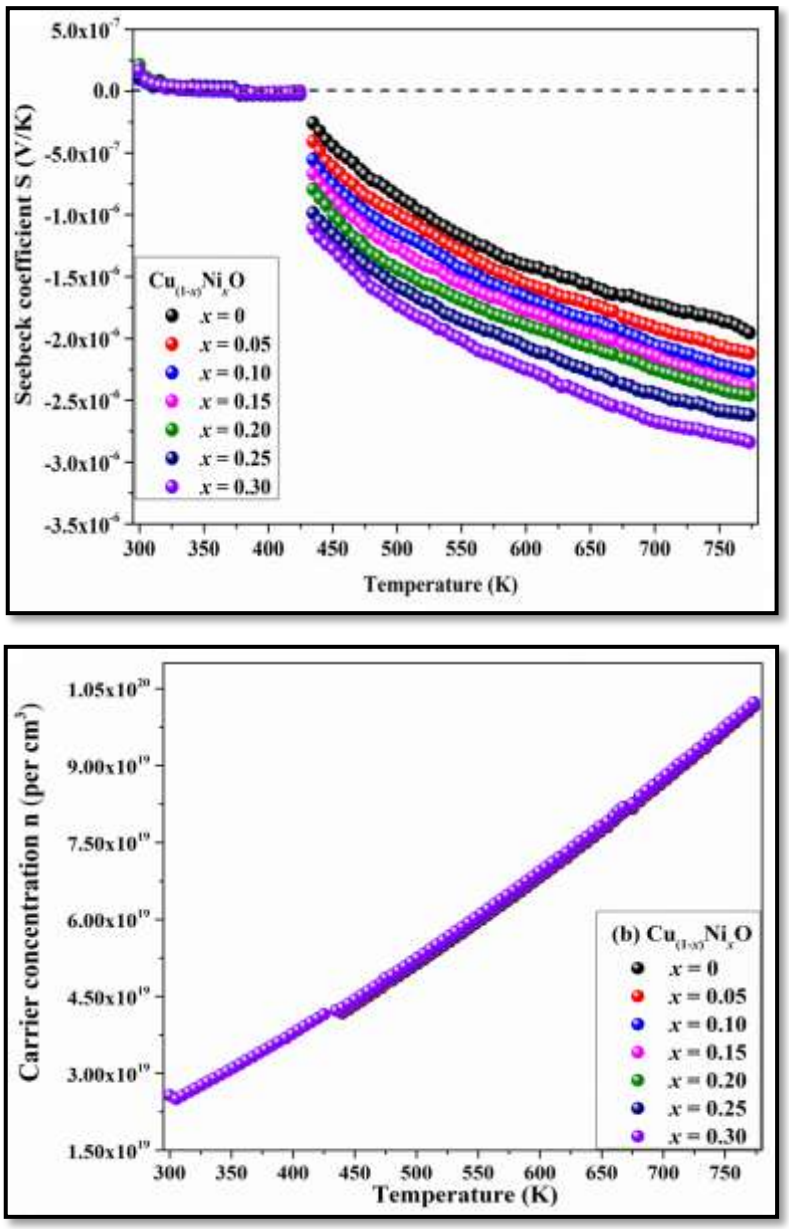

Figure 7.3.1.1: (a) Variation of Seebeck coefficient with respect to temperature and (b) Variation of carrier concentration with respect to temperature for Ni doped CuO.

Figure 7.3.1.1 (b) displays the variation of carrier concentration with respect to temperature. It is observed from the figure that the carrier concentration increases with increases in temperature for all the samples. A carrier concentration

curve reveals that with increasing Ni^{2+} concentration and with increasing the temperature of the hot junction the charge carrier concentration increases. These studies revels that the material with holes as majority charge carriers till 423K (150^{o}C) making it to be a p-type semiconductor from room to 423K (150^{o}C) temperature; becomes n-type of semiconductor beyond this temperature with electrons as a majority charge carries engaged in conduction mechanism [42]. Thus these samples can be used as p-type as well n-type of semiconductors at different temperatures, which is very interesting.

7.3.2 DC Resistivity

Figure 7.3.2.1 displays the plots of $\log_{10} \rho$ (Ω cm) with respect to 1000/T (K^{-1}) for $Cu_{(1-x)}Ni_xO$ (x = 0, 0.05, 0.10, 0.15, 0.20, 0.25, 0.30) nanoparticles. The resistivity 'ρ' for the samples at different temperature was calculated using equation 7.1.2 (a). It may be seen that the resistivity plots are similar to the plots obtained for Co^{2+} doped ZnO materials given and explained in Section 7.2.1. Figure 7.3.2.1 shows the plots that are divided in to two different sections over the temperature range from room temperature to 773K i.e. region I between 300K (27^{o}C) - 423K (150^{o}C) and region II between 423K (150^{o}C) -773K (500^{o}C) respectively.

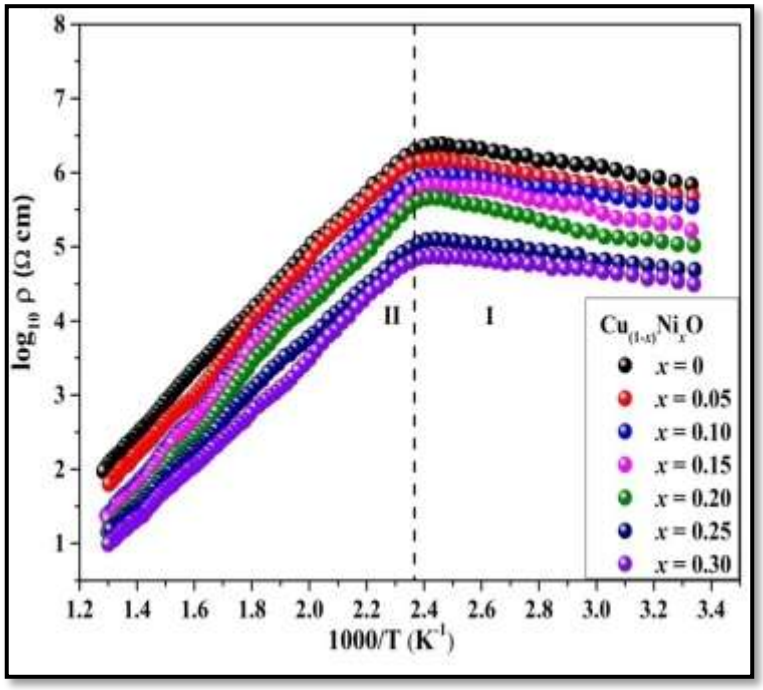

Figure 7.3.2.1: Variation of resistivity as a function of temperature for Ni doped CuO nanoparticles.

In region I a small enhancement in the resistivity values is clearly observed from the resistivity curves, that is from room temperature to 423K (150^{o}C) which is normally due to hole conductivity [43,44]. Moreover it is clearly seen from the thermopower analysis that up to 423K (150^{o}C) all the samples show p-type behavior. This implies that in region I the material has holes as a majority charge carriers. Furthermore, in the high temperature region II between 423K (150^{o}C) - 773K (500^{o}C) the resistivity of the samples decreases which means that the conductivity of the material increases with increase in temperature due to thermal excitations. The concentration of free electrons increases with increasing temperature [42]. Charge carriers get excited at particular temperature which increases the electrical conductivity of the material. Moreover thermopower studies verifies that from 423K (150^{o}C) onwards samples behaves as n-type semiconductor which implies that in region II material has electrons as a majority charge carries for conduction mechanism. Decrease in resistivity with increasing Ni^{2+} concentration in the sample could be due to enhancement of charge carriers due to replacement of Cu^{2+} ions by Ni^{2+} ions in the CuO matrix.

Using Arrhenius equation 7.1.2 (b) the activation energy for all the samples has been calculated in region II. Figure 7.3.2.2 shows linearly fitted Arrhenius plot at high temperature to obtain the activation energy (E_a) in region II. As per the research reports the activation energy depends on the crystalline nature of the material, size of the crystallite and the applied temperature [8,9]. Generally 'E_a' is the energy required for the electron to jump from valance band to the conduction band in the semiconductor material [8]. Dwindling in activation energy at high temperature is because of existence of high amount of thermal energy for the charge carriers [11]. This is obvious from the activation energy estimation made at three different temperatures at 523K (250^{o}C), 623K (350^{o}C) and 723K (450^{o}C) shown in Figure 7.3.2.3 (a). The variation of average activation energy with Ni^{2+} concentration is shown in Figure 7.3.2.3 (b). It can be seen from Figure 7.3.2.3 (a) that the 'E_a' reduces with increasing Ni^{2+} content in the sample. On the basis of band gap reduction, the reduction in 'E_a' can be explained with increasing Ni^{2+} content in the sample. The Fermi level is shifted near to the conduction band by enhancing the amount of Ni^{2+} concentration in the sample that results in increasing the density of donor charge carriers. Therefore with increasing Ni^{2+}concentration the energy band gap goes on decreasing between the donor

level and the conduction band [11,12] and thus the required energy for the charge carriers in the valance band to jump into the conduction band decreases continuously.

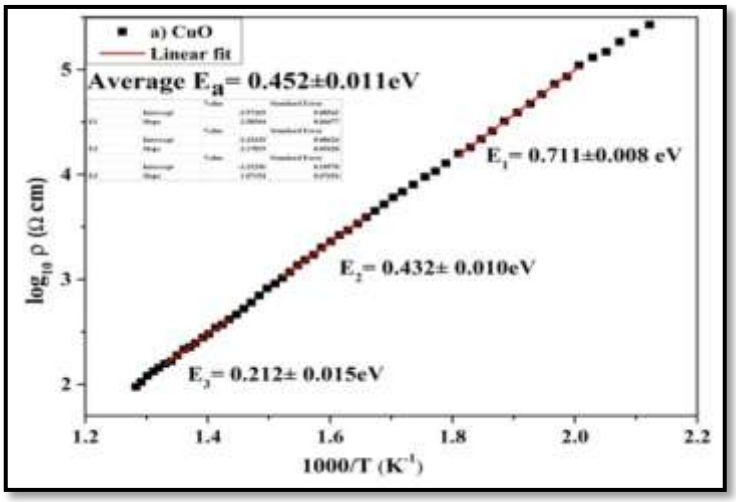

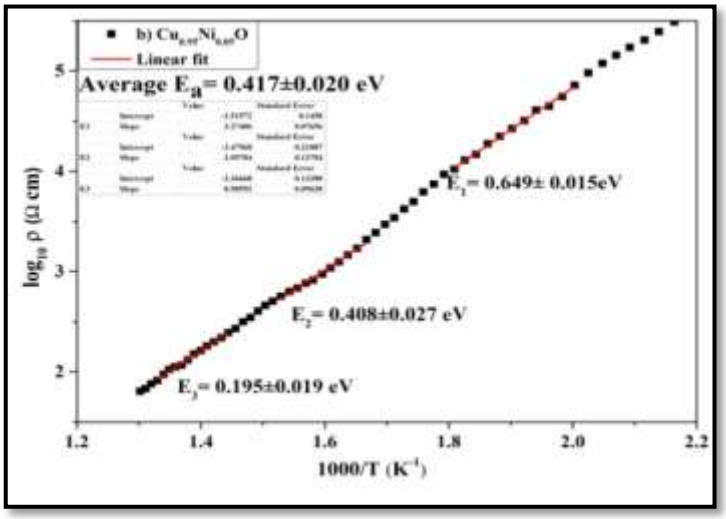

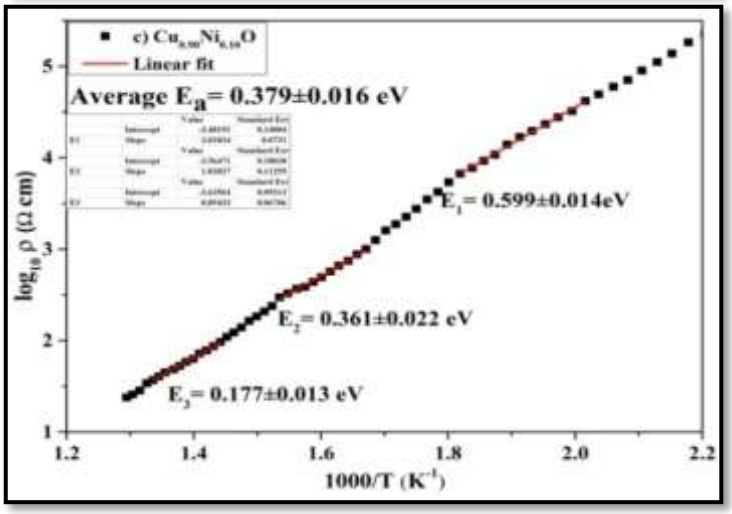

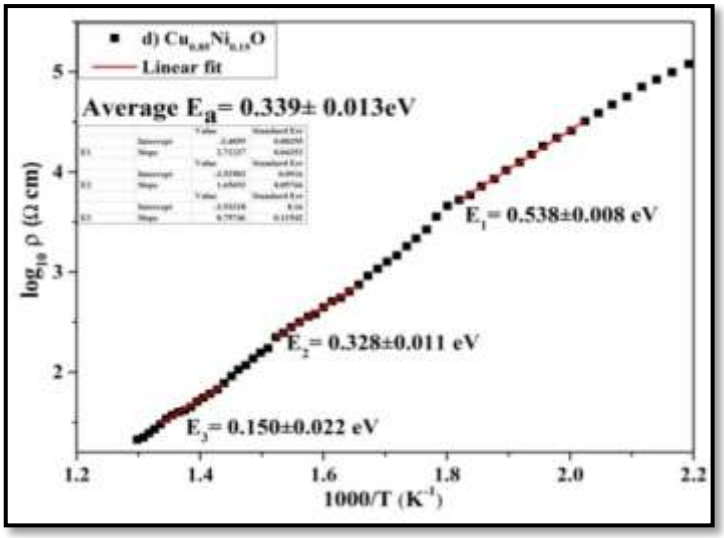
d) $Cu_{0.85}Ni_{0.15}O$
Linear fit
Average E_a= 0.339± 0.013eV
E_1= 0.538±0.008 eV
E_2= 0.328±0.011 eV
E_3= 0.150±0.022 eV
$\log_{10}\rho$ (Ω cm)
1000/T (K^{-1})

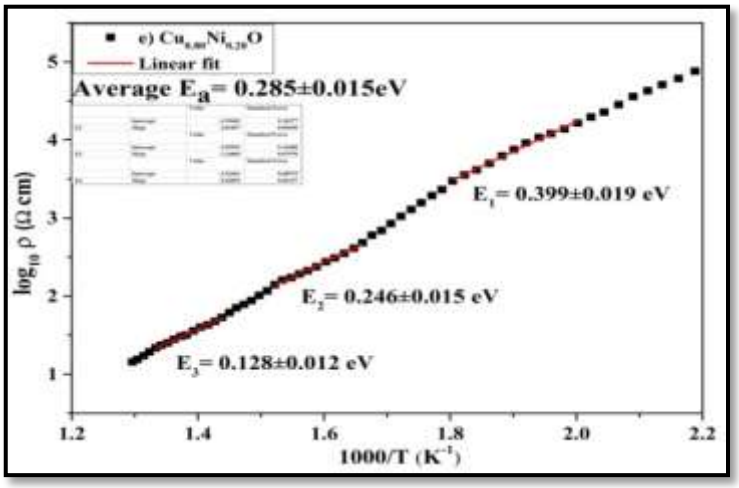
e) $Cu_{0.80}Ni_{0.20}O$
Linear fit
Average E_a= 0.285±0.015eV
E_1= 0.399±0.019 eV
E_2= 0.246±0.015 eV
E_3= 0.128±0.012 eV
$\log_{10}\rho$ (Ω cm)
1000/T (K^{-1})

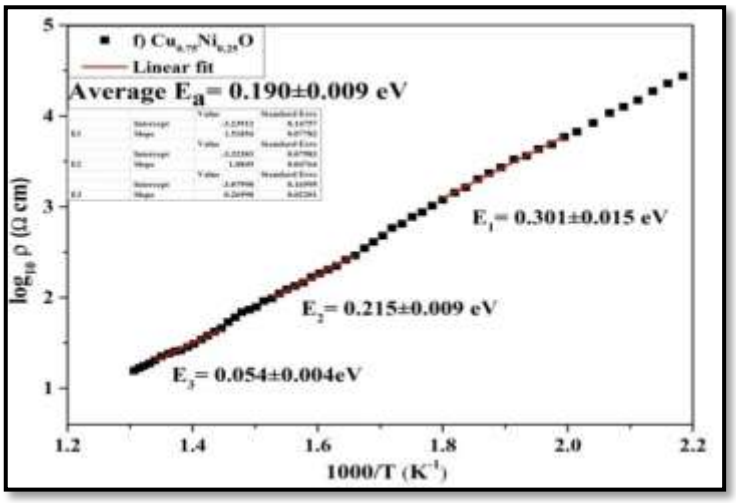
f) $Cu_{0.75}Ni_{0.25}O$
Linear fit
Average E_a= 0.190±0.009 eV
E_1= 0.301±0.015 eV
E_2= 0.215±0.009 eV
E_3= 0.054±0.004eV
$\log_{10}\rho$ (Ω cm)
1000/T (K^{-1})

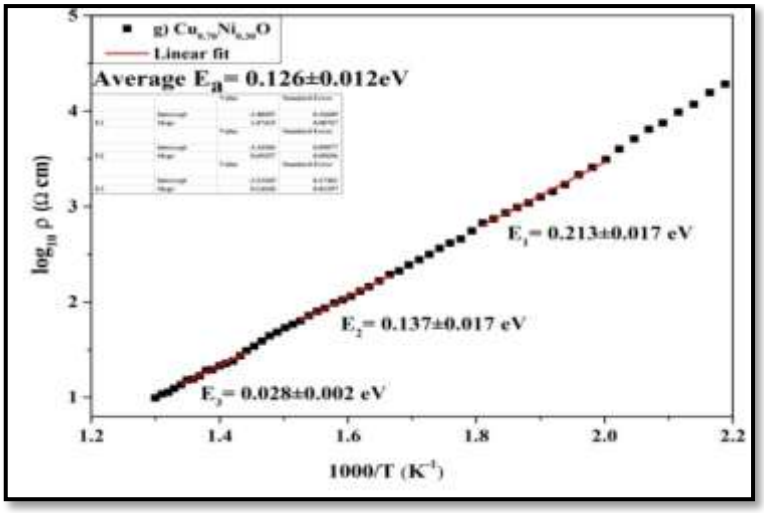

Figure 7.3.2.2: Arrhenius plot at high temperature region for (a) CuO, (b) $Cu_{0.95}Ni_{0.05}O$, (c) $Cu_{0.90}Ni_{0.10}O$, (d) $Cu_{0.85}Ni_{0.15}O$, (e) $Cu_{0.80}Ni_{0.20}O$, (f) $Cu_{0.75}Ni_{0.25}O$, (g) $Cu_{0.70}Ni_{0.30}O$.

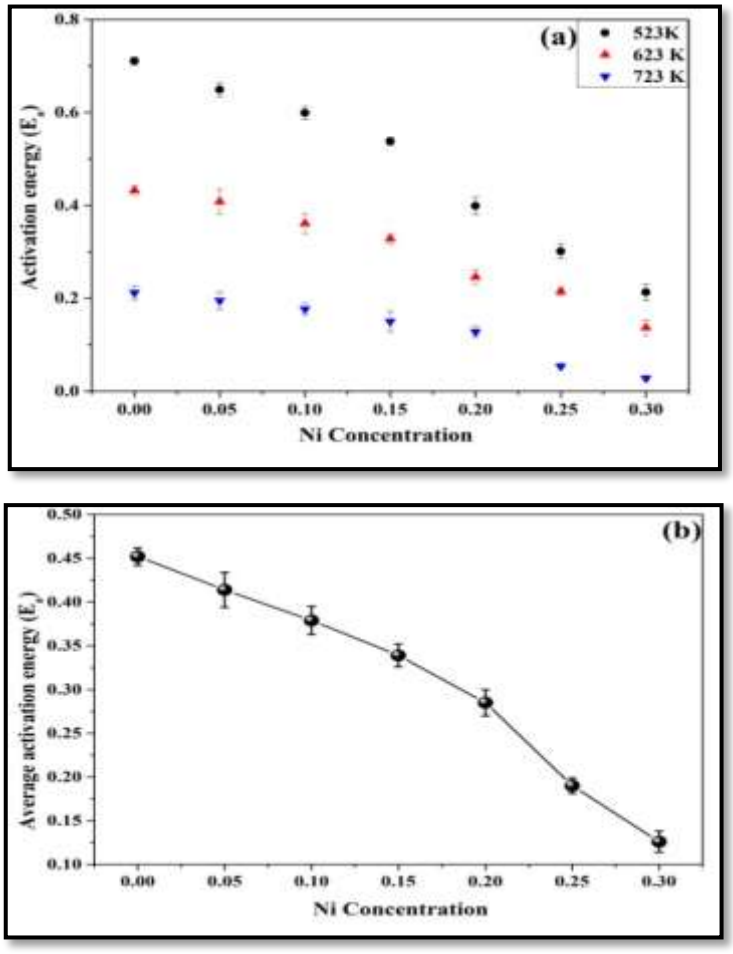

Figure 7.3.2.3: (a) Variation of activation energy 'E_a' and (b) Variation of average activation energy 'E_a' for Ni doped CuO nanoparticles at temperatures 523K (250^{o}C), 623K (350^{o}C) and 723K (450^{o}C).

7.3.3 Dielectric Properties

Figure 7.3.3.1 (a) displays the Dielectric constant (ε) with respect to frequency at room temperature for $Cu_{(1-x)}Ni_xO$ (x = 0, 0.05, 0.10, 0.15, 0.20, 0.25, 0.30) nanoparticles. The dielectric constant 'ε' was calculated using equation 7.1.3 (a). It is visible from the graph that initially dielectric constant 'ε' rapidly decreases as the applied frequency increases and on further increasing the frequency dielectric constant 'ε' dwindles gradually for all the samples. This declining behavior in dielectric constant as a function of frequency can be clarified on the basis of Maxwell-Wagner model [45].

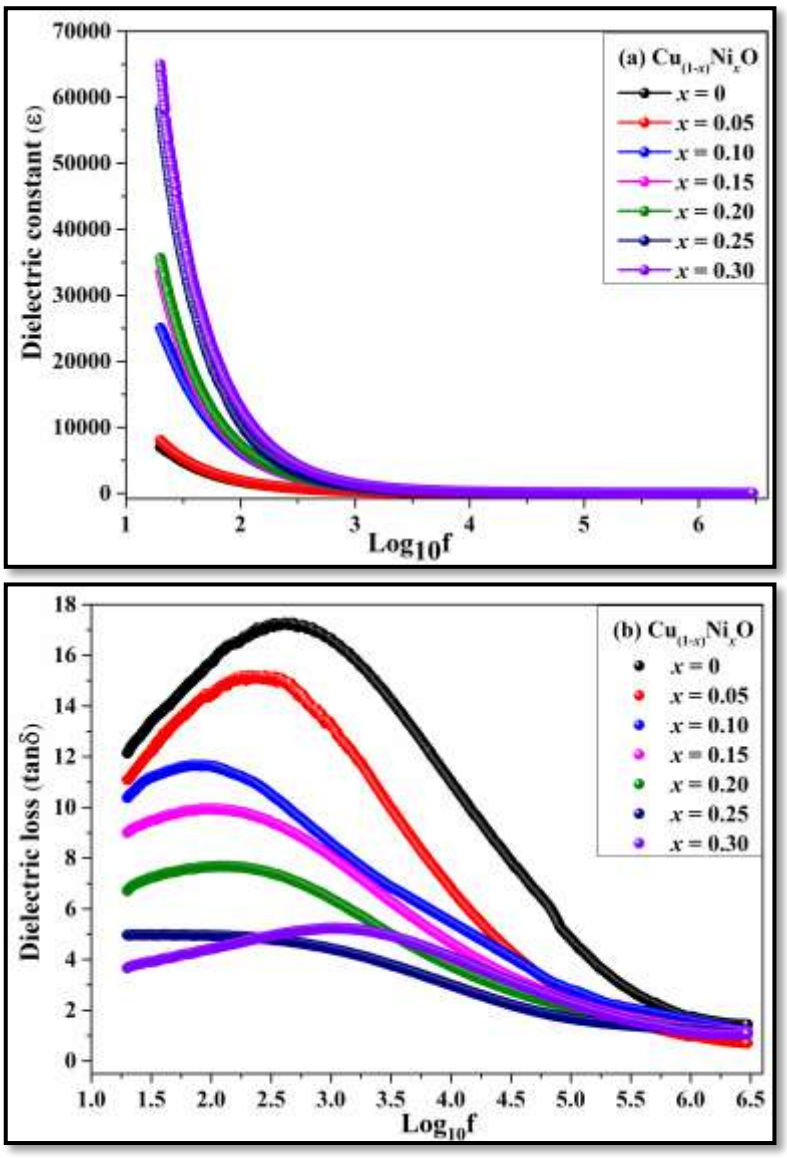

Figure 7.3.3.1: Variation of room temperature (a) Dielectric constant (ε) and (b) Dielectric loss (tanδ) as a function of frequency for Ni doped CuO nanoparticles.

High dielectric constant value at low frequency for all the Ni^{2+} samples is due to space charge polarization. Dielectric constant with variation of '*x*' shows that with increasing Ni^{2+} concentration the overall dielectric constant rises. This augmentation in dielectric constant 'ε' specifies increase in density of charge carrier that depends on both frequency and the doping concentration of Ni^{2+} ions into CuO lattice. Moreover in dielectric constant 'ε' crystallite size also plays a crucial role. Structural investigation shows dwindle of crystallite size with rising Ni^{2+} content in the CuO matrix. It is obvious that with decrease in crystallite size increases the number of crystallites per unit volume. Therefore, at low frequencies dielectric constant increases with increase in Ni^{2+} content in the sample. Consequently decreasing the crystallite size amplifies surface to volume ratio and raises the grain boundaries of the crystallite per unit volume. Thus enhancement in grain boundary and charge carrier concentration is due to increased Ni^{2+} concentration that provides high dielectric constant at lower frequencies. High dielectric constant 'ε' value keeps on falling with increasing applied frequency due to sluggishness of dipole orientation that cannot follow the high frequency field due to mismatch of Ni^{2+} and Cu^{2+} ions hopping rate [46].

Figure 7.3.3.1 (b) shows the dielectric loss 'tan δ as a function of frequency at room temperature. It is seen from the figure that all tan δ curves displays a broad hump in the lower frequency region that is referred to as relaxation peak. This occurs when the hopping frequency of charge carrier matches the frequency of applied external electric field [16]. It is seen from the graph that as the applied frequency increases 'tan δ' declines quickly and on further increasing the applied frequency 'tan δ' decreases slowly. In presence of applied ac field the polar dielectrics molecules try to align themselves in the direction of applied ac field which requires small amount of electrical energy to surmount the internal forces. Movement of molecules from one place to another and the rotary motion of dipole moment in presence of applied ac electric field uses a fraction of electrical energy which results in dielectric loss. it is noticeable from Figure 7.3.3.1 (b) that the dielectric loss is higher for $x = 0$ and lower for $x = 0.30$ in lower frequency region. Grain boundary effects, ions hopping rate and crystallite size are some factors which governs dielectric loss a material [10,46]. Our study on structural properties showed that the crystallite size decreases with increased in Ni^{2+} concentration in the sample. Decrease in crystallite size enhances the surface to volume ratio

amplifying the number of crystallites per unit volume resulting in increased surface charge polarization. As a result the energy required for the dipoles to adjust themselves in the direction of applied electric field which depends on Ni^{2+} concentration is lower at lower frequency for higher Ni^{2+} concentration [17, 38, 39]. High dielectric constant is displayed by the sample having high Ni^{2+} content with low grain size. It is seen from Figure 7.3.3.1 (b) that 'tan δ' curves continues to decline with rise in Ni^{2+} concentration due to these reasons.

Figure 7.3.3.2 shows the variation of dielectric constant with temperature from room temperature to $500^{o}C$ (773K) at different applied frequencies. It is visible from the graph that dielectric constant considerably increases with increases in temperature. The variation of dielectric constant with temperature can be elucidated on the basis of thermal energy. At lower temperature, the thermal energy is not sufficient to augment the charge carrier mobility and the charge carriers are unable to align themselves in the direction of applied field. But at elevated temperature the thermal energy is large thereby enhancing the charge carrier hopping rate and consequently the mobility of charge carrier increases, so that they are easily able to orient themselves in the direction of field [40,47]. Therefore the dielectric polarization increases and leads to increase in the dielectric constant of the material. The 'tan δ' curves displayed in Figure 7.3.3.3 shows similar kind of variation as shown by dielectric constant curves presented in Figure 7.3.3.2. Loss in dielectric material occurs when the dielectric polarization lags behind the applied field which is usually because of grain boundary effect in the crystalline material. The properties of a dielectric material may depends on factors like sample preparation technique, structure of the material, crystallite size, chemical composition and preparative condition in case of nanoparticle material [48].

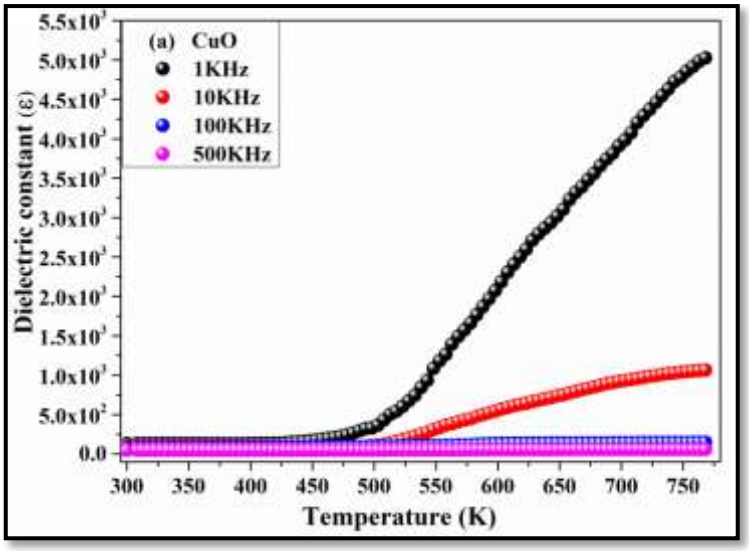
(a) CuO
1KHz
10KHz
100KHz
500KHz
Dielectric constant (ε)
Temperature (K)

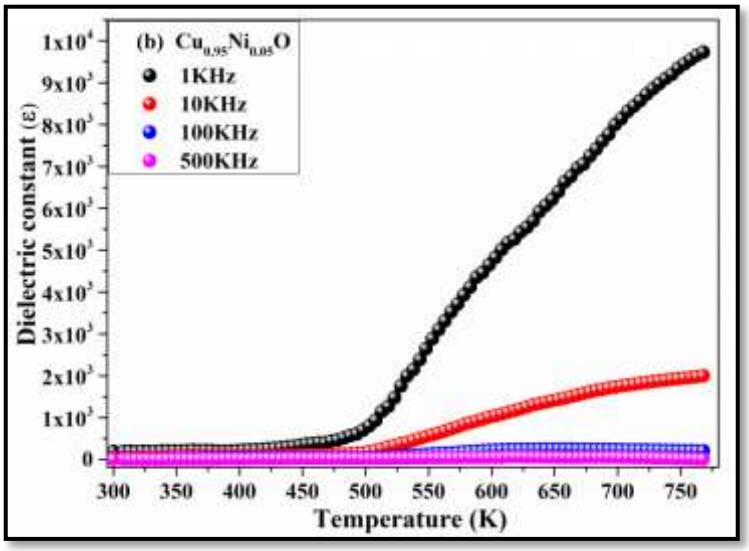
(b) Cu0.95Ni0.05O
1KHz
10KHz
100KHz
500KHz
Dielectric constant (ε)
Temperature (K)

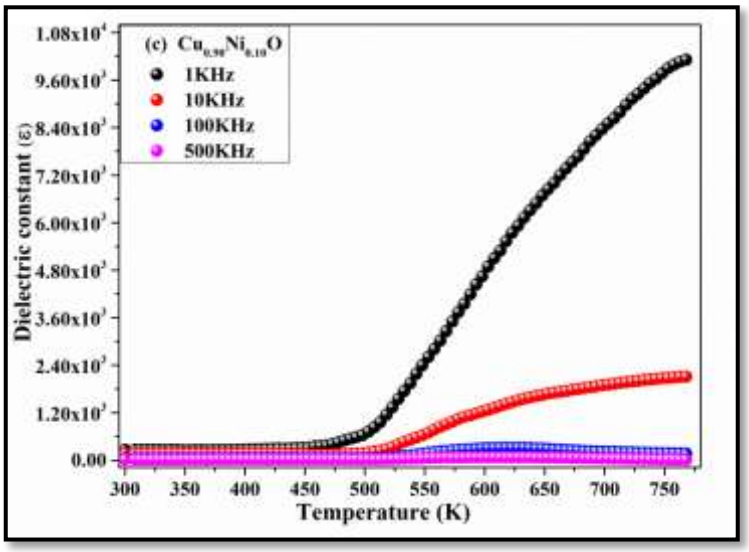
(c) Cu0.90Ni0.10O
1KHz
10KHz
100KHz
500KHz
Dielectric constant (ε)
Temperature (K)

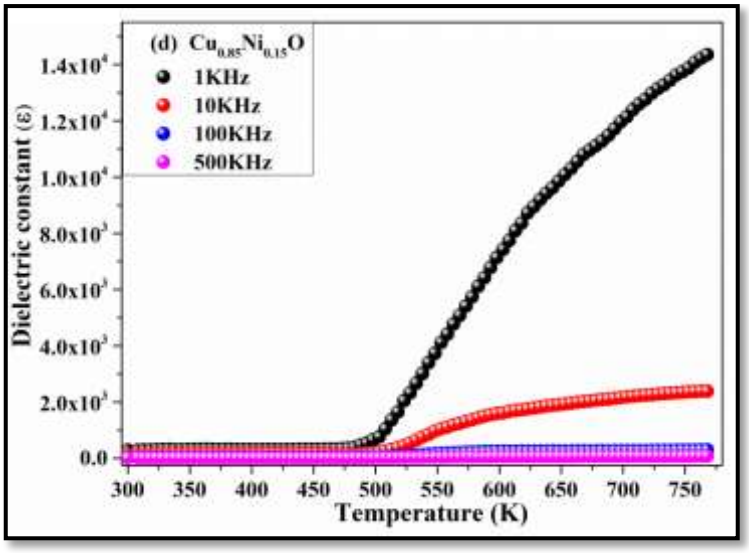
(d) $Cu_{0.85}Ni_{0.15}O$
1KHz
10KHz
100KHz
500KHz
Dielectric constant (ε)
Temperature (K)

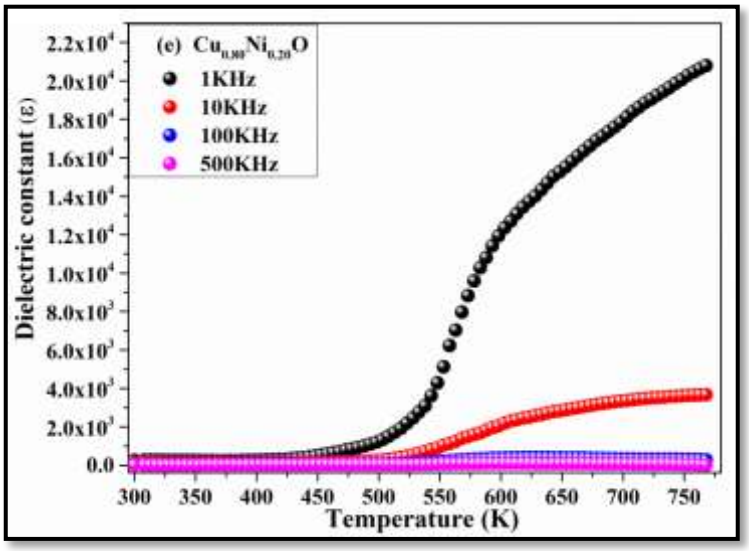
(e) $Cu_{0.80}Ni_{0.20}O$
1KHz
10KHz
100KHz
500KHz
Dielectric constant (ε)
Temperature (K)

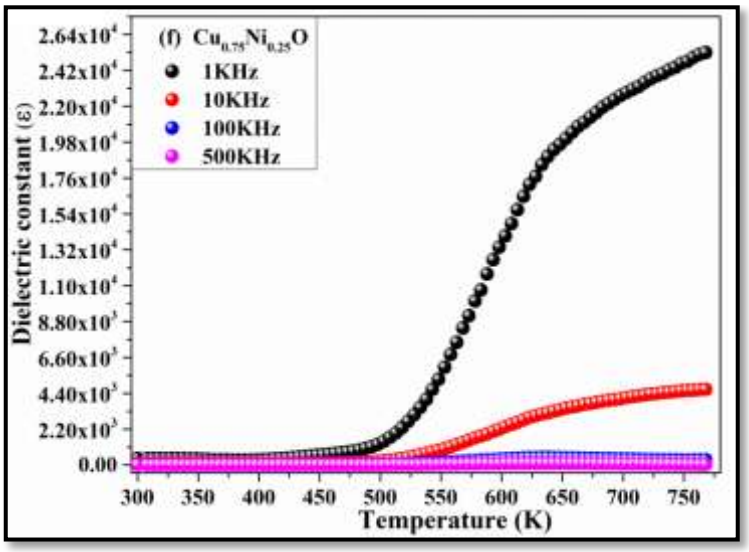
(f) $Cu_{0.75}Ni_{0.25}O$
1KHz
10KHz
100KHz
500KHz
Dielectric constant (ε)
Temperature (K)

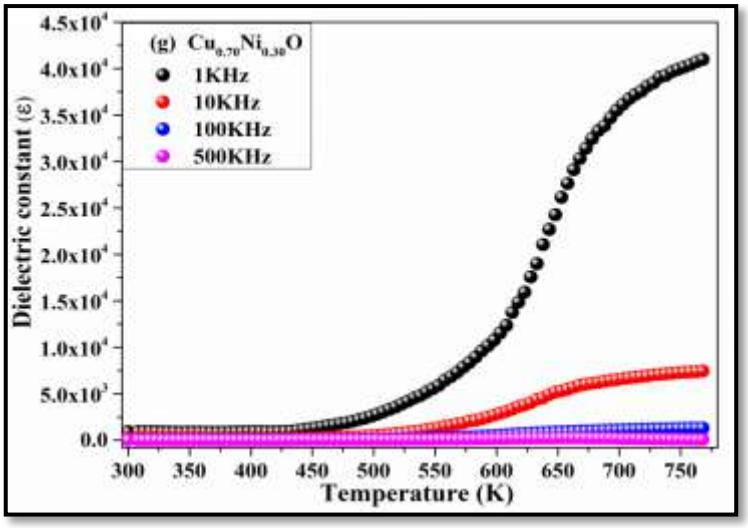

Figure 7.3.3.2: Variation of dielectric constant ('ε') with temperature for (a) CuO, (b) $Cu_{0.95}Ni_{0.05}O$, (c) $Cu_{0.90}Ni_{0.10}O$, (d) $Cu_{0.85}Ni_{0.15}O$, (e) $Cu_{0.80}Ni_{0.20}O$, (f) $Cu_{0.75}Ni_{0.25}O$, (g) $Cu_{0.70}Ni_{0.30}O$.

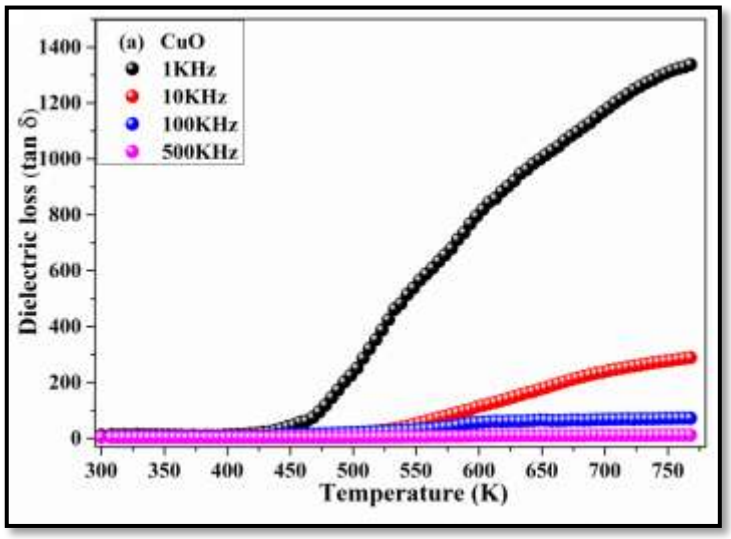

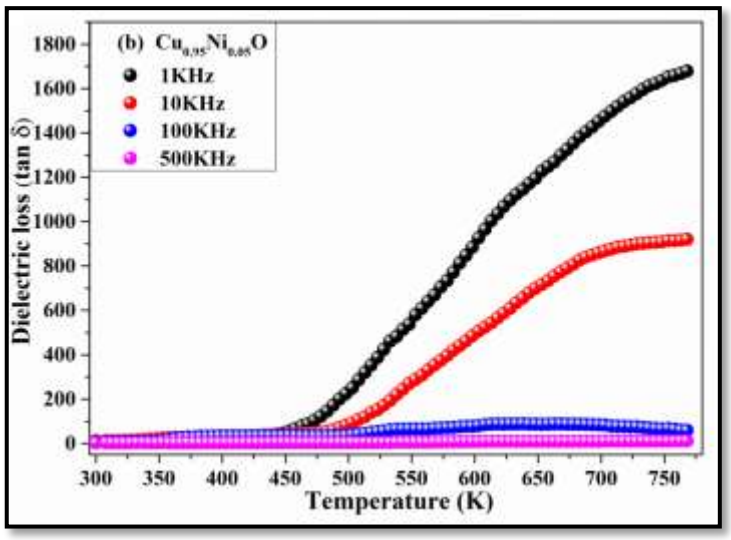

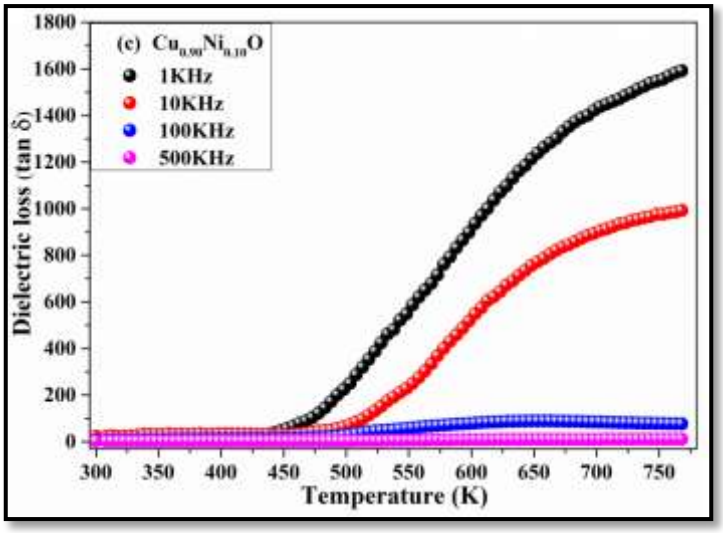
(c) $Cu_{0.90}Ni_{0.10}O$
1KHz
10KHz
100KHz
500KHz
Dielectric loss (tan δ)
Temperature (K)

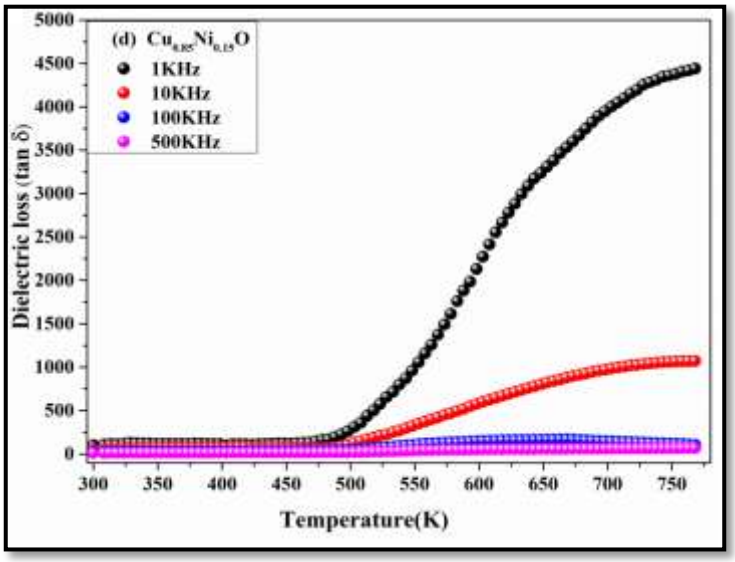
(d) $Cu_{0.85}Ni_{0.15}O$
1KHz
10KHz
100KHz
500KHz
Dielectric loss (tan δ)
Temperature(K)

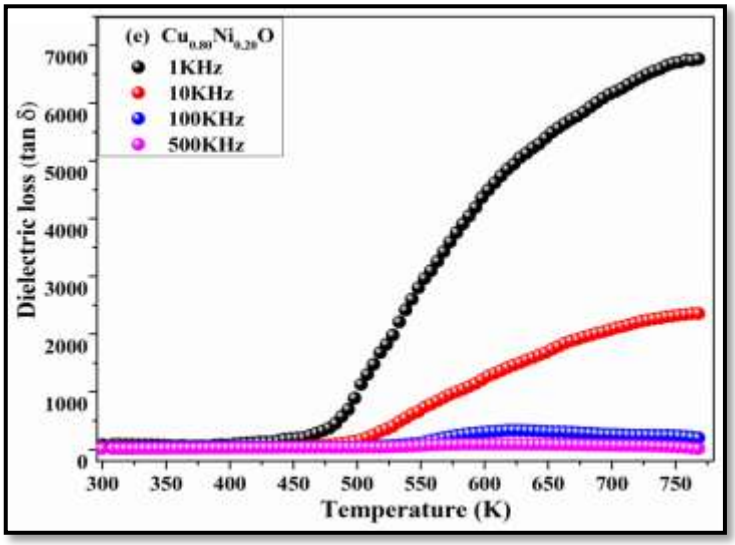
(e) $Cu_{0.80}Ni_{0.20}O$
1KHz
10KHz
100KHz
500KHz
Dielectric loss (tan δ)
Temperature (K)

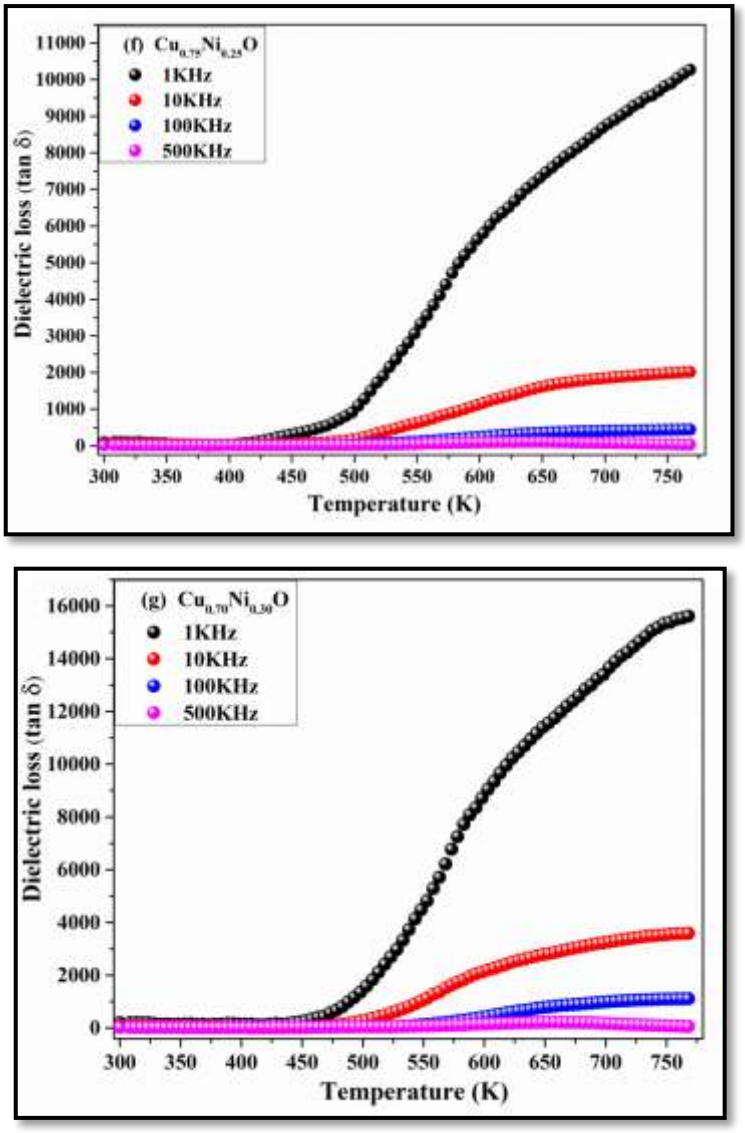

Figure 7.3.3.3: Variation of dielectric loss (tan δ) with temperature for (a) CuO, (b) $Cu_{0.95}Ni_{0.05}O$, (c) $Cu_{0.90}Ni_{0.10}O$, (d) $Cu_{0.85}Ni_{0.15}O$, (e) $Cu_{0.80}Ni_{0.20}O$, (f) $Cu_{0.75}Ni_{0.25}O$, (g) $Cu_{0.70}Ni_{0.30}O$.

7.3.4 Impedance Analysis

Figure 7.3.4.1 displays the cole-cole plot for $Cu_{(1-x)}Ni_xO$ (x = 0, 0.05, 0.10, 0.15, 0.20, 0.25, 0.30) nanoparticles. The real part of the complex impedance Z' and the imaginary part of the complex impedance Z" is the calculated using equation 7.1.4 (a) and equation 7.1.4 (b) respectively. Cole-Cole plot shows semicircular regions which belong to the different electrically active regions [50, 51].

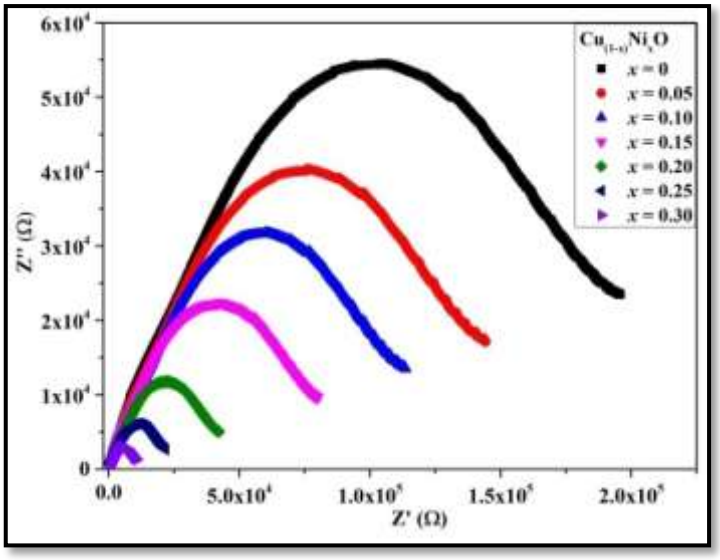

Figure 7.3.4.1: Cole-Cole plot for Ni doped CuO nanoparticles.

In cole-cole plot the first semi-circle at lower frequency is due to the grain boundaries resistance and the second semicircle at higher frequency gives the grain contribution of the material [51]. In our case only the first semicircular arcs can be seen for all the samples as shown in Figure 7.3.4.1, semicircular region shows the dominating nature of grain boundaries resistance in the material. Moreover it is observed from the figure that the semicircular arcs reduce which implies that the grain boundaries resistance decreases with increase in Ni^{2+} content. The decrement in grain boundaries resistance is due to replacement of Cu^{2+} ions by Ni^{2+} ions in CuO matrix [52,53]. On increasing Ni^{2+} content in the CuO matrix, the number of charge (electron) carrier concentration increases which results in decrease in electrical resistance of the sample [54]. Impedance analysis shows typical nature of semiconductor wherein the resistivity decrease which signifies that there is increase in conductivity with increase in Ni^{2+} content in the samples.

References:

[1] M. Raghasudha, D. Ravinder, P. Veerasomaiah, Journal of Alloys and Compounds 604 (2014) 276–280.

[2] M. Ohtaki, Kazuhiko Araki, and Kiyoshi Yamamoto, Ceramics Journal Of Electronic Materials, Vol. 38 (2009).

[3] M. Ullah, Wen Bin Su, Abdul Manan, Arbab Safeer Ahmad, Abid A. Shah, Zhonghua Yao, Ceramics International (2018).

[4] P. P. Naik, R.B. Tangsali, Journal of Alloys and Compounds 723 (2017) 266-275.

[5] A.R. Khantoul, M. Sebais, B. Rahal, B. Boudine, and O. Halimi, Acta Physica Polonica A 133 (2018).

[6] A.D. Acharya, Bhawna Sarwan, Richa Panda, S.B. Shrivastava,V. Ganesan, Superlattices and Microstructures, 67 (2014) 97–109.

[7] R. Kumar, Neeraj Khare, Thin Solid Films 516 (2008) 1302–1307.

[8] M. Yu, Hong Qiu, Xiaobai Chen, Hui Li, Wei Gong Materials Chemistry and Physics 126 (2011) 797–803

[9] R. Srivastava, Journal of Sensor Technology, 2 (2012) 8-12.

[10] C. C. Naik, A. V. Salker, Journal of Materials Science: Materials in Electronics (2017).

[11] M. R. Bryce and Michael C. Petty, Nature 374 (1995) 771-776.

[12] A.A. Yousif, N.F. Habubi, A.A. Haidar, Journal Of Nano- And Electronic Physics 4 (2012) 6.

[13] S. Sharma, Kirti Nanda, R.S. Kundu, R. Punia and N. Kishore, Structural Properties, Conductivity, Journal of Atomic, Molecular, Condensate & Nano Physics, 2 (2015) 15–31.

[14] M. Mehedi Hassan, Arham S. Ahmed, M. Chaman, Wasi Khan, A.H. Naqvi, Ameer Azam, Materials Research Bulletin, 47 (2012) 3952–3958.

[15] C. Belkhaoui, Ramzi Lefi, Nissaf Mzabi, Hichem Smaoui, Journal of Materials Science: Materials in Electronics, (2018).

[16] M. Ashokkumar, S. Muthukumaran, J. Lumin. 162 (2015) 97–103.

[17] M. Mehedi Hassan, W. Khan, A. Azam, A.H. Naqvi, J. Ind. Eng. Chem. 21 (2015) 283–291.

[18] S. Sagadevan, Kaushik Pal, Zaira Zaman Chowdhury, M. Enamul Hoque, J Sol-Gel Sci Technol, (2018).

[19] R. Zamiri, A. Kaushal, A. Rebelo, J.M.F. Ferreira, Ceram. Int. 40 (2014) 1635–1639.

[20] Y. Liu, Yuan-Hua Lin, Jinle Lan, Wei Xu, Bo-Ping Zhang, Ce-Wen Nan, and Hongmin Zhu, J. Am. Ceram. Soc., 93 (2010) 2938–2941.

[21] D. B´erardan, Emmanuel Guilmeau, Antoine Maignan, Bernard Raveau, Solid State Communications 146 (2008) 97–101.

[22] E. Combe, C. Chubilleau, D. Berardan, E. Guilmeau, A. Maignan, B. Raveau, Powder Technology, 208 (2011) 503–508.

[23] M. Raghasudha, D. Ravinder,1, P. Veerasomaiah, Journal of Alloys and Compounds 604 (2014) 276–280.

[24] M. Ohtaki, Hisako Koga, Tsutomu Tokunaga, Koichi Eguchi, Hiromichi Arai, Journal of Solid State Chemistry, 120 (1995) 105-111.

[25] M. Ullah, Wen Bin Su, Abdul Manan, Arbab Safeer Ahmad, Abid A. Shah, Zhonghua Yao, Ceramics International (2018).

[26] M. Jothibas, C. Manoharan, S. Ramalingam, S. Dhanapandian, M. Bououdina, Spectrochimica Acta Part A: Molecular and Biomolecular Spectroscopy, 122 (2014) 171–178.

[27] A. Bouhdjer, H.Saidi, A.Attaf, M.S. Aida, Mohamed JlassI, I. Bouhaf, Y.Benkhetta, H.Bendjedidi, Optik, 12 (2016) 7319-7325.

[28] K. Kato, Hideo Omoto, Takao Tomioka, Atsushi Takamatsu, Thin Solid Films, 520 (2011) 110–116.

[29] W. Fa, Wu U, Bi-Shiou Chiou, Thin Solid Films, 298 (1997) 221-227.

[30] A.D. Sheikh, V.L. Mathe, J. Mater. Sci. 43 (2008) 2018–2025.

[31] C. G. Koops, Phys. Rev. 83 (1951) 121.

[32] T. Prodromakis, C. Papavassiliu, Appl. Surf. Sci. 255 (2009) 6989–6994.

[33] C. Belkhaoui, Ramzi Lefi, Nissaf Mzabi, Hichem Smaoui, Journal of Materials Science: Materials in Electronics, (2018).

[34] A. kumar, S. Muthukumaran, Journal of Luminescence. 162 (2015) 97–103.

[35] M. Mehedi Hassan, W. Khan, A. Azam, A.H. Naqvi, J. Ind. Eng. Chem. 21 (2015) 283–291.

[36] T. Ahmad, Sarvari Khatoon, Kelsey Coolahan, Materials Research Bulletin 48 (2013) 3065–3071.

[37] S. Sagadevan, Kaushik Pal, Zaira Zaman Chowdhury, M. Enamul Hoque, J Sol-Gel Sci Technol, (2018).

[38] S. Ali Ansari, Ambreen Nisar, Bushara Fatma, Wasi Khan, A.H. Naqvi, Materials Science and Engineering B, 177 (2012) 428– 435.

[39] C.R Indulal, R. Raveendran, Indian journal of pure and applied physics, 48 (2010) 121-126.

[40] S. Ali Ansari, Ambreen Nisar, Bushara Fatma, Wasi Khan, M. Chaman, Ameer Azam, A.H. Naqvi, Materials Research Bulletin 47 (2012) 4161–4168.

[41] C. C. Naik, A. V. Salker, Journal of Materials Science: Materials in Electronics (2017).
[42] Y. Kwon Jeong and Gyeong Man Choi, Phys. Chem. Solids, 57 (1996) 81-84.
[43] M. G. Holland, Phys. Rev. 134 (1964).
[44] G.P.Srivastava, Journal of Physics and Chemistry of Solids, 41(1980) 357-368.
[45] I. Khan, Shakeel Khan, Hilal Ahmed and Razia Nongjai, Proceeding of International Conference on Recent Trends in Applied Physics and Material Science AIP Conf. Proc. 1536 (2013) 241-242.
[46] M. Bibi, Qurat-ul-Ain Javed, Hussain Abbas, Sabah Baqi, Materials Chemistry and Physics 192 (2017) 67-71.
[47] J. Koshy, Soosen Samuel, Anoop Chandran, Pournami Vijayan, K C George, International Journal of Chemical and Physical Sciences,4 (2015).
[48] S.G. Rejith, International Journal of Engineering Science Invention (IJESI), 7 (2018) 06-08.
[49] K.C. Verma, Bhatt SS, Ram M, Negi NS, Kotnala RK. Mater Chem Phys 2010;124:1188.
[50] D.K. Rana, Singh SK, Kundu SK, Roy S, Angappane S, Basu S. New J Chem 43 (2019) 3128.
[51] I. Khan, S. Khan, W. Khan, Mater. Sci. Semicond. Process. 26 (2014) 516–526.
[52] G. Singh, S. B. Shrivastava, and V. Ganesan. Journal of Chemical Engineering and Materials Science (2013) 1-6.
[53] M. Sassi, A. Bettaibi, A. Oueslati, K. Khirouni, M. Gargouri. J. Alloys Compd., 649, 642–648, 2015.
[54] M. Sajid Shafiq, Muhammad Furqan, Shahid Atiq, Murtaza Saleem, Saira Riaz, Shahzad Naseem, J Sol-Gel Sci Technol 79 (2016) 535–542.

CHAPTER 8

Conclusion

8.1 Conclusion

The concluding chapters provides a quick look of the investigations carried out and briefly gives the scope for carrying future work on Dilute Magnetic Semiconductor (DMS) materials. The research work carried out and presented in this thesis though tiny, has extensively analyzed several important aspects of some of the nanoparticle DMS materials indigenously prepared by a simple method of sample preparation. The work has enlightened the research community with many of the lesser known behavioral aspects of these materials. The important mission of this work was to prepare nanoparticles of ZnO, In_2O_3 and CuO with suitable dopant materials to introduce ferromagnetic property in them so that they could behave as DMS materials. Co, Nd and Ni respectively, on the basis of their properties were identified as suitable dopant materials. Accordingly it was felt that nanoparticles with chemical formula $Zn_{(1-x)}Co_xO$ (x = 0.05, 0.10, 0.15, 0.20), $In_{(2-x)}Nd_xO_3$ (x = 0, 0.10, 0.15, 0.20) and $Cu_{(1-x)}Ni_xO$ (x = 0, 0.05, 0.10, 0.15, 0.20, 0.25, 0.30) could be prepared using a suitable method of sample preparation to study the effect of dopant material on structural, electrical, magnetic and optical properties of these dilute magnetic semiconductor nanoparticles. As per the merits of preparative methods auto combustion method was found to be a suitable method for preparing these materials.

Structural, morphological and elemental composition investigations were carried out by using XRD, SEM, TEM, EDAX and FTIR on these materials. Detailed analysis of XRD data showed formation of monophasic wurtzite structure $Zn_{(1-x)}Co_xO$ (x=0.05, 0.10, 0.15, 0.20) nanoparticles. Interesting effects in the structural properties of the nanoparticles were observed due to introduction of Co^{2+} ions in the ZnO matrix. The lattice constants '*a*' and '*c*' increases due to Co^{2+} going in high spin state and the crystallite size reduces from 25 nm to 17 nm with the increase of Co content. Reduction in crystallite size was observed due to Zener-pinning effect in the material that hinders the crystallite growth and nucleation process. SEM Micrograph shows agglomerates or clusters of the nanoparticles that are almost spherical in shape. EDS spectra further confirmed that Zn, Co and O are the only constituent elements present in the samples.

Formation of nanoparticle samples was confirmed from TEM micrographs. FTIR spectra confirmed that Zn^{2+} ions have successfully replaced Co^{2+} ions in ZnO lattice. All other samples were prepared by the same method which provided encouraging results.

Development of single phase pure cubic bixbyite structure of $In_{(2-x)}Nd_xO_3$ nanoparticles with (x = 0, 0.10, 0.15 and 0.20) was confirmed from X-ray diffraction data [JCPDS card no. 71-2195]. Lattice constant '*a'* and Cell volume 'V' was found to increase with increasing Nd^{3+}content in the sample due to replacement of In^{3+} with Nd^{3+} in the In_2O_3 matrix. The crystallite size '*t*' found to decrease from 52nm to 44nm with increase in Nd^{3+} concentration due to Zener-pinning effect. SEM Micrograph shows agglomerates or clusters of the nanoparticles having almost spherical in shape nanoparticles. EDS spectra further substantiated formation of materials with In, Nd and O as the only constituent elements. The formation of nanoparticle samples was confirmed from TEM micrographs. FTIR spectrum further confirmed replacement of In^{3+} ions with Nd^{3+} ions in In_2O_3 matrix.

The third set of samples involving Ni doped CuO was also prepared by the same method. Formation of monophasic monoclinic crystalline structure of $Cu_{(1-x)}Ni_xO$ (x = 0, 0.05, 0.10, 0.15, 0.20, 0.25, 0.30) was confirmed from X-ray diffraction data [JCPDS card no. 65–2309]. Lattice constant '*a*', '*b*', '*c*' and Cell volume 'V' was found to decrease with increasing Ni^{2+}content in the sample due to substitution of Cu^{2+} with Ni^{2+} in the CuO matrix. The crystallite size '*t*' found to decrease from 78 nm to 48 nm with increase in Ni^{2+} concentration due to Zener-pinning effect. SEM Micrograph displayed agglomerates of the nanoparticles with almost spherical in shape. EDS spectra confirmed that Cu, Ni and O where the only constituent elements in the samples. TEM micrographs showed formation of nanoparticle samples. FTIR spectrum confirmed that Cu^{2+} ions have successfully substituted by Ni^{2+} in CuO matrix.

Optical properties such as UV-Visible spectroscopy and Photoluminescence spectroscopy measurement were made on the prepared samples. UV-Visible spectrum was employed to determine the energy band gap of all the prepared samples. The accurate measurements of energy band gap of prepared nanoparticles were determined from tauc's plot by using linear fit regression method.

UV–visible spectra for Co doped ZnO nanoparticles show that replacement of Zn^{2+} ions by Co^{2+} ions produces materials with reduced energy bang gap that changes from 3.02 ± 0.11 eV to 2.55±0.03 eV due to sp-d exchange interaction. The Photoluminescence (PL) emission spectra of the sample $Zn_{(1-x)}Co_xO$ (x = 0.05, 0.10, 0.15,0.20) obtained at room temperature with an excitation wavelength of 318 nm showed existence of defects like Zn vacancies (V_{Zn}), O vacancies (V_O), interstitial Zn (Z_{ni}), interstitial O (Oi), and formation of intermediate levels between valence band and conduction band due to Co^{2+} substitution at Zn^{2+} positions. PL lifetimes were found to range between 6μ Sec to 9μ Sec. UV–visible spectra for Nd doped In_2O_3 showed that the band gap decreases from 3.22±0.09 eV to 3.14±0.12 eV . This decrease in optical band gap could be attributed to crystal field splitting of *4f* levels in Nd^{3+} ions in In_2O_3 matrix. In case of Ni doped CuO the bang gap decreased from 3.33±0.12eV to 2.51±0.33eV. The decreasing of band gap was possibly due to *sp-d (s-d and p-d)* exchange interaction.

The magnetic properties such as Magnetic hysteresis (M-H curves), Field cooled and Zero field cooled (FC and ZFC) of Co doped ZnO, Nd doped In_2O_3 and Ni doped CuO nanoparticles were studied using vibrating sample magnetometer.

For Co doped ZnO nanoparticles, M-H curves shows that the samples behaves as diamagnetic material at lower doping concentration and as the doping concentration increases the sample behaves ferromagnetic at room temperature due to strong d-d exchange interaction. For further superior analysis about magnetic behavior Field cooled and Zero field cooled (FC and ZFC) measurement were done at 500 Oe which showed presence of ferromagnetism in the samples without any uncharacteristic behavior of antiferromagnetism in the nanosamples.

For Nd doped In_2O_3 nanoparticles, M-H curves shows typical diamagnetic nature for In_2O_3 nanoparticles and displayed ferromagnetic nature at room temperature due to exchange interaction between the localized *f* electrons in Nd^{3+} atoms as the doping concentration was increased. For further analysis about magnetic behavior Field cooled and Zero field cooled (FC and ZFC) measurement done at 500 Oe showed presence of ferromagnetism in the Nd^{3+} doped samples without any antiferromagnetism in samples.

For Ni doped CuO nanoparticles, M-H curves showed week ferromagnetic nature for CuO nanoparticles due to presence of oxygen vacancies and as the

doping concentration increases the sample showed ferromagnetic nature at room temperature due to spin-spin interaction among the nickel and the copper atoms. For further analysis about magnetic behavior Field cooled and Zero field cooled (FC and ZFC) measurement were at 500 Oe showed the presence of superparamagnetism and ferromagnetism in the Ni^{2+} doped samples.

The Electrical properties investigations namely thermoelectric power, DC resistivity, dielectric properties with respect to frequency and temperatures and impedance analysis were carried out on Co doped ZnO, Nd doped In_2O_3 and Ni doped CuO nanoparticles.

All Co doped ZnO nanoparticle samples, showed p-type semiconductor behavior for all till about 363K (90^oC) followed by a first order transition making it an n-type semiconductor beyond 363K 90^oC. DC resistivity dwindles with raise in temperature for all the samples showing semiconductor type of behavior. Dielectric constant (ε) showed decline trend with increasing frequency and similar type of behavior is shown by dielectric loss (tan δ) with a relaxation peak at lower frequencies. Dielectric constant (ε) and Dielectric loss (tan δ) with respect to temperature showed peaking behavior at lower temperature range due to relaxation phenomenon whereas 'ε' and 'tan δ' showed increasing variation with increase in temperature. Impedance analysis made on the samples displayed a semicircular arc for indicating dominating nature of grain boundaries resistance. Moreover the semicircular arc shrinks that is the grain boundary's resistance decreases with increases in Ni^{2+} content in the sample showing typical semiconductor nature of the material.

For Nd doped In_2O_3 nanoparticles, Seebeck coefficient shows that for all the materials behave like n-type semiconductor for entire temperature range. Similarly DC resistivity showed a typical semiconductor type of behavior with initial rise followed by a rapid fall with rising temperature. Dielectric constant and dielectric loss showed falling trend with increasing frequency. Dielectric constant (ε) and Dielectric loss (tan δ) dependent on temperature showed increasing variation due to space charge polarization. Impedance investigation made on the sample showed a semicircular arc indicating dominating nature of grain boundaries resistance in the material. The semicircular arc decreases that is the grain boundary's resistance decreases with increases in Ni^{2+} content in the sample signifying typical semiconductor nature of the material.

For Ni doped CuO nanoparticles. seebeck coefficient showed interesting behavior similar to Co doped ZnO samples. All the samples behave as p-type followed by a first order transition at 423K (150^{o}C) making it an n-type of semiconductors. DC resistivity analysis showed a semiconductor type of behavior for all the samples. Dielectric constant (ε) and dielectric loss (tan δ) displayed decreasing trend with increase in frequency. Dielectric constant (ε) and dielectric loss (tan δ) with respect to temperature showed rising behavior due to space charge polarization. Impedance analysis showed a semicircular arc for all the samples indicating dominating nature of grain boundaries resistance in the material. Moreover the semicircular arc reduces that is the grain boundary's resistance decreases with increases in Ni^{2+} content in the sample showing typical semiconductor nature of the material.

8.2 Further Scope of Work

Subsequent ideas for future research work in the area of nanoparticle DMS materials and unlocking the new fields of applications.

- Exploring these materials in thin film format using different methods such as pulse laser deposition technique, chemical vapor deposition technique, Molecular beam epitaxy etc. Could be very interesting.
- Development of theoretical model to visualize the structural, optical, magnetic and electrical nature of DMS nanomaterials in the powder and in the form of thin films could be another interesting area of research.
- Study on compositional changes by doping rare earth as well as transition elements to enhance other properties materials so as build up quality radiation sensors, gas sensors etc, or developing photo-catalyst with high efficiency and stability at low cost better safety to atmosphere and creatures.
- Application oriented research like making and testing of devices could be another interesting area of research in the field of engineering.

Since the field is vast lot or research is yet to be done in the area of nanoparticle DMS materials.

APPENDIX

❖ List of publications

1. Preparation characterization and magnetic properties of **$Zn_{(1-x)}Co_xO$** nanoparticle Dilute magnetic semiconductors, **Kapil Y. Salkar**, R.B. Tangsali, R.S. Gad, M. Jeyakanthan, Uma Subramanian, Superlattices and Microstructures 126 (2019) 158–173.

DOI: https://doi.org/10.1016/j.spmi.2018.12.013. Impact Factor: 2.385

2. Electrical properties of $Zn_{(1-x)}Co_xO$ dilute magnetic semiconductor Nanoparticles, **Kapil Y. Salkar**, R. B. Tangsali, R. S. Gad, Asnit Gangwar, N. K. Prasad, Journal of Materials Science: Materials in Electronics 30 (2019) 18374-18383.

DOI: https://doi.org/10.1007/s10854-019-02191-2. Impact Factor: 2.195

3. Induction of Nd^{3+} dependent ferromagnetic phase in $In_{(2-x)}Nd_xO3$ Nanoparticles prepared by combustion method. **Kapil Y. Salkar**, R. S. Gad, R. B. Tangsali (To be communicated)

4. Magnetic and Electrical properties of Ni^{2+} doped CuO DMS nanoparticles. **Kapil Y. Salkar**, R. S. Gad, R. B. Tangsali (To be communicated)

❖ Presentation/Participation In International/National Conferences

1) Presented a research paper (oral presentation) on **"Preparation And Investigation Into The Structural, Magnetic And Luminescence Properties Of $Zn_{(1-x)}Co_xo$ Nanoparticle Dilute Magnetic Semiconductor"** in an 4th International conference on Nanoscience and Nanotechnology **ICONN-2017**, organised by physics and nanotechnology, SRM university India held during 9th to 11th August 2017 in association with shizuoka university - Japan, GNS Science - New Zealand and National Chio Tung University - Taiwan co-sponsored by Science and Engineering Research Board (DST-SERB) and Council of Scientific And Industrial Research (CSIR) India.

2) Presented a research paper (oral presentation) on **"Preparation of Monophasic Co-doped ZnO DMS Nanoparticles with Enhanced Ferromagnetic Properties"** in an 4th International conference **NANOCON 018** - Nanotechnology : Applications, Advances and Innovations organised by Bharati Vidhyapeeth (Deemed to be university) College of Engineering, Pune, India in association with North Carolina state university, Greensboro, USA (NCAT), Tuskegee university, Alabama, USA (TU) and Drexel university, Philadelphia, USA held during 25th-26th October 2018.

3) Presented a research paper (oral presentation) on **"Preparation Characterization and Magnetic Property Investigations of $In_{2-x}Nd_xO_3$Nanoparticle DMS Material"** in an 1st International Conference on Materials and Environmental Science **ICMES-2018** held at shivaji University, Kolhapur India held during December 07-08, 2018, sponsored by CSIR New Delhi, organized in collaboration by Shri Yeshwant Patil Science College, Solankur and The New College, Kolhapur.

4) Presented a research paper (Poster presentation) on **"Induction of Nd^{3+} dependent ferromagnetic phase in $In_{(2-x)}Nd_xO3$ Nanoparticles prepared by combustion method"** in an International conference on Smart Materials and Nanotechnology **ICSMN-2020** held at SPSPM SKN Sinhgad College of Engineering Korti, Pandharpur, Maharashtra, India held on January 02-04, 2020.

5) Participated in the two days symposium on **"Recent Trends in Condensed Matter Physics and Materials"** held on March 12th – 13th, 2020 at Goa University.

6) Participated in the Webinar on **"Macro To Micro & Nano Approaches In Physics"** organized by PG & Research Department of Physics, Idhaya College for women, Kumbakonam, Thanjavur (Dt)-612001, on 28th may 2020 to 29th may 2020.

7) Participated in the National E-Conference on **"Smart Materials And Nanotechnology"** organized by Department of physics, Kamla Nehru Mahavidyalaya, Nagpur, India held on 30th May 2020.

❖ **Workshop Attended**

1) Attended a two days workshop on **Material Science** between University of Porto, University of Coimbra and Goa University held on November 18th and 19th 2019 at Goa University.

❖ **Awards /Studentships**

1) Awarded Goa university **Research Studentship** from the date of conformation 21/11/2017 to 30/06/2020.

2) Awarded as **Young Research Award** in **ICSMN-2020** at SPSPM SKN Sinhgad College of Engineering Korti, Pandharpur, Maharashtra, India.